MODELING VOLCANO AND EARTHQUAKE DEFORMATION FROM SATELLITE RADAR INTERFEROMETRIC OBSERVATIONS

A DISSERTATION
SUBMITTED TO THE DEPARTMENT OF GEOPHYSICS
AND THE COMMITTEE ON GRADUATE STUDIES
OF STANFORD UNIVERSITY
IN PARTIAL FULFILLMENT OF THE REQUIREMENTS
FOR THE DEGREE OF
DOCTOR OF PHILOSOPHY

Sigurjón Jónsson
June 2002

© Copyright by Sigurjón Jónsson 2002
All Rights Reserved

I certify that I have read this dissertation and that, in my opinion, it is fully adequate in scope and quality as a dissertation for the degree of Doctor of Philosophy.

Howard A. Zebker
(Principal Co-Adviser)

I certify that I have read this dissertation and that, in my opinion, it is fully adequate in scope and quality as a dissertation for the degree of Doctor of Philosophy.

Paul Segall
(Principal Co-Adviser)

I certify that I have read this dissertation and that, in my opinion, it is fully adequate in scope and quality as a dissertation for the degree of Doctor of Philosophy.

Gregory C. Beroza

Approved for the University Committee on Graduate Studies:

Abstract

Volcanic eruptions and earthquakes remain significant natural hazards that threaten life and property. While driven by underground processes inaccessible to us directly, they may nonetheless be studied by observing ground surface deformation. Here we study volcanic and seismic processes using spaceborne synthetic aperture radar interferometry (InSAR) and develop deformation modeling strategies exploiting the spatially-dense data − InSAR provides meter-scale resolution displacement maps at centimeter-level accuracy. We begin by characterizing the statistics of InSAR observations to better understand the technique's limitations and potential in studying ground deformation. We derive the covariance matrix of interferograms, identify its form with that of the atmospheric turbulence that is the main error source in these data, and show how the large data volume of an interferogram may be reduced without much loss of integrity so that inverse methods may be used in analysis. InSAR reveals unsuspected widespread volcanic deformation in the Galápagos archipelago throughout the past decade. Summit inflation and deflation patterns indicate shallow magma chambers beneath each volcano at depths ranging from 2 to 5 km. In some cases, a simple point pressure source in an elastic medium reproduces the observed inflation, while in others more complicated models are required to image the expanding magma body. On Fernandina island, a dipping dike appears to have fed a flank eruption in 1995, while time-variable deformation patterns on Sierra Negra volcano on Isabela island suggest that trapdoor faulting occurred, triggered by strong inflation. We also study the 1999 magnitude 7.1 Hector Mine, California earthquake and find mainly right-lateral strike-slip motion on a near-vertical fault, with a small reverse faulting component accounting for less than 10% of the total moment. Similar analysis for two magnitude 6.5 earthquakes in south Iceland in 2000 shows two parallel and vertical right-lateral strike-slip faults, separated by 18 km. Here observed postseismic deformation follows from poro-elastic rebound in the 1-2 months after the earthquakes. Since the aftershock sequence decays on a 3-4 year time scale, pore-pressure changes play an insignificant role in controlling aftershock decay for these events.

Acknowledgements

I want to begin to thank my advisors Howard Zebker and Paul Segall. Their advice and support have been encouraging, tireless, and fundamental to the research summarized in this thesis. I am also grateful to David Pollard, Amos Nur, Gregory Beroza, and Norman Sleep for useful advice during annual review meetings and for constructive comments that improved this thesis.

Many people deserve acknowledgement for their contribution and help on this work. Special thanks go to Falk Amelung (University of Hawaii) for the collaboration on the Galápagos project and for guiding me through the jungle of InSAR image processing, and to Rikke Pedersen (Nordic Volcanological Institute, Iceland) for enjoyable collaboration on the South Iceland project. Chapter 2 benefitted from fruitful discussions with Ramon Hanssen (Delft University, The Netherlands) and Mark Simons (Caltech). The work reported on in Chapter 3 was done in collaboration with Falk Amelung, Howard Zebker, and Paul Segall, and I thank Dennis Geist (University of Idaho) and Paul Lundgren (JPL) for constructive reviews. Dennis Geist made Chapter 4 possible by taking me along to the Galápagos, and I also thank other members of the 2001 Galápagos GPS field expedition for their help and good company. Furthermore, thanks go to Keith A. Howard (USGS, Menlo Park) for providing aerial photographs of Sierra Negra.

I acknowledge the contribution of my co-authors on the study presented in Chapter 5: Howard Zebker, Peter Cervelli, and Paul Segall at Stanford, and Harold Garbeil, Peter Mouginis-Mark, and Scott Rowland at the University of Hawaii. I also thank Falk Amelung for his help on the data processing and Mark Simons for his comments. Likewise, I thank my co-authors of the study in Chapter 6: Howard Zebker, Paul Segall, and Falk Amelung. Additional thanks go to Duncan Agnew (Scripps Institute of Oceanography) for providing campaign GPS data, Curtis Chen (JPL) for his help with phase unwrapping, Egill Hauksson (Caltech) for giving us aftershock locations, and to Pierre Briole (IPGP, Paris) and Barry Parsons (Oxford University) for thoughtful reviews.

The work in Chapter 7 and Chapter 8 was conducted in collaboration with Rikke Pedersen and Paul Segall. Thanks go also to Thóra Árnadóttir and Freysteinn Sigmundsson (both at Nordic Volcanological Institute) for providing GPS data and for discussions. Grímur Björnsson (National Energy Authority in Iceland) supplied water level data from geothermal wells. Gunnar Gudmundsson and Ragnar Stefánsson (both at the Iceland Meteorological Office) kindly gave us preliminary earthquake locations. Amy Clifton (Nordic Volcanological Institute) and Páll Einarsson (University of Iceland) provided data of the mapped surface ruptures. In addition, thanks go to Kristján Ágústsson (Iceland Meteorological Office) and Kurt Feigl (CNRS, Toulouse) for fruitful discussions.

I thank Peter Cervelli for good collaboration on various projects and for a memorable field trip to Hawaii. I have also enjoyed the company of other members of the crustal deformation group at Stanford: Jessica Murray, Maurizio Battaglia, Shelley Kenner, Kaj Johnson, Susan Owen, Noah Bechor, Andy Hooper, Yosuke Aoki, Anthony Mossop, Shinichi Miyazaki, and Jeff McGuire. Likewise, collaboration, seminars, and discussions about science and politics with members of the radar interferometry group will be remembered: Jörn Hoffmann, Weber Hoen, Leif Harcke, Curtis Chen, Margrit Gelautz, Ramon Hanssen, Fayaz Onn, Mamta Sinha, and Sang-Ho Yun.

Special thanks go to my office mate, Jörn Hoffmann, for useful discussions, countless coffee cups, lunch hours, and all the good time in and away from the office. Also, Darcy Karakelian and John Townend have often provided humorous perspective when the research was not going anywhere. Many thanks to the Scandinavian mafia at Stanford: Lasse, Kristian, Martin, Jo, Per, and others, for all the fun and soccer playing, and to Thráinn, Elsa, and Kristín for keeping my Icelandic alive with numerous fun discussions. My sister Dagbjört and my friends Ómar and Hjalti deserve to be acknowledged for realizing that California is not further away from Iceland than Iceland is from California! I also thank my family for their support, my parents Jón and Ingunn, my sisters Björg and Dagbjört, and my brother Áskell. Finally, special thanks to Nikki for everything she has done for me.

Most of the radar data used in this thesis were provided by the European Space Agency through several different research projects. The thesis work was funded by the Geophysics Department at Stanford, NASA, the National Science Foundation, and by the Geophysics Department Chair's Fellowship program. In addition, I would like to acknowledge support from the Helga Jónsdóttir and Sigurlidi Kristjánsson Memorial Fund, the NATO science fellowship program, and the Scandinavian-American Foundation.

Contents

Abstract **iv**

Acknowledgements **v**

1 Introduction **1**

1.1 Volcanoes Studied from InSAR Observations 2

1.2 Seismic Deformation Observed by InSAR 5

1.3 Contributions 6

1.4 Thesis Roadmap 9

2 InSAR Covariance Estimation and Data Reduction **11**

2.1 Abstract 11

2.2 Introduction 12

2.3 Noise Analysis of Three Interferograms 14

2.3.1 Noise Isotropy 16

2.3.2 Noise Power Spectrum 20

2.3.3 Noise Covariance Functions 23

2.4 Example of Local Covariance Function Estimation 26

2.4.1 Noise Spectral Analysis 27

2.4.2 Obtaining the Covariance Function 28

2.4.3 Covariance Function from 2D Auto-correlation 30

2.4.4 Covariance Estimation at Fernandina 31

2.5 InSAR Data Reduction in the Frequency Domain 33

2.5.1 Power Spectrum of Volcanic Inflation 33

2.5.2 Frequency Domain Optimization 34

2.5.3 Deformation due to an Earthquake 38

2.6 Data Reduction in the Image Domain . . . 39
2.6.1 Sub-sampling onto Regular Grid . . . 40
2.6.2 Quadtree Decomposition . . . 40
2.7 Model Calculations . . . 43
2.7.1 Covariance Matrix for Reduced Dataset . . . 43
2.7.2 Model Optimization . . . 44
2.8 Conclusions . . . 46
2.9 Appendix A . . . 47

3 Widespread Uplift and 'Trapdoor' Faulting on Galápagos Volcanoes Observed with Radar Interferometry 50
3.1 Abstract . . . 51
3.2 Introduction and Data Analysis . . . 51
3.3 Deformation Modeling and Discussion . . . 56

4 Sierra Negra Trapdoor Faulting: Field Observations and Radar Range Offset Measurements 61
4.1 Abstract . . . 61
4.2 Introduction . . . 62
4.3 Sierra Negra Fieldwork . . . 64
4.3.1 Map of Intra-Caldera Faults . . . 64
4.3.2 Evidence of Recent Faulting . . . 67
4.4 SAR Range Offset Measurements of Sierra Negra . . . 68
4.5 Discussion . . . 71
4.6 Conclusions . . . 74
4.7 Appendix A: Area Covered during 2001 Fieldwork . . . 75
4.8 Appendix B: Description of Faulting Evidence . . . 76

5 A Shallow-Dipping Dike fed the 1995 Flank Eruption at Fernandina Volcano, Galápagos, Observed by Satellite Radar Interferometry 80
5.1 Abstract . . . 80
5.2 Introduction . . . 81
5.3 Data Analysis and Results . . . 81
5.4 Modeling . . . 86

5.5 Discussion and Conclusions 86

6 Fault Slip Distribution of the 1999 M_w7.1 Hector Mine Earthquake, California, estimated from Satellite Radar and GPS Measurements 89

6.1 Abstract 89
6.2 Introduction 90
6.3 Data Analysis 92
6.3.1 Radar Interferograms 92
6.3.2 Azimuth offsets of radar amplitude images 95
6.3.3 Campaign GPS data 97
6.3.4 Comparison Between Datasets 97
6.3.5 Data Reduction 98
6.4 Modeling 100
6.4.1 Fault Trace 100
6.4.2 Fault Dip 101
6.4.3 Variable Strike-Slip 101
6.4.4 Strike-Slip Distribution Determined from each Dataset Independently 103
6.4.5 Importance of Dip-Slip 107
6.4.6 Comparison with Mapped Fault Offset 108
6.5 Conclusions 112
6.6 Appendix A: Smoothing Operator **D** 112

7 Fault Geometry and Slip Distribution of the June 17 and June 21, 2000 Earthquakes (M_w6.5) in South Iceland 114

7.1 Abstract 114
7.2 Introduction 115
7.3 Observed Coseismic Ground Deformation 117
7.3.1 InSAR Data 117
7.3.2 Coseismic GPS Displacements 120
7.4 Estimating the Geometry of the Two Faults 121
7.4.1 The Fault Geometry Problem 121
7.4.2 The Optimal Fault Geometry 124
7.5 Variable Fault Slip 129
7.5.1 The Slip Distribution Problem 129

7.5.2 Optimal Strike-slip Distribution 131
7.5.3 Slip Distribution Resolution 131
7.5.4 Model Prediction 133
7.6 Future Improvements 133
7.7 Conclusions 136

8 Poro-elastic Rebound after the two June 2000 South Iceland Earthquakes: Implications for Aftershock Decay 138
8.1 Abstract 138
8.2 Introduction 139
8.3 Observed Postseismic Deformation 139
8.4 Mechanisms for postseismic Deformation 141
8.5 Implications for Aftershock Decay 146

9 Bibliography 148

List of Tables

1.1 Civilian synthetic aperture radar missions 2
1.2 Published InSAR studies on volcanoes 4
1.3 InSAR studies on seismic deformation 7

2.1 Optimum model parameters using variable weighting 45

3.1 Deformation of Galápagos volcanoes 55

4.1 Categories of evidence for recent faulting at Sierra Negra volcano 77
4.2 Description of field evidence for recent faulting at Sierra Negra 77

5.1 Model parameters for the Fernandina dike intrusion 88

6.1 Hector Mine interferograms 93
6.2 Deformation data of the Hector Mine earthquake 98
6.3 Hector Mine fault models 103

7.1 Information about South Iceland coseismic deformation data 121
7.2 Parameters of the June 17 fault from various sources 125
7.3 Parameters of the June 21 fault from various sources 126

List of Figures

1-1 World's active volcanoes 3

2-1 Three interferograms of western Galápagos islands 15
2-2 Sub-images from the 6 month interferogram shown in Figure 2-1 17
2-3 Sub-images from the 13 month interferogram shown in Figure 2-1 17
2-4 Sub-images from the 61 month interferogram shown in Figure 2-1 18
2-5 A radon transform of a test image 19
2-6 Radon transform of four sub-images showing variable anisotropy 19
2-7 Calculation of rotationally averaged spectrum 20
2-8 One-dimensional rotationally averaged spectra for Galápagos sub-images . . 21
2-9 Same as Figure 2-8, except for shifted power spectra 22
2-10 Calculation of an empirical covariance function. 24
2-11 Empirical covariance functions of Galápagos sub-images. 25
2-12 Interferogram showing 20 cm uplift at Darwin volcano 26
2-13 Five noise sub-images from Darwin volcano 27
2-14 Power spectra of Darwin sub-images 28
2-15 Sample variogram calculation for the Darwin interferogram 29
2-16 Sample variogram and covariance function for Darwin volcano 30
2-17 Calculation of a covariance function using 2D auto-correlation 31
2-18 Noise power spectra from Fernandina volcano 32
2-19 Covariance function for the Fernandina interferogram 32
2-20 Power spectrum of simulated volcanic deformation 35
2-21 Low-pass filtering of simulated volcano deformation 35
2-22 Frequency domain optimization 38
2-23 Power spectra for examples of earthquake deformation 39
2-24 Quadtree partitioning of the Darwin interferogram 42

2-25 InSAR covariance matrix 44

3-1 InSAR mosaic of Isabela and Fernandina islands, western Galápagos 52
3-2 Uplift of Sierra Negra volcano during three time periods 54
3-3 Deformation at Darwin volcano during 1992-1998 57
3-4 Two models for the uplift of Sierra Negra volcano 58
3-5 Model prediction with trapdoor faulting at Sierra Negra 59

4-1 Map of Sierra Negra volcano 63
4-2 Sierra Negra intra-caldera faults and topography 65
4-3 InSAR observations in the south part of Sierra Negra caldera 66
4-4 Recent faulting in Sierra Negra caldera 68
4-5 Amount of recent faulting at Sierra Negra 69
4-6 Explanation of amplitude image range offsets 69
4-7 Amplitude image range offsets of Sierra Negra caldera 70
4-8 Trapdoor faulting at Sierra Negra 73
4-9 Fieldwork at Sierra Negra caldera 76

5-1 Map of Fernandina island, western Galápagos 82
5-2 InSAR and SPOT images of the southwest flank of Fernandina 84
5-3 Model prediction due to a dike intrusion 85
5-4 InSAR data and the model prediction along profiles 87

6-1 Map of the Hector Mine epicentral area in Mojave desert, California 91
6-2 Coseismic deformation of the Hector Mine earthquake 94
6-3 Coseismic offsets between radar amplitude images 96
6-4 Quadtree partitioning of InSAR data 99
6-5 Estimated strike-slip distribution for three different smoothing weights . . . 104
6-6 Trade-off curve between model misfit and solution smoothness 105
6-7 Strike-slip models determined using different datasets independently 106
6-8 Strike-slip and dip-slip distribution for the Hector Mine earthquake 108
6-9 InSAR model predictions and residuals 109
6-10 Model predictions and residuals for radar image offsets and GPS 110
6-11 Hector Mine fault offset at surface 111
6-12 Schematic figure showing fault patches 113

7-1 Map of the South Iceland Seismic Zone 116
7-2 Coseismic interferograms and GPS displacements in south Iceland 119
7-3 Two-dimensional quantization of the unwrapped interferograms 120
7-4 Aftershocks, fault ruptures, and the estimated fault geometry 128
7-5 Right-lateral strike-slip distribution for the south Iceland earthquakes . . . 131
7-6 Two checkerboard tests to examine strike-slip resolution 132
7-7 Model prediction and residual for the T52 interferogram. 134
7-8 Model prediction and residual for the T95 interferogram. 135

8-1 Map of south Iceland 140
8-2 Postseismic deformation in south Iceland 142
8-3 Postseismic deformation shown along profiles 143
8-4 Water-level changes in south Iceland 145
8-5 Aftershock decay in south Iceland 147

List of Abbreviations

1D, 2D, 3D	One-, Two-, Three-dimensional
ALOS	Advanced Land Observing Satellite
ASI	Italian Space Agency
DEM	Digital Elevation Model
DLR	German Aerospace Center
CSA	Canadian Space Agency
ERS	European Remote Sensing Satellite
ESA	European Space Agency
GB	Gigabytes
GPS	Global Positioning System
InSAR	Interferometric Synthetic Aperture Radar
JPL	Jet Propulsion Laboratory
MAR	Mid-Atlantic Ridge
MB	Megabytes
MORB	Mid-Ocean Ridge Basalt
LOS	Line of sight
NASA	National Aeronautics and Space Administration
NASDA	National Space Development Agency of Japan
NIMA	National Imagery and Mapping Agency
SAR	Synthetic Aperture Radar
SARIO	Synthetic Aperture Radar Image Offsets
SISZ	South Iceland Seismic Zone
SNR	Signal to Noise Ratio
SRTM	Shuttle Radar Topography Mission
TOPSAR	Topographic Synthetic Aperture Radar
VLBI	Very Long Baseline Interferometry

Chapter 1

Introduction

Volcanic eruptions and earthquakes have caused hundreds of thousands of casualties in the world during the past decades. The hazard will increase in the future as many threatened areas are in developing countries where population is fast growing. Nothing will prevent future volcanic eruptions and earthquakes from happening so preparedness is the best way to mitigate the hazard. Understanding the nature of active volcanism and earthquakes is essential to identify where and when potential danger arises. Although short term earthquake prediction remains as the holy grail of geophysics, we can now, in some cases, successfully predict volcanic eruptions where good instrumentation is in place and real-time monitoring is conducted. However, this is currently the case on only a few of world's 1500 active volcanoes.

Synthetic Aperture Radar (SAR) satellites have revolutionized the potential to monitor volcanoes and to study earthquake and volcano deformation. Repeat orbit Synthetic Aperture Radar Interferometry (InSAR) can provide ground displacement maps from anywhere on land with centimeter-level accuracy. The technique is unique for its global coverage, remote observation, and the high spatial resolution of the observations, but is sometimes limited by signal loss caused by interferometric decorrelation [*Zebker et al.,* 1992a] and by poor temporal sampling of the few satellites that currently are in orbit (Table 1.1). Many authors have already demonstrated how the various geophysical processes can be studied using InSAR data [e.g., see *Massonnet and Feigl,* 1998] and some important scientific contributions have been published, some of which we discuss later in this chapter.

In this thesis we study volcano and earthquake deformation from InSAR observations and explore some general InSAR data issues such as data noise analysis and data reduction (Chapter 2). The first study area is the Galápagos volcanic province (Chapters 3-5) where widespread deformation occurred during the last decade and various volcanic processes

Table 1.1: List of past, present, and future civilian Interferometric Synthetic Aperture Radar (InSAR) missions to explore the Earth from space. L-band corresponds to carrier wavelength of ∼24 cm, C-band to ∼5.7 cm, and X-band to ∼3.1 cm.

Satellite	*Mission period*	*Band*	*Agency*
Seasat	1978	L	NASA
SIR-B*	1984	L	NASA
ERS-1	1991-2000	C	ESA
JERS-1	1992-1998	L	NASDA
SIR-C/X-SAR*	1994	L/C/X	NASA/ASI
ERS-2	1995 - present	C	ESA
RADARSAT-1	1995 - present	C	CSA
SRTM*	2000	C/X	JPL/NASA/NIMA/DLR/ASI
ENVISAT-1	2002 - present	C	ESA
RADARSAT-2	launch in 2003	C	CSA
ALOS	launch in 2004	L	NASDA

* Space shuttle missions limited to several days.

observed, such as volcanic inflation and deflation, deformation due to dike intrusion, lava flow subsidence, etc. Then we turn our attention to coseismic deformation and use InSAR along with other deformation data to estimate the fault slip distribution of the 1999 Hector Mine, southern California, earthquake (Chapter 6). And finally we study the coseismic and postseismic deformation associated with two earthquakes that occurred in south Iceland in June of 2000 and examine what implications our interpretation has for the decay of aftershocks (Chapters 7-8).

1.1 Volcanoes Studied from InSAR Observations

Satellite radar interferometry can potentially be used to monitor all active land volcanoes in the world (Figure 1-1), which is an unthinkable task using conventional geodetic observations. The main advantages of the InSAR technique for studying volcanic deformation is (1) the high spatial resolution of these data that provide continuous maps of the deformation, (2) the low cost as no fieldwork is needed, (3) the global coverage, and (4) the safety of remotely monitoring active volcanoes from satellites. However, there are several important limitations to InSAR that commonly apply when volcanoes are studied. Interferometric decorrelation causes signal loss in areas with frequent snow cover and in densely vegetated areas [*Zebker et al.,* 1992a]. This is a major problem at high latitudes (e.g. in Alaska) and in the tropics (e.g. in Indonesia). Another problem is the poor temporal resolution of InSAR observations as only three satellites are currently in orbit making real-time monitoring

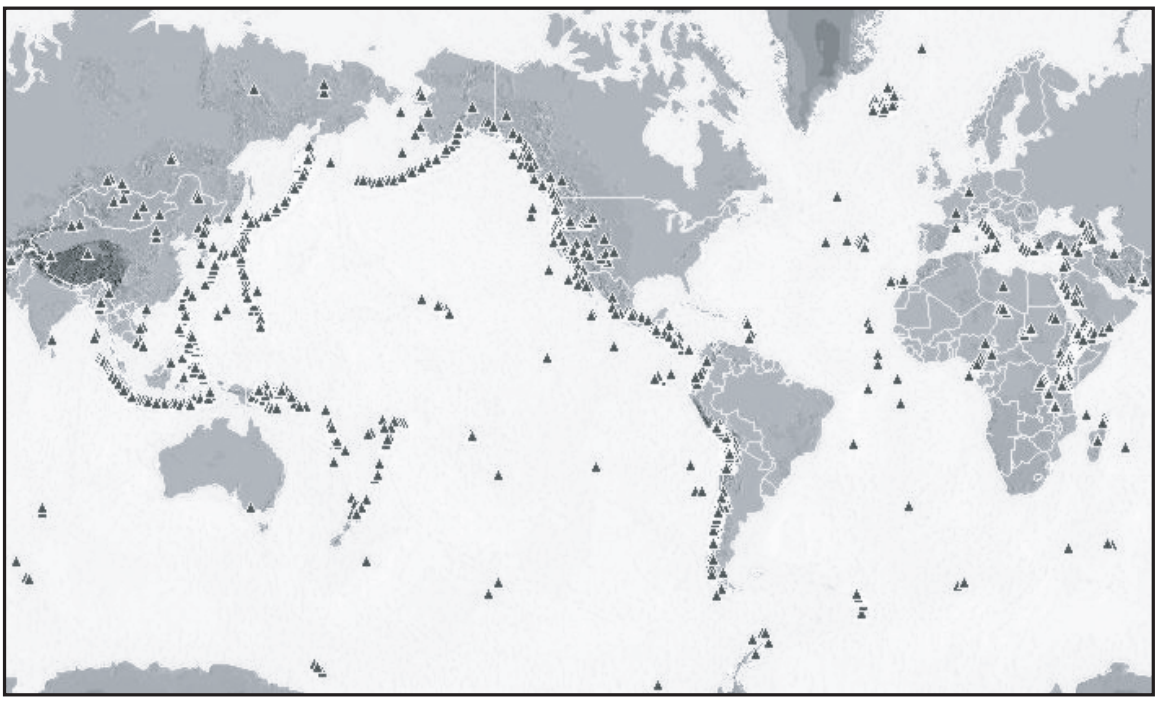

Figure 1-1: Map showing active land volcanoes around the globe (from the Global Volcanism Program online, Smithsonian Institution).

efforts limited to a single observation every few days. Atmospheric noise in InSAR data can be a problem as well and the noise is sometimes elevation dependent that makes it difficult to distinguish volcano centered deformation from atmospheric delay signals [*Delacourt et al.,* 1998; *Beauducel et al.,* 2000].

The first study on volcano deformation observed by InSAR was published in 1995 describing deflation on Etna volcano, Italy [*Massonnet et al.,* 1995]. Many InSAR studies followed describing deformation due to various volcanic processes. Several authors have reported on volcano inflation [e.g., *Lanari et al.,* 1998; *Lu et al.,* 2000a;] or deflation [e.g., *Sigmundsson et al.,* 1997; *Lu et al.,* 1998; *Avallone et al.,* 1999] due to pressure changes in subsurface magma systems or due to other processes. Deformation due to dike intrusions has been reported in the Galápagos [*Jónsson et al.,* 1999] and on La Réunion island [*Sigmundsson et al.*, 1999]. Examples of deformation due to volcano-tectonic interactions have also been studied [*Feigl et al.,* 2000; *Nishimura et al.,* 2001]. Most of published volcano studies based on InSAR observations are listed in Table 1.2.

Table 1.2: List of publications that have used InSAR to study volcanoes.

References	*Volcano studied*	*Satellite*
Massonnet et al., 1995	Etna, Italy	ERS-1
Zebker et al., 1996	Kilauea, Hawaii	SIR-C
Briole et al., 1997	Etna, Italy	ERS-1
Lu et al., 1997	New Trident volcano, Katmai, Alaska	ERS-1
Sigmundsson et al., 1997	Krafla volcano, Iceland	ERS-1/2
Thatcher et al., 1997	Long Valley caldera, California	ERS-1/2
Vadon and Sigmundsson, 1997	Reykjanes peninsula, Iceland	ERS-1
Jónsson et al., 1998	Vatnajökull, Iceland	ERS-1/2
Lanari et al., 1998	Etna, Italy	ERS-1/2
Lu and Freymueller, 1998	Katmai volcano group, Alaska	ERS-1
Lu et al., 1998	Okmok, Alaska	ERS-1/2
Wicks et al., 1998	Yellowstone caldera, Wyoming	ERS-1/2
Avallone et al., 1999	Campi Flegrei, Italy	ERS-1/2
Jónsson et al., 1999	Fernandina volcano, Galápagos	ERS-1/2
Sigmundsson et al., 1999	Piton du la Fournaise, La Réunion	RADARSAT-1
Amelung et al., 2000a	Galápagos volcanoes	ERS-1/2
Amelung et al., 2000b	Gada 'Ale volcano, Afar, Ethiopia	ERS-1/2
Feigl et al., 2000	Hengill, Iceland	ERS-1/2
Lu et al., 2000a	Westdahl, Alaska	ERS-1/2
Lu et al., 2000b	Akutan, Alaska	ERS-1/2
Lu et al., 2000c	Okmok, Alaska	ERS-1/2
Massonnet and Sigmundsson, 2000	various volcanoes	various
Zebker et al., 2000	various volcanoes	various
Fialko and Simons, 2001	Socorro magma body, New Mexico	ERS-1/2
Henriot et al., 2001	Krafla, Iceland	ERS-1/2
Nishimura et al., 2001	Iwate, Japan	JERS-1
Stevens et al., 2001	Etna, Italy	ERS-1/2
Mann et al., 2002	Okmok, Alaska	ERS-1/2

The high spatial resolution of InSAR allows scientists to study small scale deformation due to shallow or surface processes that usually are not detected with other measurements as conventional geodetic networks are sparse. Lava flow subsidence due to cooling or physical settling has been observed by InSAR in several places such as on Etna, in Iceland, and in the Galápagos [*Briole et al.,* 1997; *Sigmundsson et al.*, 1997; *Amelung et al.,* 2000a; *Stevens et al.*, 2001]. In addition, interferometric decorrelation mapping was used to study daily lava flow activity on Kilauea volcano, Hawaii [*Zebker et al.,* 1996].

Many authors have used InSAR observations to study volcanoes where no other deformation measurements are available due to the remoteness of the volcanoes or limited resources, e.g., in areas like the Aleutians, Alaska [e.g., *Lu et al.,* 2000a,b,c], and in the Galápagos (see Chapter 3). These studies have opened the doors to a new world of knowledge about these volcanoes, revealing a number of different volcanic processes. This also illustrates the monitoring potential of InSAR in identifying volcanoes that are inflating.

1.2 Seismic Deformation Observed by InSAR

The earthquake prediction potential of InSAR observations is limited. However, the technique offers unique possibilities to observe and study coseismic and postseismic deformation, and even inter-seismic deformation. The main advantages of InSAR for studying coseismic deformation is again the low cost and the high spatial resolution of the observations, but also the existing SAR data archive that covers most subaerial areas in the world. This is particularly important because many earthquakes occur in areas where no conventional geodetic measurement networks exist, and therefore, InSAR observations are often the only measurements available of the coseismic deformation field.

The first earthquake studies using InSAR were on the 1992 Landers (California) earthquake and these studies clearly demonstrated the power of this technique to observe coseismic deformation [*Massonnet et al.,* 1993; *Zebker et al.,* 1994]. Many studies followed and some authors have made important contributions to earthquake science. InSAR measurements have allowed researchers to estimate the fault slip distribution of large earthquake, such as the 1992 Landers and 1999 Hector Mine (California) earthquakes [e.g. *Hernandez et al.,* 1999; *Jónsson et al.,* 2002a]. Signs of asymmetric coseismic displacements were observed after the M_w7.6 Manyi (Tibet) earthquake, indicating a factor of two difference between the compressional and extensional Young's modulii in the shallow crust [*Peltzer*

et al., 1999]. *Michel et al.* [1999a] began to use pixel offsets between two radar amplitude images to measure ground displacements parallel to the satellite azimuth direction. Later, these measurements were used along with InSAR data from both ascending and descending orbits to reconstruct the full 3D coseismic ground displacements of the Hector Mine, southern California earthquake [*Fialko et al.,* 2001]. Several other seismic deformation studies based on InSAR observations are listed in Table 1.3.

Some important contributions have been made in studying postseismic deformation using InSAR data. *Peltzer et al.* [1996] explained postseismic deformation observed in fault step-overs after the Landers earthquake with poro-elastic rebound caused by pore-pressure dissipation after the earthquake. Signs of non-linear sub-crustal viscosity were reported by *Pollitz et al.* [2001] after the Landers and Hector Mine earthquakes showing gradual viscosity increase during the years following the earthquakes.

Inter-seismic deformation is difficult to observe with InSAR as the long spatial wavelengths of the deformation can be impossible to distinguish from residual orbital signals and long wavelength noise in interferograms. However, *Wright et al.* [2001a] successfully observed strain buildup in interferograms across the eastern Anatolian fault in Turkey.

1.3 Contributions

In this thesis we use InSAR to study both volcanic deformation in the Galápagos and seismic deformation in California and in Iceland. The scientific contributions of this work can be put in three categories. First are contributions to volcano and earthquake research in general where we observe, explain, and simulate many ground deformation phenomena to learn about various geophysical processes, some of which have not been observed or realized before. Second are contributions to the ongoing research activity at the study locations mentioned above, which are of particular interest to those who also study these areas or similar ones. And third are contributions to the methodology on how to use InSAR observations in crustal deformation studies, which are of interest to scientists who use InSAR data to study various geophysical problems.

The research reported on in this thesis is not focussed on solving a single large geophysical problem. Instead we have tackled a number of smaller problems that may sometimes seem only loosely related to one another. Below we summarize the main scientific contributions of this thesis:

Table 1.3: List of several publications that have used InSAR data to study seismic deformation.

Coseismic deformation:	Event	Satellite
Massonnet et al., 1993	1992 Landers, California	ERS-1
Zebker et al., 1994	1992 Landers, California	ERS-1
Feigl et al., 1995	1992 Landers aftershock, California	ERS-1
Massonnet and Feigl, 1995	1993 Eureka Valley, California	ERS-1
Peltzer and Rosen, 1995	1993 Eureka Valley, California	ERS-1
Meyer et al., 1996	1995 Grevena, Greece	ERS-1
Murakami et al., 1996	1994 Northridge, California	JERS-1
Ozawa et al., 1997	1995 Kobe, Japan	JERS-1
Fujiwara et al., 1998	1997 Kagoshima-ken-hokuseibu, Japan	JERS-1
Tobita et al., 1998	1995 North Sakhalin, Russia	JERS-1
Hernandez et al., 1999	1992 Landers, California	ERS-1
Peltzer et al., 1999	1997 Manyi earthquake, Tibet	ERS-2
Wright et al., 1999	1995 Dinar earthquake, Turkey	ERS-1/2
Pedersen et al., 2001	2000 South Iceland earthquakes	ERS-2
Wright et al., 2001b	1999 Izmit, Turkey	ERS-1/2
Bürgmann et al., 2002	1999 Düzce, Turkey	ESR-1/2
Feigl et al., 2002	1999 Izmit, Turkey	ERS-1/RADARSAT-1
Jónsson et al., 2002a	1999 Hector Mine, California	ERS-2
Pedersen et al., 2002	2000 South Iceland earthquakes	ERS-2
Postseismic deformation:		
Massonnet et al., 1994; 1996	1992 Landers, California	ERS-1
Peltzer et al., 1996; 1998	1992 Landers, California	ERS-1
Pollitz et al., 2001	1999 Hector Mine, California	ERS-2
Jónsson et al., 2002b	2000 South Iceland earthquakes	ERS-2
Aseismic deformation:		
Rosen et al., 1998	San Andreas fault, California	ERS-1
Bürgmann et al., 2000	Hayward fault, California	ERS-1/2
Fruneau et al., 2001	Southwest Taiwan	ERS-1/2
Wright et al., 2001a	North Anatolian Fault, Turkey	ERS-1/2

1. We find InSAR noise to have most of its power in the low frequencies with a noise spectrum that often follows a power law with index between -3 and -1. This noise structure implies that the distance at which two data points become uncorrelated in an interferogram depends on the spatial support of the data, i.e., the size of the image that is being studied, because the noise affects all spatial scales.

2. InSAR observations show that nearly all the volcanoes in the western Galápagos have been actively deforming during the past decade due to various volcanic processes. Nothing was known about the present day deformation in the Galápagos prior to our observations. Inflation and deflation of Galápagos volcanoes indicate that magma resides in shallow magma chambers beneath each volcano. The magma chamber depths vary from 2 to 5 km.

3. For 40 years, the simple Mogi point source model has successfully explained observed inflation and deflations on number of volcanoes. However, at Sierra Negra volcano (Galápagos) we can rule out point source models and are able to move on to use InSAR observations to image the expanding magma body and simulate it with a variable opening sill.

4. We find that inflation at Sierra Negra triggered faulting on inner caldera fault system such that the caldera floor hinged up like a 'trapdoor'. Repeated trapdoor faulting may help accommodating large magma volumes and prevent summit eruptions. The amount of the near-vertical faulting was observed directly using range pixel offsets between two radar amplitude images, a method that has never been applied before to study crustal deformation.

5. We find that postseismic deformation in south Iceland after two M_w6.5 earthquakes is due to poro-elastic rebound while we can rule out competing mechanisms such as fault afterslip and viscous flow of the crustal substrate. The duration of the rebound was 1-2 months indicating that pore-pressures dissipated during this time. The aftershocks, however, are projected to last for 3-4 years. Therefore, we conclude that pore-pressure changes play an insignificant role in controlling the aftershock decay for these events.

1.4 Thesis Roadmap

Each chapter of this thesis is written as an independent study with some chapters based on manuscripts that have already been published in scientific journals or are in preparation for journal submission. Therefore, the reader can read the chapters of interest without having to look up background material in previous chapters. Each chapter begins with an abstract that is followed by an introduction to the material of that chapter, and each chapter ends with a conclusion section where the main results are described.

In Chapter 2 we analyze InSAR noise and construct simple methods to determine data covariance locally in deformation interferograms. We also address several data reduction algorithms to ease model calculations, and propagate the full interferogram data covariance to the reduced data set. The importance of including InSAR data covariances in model calculations is briefly investigated as well. The research project reported on in this chapter is still in progress. Upon completion the plan is to submit this material to the Journal of Geophysical Research.

In Chapter 3 we turn our attention to volcanic deformation in the western Galápagos where we find that most of the volcanoes have been inflating during the past decade. We look in detail at the deformation at Darwin and Sierra Negra volcanoes. Inflation at Darwin is circularly symmetric and can be modeled as a response to a point pressure increase at 3 km depth. Meanwhile, inflation at Sierra Negra is both spatially and temporarily variable and can not be explained with simple models. There we attempt to image the expanding magma body using a variable opening sill. We also describe and model trapdoor faulting observed within Sierra Negra caldera on an intra caldera fault system. This chapter is based on material that we have already completed and was published as the cover feature of Nature in October 2000 [*Amelung et al.,* 2000a].

In the following chapter we study Sierra Negra volcano in further detail to verify that trapdoor faulting did occur and discuss the mechanisms driving the faulting. We report on evidence of recent faulting detected during fieldwork in 2001. In addition, we provide direct measurements of the faulting using range pixel offset measurements between two SAR amplitude images acquired before and after the faulting occurred.

In Chapter 5 we analyze the deformation observed following the 1995 flank eruption on Fernandina volcano, Galápagos. The deformation indicates that a non-vertical dike propagated from the central caldera into the southwest flank to feed this radial fissure

eruption. This material has been published in Geophysical Research Letters [*Jónsson et al.,* 1999].

We leave volcanic deformation and begin to study seismic deformation in Chapter 6. Here we examine the coseismic deformation of the 1999 M_w7.1 Hector Mine earthquake, southern California. We combine InSAR and GPS data as well as azimuth pixel offset measurements of radar amplitude images to derive the fault slip distribution of the earthquake. This study has been published in Bulletin of Seismological Society of America [*Jónsson et al.,* 2002a].

In Chapter 7 we turn our focus to south Iceland where two M_w6.5 earthquakes occurred in June of 2000. Here we analyze the observed coseismic deformation to estimate the geometry of the two faults and derive the slip distribution on the faults. The material in this chapter is a contribution to a collaborative study with scientists at the Nordic Volcanological Institute in Iceland, which will be submitted to the Journal of Geophysical Research [*Pedersen et al.,* 2002].

Chapter 8 takes on the postseismic deformation observed after the two earthquakes in south Iceland. We are able to explain the deformation as poro-elastic rebound during pore-pressure re-adjustment following the earthquakes. Interestingly, the deformation transient lasts only 1-2 months while aftershocks are projected to last for 3-4 years, indicating that pore-pressures do not control aftershock activity.

Chapter 2

InSAR Covariance Estimation and Data Reduction

In this chapter we analyze noise in synthetic aperture radar interferograms and examine several data reduction methods. We begin by exploring the noise structure in several examples of deformation interferograms and present simple empirical methods to locally estimate the noise covariance function. We then address several data reduction algorithms to ease model calculations, and propagate the full interferogram data covariance to the reduced data set. The importance of including the full data covariance matrix in model calculations is briefly investigated as well.

2.1 Abstract

Synthetic aperture radar interferometry (InSAR) has become an important tool to study earthquake and volcanic deformation. Dozens of studies have been published in which InSAR observations and subsequent crustal deformation modeling have shed light on earthquake and volcanic processes. To date, however, InSAR errors have been widely ignored in model calculations, which can lead to biased modeling results. Here we investigate InSAR errors and present some data reduction methods to facilitate model calculations. First we analyze the noise structure of actual deformation interferograms and estimate empirical local covariance functions in areas of interest. The noise variance and the distance within an interferogram at which two data points become uncorrelated depends on the spatial support of the data, i.e., the size of the image that is being studied, because the noise affects all spatial scales. We find that the InSAR noise spectra follow a power law index from $-8/3$ to $-3/3$ for intermediate spatial scales (0.5-2 km) while the index is lower for shorter

(< 0.5 km) and longer (> 2 km) spatial scales. We next sub-sample InSAR data with a linear two-dimensional quantization method that reduces the data quantity by 2-3 orders of magnitude, and propagate the full covariance matrix to derive the covariance matrix for the reduced data. Our preliminary results show that optimum model parameters, with and without weighting of the full data covariance matrix, are nearly identical. However, different data sub-sampling can result in different modeling results. Further research is required to better understand when including InSAR covariances becomes important, and systematic examination is needed of the effects the different data reduction algorithms have on modeling results.

2.2 Introduction

Since the first earthquake study using InSAR was published [*Massonnet et al.,* 1993], the technique has progressively gained ground to become a significant tool to study crustal deformation, rivaling the Global Positioning System (GPS). Several authors have comprehensively described satellite radar interferometry, both the technique itself and its use in crustal deformation applications [e.g., *Zebker et al.,* 1994; *Massonnet and Feigl,* 1998; *Hanssen,* 2001]. To date, many InSAR studies have contributed to the understanding of earthquakes and the earthquake cycle through observations of co-seismic deformation [e.g., *Peltzer et al.,* 1999; *Jónsson et al.,* 2002a], post-seismic deformation [e.g. *Peltzer et al.,* 1996; *Pollitz et al.,* 2001], and interseismic deformation [e.g., *Bürgmann et al.,* 2000; *Wright et al.,* 2001a]. Other studies have demonstrated the power of InSAR in studying volcanic deformation [e.g., *Massonnet et al.,* 1995; *Lanari et al.,* 1998; *Wicks et al.,* 1998; *Lu et al.,* 1998; *Jónsson et al.,* 1999; *Sigmundsson et al.,* 1997, 1999; *Amelung et al.,* 2000a].

InSAR observations contain measurement errors, as do any geodetic data. However, InSAR errors have been poorly understood and thus widely ignored by authors modeling crustal deformation observed by InSAR. In particular, authors have neglected spatial correlations between data points within interferograms and treated the data as independent. Ignoring correlations in geodetic measurements can lead to biased modeling results, as was demonstrated in co-seismic deformation modeling of the Loma Prieta earthquake, California, using leveling data [*Árnadóttir et al.,* 1992].

Unwanted signals or noise in deformation interferograms are of various origin. One of the main sources of error is due to variations in atmospheric refractivity that causes spatially

variable delay of the radar signal [*Zebker et al.,* 1997; *Hanssen et al.,* 1999]. Relative delay within an interferogram is a measure of the difference between the integrated refractivity structure at the two acquisition times, and can be as large as several centimeters (range-change equivalent). Atmospheric noise in InSAR data falls in two main categories: First, turbulent mixing in the troposphere results in variable signal delays within the image at all frequencies, and second, vertical stratification of the atmosphere can be different on the two acquisition days, resulting in elevation dependent residual signals [*Hanssen,* 2001]. Elevation dependent errors can often be reduced by good knowledge of the topography, but the turbulent part is difficult to eliminate because there is currently no instrumentation that can measure the three-dimensional refractivity structure of the atmosphere with sufficient accuracy or spatial resolution.

Other InSAR errors follow from inaccurate satellite orbit information, DEM errors, interferometric decorrelation, inaccurate image co-registration, unwrapping errors, etc. Orbital residual in interferograms appears as a phase ramp that is usually easy to remove, either by eye or with bi-linear estimation, except when large scale deformation is present that extends across the entire interferogram. Topographic signals in deformation interferograms depend on the perpendicular baseline between the two satellite passes and the terrain in the area of interest. The topographic signature can be removed either by a simulated interferogram using a DEM (two-pass method) or by using the three/four-pass method [*Massonnet and Feigl,* 1998; *Zebker et al.,* 1994]. However, this removal often introduces errors. In the two pass case errors can be introduced when the orbit or the DEM information is inaccurate, or when the interferogram and the simulation are not co-registered properly. The problem with the three/four-pass method is that additional atmospheric artifacts may be introduced into the deformation interferogram. Yet another InSAR error is due to interferometric decorrelation, causing high frequency noise and signal loss; it can be due to several different factors [*Zebker et al.,* 1992a; *Hanssen,* 2001]. Finally, absolute range changes are calculated by integrating the wrapped phase in interferograms, i.e., by phase unwrapping [*Zebker and Lu,* 1998]. The unwrapping step can introduce significant errors, especially when interferograms are noisy or when phase gradients are high.

A few studies have been published where the spatial structure of InSAR noise has been investigated. Authors have in most cases concentrated on atmospheric noise in interferograms, rather than looking at more practical examples where noise from multiple sources is

present. *Goldstein* [1995] analyzed an interferogram from Mojave desert in southern California, and found that the spatial spectrum of InSAR atmospheric noise follows a power-law with index $-8/3$ for spatial scales between 0.4 and 6 km, consistent with Kolmogorov turbulence theory [*Tatarski*, 1961]. Similar noise structure was found in C and L-band interferograms in Hawaii [*Zebker et al.,* 1997]. *Williams et al.* [1998] developed a statistical model to produce covariance between InSAR data points separated in space and/or time using results previously obtained for very long baseline interferometry (VLBI) measurements [*Treuhaft and Lanyi,* 1987].

The most detailed analysis of InSAR errors to date was conducted by *Hanssen* [2001]. He described how the various error sources map into interferograms and discussed methods to reduce or remove the errors. In particular, he studied atmospheric effects and found that the noise power spectrum typically has similar power-law structure from one interferogram to another, although the absolute power may vary. This average power-law behavior has power index of $-5/3$ for spatial scales larger than 2 km, $-8/3$ for intermediate scales between 0.5 km and 2 km, and $-2/3$ for spatial scales smaller than 0.5 km [*Hanssen,* 2001]. The intermediate scales are smaller than the thickness of the turbulent layer in the troposphere and here the noise structure is consistent with 3D isotropic Kolmogorov turbulence theory [*Tatarski*, 1961]. The approximation of 2D turbulence can be used for scales greater than the thickness of the turbulent layer to scales as large as the extent of the interferograms [*Hanssen,* 2001]. The noise structure of the smallest spatial scales (< 0.5 km) is likely from another origin rather than atmospheric turbulence, e.g., due to decorrelation [*Hanssen,* 2001].

In this study we investigate three main topics. First, we analyze noise in deformation interferograms to determine the spatial covariance of the data. Second, we explore different InSAR data reduction methods to facilitate model calculations. And finally, we combine these two topics to calculate a data covariance matrix for reduced InSAR data and investigate the significance of including the full data covariance structure in model calculations.

2.3 Noise Analysis of Three Interferograms

We examine the spatial structure of interferogram noise in three deformation interferograms of the Galápagos islands. The three interferograms span 6, 13, and 61 month time interval

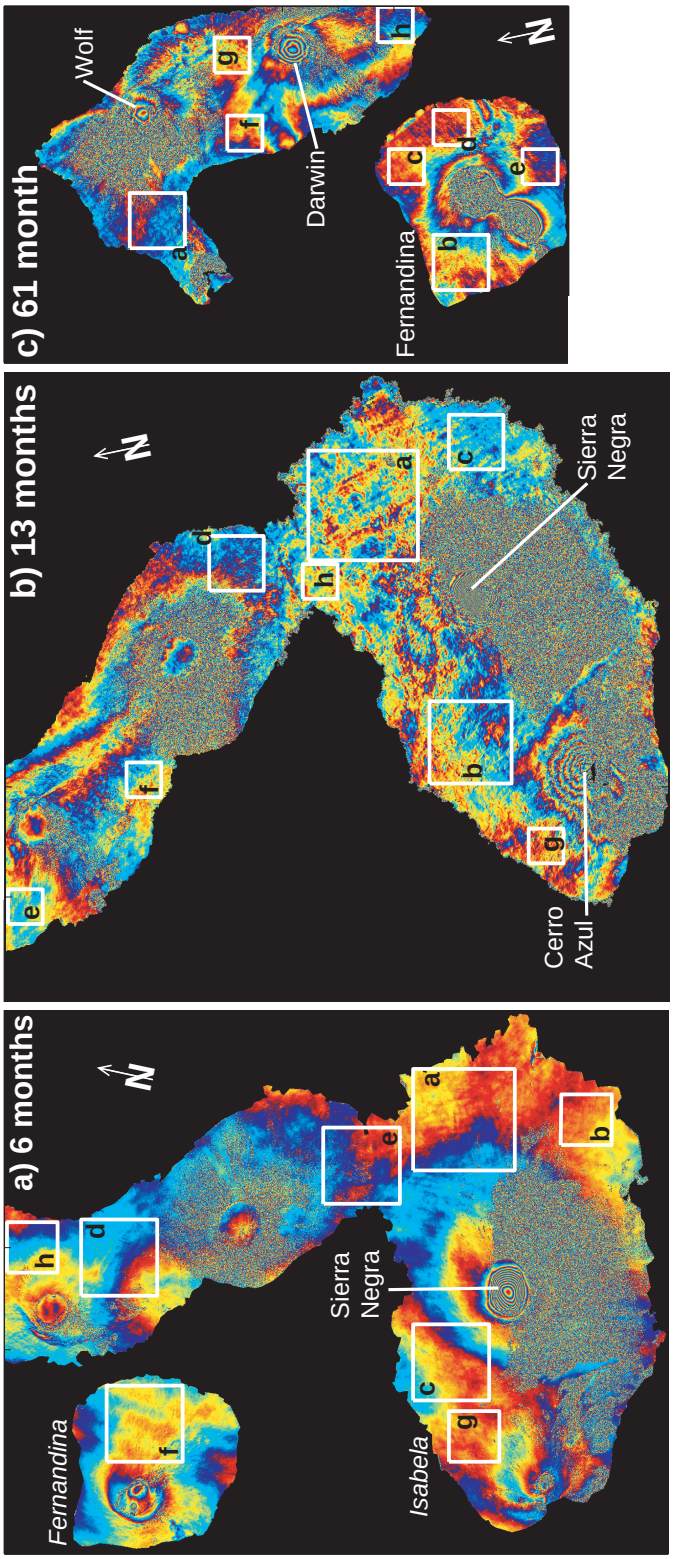

Figure 2-1: Three interferograms of western Galápagos islands. (a) 6 month interferogram showing Fernandina and Isabela islands (9/1998-3/1999, $B_\perp = 5$ m, ascending orbit). (b) 13 month interferogram of southern Isabela (10/1997-11/1998, $B_\perp = 367$ m, descending orbit). (c) 61 month interferogram (6/1992-11/1998, $B_\perp = 85$ m, descending orbit) showing Fernandina and northern Isabela. White frames mark the sub-images shown in Figures 2-2 to 2-4.

and have perpendicular baselines of 5, 367, and 85 m, respectively (Figure 2-1). Simulated interferograms, generated using satellite orbit information and a TOPSAR DEM of Galápagos [*Zebker et al.,* 1992b; *Mouginis-Mark et al.,* 1996], were used to remove the topographic signature from the interferograms, leaving only ground deformation and noise. One color cycle in the interferograms represents 2.83 cm of ground movement towards (yellow-red-blue) or away (yellow-blue-red) from the satellite. There are clear signs of deformation in the interferograms. The 6 month interferogram shows about 10 cycles (30 cm) of uplift on Sierra Negra volcano and about 10 cm uplift on Fernandina. The 13 month interferogram is much noisier than the 6 month interferogram. However, we see that Cerro Azul volcano exhibits 20 cm subsidence following an eruption in September 1998. The 61 month interferogram has 10 cm of uplift on Wolf volcano and 20 cm uplift on Darwin volcano. In addition, there is a strong signal seen on the southwest flank of Fernandina from the dike intrusion that fed the 1995 eruption [*Jónsson et al.,* 1999].

We carefully selected 8 sub-images from each interferogram from areas that are not affected by volcanic deformation. The sub-images are shown in Figures 2-2 to 2-4 after a plane has been removed from each sub-image. The interferogram posting is 80 m $\times$ 80 m and the sub-images vary in size from 64×64 pixels to 200×200 pixels, or 5 km $\times$ 5 km to 16 km $\times$ 16 km. Visual inspection reveals clear differences between the sub-images. Some have relatively low noise power (e.g., Figure 2-2b) while others exhibit much stronger noise power (e.g., Figure 2-3a). Some of the sub-images mostly have long period noise (e.g., Figure 2-2c) while still others exhibit strong high spatial frequency noise (e.g., Figure 2-2e). The noise can be fairly homogeneous (Figure 2-3c), but sometimes the noise is spatially heterogeneous within one sub-image, for example Figure 2-2e has more high frequency noise in the north than in the south. In addition, there is variability in the noise isotropy, e.g., the noise of Figure 2-2b appears isotropic as compared to Figure 2-2f.

2.3.1 Noise Isotropy

We use a radon transform to investigate anisotropy in images because systematic intensity variations in a particular direction will be quite visible in the radon transform. A single radon transform is a mapping from two dimensions to one dimension in which the image intensities collapse to a profile. The radon transform $\mathfrak{R}_\theta$ can be formulated as follows [*Bracewell*, 1995] :

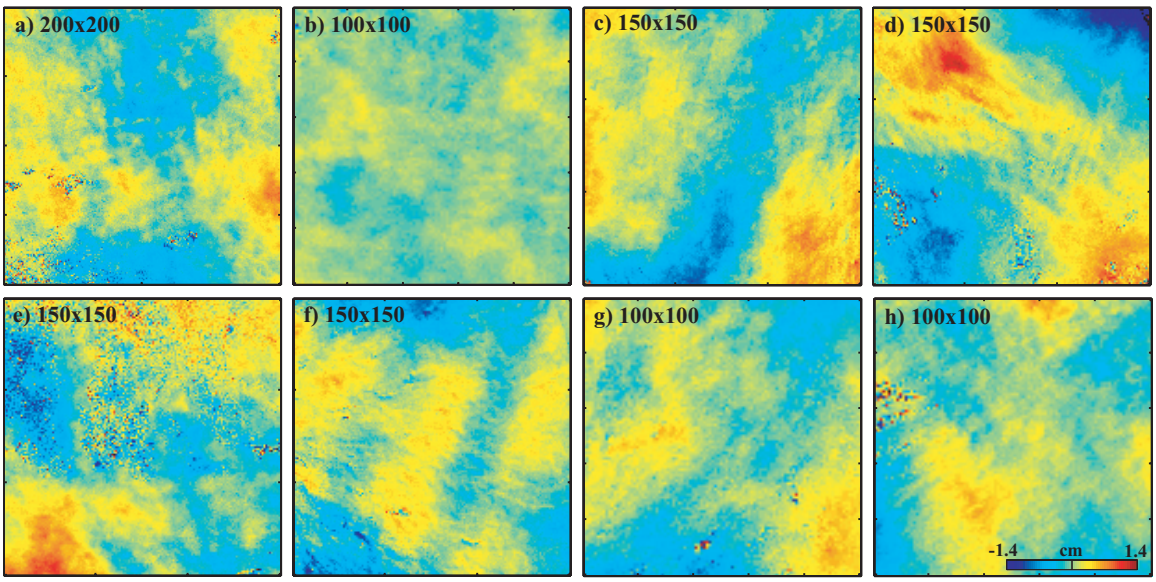

Figure 2-2: Sub-images from the 6 month interferogram shown in Figure 2-1. The images are plotted wrapped with 2.83 cm cycles. Bi-linear trend has been removed from the images. The numbers indicate the size (in pixels) of each sub-image. The pixel size is 80 m $\times$ 80 m.

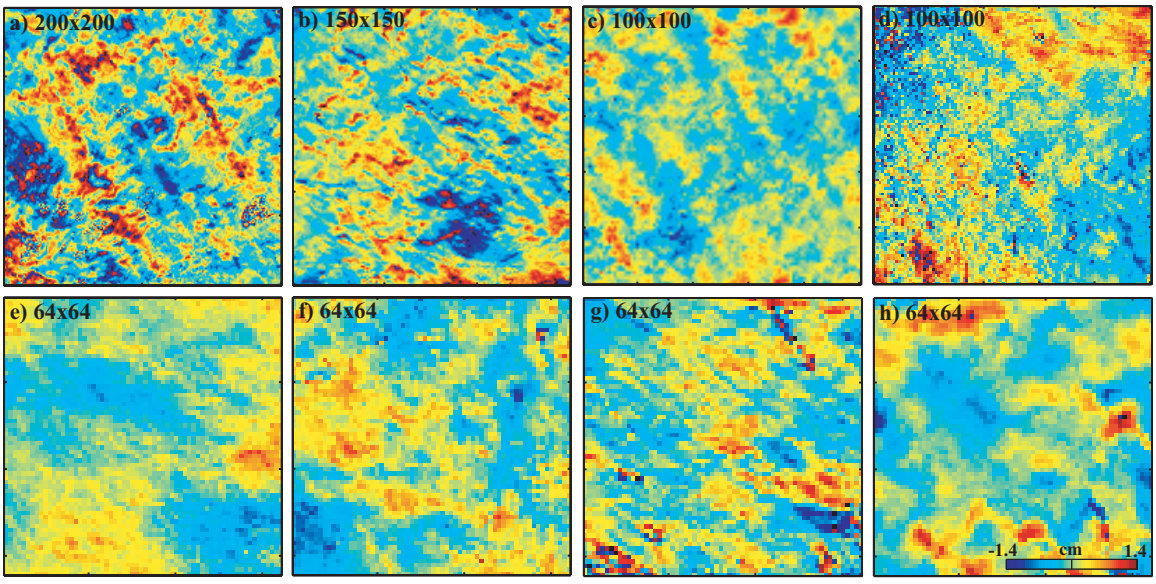

Figure 2-3: Same as 2-2, except for the 13 month interferogram shown in Figure 2-1.

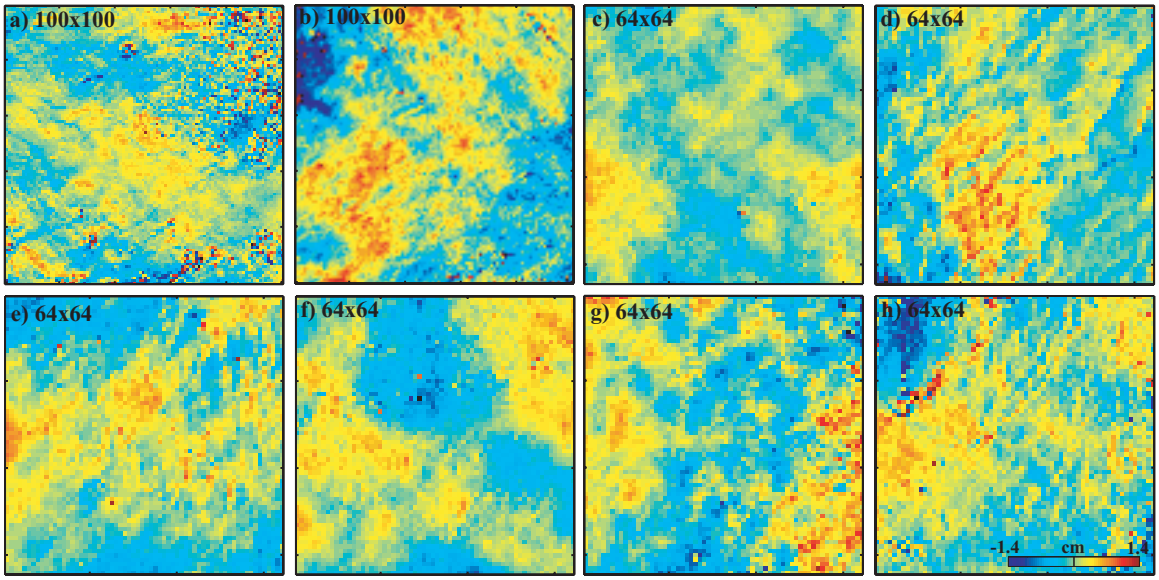

Figure 2-4: Same as 2-2, except for the 61 month interferogram shown in Figure 2-1.

$$\Re_\theta \{ f(x,y) \} (r) = \int_{-\infty}^{\infty} \int_{-\infty}^{\infty} f(x,y) \delta(r - x\cos\theta - y\sin\theta) dx dy \tag{2.1}$$

where $f(x,y)$ is the image intensity, θ is the profile direction, and δ is the delta function. When working with a discrete image d_{ij} the radon transform is:

$$\Re_\theta \{ d_{ij} \}_k = \sum_{l=1}^{N} d'_{kl} \tag{2.2}$$

where d'_{kl} is the original image rotated by an angle θ and N is the l-dimension of the rotated image.

To systematically explore image anisotropy we calculate the radon transform of each interferogram. A sample transform is demonstrated for a simple test image of two squares as in Figure 2-5. Note for angles around 45 degrees the squares add up, but for angles 100-170 degrees we see the "hole" between the two squares. In our analysis of the sub-images we use a normalized version of the radon transform: $\Re'_\theta \{ d_{ij} \}_k = \Re_\theta \{ d_{ij} \}_k / N$, which describes the average pixel value along lines perpendicular to profile direction θ.

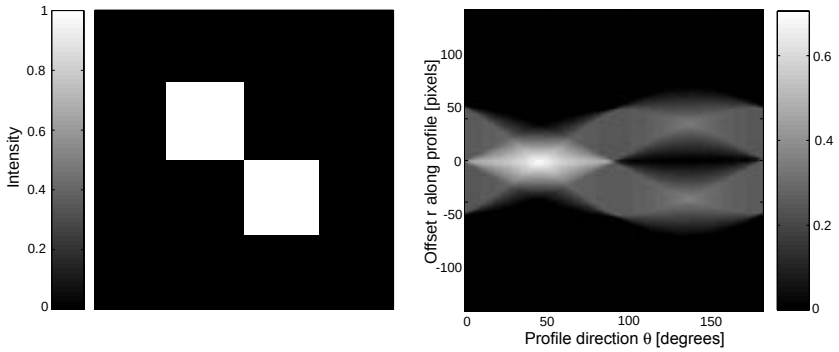

Figure 2-5: Test image (left) of two squares and its radon transform (right) showing the average image intensity along lines perpendicular to profile direction θ. The Radon transform has a maximum at 45 degrees where the intensity of both squares adds up.

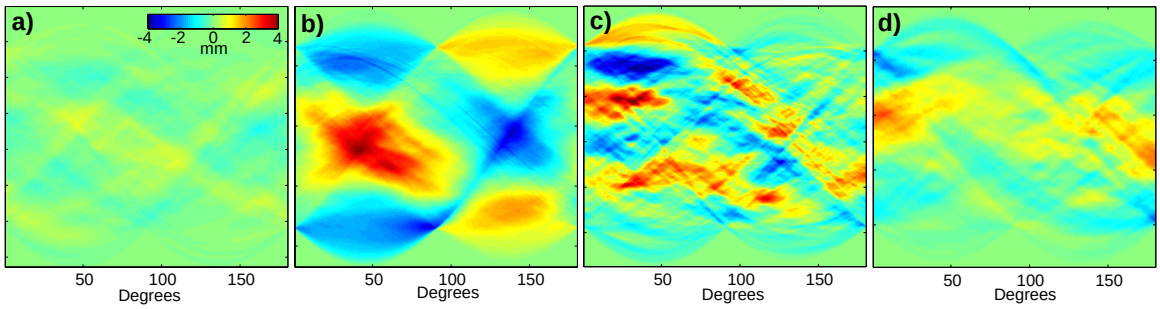

Figure 2-6: Radon transform of four sub-images showing variable anisotropy. The corresponding sub-images are shown in (a) Figure 2-2b, (b) Figure 2-2d, (c) Figure 2-3a, and (d) Figure 2-4d.

Some of the sub-images are nearly isotropic while other are not. Figure 2-6 shows the radon transform of four selected sub-images. The color-scale is the same for all transforms and it shows the mean unwrapped phase value (in mm) of pixels along lines perpendicular to given profile directions. The first radon transform (sub-image in Figure 2-2b) is a good example of an isotropic image while the second sub-image (Figure 2-2d) has a transform reflecting strong trends at 45° and 135°. The third radon transform in Figure 2-6 clearly shows linear trends around 33° that we also see by looking at the sub-image directly (Figure 2-3a). The last radon transform is fairly isotropic. The main indication for a linear trend is at 0° where negative values of the west part of the image add up (Figure 2-4d).

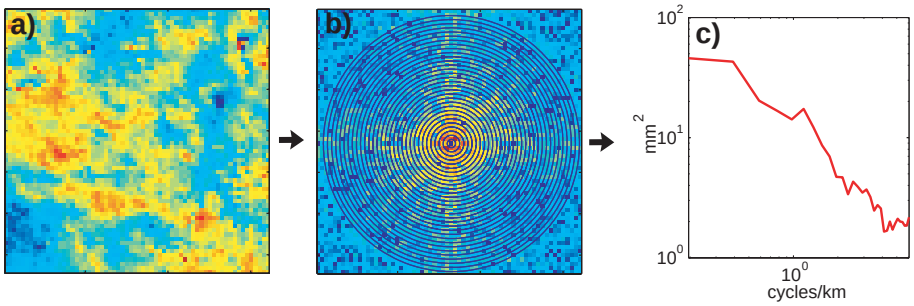

Figure 2-7: Calculation of rotationally averaged spectrum. (a) Interferometric sub-image, (b) 2D power spectrum of (a) with circles plotted on top, (c) 1D power spectrum obtained from integration along circles in (b).

2.3.2 Noise Power Spectrum

We next examine the spectral properties of the sub-images, and calculate the rotationally averaged spectra. We do this by first calculating the 2D power spectrum and then integrating along circles to get the 1D spectrum (Figure 2-7). The 1D power spectrum for each of the sub-images is shown in Figure 2-8. Remember that we removed a plane from each sub-image, and we therefore do not plot the two lowest frequency coefficients. The noise power clearly decreases with higher frequency in all cases although the slope of the fall-off varies. Many of the visual characteristics are confirmed here. For the 6 month sub-images we can see that Figure 2-2b has the lowest power while sub-image (d) has relatively high power throughout the spectrum. Sub-image (e) shows strong high frequency noise due to significant decorrelation. The 13 month sub-images generally exhibit stronger noise power than the 6 month sub-images. Sub-image (h) has relatively little high frequency noise power and sub-image (e) has low power for intermediate frequencies. The 61 month sub-images all have similar low frequency structure but the high frequency structure appears to be quite variable (Figure 2-8c). The mean power spectrum is plotted as a thick black line on each of the plots (Figure 2-8a-c) and Figure 2-8d shows the means of the three sets of sub-images together. We see that the 13 and 61 month averages exhibit similar low frequency structure but the 61 month average has relatively stronger high frequency noise. For spatial scales > 0.3 km these averages seem to follow a power law with an exponent of -1. For smaller spatial scales the 13 month average follows power law slope $-2/3$ while the 61 month average still follows -1. The 6 month average is different: the power is lower and it follows $-5/3$ slope for frequencies lower than 2 km^{-1} but has a slope close to 0 for higher frequencies.

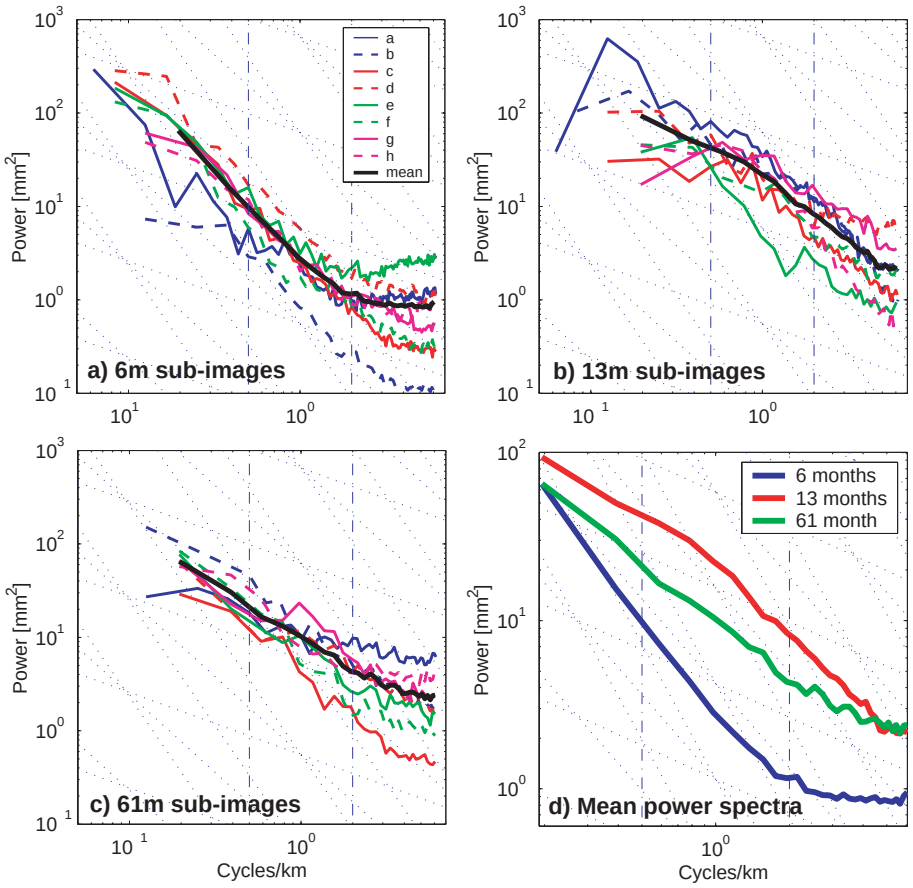

Figure 2-8: One-dimensional rotationally averaged power spectra of the (a) 6 month, (b) 13 month, (c) 61 month sub-images. Plots (a)-(c) have the same scale. Thick black line in (a)-(c) shows the mean power. (d) The average power spectra for the three sets of sub-images. The diagonal lines (dotted) represent $-8/3$, $-5/3$, and $-2/3$ power-law behavior.

To better compare the spectral properties of the sub-images we scale the power spectra so that all have the same power at 1 km^{-1} (Figure 2-9). We can see that the 6 month sub-images show similar power-law behavior for spatial frequencies lower than 2 km^{-1} and so do the 13 month sub-images. The 61 month sub-images now show more variability. For higher frequencies the sub-images start to diverge from each other as some of them have areas affected by interferometric decorrelation, increasing the high frequency power.

Hanssen [2001] analyzed 8 interferograms from the Netherlands to investigate atmospheric heterogeneities visible by interferometry and selected the scenes and the study area to minimize signals from other sources. The interferograms were formed using tandem

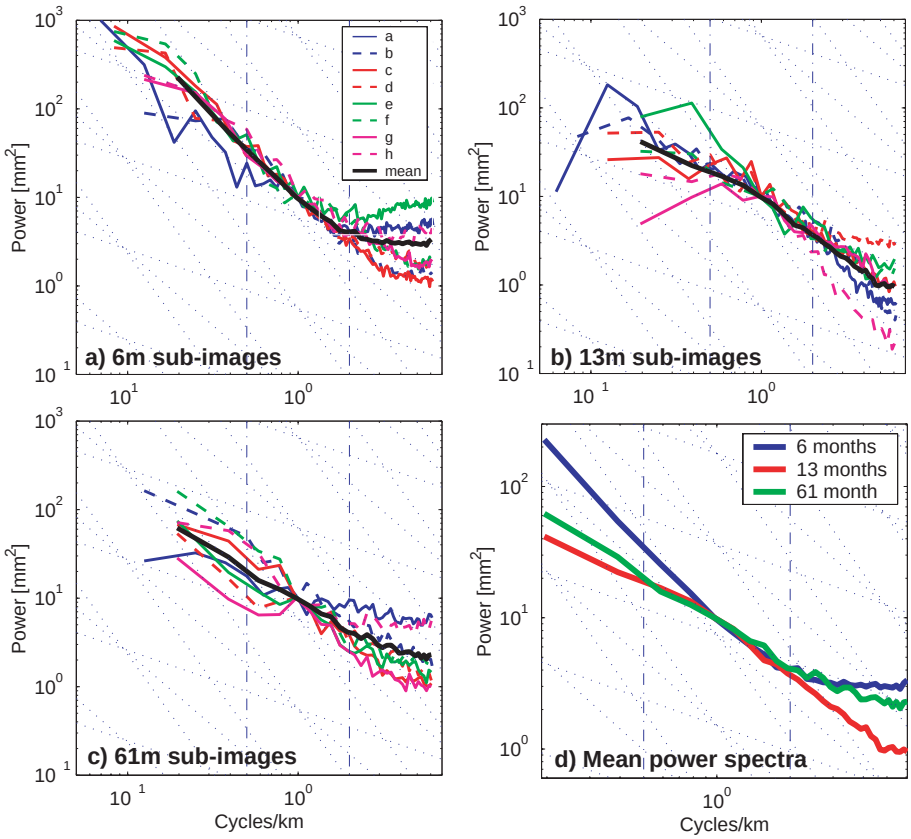

Figure 2-9: Same as Figure 2-8, except here the power-spectra have been shifted such that all sub-images have the same power at 1 km^{-1}.

images with a time separation of only one day and thus contained insignificant deformation and decorrelation. His study area is a flat region in the Netherlands and he selected images with small baselines, so no residual topographic signature is present in the interferograms. *Hanssen* [2001] found that on the average these interferograms showed power spectra following power-law of $-5/3$ for low frequencies (spatial scales > 2 km), $-8/3$ for intermediate frequencies (spatial scales 0.5-2 km), and $-2/3$ for high frequencies (spatial scales < 0.5 km). He argued that the $-5/3$ power law behavior represented scales larger than the turbulent layer of the atmosphere where an approximation of two dimensional turbulence can be applied, while for 0.5-2 km turbulence scales are smaller than the thickness of the turbulent layer. These values of the power-law exponent are consistent with Kolmogorov turbulence theory [*Tatarski*, 1961; *Hanssen*, 2001]. The power law behavior at

the smallest spatial scales (< 0.5) km is probably not of atmospheric origin, but more likely from interferometric decorrelation and noise introduced by interpolation [*Hanssen*, 2001].

The Galápagos sub-images exhibit power spectrum structure similar to a power-law behavior between $-5/3$ to $-3/3$ for the larger spatial scales > 0.5 km, and $-2/3$ to 0 for smaller spatial scales. These power-law indices are somewhat lower than those found be *Hanssen* [2001]. Not in a single case do we observe an index as high as $-8/3$ for intermediate scales and our indices are generally lower than $-5/3$ for the longest scales. For the smallest scales however, we generally see slopes close to $-2/3$, except in cases where decorrelation is present (sub-images in Figures 2-2a,e,h, 2-3d, 2-4a,h). The images analyzed by *Hanssen* [2001] were 50×50 km^2 in size and suitable to study larger spatial scales than our sub-images (up to 16×16 km^2). But, the images we analyzed present a more practical scenario for deformation studies, where we have long time separation, variable baseline lengths, and potentially a great degree of decorrelation. Because the noise we observe is likely from a combination of many processes, we refer to it as interferogram noise, rather than atmospheric noise.

Our results and those of *Hanssen* [2001] show that InSAR noise can be quite variable, and is not always structured as predicted by Kolmogorov turbulence theory. Although our sub-images came from only three interferograms and do not constitute a large sample statistically, they demonstrate that spatial characteristics of InSAR noise can be very different from one interferogram to another and within one interferogram from one region to another. Unfortunately, it appears to be hard to find a general structure for InSAR noise although some bounds may be determined, e.g., that for spatial scales > 0.5 km the noise follows a power law between $-10/3$ and $-3/3$.

2.3.3 Noise Covariance Functions

We now calculate covariance functions for the sub-images. Here we assume 2nd order stationarity, i.e., that the expected value $m = \mathrm{E}[f(x,y)]$ exists and is invariant with location (x,y) in the interferogram, and that the covariance depends only on distance but not direction or location (see Appendix A). We calculate the covariance functions from the rotationally averaged 2D auto-correlation function. This procedure is explained in Figure 2-10.

It is important to note that the covariance function depends in part on the spatial support of the data. This means that if we want to compare covariance functions of different sub-images they need to be of the same size. Therefore, we calculate covariance functions

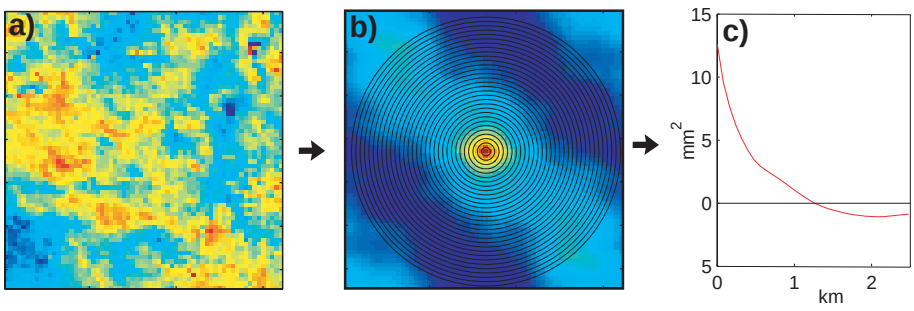

Figure 2-10: Covariance function calculation. (a) Interferometric sub-image, (b) 2D auto-correlation of (a) with circles plotted on top. (c) 1D covariance function of (a) obtained from a rotational average of (b) (i.e., the mean value along each of the circles in (b)).

for 64×64 pixel images and select only the center region when sub-images are larger than 64×64 pixels.

The covariance functions of the 6 month sub-images are similar to one another with variances of 2-3 mm^2 and falling nearly linearly to zero at a distance of 1.5 km (Figure 2-11a). There are two exceptions: sub-image (b) shows weaker covariance as the noise power in this image is exceptionally low (Figures 2-2b and 2-8a), and sub-image (e) has much higher variance than other images, about 9 mm^2. The covariance function for sub-image (e) falls to a normal level with distances > 0.1 km. Its high variance follows from extensive interferometric decorrelation (Figure 2-2e).

The 13 month sub-images have variances 7-23 mm^2 with an exception of sub-image (a), where the variance is 36 mm^2 (Figure 2-11b). The covariance function of sub-image (a) is 5 times stronger than for sub-image (c). These covariance functions demonstrate the large variability that one may expect within one interferogram.

The 61 month sub-images have variances between 5 and 13 mm^2 with less variability than the 13 month covariance functions. The strongest covariance function is only about twice as strong as the weakest. The mean covariance function of each set of sub-images is shown in Figure 2-11d. The means again show the high noise power in the 13 month interferogram and the low noise power in the 6 month interferogram. The average of the three mean covariance functions appears to be similar to the 61 month mean.

The covariance functions fall to zero around 2 km, implying that the noise is uncorrelated at distances beyond 2 km in these small sub-images (after a plane in phase has been removed). When a larger area is considered this correlation distance could increase along

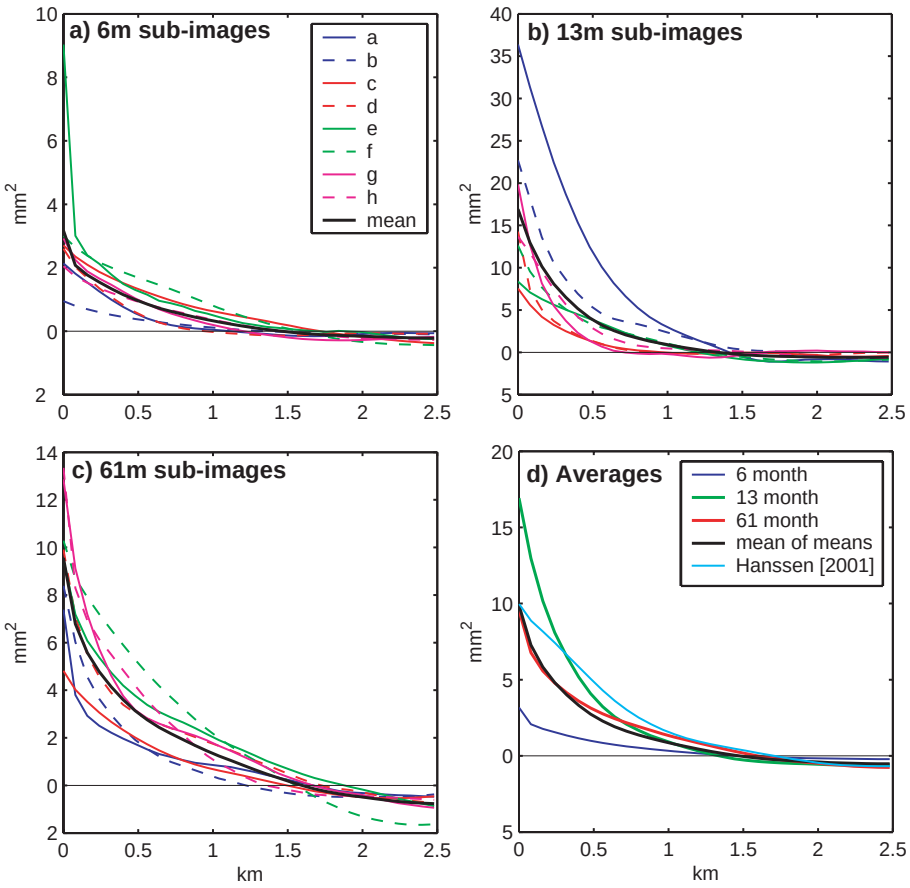

Figure 2-11: Covariance functions of 64×64 pixel sub-images. Note different vertical scales in plots. Covariance functions for (a) the 6 month, (b) 13 month, and (c) 61 month sub-images. (d) The mean of each set of sub-images. The variance of the 13 month sub-images is highest while the 6 month sub-images have generally low variance. Some sub-images show very steep slope between 0 and 0.1 km, which is due to high frequency noise from interferometric decorrelation. Covariance function of an image with a typical noise structure as estimated by *Hanssen* [2001] and variance of 10 mm^2 is also shown in (d).

with the variance as the covariance functions depend on the spatial support of the data.

Also shown is a covariance function of an image that has a typical noise structure as estimated by *Hanssen* [2001] and a variance of 10 mm^2 (Figure 2-11d). This covariance function has a slower fall off with distance than our covariance functions due to the different power-law behavior of the power spectrum. A high power-law index for the spectrum (such as $-8/3$ and $-5/3$) results in relatively strong long period noise and strong covariance for long distances.

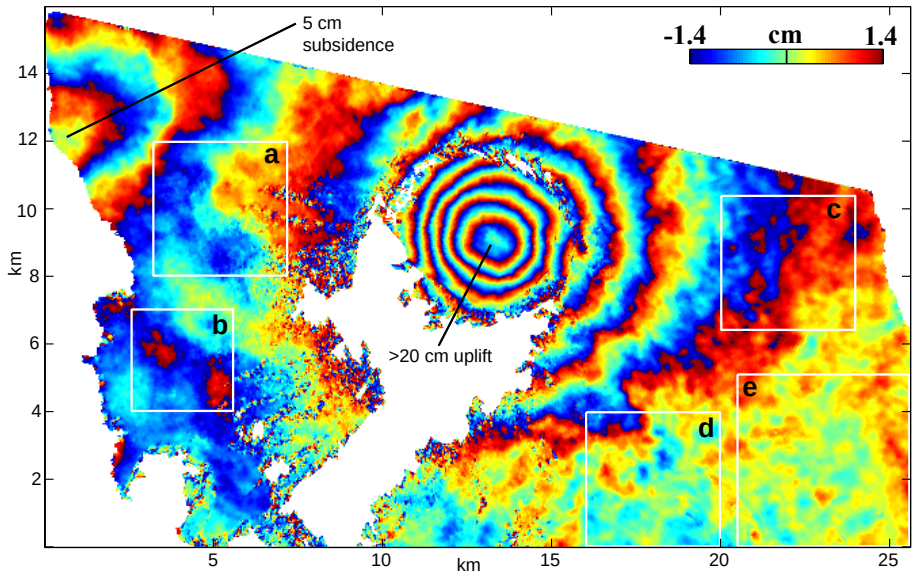

Figure 2-12: Interferogram showing uplift on Darwin volcano. White frames mark selected subimages shown in Figure 2-13.

The large noise structure variability we observe between interferograms and within any one interferogram shows the importance of analyzing the noise structure in every case to determine the local noise behavior in the area of interest.

2.4 Example of Local Covariance Function Estimation

In this section we examine the local covariance functions for interferograms that include volcanic deformation. For these we select interferograms of Darwin and Fernandina volcanoes, western Galápagos. The Darwin data are from an interferogram spanning 77 months from June 1992 to November 1998 acquired from a descending ERS orbit ($B_\perp = 85$ m). As before, the topography was removed using a simulated interferogram generated from the Galápagos TOPSAR DEM [*Zebker et al.,* 1992b]. The interferogram shows 7 fringes centered on Darwin caldera and represents 20 cm of range decrease, that is line-of-sight (LOS) ground uplift towards the satellite (Figure 2-12). In addition to the volcano inflation, 5 cm subsidence is observed near the coast in the northwestern part of the image. The cause of the subsidence is unknown, and it is observed in multiple interferograms.

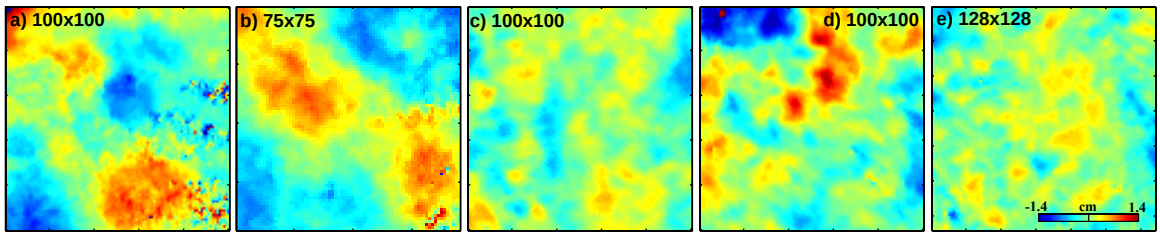

Figure 2-13: Five sub-images from Darwin volcano from Figure 2-12. A plane has been removed from each sub-image. The numbers represent the image size in pixels. The pixel size is 40 m × 40 m, so the smallest image is 3 km × 3 km and the largest one is 5 km × 5 km.

2.4.1 Noise Spectral Analysis

First, we examine the spectral properties of the noise. We select 5 sub-images around Darwin volcano, choosing areas that are little affected by the volcanic deformation (Figure 2-12). The sub-images are 75×75 pixels to 128×128 pixels in size, representing 3×3 km^2 to 5×5 km^2 (Figure 2-13). A phase plane has been removed from each sub-image to eliminate any linear trends across the sub-images. The images appear to be fairly homogeneous. Sub-images (a)-(b) seem to have stronger long period noise than other images and only sub-image (a) contains high frequency noise due to decorrelation (Figure 2-13).

The 1D power spectra indicate that the noise structure of the sub-images is quite similar although the noise power of sub-images (c) and (e) is somewhat lower than that of the other images (Figure 2-14). This difference is largest for the lowest and the highest frequencies. Sub-image (a) has stronger high frequency noise than other images, as it is more affected by interferometric decorrelation (Figure 2-13a). At spatial scales between 0.2 and 1.5 km the mean noise spectra shows power-law behavior with index of -2.1, in between turbulence power indices -2.67 (-8/3) and -1.67 (-5/3). This index is higher than in the three previous Galápagos interferograms (see Section 2.3.2) and closer to values *Hanssen* [2001] observed above the Netherlands. For the highest frequencies the mean spectrum follows a power-law of -2/3.

Volcanic deformation at Darwin covers an area 20 km in diameter, a much larger value than the spatial scales we can analyze in these small sub-images. We are only able to study spatial scales smaller than 2 km as the sub-images are only 3-5 km on a side. Since the covariance function is dependent of the spatial support of the image analyzed, we cannot use these power spectra to calculate the covariance function for the entire Darwin image,

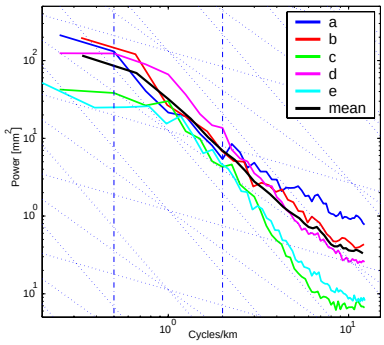

Figure 2-14: Power spectra of the five sub-images shown in Figure 2-13. Sub-images (c) and (e) have somewhat lower noise power than other sub-images.

unless we make some assumptions about the structure of the long period noise. For example, we could assume that the long period noise follows a power law of $-5/3$ for spatial scales beyond 2 km [*Hanssen*, 2001]. We could also assume that the power-law behavior would slowly decay and go to zero for spatial scales of 5 km. The latter would mean that data points within the image would become uncorrelated with each other at distances greater than 5 km.

2.4.2 Obtaining the Covariance Function

Because we cannot find sub-images large enough to estimate the noise statistics at all scales, we instead estimate the covariance function by calculating a sample covariance function using all the data that do not contain deformation. In this approach we can study the larger spatial scales as well. We begin by removing any data that exhibits deformation (see Figure 2-15a-b). We remove the area around Darwin caldera and the subsidence area on the west coast. We then subtract the best-fitting phase plane as before from the remaining image to remove a potential error ramp caused by inaccurate orbital information. The remaining image is 'flat' and the local mean values are seen to be close to zero.

For this deformation-free image, we calculate a sample variogram and sample covariance function as follows. For each distance r we select many random locations (x_i, y_i) within the image and many random directions θ_i and compare the values at (x_i, y_i) and $(x_i + r\cos\theta_i, y_i + r\sin\theta_i)$. We calculate the variogram and the covariance function using Equations 2.22 and 2.28 in Appendix A, respectively. We assume second order stationarity because a plane has

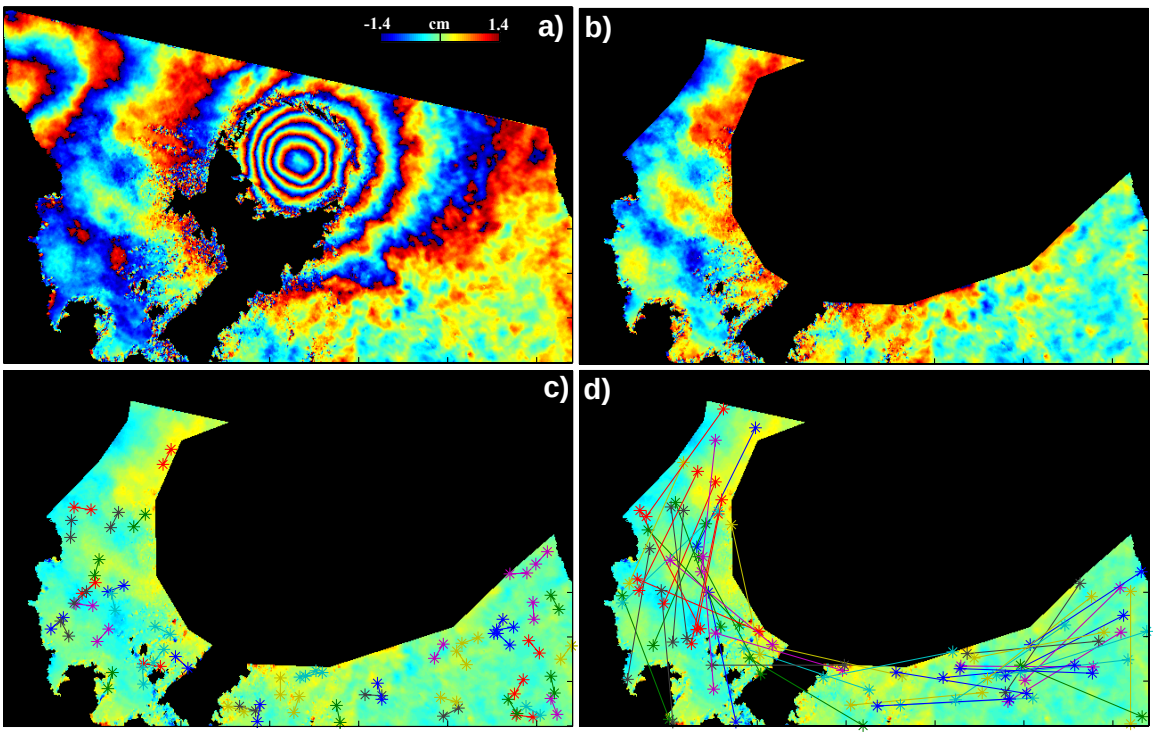

Figure 2-15: (a) Interferogram of Darwin volcano. (b) Same as (a) except areas containing deformation signal have been removed. (c)-(d) Calculation of a sample variogram for two variogram distances 0.8 km and 6 km.

been removed from the image leaving the sample mean value equal to zero. Figure 2-15c-d shows a few randomly selected data pairs for 0.8 km and 6 km lags. We selected 500 random data pairs for each distance r.

The variogram values increase from 0 to about 23 mm^2 at a distance of 2 km (Figure 2-16). Beyond 2 km the variogram has nearly a constant value, plus a slight increase beyond 5 km. The sample covariance function shows opposite behavior, it falls off exponentially from 25 mm^2 to zero at a distance of 2 km. This implies that two data points with in the image are not correlated when the distance between them becomes larger than 2 km and the corresponding noise power spectrum structure would be constant for spatial scales larger than 2 km. This is also different from *Hanssen* [2001] who observed noise structure that follows a power law of $-5/3$ for spatial scales larger than 2 km. If we would have assumed $-5/3$ power law behavior for the long period noise we would get a covariance function with higher variance and with slower decay to zero.

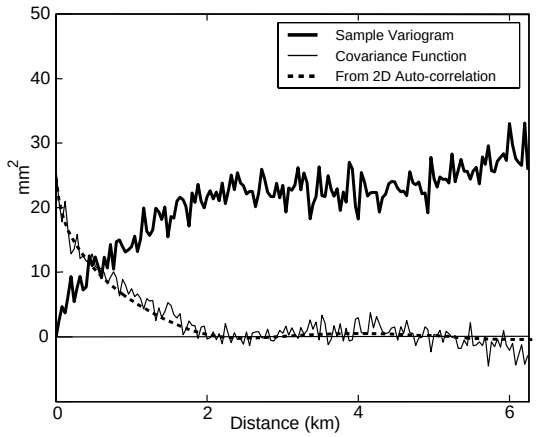

Figure 2-16: Sample variogram (thick solid line) and sample covariance function (thin solid line) for the Darwin interferogram. Also shown is a covariance function from rotational average of the 2D auto-correlation (dashed line), see Section 2.4.3 and Figure 2-17b.

2.4.3 Covariance Function from 2D Auto-correlation

Another method to estimate the covariance function, both for the smaller and the larger scales, is to simply introduce zeros in the areas with no data, and calculate the 2D auto-correlation from the inverse Fourier transform of the power spectrum (Figure 2-17). Although steps on the image boundaries introduce constant shifts in the frequency domain, the shifts tend to cancel out as they are equally likely to be positive or negative since the image mean is zero. The only deviation from the standard 2D autocorrelation is that we need to weight the power spectrum by the number of non-zero data points to normalize the autocorrelation. For an image g_{ij} with discrete 2D Fourier transform G_{kl} we calculate the power spectrum as:

$$P_{kl} = \frac{G_{kl} \cdot G_{kl}^{*}}{N_{nz}} \tag{2.3}$$

where N_{nz} is the number of non-zero data points in g_{ij}, that is, the number of data points left after we excised the deformation signal.

The 1D covariance function is now estimated from calculating the rotational average of the 2D auto-correlation. The covariance function shows the same structure as the sample covariance function, except it is smooth (Figure 2-16). It has variance of 25 mm^2 and it

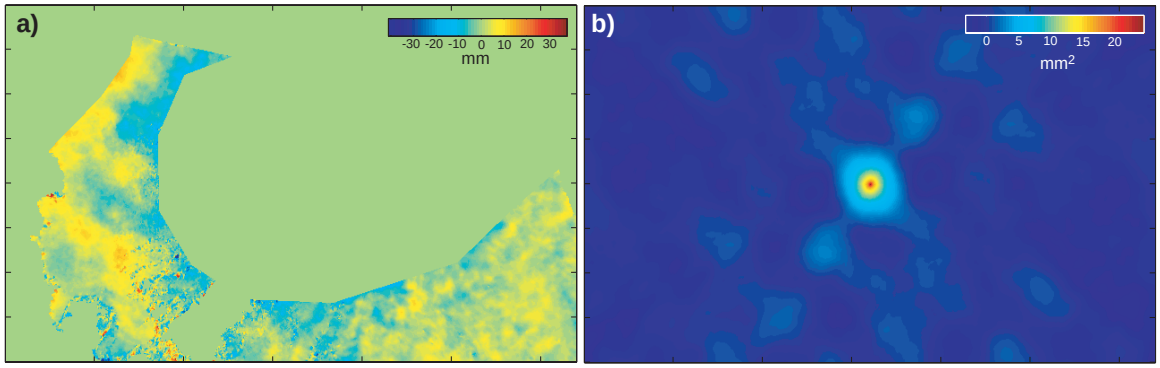

Figure 2-17: (a) Same as Figure 2-15b, except here the image is unwrapped and with zeros introduced in areas that contain no data. (b) Two-dimensional auto-correlation of (a).

falls to zero at a distance of 2 km. Beyond 2 km its value is close to zero indicating that data points that are more than 2 km apart are practically uncorrelated.

The main practical problem with this approach is that the deformation is not always localized, but can extend across the entire image or the entire area with good coherence. For example deformation due to a large earthquake can extend throughout an entire InSAR image that is 100×100 km^2 in size, or a small volcanic island can be inflating such that deformation is observed everywhere. Interferometric decorrelation is often a problem as well. The summit area of volcanoes can be the only area where the image is not decorrelated as volcano flanks are often heavily vegetated. The entire summit area can be undergoing deformation. In these cases we are limited to approximating the covariance function, e.g., by using the average noise structure determined by *Hanssen* [2001].

2.4.4 Covariance Estimation at Fernandina

We can compare covariance analysis of InSAR data over Fernandina volcano to that of Darwin. Here we use the 61 month interferogram shown in Figure 2-1c and excise deforming areas from the center of the volcano and on the southwest flank. The image area is larger than in the Darwin case, about 25 km in diameter (Figure 2-18a). The power spectra of three Fernandina sub-images all show the same noise structure with -5/3 slope for the longest spatial scales, -8/3 for intermediate scales, and -2/3 for shorter scales (Figure 2-18b). This power-law behavior agrees with the average power-law structure determined by *Hanssen* [2001], but has higher indices than we previously found at Darwin and in the three

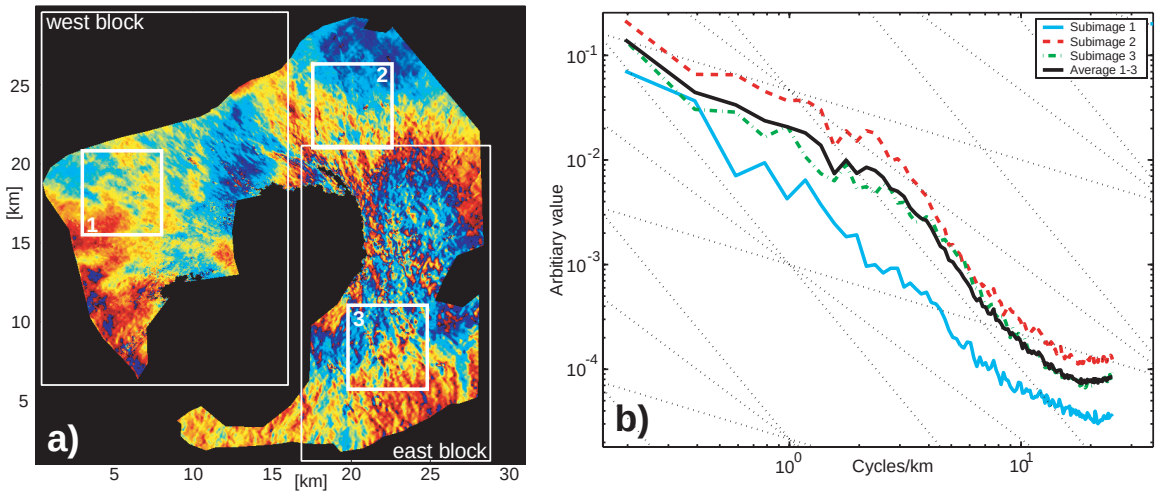

Figure 2-18: Noise power-spectra from Fernandina volcano. (a) 61 month interferogram of Fernandina volcano where deforming areas have been removed. (b) Power-spectra of sub-images 1-3 shown in (a) and their average.

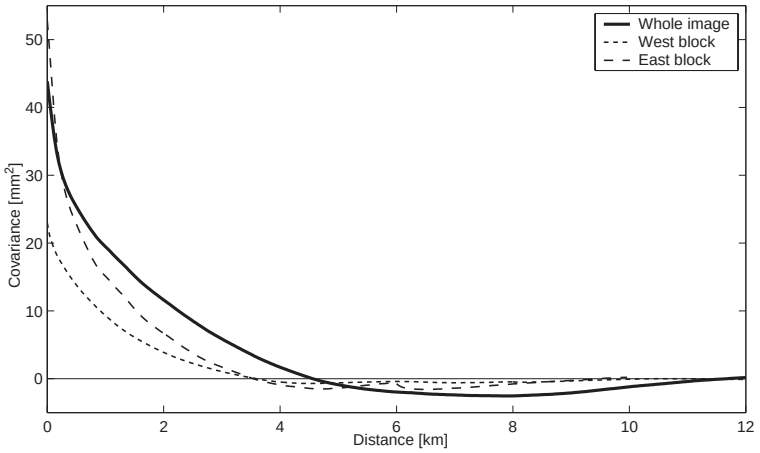

Figure 2-19: Covariance function for the Fernandina interferogram shown in Figure 2-18 as well as local covariance functions determined from data in the western and eastern part of Fernandina island.

Galápagos interferograms.

The estimated covariance function has variance of 50 mm^2 and the data become uncorrelated at a distance of 4.5 km (Figure 2-19). The Fernandina variance is twice as high as in the Darwin case and so is the correlation distance. There is also local variation in the noise power as indicated by the constant shift between the sub-image power spectra

(Figure 2-18b). Calculation of the covariance function for the east and the west part of the island further illustrates this showing noise variance over 50 mm^2 in the eastern part but only 23 mm^2 in the western part (Figure 2-19).

So far, we have shown two practical examples of covariance function estimation near deforming volcanoes. These examples further illustrate the variability of the noise structure between local areas within interferograms and from one interferogram to another. We will now turn our attention to InSAR data reduction methods and later use the results of this section when we combine data reduction with InSAR covariance functions.

2.5 InSAR Data Reduction in the Frequency Domain

A major problem in modeling radar data is the large number of data points in interferograms. When searching for the model parameters that best suite the data we commonly use iterative non-linear methods requiring numerous model prediction calculations. Calculating the model prediction thousands of times for thousands to millions of data points quickly becomes a computationally difficult task. Thus, we seek to reduce the data quantity without losing significant information about the deformation.

InSAR data reduction is a form of image compression in which we seek to preserve the deformation signal. Any image compression techniques involve transforming images into another domain, such as to a frequency domain using the Fourier transform, or to some wavelet domain using a chosen wavelet transform. The compression is achieved by storing only a fraction of the coefficients in the transform domain or by quantizing them. The image can then be restored with an inverse transform of the stored coefficients. Although our problem is not storage capacity we will in this section explore how we can use image compression techniques to facilitate the model optimization.

2.5.1 Power Spectrum of Volcanic Inflation

Inflation and deflation on volcanoes is often caused by pressure changes in sub-surface magma storage systems or reservoirs. The observed surface deformation due to these processes is generally smooth and can often be modeled with the simple Mogi model, an inflating point source in an elastic half-space [*Mogi,* 1958; *Dvorak and Dzurizin,* 1997]. Let's assume we observe an inflation signal that can be represented by a Mogi source. We can describe the observed line-of-sight (LOS) data at location (x,y) as :

$$d_o(x,y) = \mathbf{i}^{\mathbf{T}}\mathbf{u} + \varepsilon \tag{2.4}$$

where $\mathbf{i}$ is a unit vector pointing towards the satellite, $\mathbf{u}(x,y,\mathbf{m})$ is the 3-dimensional ground displacement predicted at (x,y) by a Mogi source with model parameters $\mathbf{m}$, and ε is noise. Our task is to estimate the four model parameters that describe a Mogi source: the volume change ΔV, the depth d, and the source location (x',y'). The model equations that describe the ground displacements at (x,y) due to a Mogi source at (x',y') are [*Mogi*, 1958]:

$$\mathbf{u}(x,y,\mathbf{m}) = \begin{bmatrix} u_x \\ u_y \\ u_z \end{bmatrix} = \frac{(1-\nu)\cdot\Delta V}{\pi d^2} \frac{1}{(1+(R/d)^2)^{3/2}} \begin{bmatrix} (x-x')/d \\ (y-y')/d \\ 1 \end{bmatrix} \tag{2.5}$$

where ν is Poisson's ratio and $R = \sqrt{(x-x')^2+(y-y')^2}$ is the horizontal distance between the Mogi source and the observation point (x,y).

Figure 2-20 shows a simulated interferogram of a Mogi source located at 3 km depth. We add spatially correlated noise with a typical interferogram noise structure [*Hanssen*, 2001]. The peak signal to noise ratio is 2.5. Figure 2-20d shows that the Mogi signal (green) has most of its power in the low frequencies while the noise (red) dominates the high frequencies. This implies that we should be able to represent the deformation signal with only a few low-frequency spectral coefficients. In other words, we can low pass filter the data without harming the true deformation signal. Figure 2-21 shows low-pass filtering of the original simulated data where only 0.2% of the spectral components were stored. The signal characteristics and amplitude are preserved in the low-pass filtered version. Hence, if a Mogi model accurately conveys the observed deformation, we can compress the data volume by a factor of 500.

2.5.2 Frequency Domain Optimization

Since we can represent Mogi deformation by a few spectral coefficients, we examine implementing the inversion for source parameters directly from the frequency domain measurements. We want to find the model $\mathbf{m}$ that minimizes the length of the residual vector $\mathbf{r}$, the difference between the observed data and the model prediction:

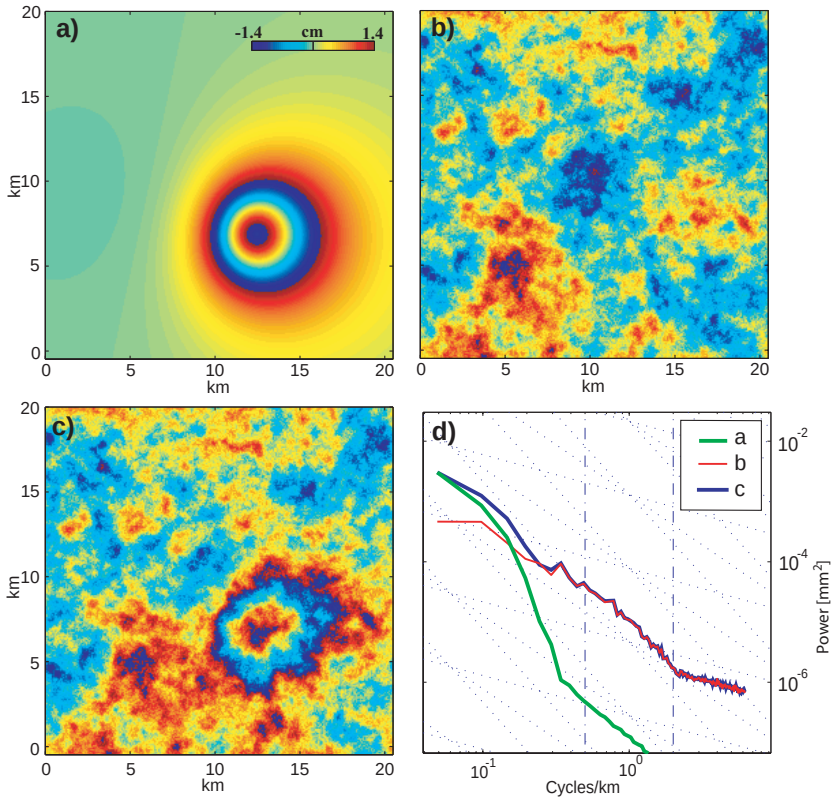

Figure 2-20: Power spectrum of simulated volcanic deformation. (a) Simulated Mogi source at 3 km depth, located at [12,7] km, and with volume change of 1.8×10^6 m^3. (b) Simulated noise using typical interferogram noise structure. (c) Noisy data obtained from addition of (a) and (b) with peak-to-peak SNR of 2.5. (d) One dimensional power spectra for (a)-(c).

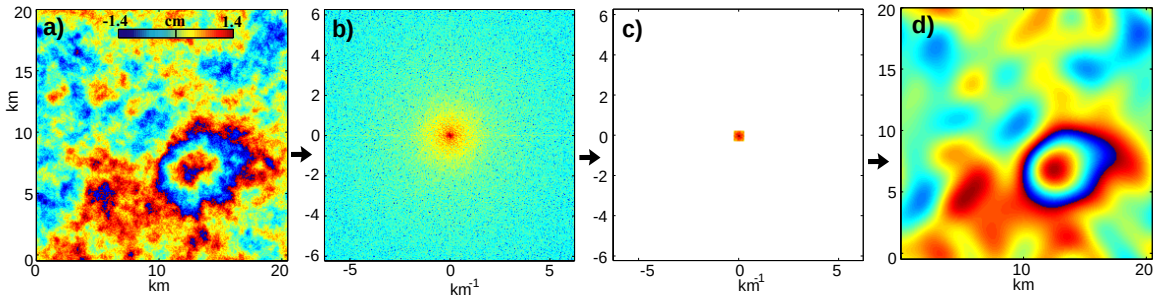

Figure 2-21: Low-pass filtering of simulated volcano deformation. (a) The simulated noisy data and (b) its two-dimensional power spectrum. (c) Low-pass filtered power-spectrum, only 0.2% of the spectrum are non-zeros, and (d) the corresponding low-pass filtered image.

$$\mathbf{r} = \mathbf{d} - \mathbf{g}(\mathbf{m}) \tag{2.6}$$

where $\mathbf{g}(\mathbf{m}) = \mathbf{i}^{\mathbf{T}}\mathbf{u}(\mathbf{m})$. We can look at these quantities as discrete images instead of vectors. Thus, the residual image r_{ij} is the difference between the observed and the predicted image:

$$r_{ij} = d_{ij} - g_{ij}(\mathbf{m}). \tag{2.7}$$

Now we can transform both sides using 2D discrete Fourier transform and get:

$$R_{kl} = D_{kl} - G_{kl}(\mathbf{m}) \tag{2.8}$$

and adjust $\mathbf{m}$ in the frequency domain. Optimization of $\mathbf{m}$ in the frequency domain is equivalent to optimization in the image domain because Rayleigh's theorem states that the power of the residual in both domains is the same [*Bracewell*, 1995]:

$$\int_{-\infty}^{\infty}\int_{-\infty}^{\infty} |f(x,y)|^2 dxdy = \int_{-\infty}^{\infty}\int_{-\infty}^{\infty} |F(u,v)|^2 dudv \tag{2.9}$$

or in the discrete case

$$\sum_{i=1}^{N}\sum_{j=1}^{M} r_{ij}\cdot r_{ij}^{*} = \sum_{i=1}^{N}\sum_{j=1}^{M} r_{ij}^{2} = \sum_{k=1}^{N}\sum_{l=1}^{M} R_{kl}\cdot R_{kl}^{*}. \tag{2.10}$$

where the '*' denotes a complex conjugate. Finding the Fourier transform of the model equations analytically is somewhat complicated. Instead we can transform a model prediction image for a Mogi source at some given location, and then adjust its location and strength in the frequency domain. We can pick some initial model parameters $\mathbf{m_0^T} = [d_0, \Delta V_0, x_0', y_0']$, calculate the model prediction image $g_{ij}(\mathbf{m_0})$, and transform that image to obtain $G_{kl}(\mathbf{m_0})$. We can adjust the location of $\mathbf{m_0}$ in the frequency domain using the 2D shift theorem [*Bracewell*, 1995]:

$$\mathfrak{F}\{f(x-a,y-b)\}(u,v) = e^{-i2\pi(au+bv)}F(u,v) \tag{2.11}$$

where $\mathfrak{F}\{\cdot\}$ denotes the Fourier transform operator and $F(u,v)$ is the 2D Fourier transform of $f(x,y)$. We can also adjust the volume change ΔV as it relates to the surface displacements linearly: $\mathbf{g}(\mathbf{m}) = \Delta V \mathbf{g}'(\mathbf{m}')$ and the Fourier transform is a linear operation:

$$\mathfrak{F}\{C\cdot f(x,y)\}(u,v) = C\cdot\mathfrak{F}\{f(x,y)\}(u,v) = C\cdot F(u,v) \tag{2.12}$$

We can now rewrite our discrete residual image in the frequency domain:

$$R_{kl} = D_{kl} - G_{kl}(\mathbf{m}) = D_{kl} - C\cdot e^{-i2\pi(ak+bl)}G_{ik}(\mathbf{m_0}) \tag{2.13}$$

where $\Delta V = C\cdot\Delta V_0$. Now we can optimize $\mathbf{m}$ by adjusting $[C,a,b]$ knowing that:

$$\mathbf{m} = \begin{bmatrix} \Delta V \\ d \\ x' \\ y' \end{bmatrix} = \begin{bmatrix} C\cdot\Delta V_0 \\ d \\ x_0 - a \\ y_0 - b \end{bmatrix}. \tag{2.14}$$

The advantage here is that we can perform the optimization on the reduced number of spectral components, e.g., 11×11 pixels instead of 256×256 pixels (Figure 2-21) to find $[C,a,b]$, the deviations from the starting model $\mathbf{m_0}$.

Figure 2-22a-b shows a starting model prediction image $g_{ij}(\mathbf{m_0})$ with $\mathbf{m_0^T} = [3$ km, 7×10^6 m^3, 10 km, 10 km], and the inverse Fourier transform of the reduced image spectrum. Again, only 0.2% of the spectral components were used. The best fit model (Figure 2-22c) has $\Delta V = 1.8\times 10^6$ m^3, located [12.2 km, 6.9 km], and it fits our simulated data $\mathbf{m_{true}^T} = [3$ km, 1.7×10^6 m^3, 12 km, 7 km] well as indicated by the low residual (Figure 2-22d).

Hence, in cases where the deformation is smooth we can optimize the model parameters in the frequency domain, using only a fraction (here 0.2%) of the original data volume. This procedure may speed up the model calculations by three orders of magnitude.

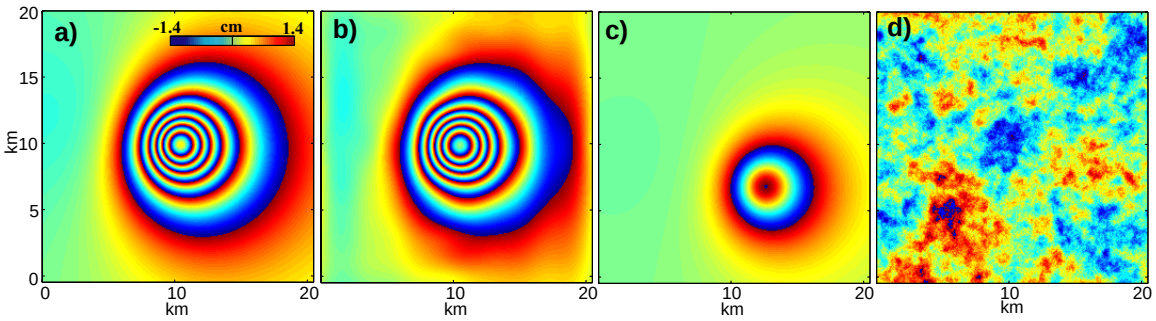

Figure 2-22: Frequency domain optimization. (a) Mogi model template, centered at [10,10] km, and with some arbitrary volume change, (b) Low-pass filtered (a). (c) Optimal model with $\hat{\mathbf{m}}^{\mathbf{T}}$ =[1.8 × 10^6 m^3, 3 km, 12.2 km, 6.9 km], (d) residual between Figure 2-21a and (c).

2.5.3 Deformation due to an Earthquake

Now we examine the power spectra for two cases of earthquake deformation. The first case is a strike-slip fault earthquake where faulting reaches surface and the second case is a buried normal faulting earthquake. In both cases the faults are 10 km long, extend 10 km down dip, and strike N45°E. The strike-slip fault is vertical, it breaks the surface, and it has a fault-slip of 50 cm. The dip-slip fault dips 60° to the northwest, has 25 cm of slip and the upper fault edge is buried at 2 km depth. Figure 2-23 shows simulated deformation interferograms for the two cases before and after noise has been added. The peak-to-peak SNR is 5.

For the strike-slip case the power spectrum of the deformation signal and the noise exhibit similar structure. The signal has strong power over all frequencies that prohibits us from using spectral filtering to reduce the noise in the simulated image. The strike-slip fault breaks the surface, causing a sharp step in the simulated interferogram. This discontinuity results in strong response in the frequency domain for all frequencies.

Deformation due to slip on a buried fault does not have sharp discontinuities or generate high-spatial frequency patterns. This is reflected in relatively low signal power of the high frequencies, where the deformation signal dominates the low frequencies. In this case we can remove the high frequency noise with low-pass filtering and optimize the model in the frequency domain using a reduced number of spectral coefficients. However, we can not remove as much of the signal in the frequency domain as we could in the Mogi case, as the buried fault deformation has significant high-frequency signals in the area where the buried

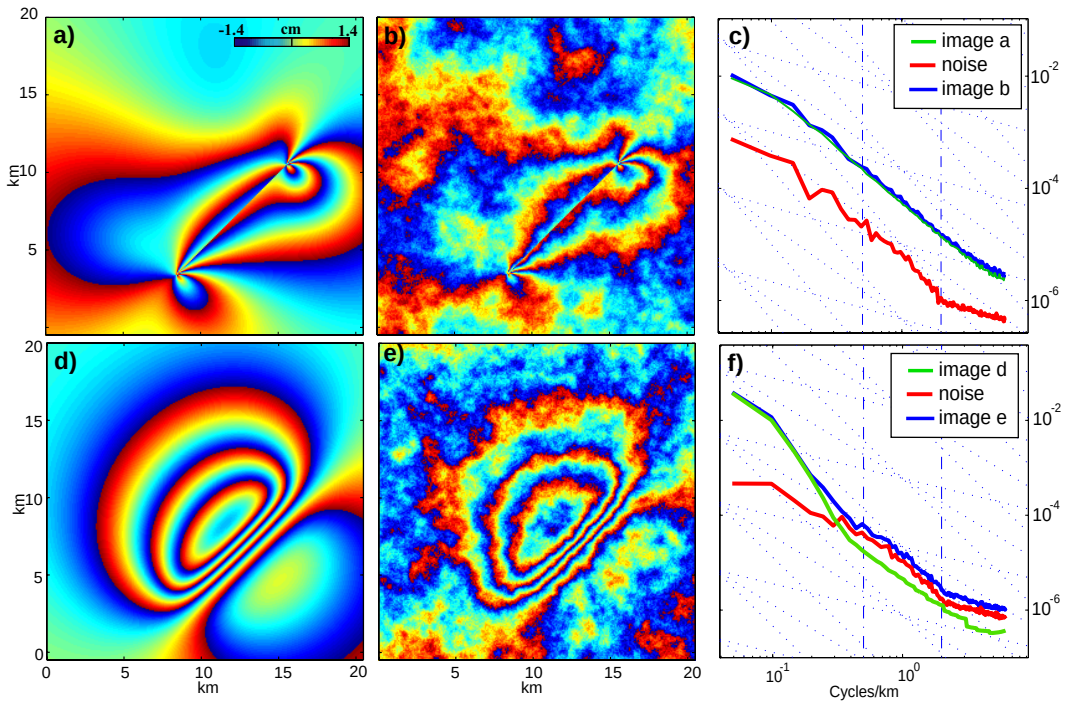

Figure 2-23: Power spectra for examples of earthquake deformation. (a) and (d) Simulated earthquake deformation interferograms with noise added in (b) and (e). (c) and (f) The power spectra of the two examples.

fault is shallowest.

There are two main disadvantages of frequency domain optimization for InSAR deformation data. First, deformation signals are not always smooth, and when they are not we lose information with low-pass filtering. And second, frequency domain optimization requires the Fourier transform of the model equations which often is not achievable. We may be able to overcome the first problem by choosing another transform that better preserves the deformation signal at all frequencies, e.g., a wavelet transform. However, the problem of transforming the model equations to the transform domain remains, making this optimization procedure infeasible.

2.6 Data Reduction in the Image Domain

In the previous section we saw that InSAR data reduction in a transform domain is of limited use as we have to optimize the model in the image domain. Here we discuss a few

methods to reduce InSAR data in the image domain.

2.6.1 Sub-sampling onto Regular Grid

The simplest way to reduce InSAR data volume is to sub-sample unwrapped interferograms to a coarser grid with regular spacing. This can be done by simply calculating the mean or the median value of some or all values within a previously determined box-size, e.g., 10×10 pixel box, and assign the resulting value to the center coordinate of the box. The data quantity in this case would be reduced by two orders of magnitude. Although this method often works well and is simple to use, there is an important trade-off between the data reduction efficiency and the deformation details visible after the reduction. In other words, if we sub-sample to a coarse grid we achieve good data reduction but we are likely to loose small scale details of the deformation field. In addition, the averaging or the filtering has its own problems. Median-filtering is a non-linear operation so we are unable to propagate errors from the full interferogram to the filtered one, and the problem with a mean value filter is that the mean-value can get biased by a few outliers within the box, e.g., outliers due to decorrelation.

2.6.2 Quadtree Decomposition

Spatially variable two-dimensional quantization of images is an alternative approach to uniform sub-sampling with median or mean value filtering. This form of image partitioning is sometimes called the quadtree algorithm [*Welstead,* 1999]. The algorithm works as follows: First the image is expanded by adding zero value lines and columns such that the image dimensions become a power of 2 (e.g., 1024×1024). Then the image is split up to four equal quadrants and the variance of the unwrapped phase values is calculated in each quadrant. If a quadrant variance exceeds a pre-determined threshold value, then that quadrant is split into four new quadrants and the procedure is repeated until convergence. When a quadrant variance is lower than the threshold value, then the mean (or the median) of the quadrant values is assigned to the center coordinate of the quadrant.

The main advantage of the quadtree algorithm is that it leaves many data points in areas where LOS displacement gradients are high but few where constant LOS values are observed. It therefore preserves better the details of the deformation than uniform sub-sampling but still can achieve efficient data reduction. However, there are several disadvantages to this

algorithm. Suppose that a quadrant has near constant values everywhere except in a small region where deformation is observed. Although the variance in the small deforming area could be higher than the threshold variance, the variance in the quadrant as a whole could be much lower. Thus, only one value might be assigned to the center coordinate of the quadrant and the small deforming area would be un-detected. This problem can be avoided by defining a maximum quadrant size or by using a reversed quadtree algorithm that would begin with small squares and expand them if variance is low. Another problem with the quadtree algorithm is that it is sensitive to image rotation. Two quadtree decompositions of the same image, with one image rotated by 45°, will result in different number of reduced data points.

There are two parameters for the quadtree algorithm that need to be selected before an image is quantized, the quadrant threshold value and the maximum quadrant size. The quadtree threshold value should be higher than the noise variance but low enough to pick up the details of the deformation of interest. The maximum distance between quadtree squares can be set equal to the distance at which data points within the interferogram become uncorrelated.

The threshold calculation can be done in a several ways. One method is to calculate the variance about the best fitting bi-linear plane within each quadrant instead of the variance of about the mean. This typically results in more efficient data reduction by a factor of about three for the same threshold value. The main argument for using the planar quadtree is that scaling of the amplitude of the deformation results in equal number of reduced data points. When a quadrant variance about the best plane is lower than the threshold the quadrant mean or median value can be assigned to the central coordinate. Another way is to assign a median value of the central region of the quadrant to the central coordinate [*Mark Simons, pers. comm.,* 2001]. However, this method has the disadvantage of non-linear median-filtering.

In this work we use quadree partitioning with the mean quadrant value assigned to the center quadrant coordinates when the variance is below the given threshold. This keeps the data reduction operation linear and will allow us to propagate the full InSAR covariance to the reduced data set. As an example, we use the Darwin interferogram (Figure 2-12) and begin by unwrapping the image to determine absolute range changes between the ground and the satellite. The unwrapped image shows uplift centered at Darwin caldera with a maximum LOS displacement of 20 cm (Figure 2-24a). The quadtree decomposition of the

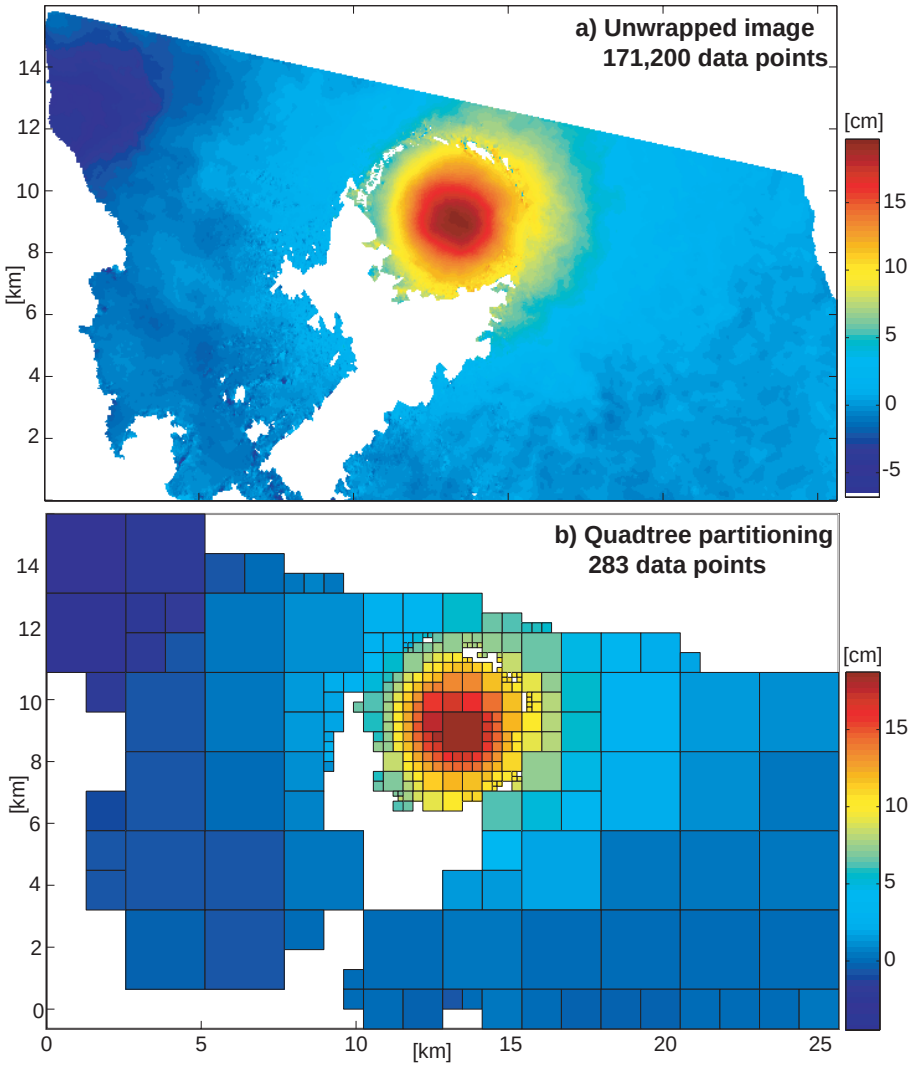

Figure 2-24: Unwrapping and Quadtree partitioning of the Darwin interferogram shown in Figure 2-12. (a) Unwrapped interferogram showing 20 cm line-of-sight uplift towards the satellite. (b) Quadtree partitioned data.

unwrapped data is shown in Figure 2-24b. Here the threshold variance was chosen 1 cm^2 (four times the noise variance) and the maximum distance between squares is 2 km (square size 2×2 km^2), equal to the noise correlation distance. The data volume was reduced from 171200 data points to 283, i.e., to 0.17% of its original volume. Still, most of the signal details are visible (Figure 2-24).

2.7 Model Calculations

Now we are ready to combine the results of previous sections to examine what influence the data reduction and the covariance estimation have on results of modeling. We first calculate a covariance matrix for the reduced Darwin dataset by propagating the covariance matrix of the full interferogram to the reduced data set. We then optimize model parameters to see if including the full InSAR data covariance makes a difference.

2.7.1 Covariance Matrix for Reduced Dataset

Quadtree sub-sampling is a linear operation when mean value filtering is used. Thus, we can represent this data reduction operation as a matrix **A**. In the case of Darwin, the original data volume has 171200 data points and the reduced version has 283 data points. Therefore, matrix **A** will be 283×171200 in size. The original data vector **d** is reduced with a simple multiplication:

$$\mathbf{d_q} = \mathbf{Ad} \tag{2.15}$$

where $\mathbf{d_q}$ is the reduced data vector of size 283×1. The i-th line of matrix **A** calculates the mean value for the i-th quadtree square.

The covariance matrix for the full unwrapped interferogram in Figure 2-24a can be calculated using the covariance function shown in Figure 2-16. The covariance function has variance of 25 mm^2 and the function indicates that two data points within the image become uncorrelated at a distance of more than 2 km. The full interferogram covariance matrix Σ_d is of size 171200×171200 and would occupy $\sim$100GB of memory if stored all at once. However, most of the matrix entries are zeros and we only have to store a single column of this large matrix at any given time. The covariance matrix of the reduced dataset Σ_q is found by propagating the full interferogram covariance matrix Σ_d:

$$\Sigma_q = \mathbf{A}\Sigma_d\mathbf{A^T}. \tag{2.16}$$

Remember that matrix **A** is only 283×171200 ($\sim$200MB) and the multiplication $\mathbf{A}\Sigma_d$ results in another 283×171200 matrix. To avoid storing Σ_d we calculate each column of it on the

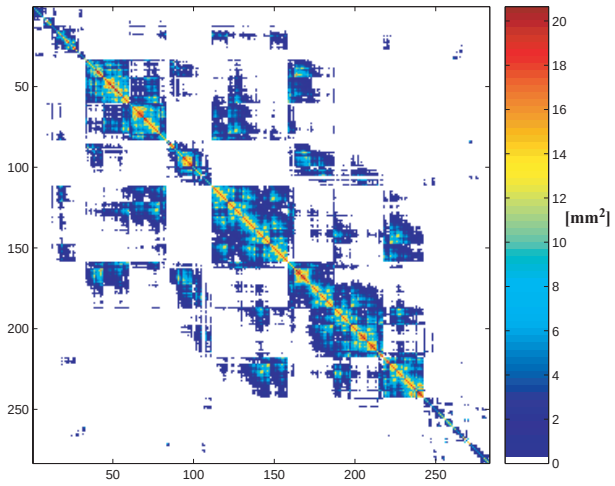

Figure 2-25: Covariance matrix for the Darwin InSAR data shown in Figure 2-24b.

fly and multiply column by column in $\mathbf{A}$. Therefore, we will only need $\sim$500MB of memory for the calculations. Multiplying $\mathbf{A}\Sigma_d$ and $\mathbf{A^T}$ then results in the reduced data covariance matrix Σ_q that is only 283×283 ($\sim$0.3MB) in size and it is shown in Figure 2-25. The matrix variances (on the diagonal line) range from 5 mm^2 to 21 mm^2. No data points are completely independent because even though the maximum square size exceeds the maximum correlation distance, some points within a quadtree square are less than 2 km from points in the neighboring square. Therefore, neighboring quadtree data points are always correlated. The blocky appearance of the matrix only reflects how the algorithm enumerates reduced data values.

2.7.2 Model Optimization

The circularly symmetric uplift observed at Darwin suggests that a Mogi point source model may fit the data well. The Mogi model equations are shown in Section 2.5.1 and here we assume we can write the Darwin data $\mathbf{d_q}$ as:

$$\mathbf{d_q} = g(\mathbf{m}) + \boldsymbol{\varepsilon} = \mathbf{i^T u} + \boldsymbol{\varepsilon} \tag{2.17}$$

where $\mathbf{i}$ is a unit vector pointing into line of sight, $\mathbf{u}$ are the predicted ground displacements by model $\mathbf{m}$ (see Equations 2.5), and $\boldsymbol{\varepsilon}$ are observational errors. We seek to find the model

Table 2.1: Optimum model parameters for a Mogi source at Darwin volcano for three different model calculations.

Case	*Depth [km]*	ΔV $[\times 10^6$ m$^6]$	*East [km]*	*North [km]*
Quadtree data, full covariance	3.28	9.05	12.68	34.26
Quadtree data, no covariance	3.23	8.75	12.72	34.18
Median filtered data	3.41	9.75	12.67	34.23

m that minimizes the L2 norm of the weighted misfit function:

$$\Phi = \|\mathbf{W}[\mathbf{d_q} - g(\mathbf{m})]\|_{\mathrm{L2}} \tag{2.18}$$

where weight matrix **W** comes from the Cholesky decomposition of the data covariance matrix inverse: $\Sigma_p^{-1} = \mathbf{W^T W}$. We determine the best model parameters using non-linear optimization methods.

We estimate the optimal model for two cases: 1) We use the estimated covariance matrix as a weight (Equation 2.18), and 2) we ignore the covariances and approximate Σ_q as a diagonal matrix: $\Sigma_q = \sigma^2\mathbf{I}$, where σ^2 is the variance and **I** is the identity matrix. In the second case the data points are assumed independent and they all have equal weight in the model parameter estimation. The optimum model parameters for these two cases are very similar; they vary less than 5% (Table 2.1). This seems to indicate that in cases like Darwin, where the SNR is high, one can treat reduced InSAR data as independent and avoid the difficulty of estimating the data covariance matrix. Surprisingly however, simulations of a Mogi source in low SNR cases also gave similar results, i.e., near identical optimum model parameters when using the full data covariance matrix and when using only a diagonal covariance matrix. The reason may be related to the low-pass filtering nature of quadtree sub-sampling, which eliminates the high frequency part of the image where noise dominates (see Figure 2-20).

Optimization for model parameters using a dataset that was reduced to a regular grid with median-filtering shows results that differ from the two previous results using the quadtree sub-sampled data (Table 2.1). Here the source is found to be deeper because data points far from the center of uplift have more weight (relative to the quadtree case), which tends to result in a deeper source. This simple example implies that different data

sub-sampling method may affect modeling results more than ignoring data covariances in the inversion.

Further investigation is required to evaluate better the effect data sub-sampling and data covariances have on modeling results. Various simulated earthquake and volcanic deformation interferograms should be examined using many different SNRs and a variety of noise structures. Model parameter optimization, using these simulated noisy interferograms, could then be systematically tested using the different data reduction methods and data weights.

2.8 Conclusions

In this chapter we have investigated various aspects of covariance estimation and data reduction for InSAR data. Although this research topic is still in progress we summarize here the main conclusions below.

We observe that the InSAR noise spectrum, in a few examples of deformation interferograms, commonly has a power-law structure. The power-law index varies from $-8/3$ to $-3/3$ for intermediate spatial scales (0.5-2 km) while it is usually lower (-5/3 to 0) for shorter and longer scales. In general, the power-law indices we observe are equal or lower than those found by *Hanssen,* [2001]. It is important to note that the noise variance and the correlation distance at which data points become decorrelated are dependent on the spatial support of the image. In other words, these parameter estimates are generally not the same for 5×5 km^2 and 10×10 km^2 noise images even though the true structure of the noise is the same structure in both images. Empirical covariance functions can be determined in deformation interferograms if deforming areas cover only a part of the image. The function can be calculated using a sample covariance estimation or from the 2D autocorrelation of the image.

InSAR data reduction using the Fourier transform or a wavelet transform can be effective but has the major disadvantage that model equations need to be transformed as well to optimize model parameters using the reduced dataset. Thus, transform domain data reduction is not useful to make model calculations more efficient. Image domain data reduction using 2D quantization (quadtree) has the advantage of preserving details of the deformation signal and achieves effective data reduction. This reduction operation can be linear allowing the full interferogram covariance to be propagated to calculate a data covariance matrix for

a reduced dataset.

Our preliminary results show that omitting data covariances in Mogi model optimization does not significantly bias the modeling results, even when the SNR is low. This may, however, be dependent on the sub-sampling method used, as we find different modeling results for different sub-sampling methods. More thorough investigation is required to better understand the limits of when including InSAR covariances becomes important as well as systematic examination of the effects the different data reduction algorithms have on modeling results.

2.9 Appendix A

Structure Functions and Variograms

Structure functions are commonly used to describe two-dimensional random functions. For a random function $f(\mathbf{x})$ where $\mathbf{x}$ is a location and $\mathbf{r}$ is a displacement vector, structure function is defined as the expected value of the squared difference of f at $\mathbf{x}$ and $\mathbf{x}+\mathbf{r}$ [*Tatarski*, 1961; *Treuhaft and Lanyi*, 1987]:

$$D_f(\mathbf{x},\mathbf{r}) = \mathrm{E}\left[[f(\mathbf{x}) - f(\mathbf{x}+\mathbf{r})]^2\right]. \tag{2.19}$$

When a random field is homogeneous the structure function is invariant of location $\mathbf{x}$ and when it is isotropic the direction of $\mathbf{r}$ is not important, only its length. Thus, assuming both homogeneity and isotropy the structure function depends only on the distance $r = |\mathbf{r}|$ and becomes:

$$D_f(\mathbf{x},\mathbf{r}) = D_f(r). \tag{2.20}$$

Furthermore, many geophysical data can be described with a structure function following a power-law [*Williams et al.,* 1998]:

$$D_f(r) = C^2 r^{\nu} \tag{2.21}$$

where C^2 characterizes the intensity or the roughness of the process and ν is the power index. A process with a structure function like in Equation 2.21 has a power spectrum that also follows a power law with index $-(\nu+1)$ [*Tatarski*, 1961].

The structure function is similar to what is called a variogram in geostatistics. An experimental or sample variogram is defined as [*Stein et al.*, 1999]:

$$\gamma(r) = \frac{1}{2P(r)} \sum_{i=1}^{P(r)} [f(\mathbf{x}_i) - f(\mathbf{x}_i + \mathbf{r}_i)]^2 \tag{2.22}$$

where $\mathbf{x}_i$ and $\mathbf{r}_i$ are random sample locations and lags ($r = |\mathbf{r}_i|$) within the image, and $P(r)$ is the number of samples for each length r. From Equation 2.19 we can see that a sample variogram is an estimate of the structure function:

$$D_f(r) \approx 2 \cdot \gamma(r). \tag{2.23}$$

Power-spectrum

Isotropic 3D Kolmogorov turbulence has a power law structure function with index $\nu = 2/3$ [*Tatarski*, 1961]. The radar signal travels down through the atmosphere and out again, and the difference in the signal delay due to the atmosphere can be described as the integration of the refractive index along the path travelled. Thus, the structure function of the atmospheric signal delay $D_s(r)$ becomes [*Tatarski*, 1961; *Treuhaft and Lanyi*, 1987]:

$$D_s(r) = C_s^2 \cdot r^{5/3}. \tag{2.24}$$

The corresponding power spectrum of the signal delay is then [*Tatarski*, 1961; *Hanssen*, 2001]:

$$P_s(k) \propto \begin{cases} k^{-8/3} & \text{for a 1D profile over a 2D surface, with } k = k_1 \\ k^{-11/3} & \text{for the 2D surface, with } k^2 = k_1^2 + k_2^2 \end{cases} \tag{2.25}$$

Covariance Functions

Spatial covariance describes the relation between two points in an image. For an image f and two locations $\mathbf{x}$ and $\mathbf{x}+\mathbf{r}$ the covariance is defined as:

$$\mathrm{COV}(\mathbf{x},\mathbf{x}+\mathbf{r}) = \frac{1}{2}\mathrm{E}[f(\mathbf{x})f(\mathbf{x}+\mathbf{r})] - \frac{1}{2}\mathrm{E}[f(\mathbf{x})]\,\mathrm{E}[f(\mathbf{x}+\mathbf{r})]. \tag{2.26}$$

Sample Covariance function can be calculated in a similar way as the sample variogram and describes the spatial relation between data pairs at $\mathbf{x}_i$ and $\mathbf{x}_i+\mathbf{r}_i$:

$$C(r) = \frac{1}{P(r)}\sum_{i=1}^{P(r)} f(\mathbf{x}_i)\cdot f(\mathbf{x}_i+\mathbf{r}_i) - (m_i \cdot m_r) \tag{2.27}$$

where m_i and m_r are local means of f at $\mathbf{x}_i$ and at $\mathbf{x}_i+\mathbf{r}_i$, respectively. Assuming second order stationarity the local mean within the image is constant and the equation above simplifies to:

$$C(r) = \frac{1}{P(r)}\sum_{\alpha=1}^{P(r)} f(\mathbf{x}_i)\cdot f(\mathbf{x}_i+\mathbf{r}_i) - \bar{f}^2. \tag{2.28}$$

Thus, in this case we can relate the variogram $\gamma(r)$ and the covariance function with:

$$\gamma(r) = C(0) - C(r). \tag{2.29}$$

Chapter 3

Widespread Uplift and 'Trapdoor' Faulting on Galápagos Volcanoes Observed with Radar Interferometry

In the previous chapter we addressed some of the technical issues of using InSAR data in studying crustal deformation. We analyzed the structure of InSAR noise in examples of deformation interferograms and presented empirical methods to locally estimate covariance functions. We also discussed some data reduction methods and modeling strategies. We now turn our attention to what we can learn about geophysical processes from InSAR deformation observations. We begin by studying volcanic deformation in the western Galápagos that is the subject of the next three chapters.

In this chapter we study the deformation of Isabela and Fernandina islands, western Galápagos, where we find that most of the volcanoes have been actively deforming during the past decade due to a variety of subsurface processes. We look in detail at the deformation at two volcanoes, Darwin and Sierra Negra. Inflation at Darwin is circularly symmetric and can be modeled as a response to a point pressure increase at 3 km depth. Meanwhile, inflation at Sierra Negra is both spatially and temporarily variable and can not be explained with simple models. Here we image the expanding magma body using a variable opening sill. We also describe and model trapdoor faulting within Sierra Negra caldera that occurred on an intra-caldera fault system. This chapter is based on material that we have already completed and was published as the cover feature of Nature in October 2000 [*Amelung et al.,* 2000a].

3.1 Abstract

Volcanic uplift, caused by accumulation of magma in subsurface reservoirs, is a common precursor to eruptions [*Dvorak and Dzurisin,* 1997; *Lipman et al.,* 1981]. But, for some volcanoes, uplift of meters or more has not yet led to an eruption [*Newhall and Dzurisin*, 1988]. Here we present displacement maps of volcanoes in the Galápagos Islands, constructed using satellite radar interferometry, that might help explain this dichotomy. We show that all but one of the seven volcanoes on the islands of Isabela and Fernandina deformed during 1992-99. Cerro Azul and Fernandina erupted [*Naumann and Geist,* 2000; *Mouginis-Mark et al.,* 2000; *Jónsson et al.,* 1999] during the observation period and show evidence of inflation, co-eruptive deflation, and shallow dike intrusion. In contrast, the largest volcano, Sierra Negra, has not erupted, yet exhibits spatially and temporally variable deformation, with maximum uplift of 2.7 m between 1992 and 1999, which can be modeled by a shallow sill. Inflation during 1997-98, however, was accompanied by 'trapdoor' faulting on a steeply dipping fracture system within the caldera. Repeated trapdoor faulting over geologic time has formed an arcuate intra-caldera ridge within Sierra Negra and may have acted to relax stresses above the magma chamber, inhibiting summit eruptions. Similar processes may help explain large uplift unaccompanied by eruptive activity at other volcanoes.

3.2 Introduction and Data Analysis

A mosaic of two deformation interferograms spanning 1992-7 and 1992-8 shows that all volcanoes on the islands of Fernandina and Isabela, except Ecuador, deformed during the observation period (Figure 3-1). The map shows line-of sight (LOS) ground displacements towards the European radar satellites ERS-1 and ERS-2, produced from interferograms spanning 5 years from 1992 to 1997 (Ecuador, Wolf, Fernandina) and 6.4 years from 1992 to 1998 (Darwin, Alcedo, Sierra Negra and Cerro Azul; Table 3.1). The radar echoes were reduced to interferograms by calculating the phase difference between images from two satellite passes [*Massonnet et al.,* 1993; *Zebker et al.,* 1994; *Massonnet and Feigl,* 1998]. The topographic contribution to the observed phase was removed using a digital elevation model [*Mouginis-Mark,* 1996]. The interferometric phase, which is measured modulo 2π, is unwrapped [*Goldstein et al.,* 1988] to produce LOS displacement, and presented here so that each color-cycle represents 20 cm displacement (Figure 3-1). The incidence angle of the ERS radars is 23° from vertical. All the volcanoes actively deformed during the observation

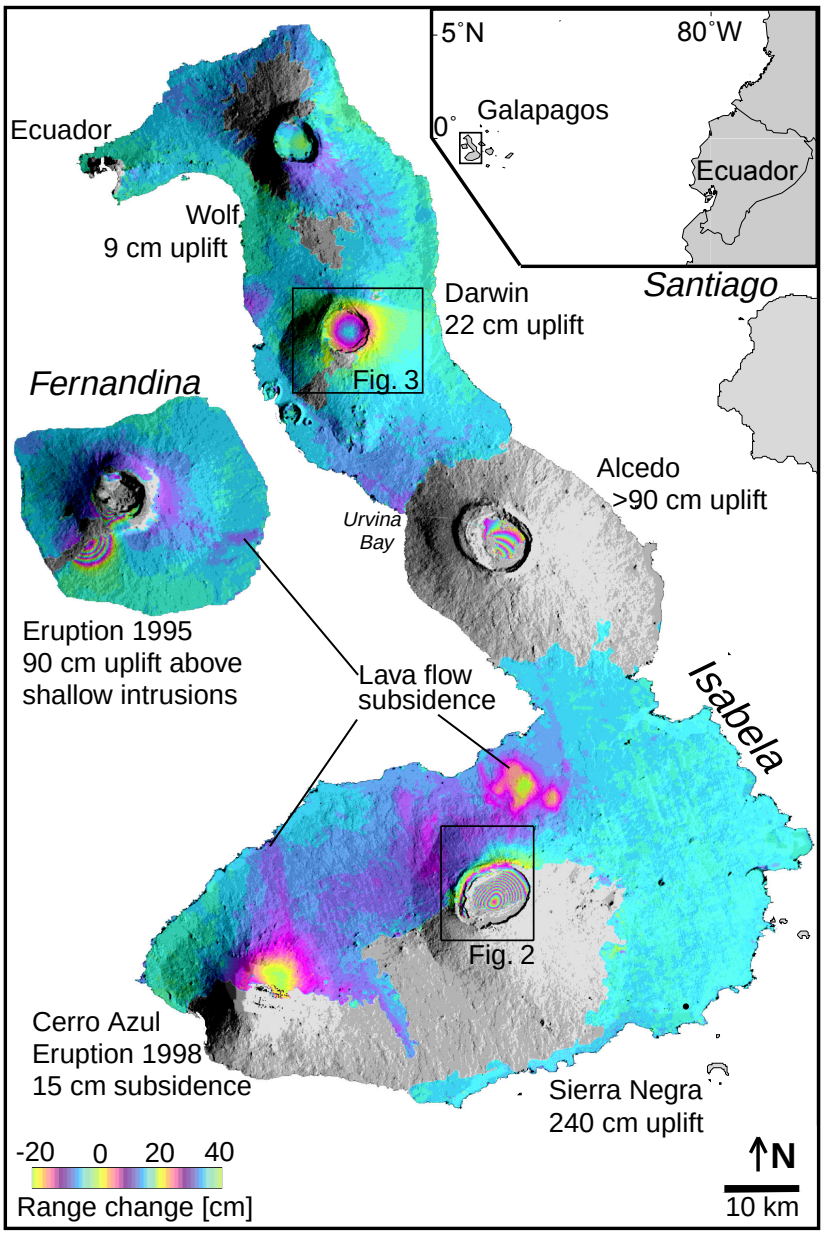

Figure 3-1: Observed deformation at Isabela and Fernandina (main image), the westernmost islands in the Galápagos archipelago (inset). Each color cycle represents of 20 cm of ground displacements into the line of sight to the satellites. Areas where the interferometric coherence is lost, presumably because of dense vegetation are shown gray. Also shown is maximum uplift at each volcano, assuming that displacements are vertical.

period except Ecuador volcano (see Table 3.1). Ecuador is also the only volcano not to have any recorded eruptions since the Galápagos islands were discovered in 1535 [*Rowland et al.,* 1994].

Before these observations there were no instrumental measurements of active deformation in the Galápagos, although 5-7 m of uplift occurred in Urvina Bay in 1954, six months before an eruption of Sierra Negra [*Geist et al.,* 1994; *Simkin and Siebert,* 1994]. We derived uplift rates ranging from several millimeters per year at Wolf to 0.9 m per year at Sierra Negra using satellite radar interferometry (InSAR); these rates indicate accumulation of magma in reservoirs beneath the summit calderas of each volcano. Only Cerro Azul and Fernandina erupted during the observation period. At Cerro Azul, pre-eruptive uplift (June 1992 to October 1997), as well as subsidence (October 1997 to November 1998), are associated with the September-October 1998 eruption [*Naumann and Geist,* 2000; *Mouginis-Mark et al.,* 2000]. Fernandina exhibits a semi-circular fringe pattern on its southwest flank (Figure 3-1), which has been modeled with a dipping, radial dike coincident with the 1995 eruption [*Jónsson et al.,* 1999]. Uplift of 0.1 m from September 1998 to March 1999 suggests refilling of a shallow magma chamber. Uplift of some volcanoes (e.g. Campi Flegrei and Yellowstone [*Bonafede and Mazzanti,* 1988; *Wicks et al.,* 1998]) may be related to hydrothermal rather than magmatic processes. Because of the high eruption frequency of the Galápagos volcanoes, and our observations of pre-eruptive uplift and co-eruptive subsidence at Cerro Azul, we suggest that the uplift at the various volcanoes in the Galápagos is due to magma accumulation.

The interferograms also show surprisingly large evidence for subsidence of lava flows on Fernandina, Cerro Azul, and Sierra Negra (see Figure 3-1). Up to 20 cm of subsidence was observed on the 1979 flows on the north flank of Sierra Negra (between 1992 and 1998), roughly 13-19 years after their emplacement [*Reynolds et al.,* 1995]. The subsidence on the north flank of Cerro Azul and on the southeast flank of Fernandina is found on lava flows of unknown age. Potential explanations for the subsidence include thermal contraction, and compaction of the flow, or lava substrate [*Murray,* 1988; *Briole et al.,* 1997; *Stevens,* 2001].

Sierra Negra experienced particularly dramatic and variable ground deformation. We observe a peak radar line-of-sight (LOS) displacement (range decrease) of 2.2 m between 1992 and 1998 (corresponding to 2.4 m uplift; see Figure 3-1) and 0.3 m during the September 1998 to March 1999 period. The corresponding displacement rates vary from 0.32 m/year during 1992-97, to 0.90 m/year during 1997-98, and 0.65 m/year during 1998-99. Figure 3-2

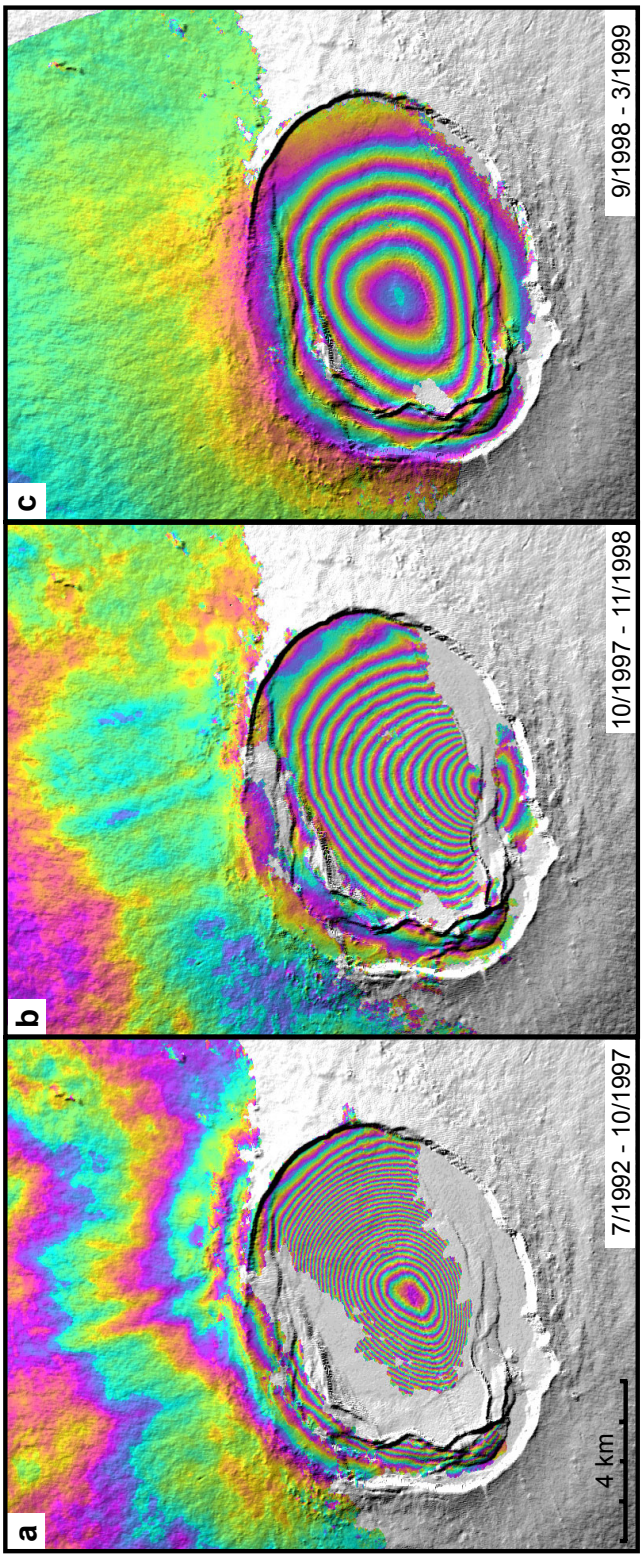

Figure 3-2: Radar interferograms of Sierra Negra volcano showing uplift during three time periods. (a) 1992-97 (5.3 years, descending orbit). (b) 1997-98 (1.1 years, descending orbit). (c) 1998-99 (0.5 years, ascending orbit). Each color cycle represents 5 cm LOS displacement. The deformation pattern during the first and third time period is similar, but is markedly different during the intervening period. In (b) the interferometric phase is discontinuous across the pre-existing fault (arcuate ridge) in the southern part of the caldera, the location of the proposed trapdoor faulting.

Table 3.1: Maximum LOS displacements at various volcanoes as observed in five different interferograms derived from 9 available radar scenes acquired in 1992 and in 1997-1999. $B_\perp$ is the perpendicular component of the spatial separation between two satellite passes. Images from track 140 and 412 are acquired from descending satellite orbits but the images from track 61 from ascending orbits.

Volcano	*Last Eruption*	*Track 140* *6/15/92-10/16/97* *5.3 years* $B_\perp = 453\ m$	*Track 140* *10/16/97-11/5/98* *1.1 years* $B_\perp = 367\ m$	*Track 140* *6/15/92-11/5/98* *6.4 years*$^+$ $B_\perp = 85\ m$	*Track 412* *9/12/92-9/30//97* *5 years*$^+$ $B_\perp = 279\ m$	*Track 61* *9/26/98-3/20/99* *0.5 years* $B_\perp = 5\ m$
Ecuador	Not known *Rowland et al.,* 1994	-	-	-	0	-
Wolf	1982 *Simkin and Siebert,* 1994	-	-	-	0.08 m	-
Fernandina	1995 *Jónsson et al.,* 1999	-	-	-	0.85* m	0.08 m
Darwin	1812 *Simkin and Siebert,* 1994	0.17 m	< 0.05 m	0.20 m	0.14 m	< 0.03 m
Alcedo	$\sim 1946 - 1960$ *Geist et al.,* 1994	> 0.80 m	< 0.05 m	> 0.85 m	-	< 0.03 m
Sierra Negra	1979 *Reynolds et al.,* 1995	1.59 m	0.90 m	2.20 m	-	0.30 m
Cerro Azul	1998 *Mouginis-Mark et al.,* 2000	0.13 m	-0.26* m	-0.14* m	-	< 0.03 m

*Eruption occurred during this time period.
$^+$In Figure 3-1.

illustrates that while the spatial pattern of deformation in 1992-97 and 1998-99 was similar, with the maximum uplift near the center of the caldera, the deformation pattern during the intermediate period (1997-98) was markedly asymmetric with maximum uplift near the south rim of the caldera. Discontinuities in interferometric phase and loss of image coherence coincide with a previously mapped inner caldera fracture system (Figure 3-2b). The fracture system, consisting of outward-dipping (60-90°) normal faults, is marked by a 14 km long curving arcuate ridge, open to the east, which surrounds a tilted and elevated inner caldera floor [*Reynolds et al.,* 1995]. We interpret the InSAR data as indicative of faulting along the southern part of the pre-existing fault system during the 1997-98 period. We observed similar fringe discontinuities near intra-caldera faults on Alcedo during 1992-98, but lack of data across the faults and on the volcano's flanks hindered a more detailed analysis.

3.3 Deformation Modeling and Discussion

We inverted the InSAR observations for magma chamber geometry and volume change in an elastic half-space using robust non-linear optimization methods [*Cervelli et al.,* 2001], ignoring second-order effects of elastic and structural heterogeneity, and topography. For Darwin, Wolf, and Cerro Azul, point centers of dilatation ("Mogi sources") [*Mogi,* 1958] accurately reproduce the near-radial symmetry observed in the fringe pattern (Figure 3-3). These models are consistent with magma accumulation in shallow chambers 2-3 km beneath the calderas, except at Cerro Azul which yields a source depth of about 5 km. Shallow magma accumulation is compatible with inferred depths of fractional crystallization of evolved, well-mixed basalts [*Geist et al.,* 1998; *Allan and Simkin,* 2000]. In contrast with Darwin, Wolf and Cerro Azul, simple point-source models do not accurately describe the data from Sierra Negra or Alcedo. The elliptical deformation pattern and absence of fringes outside the caldera at Sierra Negra require a more realistic magma chamber model than a Mogi source (Figure 3-4a-b).

The radar data alone cannot uniquely resolve the shape of what are undoubtedly complex magma chambers, but we can fit the data with geologically plausible sources of deformation. The Sierra Negra data from the first and third time periods (Figures 3-2a and 3-2c) can be fitted with a sill whose opening varies spatially. We first assume a horizontal sill with uniform opening and solve for the length, width, depth and opening. We retain the optimal depth of 1.9 km, enlarge the surface area, and solve for the spatial distribution of opening.

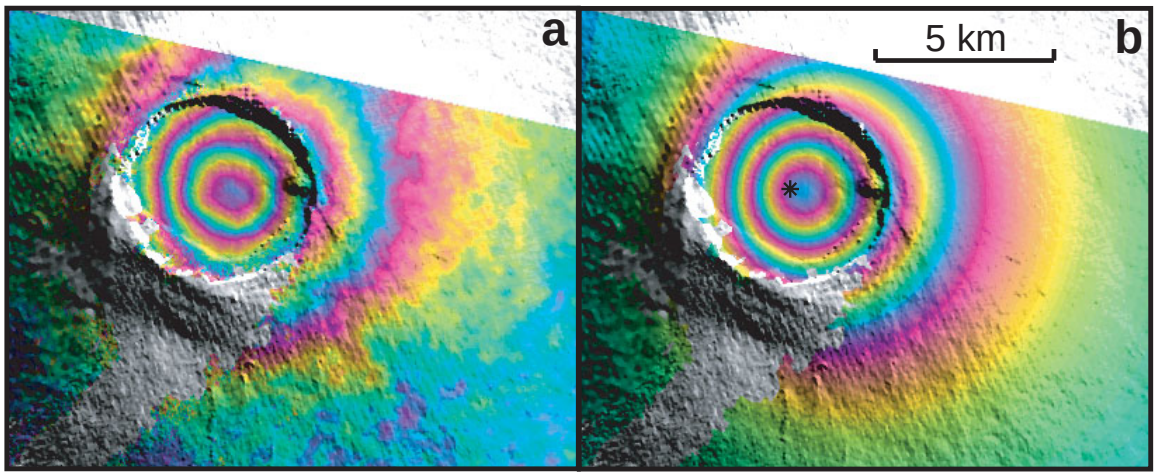

Figure 3-3: Deformation at Darwin volcano during 1992-98. (a) Radar interferogram of Darwin volcano showing 0.2 m of LOS displacement (uplift). (b) Predicted interferogram from best-fit Mogi model with source location in the center of the caldera (star) and depth of 3 km. Each color cycle represents 5 cm LOS displacement. Observations at Wolf and Cerro Azul during 1992-97/98, and at Fernandina during 1998-99 are also well fitted with Mogi models at depths of approximately 2, 5 and 3 km, respectively.

We find a distribution of opening that fits the radar data in a least squares sense, is reasonably smooth, and constrains the opening to be non-negative [*Lawson and Hanson,* 1974]. We find openings of up to 0.5 m between September 1998 and March 1999 (Figure 3-4c-d). The magma body itself may be much thicker as the data is only sensitive to the change in thickness. This model is geologically reasonable and provides a much better fit to the observations than the point source model (Figure 3-4).

The 1997-98 observations at Sierra Negra (Figure 3-2b) require a combination of two processes; uplift due to the expanding magma body and faulting along the inner caldera fracture system. We model the data with uniform sill opening and allow slip on a 75° dipping normal fault coincident with the mapped fracture system [*Reynolds et al.,* 1995]. We found fault slip of up to 1.2 meters; the estimated seismic moment would correspond to an earthquake of magnitude 5.7 [*Kanamori and Anderson,* 1975], assuming a shear modulus of 30 GPa. The largest reported earthquake in the Sierra Negra area during this time interval was a $M_w = 5.0$ event on 11 January 1998 (see data from the National Earthquake Information Center (NEIC) at http://wwwneic.cr.usgs.gov/). Unless the shear modulus of the near surface rocks is an order of magnitude less than assumed, this earthquake accounts for only

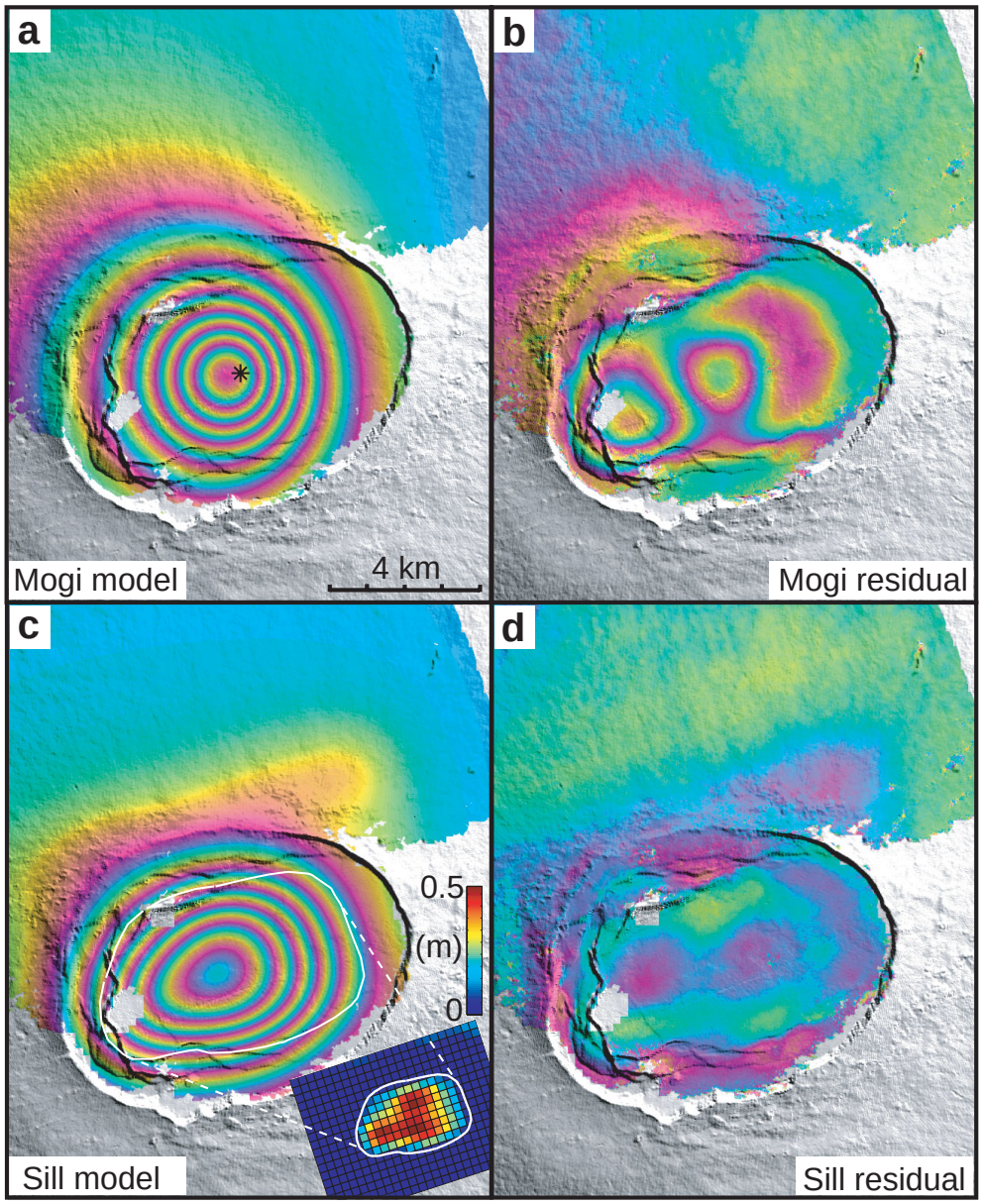

Figure 3-4: Two models for the Sierra Negra deformation during 1998-99. See data in Figure 3-2c. (a) Best-fit Mogi model. (b) The residual, the difference between the data and the Mogi model prediction; large residual indicates a poor fit. (c) Model of a horizontal sill at 1.9 km depth with variable opening of up to 0.5 m (shown in the lower right corner). (d) The corresponding residual between the data and the sill model. The deformation on Sierra Negra from 1992-97 (Figure 3-2a) is likewise better described by a sill than a point source model.

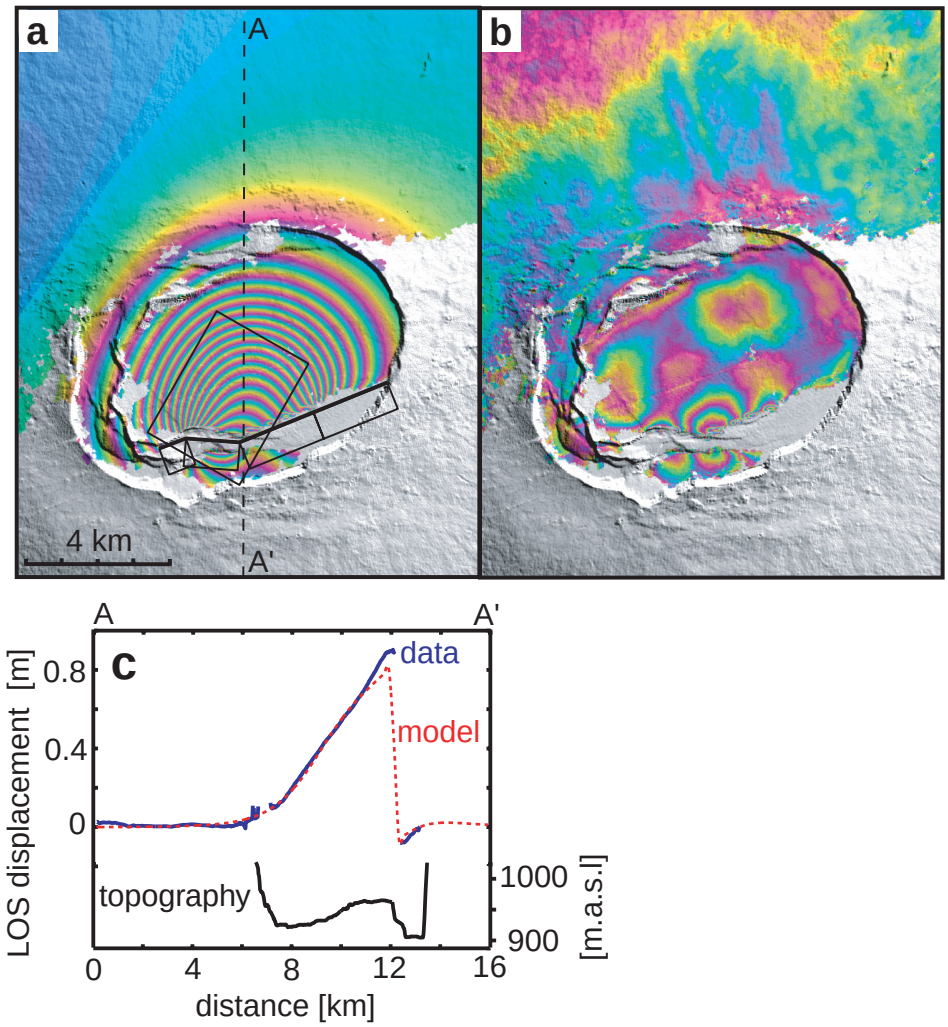

Figure 3-5: Model for the observed deformation on Sierra Negra during 1997-98. See data in Figure 3-2b. (a) The model has uniform opening of a horizontal sill (large rectangle) and slip on the normal faults that bound the elevated inner caldera floor. The four smaller rectangles show the surface projection of normal fault patches used in the modeling; a thick line marks the upper edge. The depth of the sill is not well constrained in this case; estimates range between 2.3 and 2.9 km. The difference between this and the depth obtained when trapdoor faulting was not present (2.2 km in 1992-97 and 1.9 km in 1998-99) is unlikely to be significant owing to imperfect resolution and model approximations. (b) Residual between the data and the model prediction. Localized fringes near the fault are due to the simplified representation of the fault as four rectangular dislocation segments. (c) Comparison between the data and the model prediction showing the LOS displacement along the profile A-A' as well as the intra-caldera surface topography. The observed displacement follows the topography indicating repeated slip events.

8% of the estimated moment release, suggesting that the slip was predominantly aseismic. Fault slip allowed the crust above the magma body to hinge upward like a trapdoor, with the sill opening occurring north of the normal fault system.

Uplift before 1997-98 caused extension of the caldera floor, eventually leading to trapdoor faulting sometime in 1997-98. The stress perturbations caused by magma chamber pressurization were thus sufficient to initiate slip on the fault, although conditions for a dike to propagate to the surface were not achieved. Slip on the arcuate fault system apparently relaxed shear stresses along the fault because slip was not observed between 1998 and 1999, although uplift continued. Cumulative vertical offsets along the arcuate fault structure observed in the topography range from 10 m in the area of maximum uplift in 1997-98 to over 100 m in the western caldera. In places the ridge actually extends above the caldera rim, indicating that trapdoor faulting has occurred numerous times since the caldera floor was resurfaced. The last four eruptions (and perhaps more) were not intra-caldera eruptions but occurred in the area north of the caldera. Our observations suggest that repeated slip on intra-caldera (or caldera bounding) faults may allow uplift without accumulating sufficient stress to permit vertical dike propagation. Similar processes may explain large uplifts without eruptions at other rapidly deforming volcanoes [*Newhall and Dzurisin,* 1988].

Chapter 4

Sierra Negra Trapdoor Faulting: Field Observations and Radar Range Offset Measurements

In the previous chapter we studied volcanic deformation observed on the islands of Fernandina and Isabela, western Galápagos. More specifically, we first looked at Darwin volcano that exhibits circularly symmetric deformation that can be simulated by a simple point source model. We then studied Sierra Negra volcano where the deformation is both spatially and temporarily variable, including caldera centered inflation and deformation due to trapdoor faulting on an intra-caldera fault system.

In this chapter we further investigate Sierra Negra to verify that our previous interpretation of trapdoor faulting occurring inside the caldera is correct and we also discuss what mechanisms may be responsible for the faulting. We report on evidence of recent faulting detected during fieldwork in 2001, which supports our trapdoor interpretation. In addition, we provide direct measurements of the faulting using range pixel offset measurements between two SAR amplitude images acquired before and after the faulting occurred.

4.1 Abstract

Rapid uplift observed during 1992-1997 at Sierra Negra volcano, western Galápagos, was followed by a deformation pattern that has been interpreted and modeled as trapdoor faulting on an intra-caldera fracture system (Chapter 3). However, no direct evidence for the trapdoor faulting was available to support this interpretation. Here we report on field evidence of recent faulting at Sierra Negra and provide direct measurements of the faulting using satellite radar range offsets. Field observations in 2001 indicate that recent faulting

occurred along the southern part of the intra-caldera fault system with maximum offset of at least 0.5-1 m. Range offsets measured between two synthetic aperture radar amplitude images show 1.4 ± 0.2 m range change across the intra-caldera fault system. This suggests that 1.5 ± 0.2 m of faulting occurred, assuming vertical ground displacements, which is consistent with our previous modeling results (Chapter 3). Boundary element modeling of *Fialko* [2001] shows that growing sills can favor faulting of the intrusion roof on outward-dipping or nearly vertical faults. This occurs for sufficiently high magma excess pressures when the lateral extent (half-length) of the sill becomes greater than its depth. The Sierra Negra sill is modeled at ~ 2 km depth with trapdoor faulting occurring ~ 3 km south of the center of the sill. Therefore, this model provides a plausible mechanical explanation for the trapdoor at Sierra Negra. Another mechanism, with a low density caldera floor moving up like a piston with increasing magma pressure, may also contribute to the processes observed at Sierra Negra.

4.2 Introduction

Sierra Negra Volcano is located on southern Isabela island and is the most voluminous volcano in the western Galápagos. It is 60 km long and 40 km wide subaerially with a height of 1140 m (Figure 4-1). Sierra Negra has a caldera that is larger (7 km $\times$ 10 km), but also shallower (110 m deep), than other calderas in the western Galápagos [*Reynolds et al.,* 1995; *Munro and Rowland,* 1996]. Eleven historical eruptions have occurred on Sierra Negra since 1813 [*Simkin and Siebert,* 1994]. The last eruption occurred in 1979 after a 16 year hiatus, producing a large lava flow (0.9 km^3) on the north flank of the volcano [*Reynolds et al.,* 1995]. Most of the recent eruptions have produced lavas on the north flank, while intra-caldera lava flows are older, estimated to be 1000-3000 years old [*Reynolds et al.,* 1995].

Interferometric Synthetic Aperture Radar (InSAR) observations exhibit spatially and temporally variable uplift on Sierra Negra during 1992-1999 (see Chapter 3 and *Amelung et al.* [2000a]). The maximum uplift during this time period was 2.7 m in the center of the caldera, but uplift ceased after mid-1999. Uplift during 1992-1997 and during 1998-1999 can be modeled by a shallow inflating sill. Inflation during 1997-1998, however, was markedly asymmetric with maximum uplift near the south rim of the caldera (see Figure 3-2b). The interferometric phase is discontinuous south of the uplift maximum near south facing normal

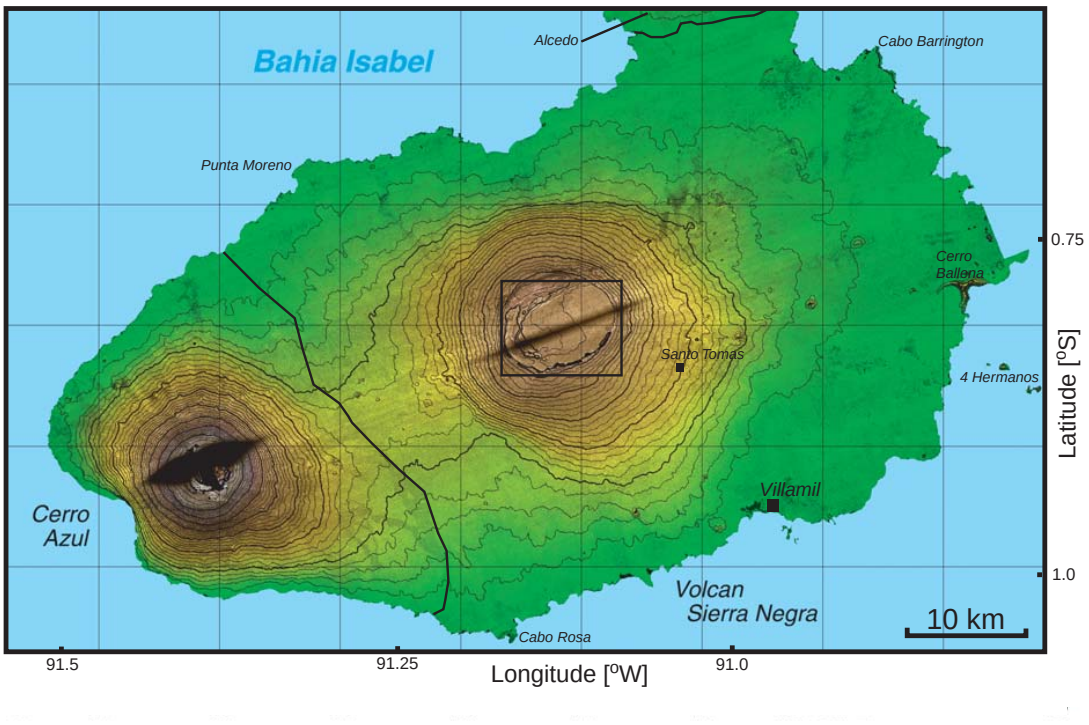

Figure 4-1: Map of Sierra Negra volcano located on southern Isabela island, western Galápagos. The rectangle marks the area shown in Figure 4-2. Also shown is the approximate boundary between Sierra Negra and the neighboring volcanoes, Cerro Azul and Alcedo [after *Reynolds et al.,* 1995]. Elevation contour lines are drawn every 40 m (thicker lines every 200 m).

faults that bound an elevated inner-caldera floor. A small patch with coherent InSAR phase exists south of the faults, just north of the caldera rim (Figure 3-2b and 4-3). The InSAR observations are incoherent everywhere around the patch making it impossible to determine the absolute displacement of the patch relative to the area north of the faults.

Our interpretation is that uplift prior to 1997 caused extension of the caldera floor, eventually leading to trapdoor faulting on the intra-caldera faults sometime in 1997-1998 (Chapter 3). When modeling the 1997-1998 data we used an expanding sill intrusion and four fault patches representing the southern intra-caldera faults. The modeling results suggest that up to 1.2 m of faulting occurred. However, no direct measurements have been available of the recency and amount of faulting.

Here we investigate if the interpretation of trapdoor faulting at Sierra Negra is correct using two different methods. First, we report evidence of recent faulting detected along the intra-caldera faults during fieldwork in January 2001, and second, we use SAR amplitude image range offsets to measure directly the line-of-sight offset across the faults.

4.3 Sierra Negra Fieldwork

The intra-caldera faults on Sierra Negra Volcano were investigated in the field in January of 2001. The fieldwork was carried out in logistic cooperation with Prof. Dennis Geist (University of Idaho) and his co-workers who conducted a GPS geodetic campaign at Sierra Negra at the same time. Most of the fieldwork consisted of walking along the faults looking for fresh fault surfaces, fresh talus, or other evidence of recent fault movement.

4.3.1 Map of Intra-Caldera Faults

The summit caldera on Sierra Negra is relatively shallow in comparison to other western Galápagos calderas. It has near vertical ring faults on all sides, except in the north, exposing 100-140 m of lava flows [*Reynolds et al.,* 1995]. The elevated central caldera floor is covered with aa flows that dip slightly to the east and it is bounded in the west and south by a 'C'-shaped intra-caldera fault system that consists of outward dipping normal faults. The fault scarps are steep ($60^\circ - 90^\circ$) and are over 100 m high in the west, but lower in the south (Figure 4-2). The western part of the fault system has a prominent sinuous ridge with lava flows on top that dip steeply inward ($20^\circ - 60^\circ$) and then bend sharply to merge with the gently dipping ($1^\circ - 3^\circ$) central caldera floor [*Reynolds et al.,* 1995]. Between the

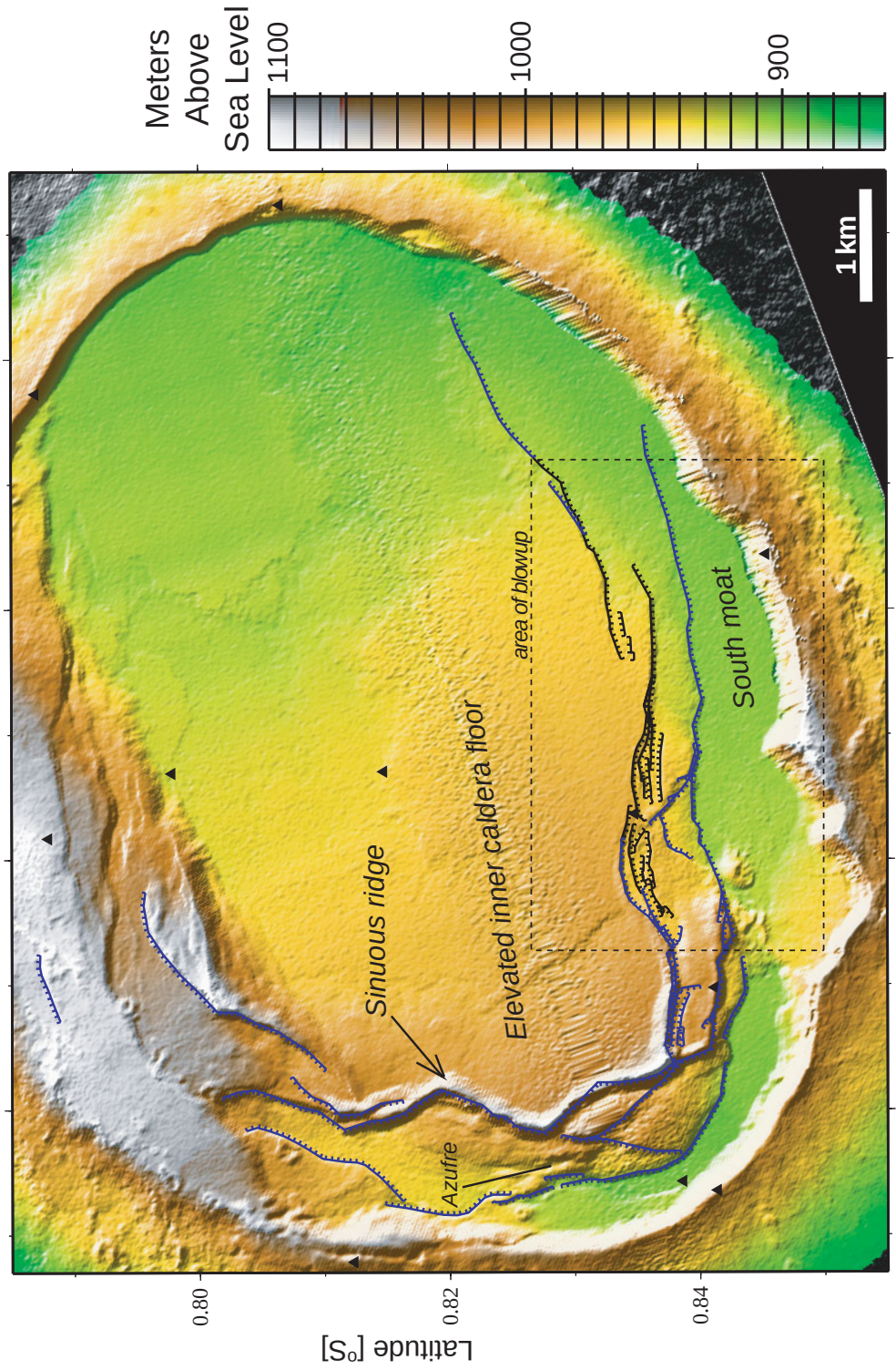

Figure 4-2: Topography of Sierra Negra caldera showing intra-caldera faults mapped in 2001. Faults in black were mapped in the field using GPS measurements and faults in blue were mapped using a DEM and aerial photographs. Triangles show campaign GPS stations installed in 2000 (a few more stations were added in 2001). Dashed rectangle marks the area shown in Figures 4-3 and 4-4.

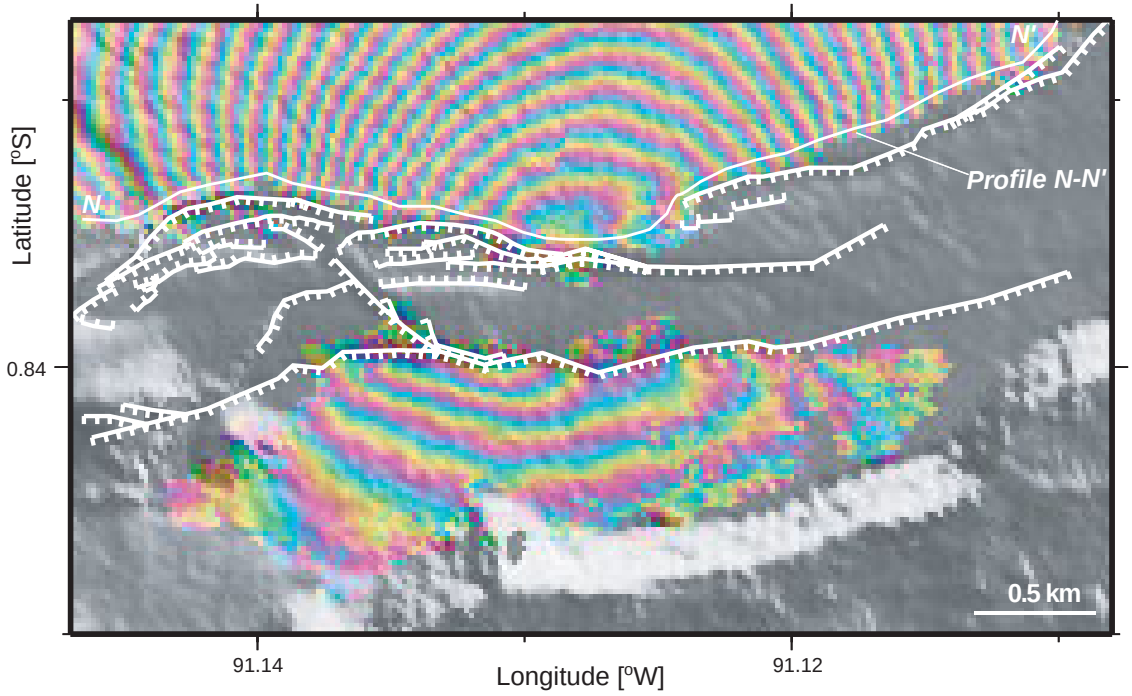

Figure 4-3: A blowup of the InSAR observations from 1997-1998 in the southern part of Sierra Negra caldera (here each color-cycle is 2.8 cm). The measurements are discontinuous across the faults and it is not possible to determine the absolute amount of offset across the faults from these data. Line-of-sight (LOS) displacements along profile N-N' are shown in Figure 4-5.

ridge and the western caldera rim is a 1-2 km wide moat that extends to the east along the caldera rim where the moat becomes broader. The sinuous ridge becomes less prominent after it turns east, until it disappears north of the southern intra-caldera faults. Here the fault system consists of several parallel south dipping normal faults (Figure 4-2).

The southern part of the intra-caldera fault system was mapped with GPS during the fieldwork in 2001 (Figure 4-2). The larger faults in the west were mapped using aerial photographs and a DEM of the volcano. The caldera ring fault is not shown in Figure 4-2 as its location is obvious from the topography. Faults in the northern part of the caldera were not mapped. The fault map shows that the intra-caldera system in the south is quite complex with several parallel and overlapping south facing normal faults. The total height of each fault is typically 0-20 m, increasing towards the west to about 100 m where the sinuous ridge has a sharp bend towards the north. Small grabens exist near some of the faults, further illustrating the extensional regime under which these faults must have formed.

4.3.2 Evidence of Recent Faulting

Evidence of recent faulting was detected in the field at various locations along the southern part of the fault system. In most cases we were only able to verify that recent faulting occurred but not the amount of faulting. Figure 4-4 shows the locations where signs of recent faulting were found and a description of each case is given in Appendix B. Appendix A shows the faults that were investigated. In some instances the evidence was continuous or near-continuous along a portion of a fault, but in some cases there was only an isolated indirect sign of recent fault movement, such as fresh talus. Most of the detected evidence is located within 1 km east and west of the line-of-sight (LOS) displacement maximum observed in the InSAR data (Figures 4-3 and 4-4). Signs of recent faulting were less clear further east and west. The InSAR data also indicate that less faulting occurred at these locations. In some cases we found evidence on parallel fault strands in this area indicating that the near-surface faulting may have been distributed among several faults, rather than concentrated on one fault.

The amount of recent faulting was estimated at a few locations where sparse vegetation or moss could be matched across the rupture. In no case was this clearly quantifiable as some 3 years had passed since the faulting took place, thus, these estimates are not accurate. The results are shown in Figure 4-5 in comparison to the InSAR LOS displacement just north of the faults. When faulting was quantified at parallel faults the values were added. Note that the LOS displacements do not show directly the amount of faulting that occurred, they only show by how much the northern wall moved up towards the satellites, i.e., somewhat less than the inferred faulting. The amount of faulting estimated in the field is generally smaller than the LOS displacements, however, the two maxima of are co-located. It is not surprising that the amount of faulting, at the few locations it could be estimated, is smaller than the faulting inferred by the modeling as the near surface expression of the faulting is likely to be distributed, instead of being concentrated on one fault.

In conclusion we can say that recent faulting occurred along the southern intra-caldera faults, possibly in 1997-1998. The field observations indicate that the amount of faulting was at least 0.5-1 m with maximum faulting occurring where the maximum InSAR LOS displacement is observed.

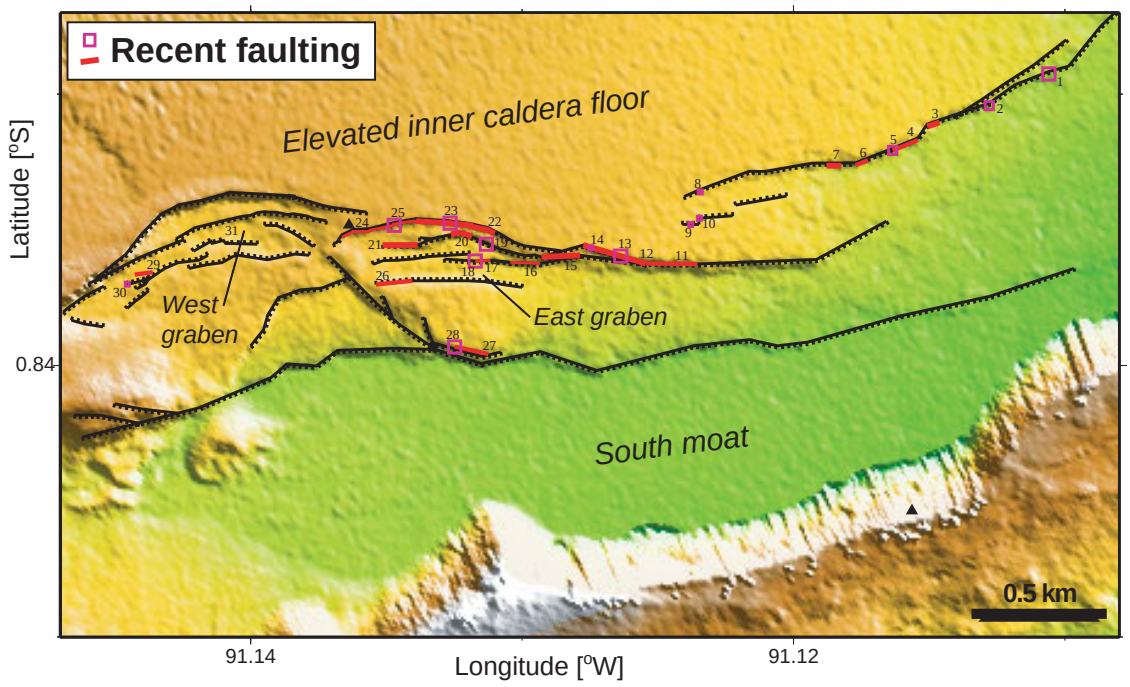

Figure 4-4: Evidence of recent faulting in the southern part of Sierra Negra caldera. Red lines show where near continuous evidence of recent faulting was detected along the faults. Thicker lines mark stronger evidence. Purple squares show single localities where evidence was detected. Numbers refer to descriptions in Appendix B.

4.4 SAR Range Offset Measurements of Sierra Negra

The InSAR measurements are discontinuous across the intra-caldera faults making it impossible to measure the fault offset that occurred from the interferogram (Figure 4-3). However, the radar data can be used to make a direct measurement of the faulting using range offsets between pixels in two amplitude images (Figure 4-6).

SAR image offsets (SARIO) between two radar amplitude images have been used to measure ground displacements in large earthquakes [e.g., *Michel et al.,* 1999a; *Peltzer et al.,* 1999] and can provide useful information about the location of the fault trace [*Jónsson et al.,* 2002a]. All previous studies used only azimuth SARIO measurements while range offsets have usually been ignored. The main reason is that azimuth offsets provide information about horizontal ground displacements parallel to the satellite flying direction that are perpendicular to the InSAR phase measurements. The range offsets, on the other hand, are

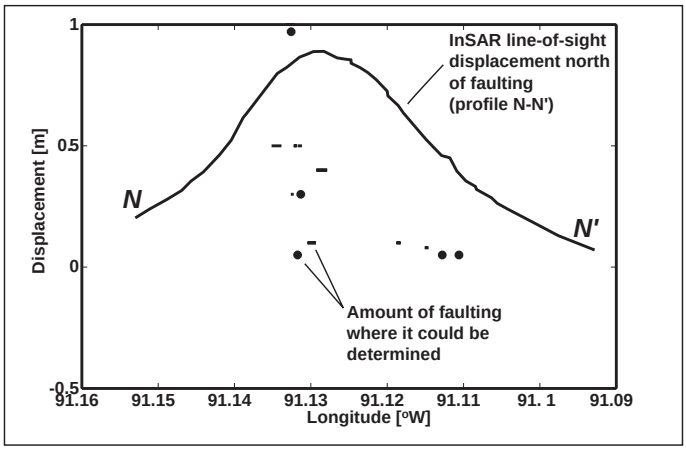

Figure 4-5: Amount of recent faulting where it could be determined in the field. The dots and dashes show cumulative faulting estimates across the several parallel faults. InSAR LOS displacements north of the faults (see profile N-N' in Figure 4-3), relative to a far-field zero, are shown in comparison to the field estimates.

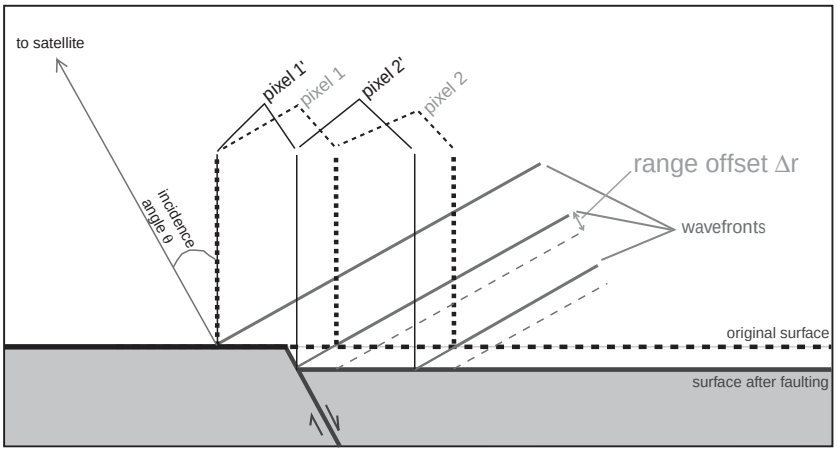

Figure 4-6: Schematic figure showing how faulting can be detected by range offset measurements. Like InSAR measurements, the range offsets are most sensitive to vertical movements (i.e., for ERS incidence angle of 23°). The slant range spacing of the ERS radars is 7.95 m, corresponding to roughly 20 m on the ground.

sensitive to the same line-of-sight component as the more precise InSAR phase measurements, and therefore generally provide no extra information. One can use azimuth SARIO measurements to reconstruct the full three-dimensional ground displacement field when combined with InSAR data from both ascending and descending orbits [*Fialko et al.,* 2001].

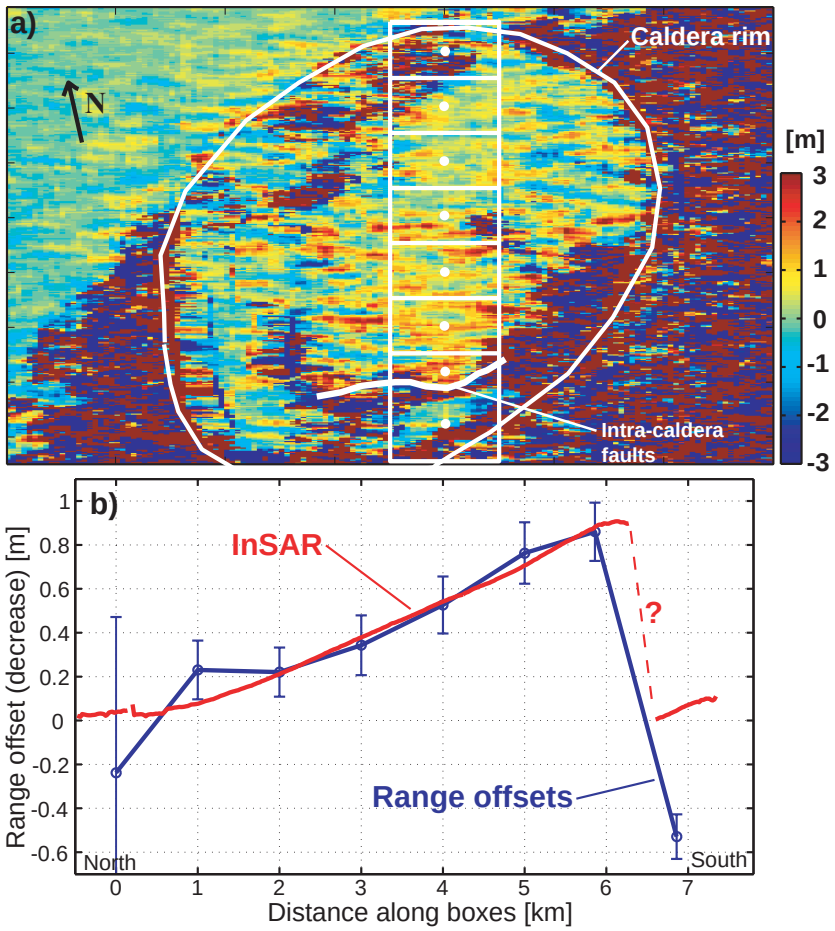

Figure 4-7: SAR range offset measurements of Sierra Negra caldera. (a) Map showing range offsets measured in the caldera during 1997-98. Uplift into line-of-sight towards the satellite is shown positive. (b) Range offset averages from boxes in (a) from north to south in comparison to the InSAR data. The range offsets show 1.4 ± 0.2 m step across the southern intra-caldera faults.

Azimuth SARIO measurements are also more accurate than range SARIO measurements because the azimuth ground resolution is generally better (4 m for the ERS satellites) than the range ground resolution (20 m). Assuming that we can measure pixel offsets locally between two images to 1/32 of a pixel, the accuracy of the azimuth SARIO is 12.5 cm, but 62.5 cm for the range SARIO [*Jónsson et al.,* 2002a]. Sierra Negra presents a case where range SARIO may be useful, despite the large uncertainties, as we believe that large vertical displacements occurred across the intra-caldera faults.

We measure range offsets at Sierra Negra between two amplitude images, acquired in

September 1997 and October 1998. The radar images are the same as those used to form the 1997-1998 interferogram (Figures 3-2b and 4-3). The range offsets are estimated locally by cross-correlation of 32×32 pixel sub-images. The resulting range offsets Δr are noisy with values ranging from negative 1-2 m to positive 1-2 m (Figure 4-7a). East and west of the caldera the offset values are out of scale because sub-images there do not correlate well due to dense vegetation. Within the caldera the offset image has more positive values than negative, indicating uplift towards the satellite relative to the area northeast of the caldera. To see this uplift better, we calculate the average range offset along a profile (boxes in Figure 4-7a) and plot the averages from north to south in Figure 4-7b. The averages show a clear range decrease (uplift towards the satellites) of the central caldera floor that becomes more prominent towards the south and agrees well with the InSAR data. The range offsets show a sharp 1.4 ± 0.2 m step across the southern intra-caldera faults. Note that even though the range offsets are discontinuous across the faults, the discontinuity is not ambiguous as is the case for the InSAR phase discontinuity.

Azimuth SARIO measurements of Sierra Negra (not shown here) during the same time period do not show large displacements, indicating that the ground motion was primarily vertical. If we assume that vertical ground motion was responsible for observed range offsets at Sierra Negra, we can infer the amount of vertical displacements needed to produce the observed offsets: $\Delta h = \Delta r / \cos\theta$, where Δr is the measured offset in the range direction and θ is the incidence angle (see Figure 4-6). This implies that uplift of 0.9 ± 0.1 m occurred just north of the intra-caldera faults and subsidence of 0.6 ± 0.1 m south of the faults. Thus, the range measurements provide a direct estimate of the intra-caldera faulting of 1.5 ± 0.2 m. This estimate agrees with our previous modeling result at a 95% confidence interval, which has up to 1.2 m faulting (Chapter 3).

4.5 Discussion

The results of the fieldwork and the range offset measurements leave no doubt that our previous interpretation from the InSAR data of trapdoor faulting occurring at Sierra Negra is correct. In addition, our model estimate with up to 1.2 m of trapdoor faulting is consistent with the offset measurements. The height of the intra-caldera fault system indicates that trapdoor faulting must have occurred repeatedly in the past to form the faults that are up to 100 m high. The lava flows that fill the caldera are 1000-3000 years old [*Reynolds et al.,*

1995], which provides an upper bound on the age of the surface faults, although the fault system may be older.

But why does trapdoor faulting occur? The strong uplift prior to 1997 (Figure 3-2a), which can be modeled by an inflating sill at $\sim$2 km depth (Chapter 3), caused extension of the caldera floor leading to trapdoor faulting sometime in 1997-1998. Boundary element modeling of growing sill intrusions (treated as a fluid-pressurized cracks in elastic medium) shows that when the lateral extent (half-length) of an intruding sill becomes comparable to and exceeds its depth, the intrusion will increasingly start to interact with the free surface [*Fialko,* 2001]. When this occurs the sill begins to propagate towards the surface and will eventually lead to an 'eruption' at a distance of about three times the initial sill depth. These modeling results also show that when the sill starts to propagate to the surface it causes stress concentrations in the intrusion roof that can lead to faulting on outward-dipping or nearly vertical normal faults, given sufficiently high excess magma pressures [*Fialko,* 2001]. The dimensions of Sierra Negra caldera and the sill depth are consistent with this model. Our estimated sill depth is $\sim$2 km, with faulting occurring $\sim$3 km south of the sill center and eruptions occurring along fissures 5-6 km to the north (Figure 4-8). Therefore, this model provides a plausible mechanical explanation for the uplift and trapdoor faulting observed at Sierra Negra.

An alternative explanation was inspired by interesting processes that occurred at Grímsvötn volcano in Iceland under entirely different circumstances. Grímsvötn has a subglacial caldera that is partially filled with a meltwater reservoir under 250-300 m thick ice-shelf [*Gudmundsson et al.,* 1995]. A subglacial eruption in 1996, just north of the caldera, produced 3 km^3 of melt-water that drained into the caldera lifting up the floating ice-shelf [*Gudmundsson et al.,* 1997]. The rapid draining caused convex bending of the ice-shelf and 'faulting' repeatedly occurred on the ice-rock interface at the south caldera rim. When the meltwater burst out in a catastrophic flood the ice-shelf subsided by 175 m [*Gudmundsson et al.,* 1997]. At Grímsvötn we know clearly that the roof was floating on the meltwater as ice density is only $\sim 9/10$ that of water. However, this raises the question if similar processes can be at work at Sierra Negra; is a low density caldera floor 'floating' on top of denser magma intrusion? Sierra Negra melts are iron rich and are denser than typical MORB basalts and denser than other magmas in the Galápagos, with estimated density of 2.73-2.77 g/cm^3 at 1 atm and 1150°C [*Reynolds and Geist,* 1995]. The density of the solid phase is higher, of course, or about 2.87 g/cm^3 [*Robert Reynolds, pers. Comm.,* 2002]. However,

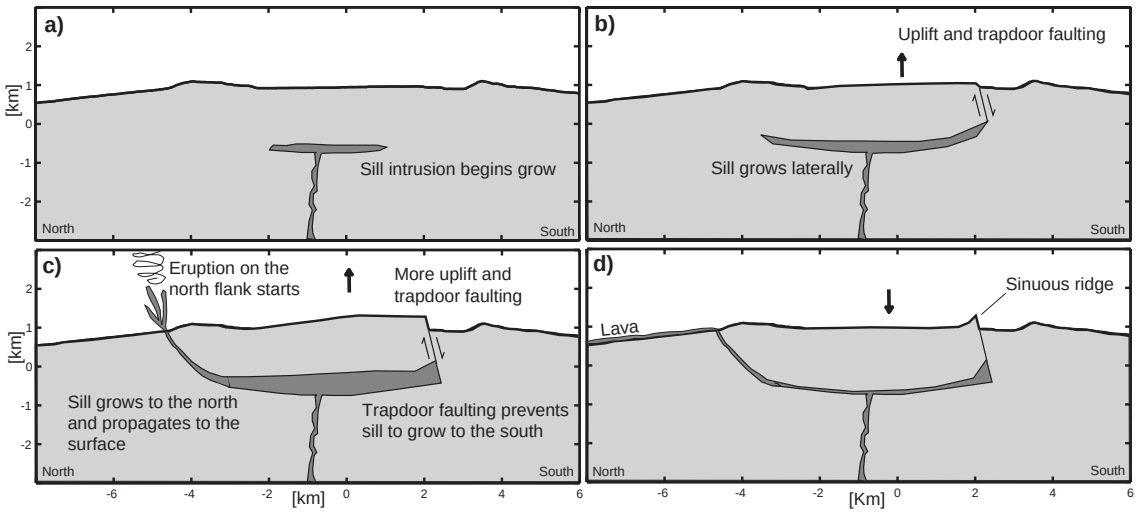

Figure 4-8: Schematic figures showing the processes at Sierra Negra. (a) A sill intrusion begins to grow under the central caldera floor. (b) The sill grows laterally causing trapdoor faulting on the southern intra-caldera faults. (c) Further trapdoor faulting prevents sill growing to the south but it grows to the north leading to an eruption on the north flank. (d) The floor deflates following the eruption leaving a ridge structure in the south.

Sierra Negra lavas are 14% vesicular on the average [*Reynolds and Geist,* 1995], making the caldera floor density ∼2.47 g/cm^3, which is lower than the magma density. Therefore, a floating caldera floor that moves up like a piston with increasing magma pressure is a possible explanation for the trapdoor faulting at Sierra Negra.

The former explanation described above is more plausible as it is based on rigorous model calculations while the latter relies on the assumption that the caldera floor lavas are >5% vesicular down to 2 km depth. However, the two mechanisms do not necessarily contradict each other and may both play a role at Sierra Negra. We know that magma sill excess pressure occurs, causing uplift and deformation of the intrusion roof (i.e., the caldera floor) as was observed in 1992-1997 and after 1998 (Figures 3-2a and 3-2c). However, trapdoor faulting temporarily relieves part of the magma excess pressure and probably prevents lateral growth of the sill to the south (Figure 4-8). A relatively light intrusion roof would facilitate trapdoor faulting and repeated piston-like upward movement of the roof could result in a voluminous intrusion. Sierra Negra generally has eruptions of large volume, e.g., the 1979 lava is about 0.9 km^3 [*Reynolds et al.,* 1995]. If the 1979 eruption was fed by a shallow sill reservoir under central Sierra Negra caldera (area ∼30 km^2) the

sill must have been at least 30 m thick on the average.

The dense magma at Sierra Negra may partly explain the lack of eruptive activity inside the caldera during the last 1000-3000 years. Instead of erupting, the over-pressurized magma causes uplift with trapdoor faulting until the sill has grown enough laterally to erupt on fissures on the north flank (Figure 4-8c). The elevation of the 1979 vents was not measured during the 2001 fieldwork, but according to maps the vents are at ∼900-1000 m, or at a similar elevation as the caldera floor and 2 km higher than the sill depth. This indicates sill bending towards the surface under the northern caldera rim.

The western part of the fault system consists of a remarkable sinuous ridge with 100 m high faults in the west and steeply dipping lava flows on top that sharply bend to merge with the gently dipping caldera floor [*Reynolds et al.,* 1995]. Here the faults are 60-80 m higher than the central caldera floor that they bound. This implies that the elevated intra-caldera floor stood much higher at the time the western faults formed, but has since subsided considerably, probably due to voluminous magma withdrawal from a shallow reservoir, possibly to fissure eruptions on the north flank. During subsidence the fault system is put under compression, preventing the faults from 'slipping back', resulting in the ridge formation when the central floor becomes lower than the faults (Figure 4-8d). In other words, the trapdoor does not close properly. If this interpretation is correct, it indicates that the magma sill was 60-80 m thicker when the caldera floor was at its highest position, than it is today. This explanation for the formation of the sinuous ridge is similar to the one provided by *Reynolds et al.,* [1995]. They discussed a few different possibilities but their preferred explanation is that incremental subsidence of the caldera floor, after initial uplift, 'resulted in the rigid floor becoming jammed along its western and northern edges where it broke rigidly in several places and formed the unusual blocks that make up the sinuous ridge' [*Reynolds et al.,* 1995]. Although we believe that the uplift was incremental and the subsidence with the ridge formation relatively fast, the two explanations for the formation of the sinuous ridge are essentially the same.

4.6 Conclusions

This study proves that our previous interpretation of trapdoor faulting at Sierra Negra is correct. More specifically, the main conclusions of this study can be summarized in the following points:

1. Field observations at Sierra Negra in 2001 indicate that recent trapdoor faulting occurred along the southern intra-caldera faults, maybe sometime in 1997-1998. The maximum amount of faulting was estimated to be at least 0.5-1 m.

2. Range offset measurements of radar amplitude images show 1.4 ± 0.2 m line-of-sight displacement across the southern intra-caldera faults. This indicates that 1.5 ± 0.2 m of faulting occurred, assuming vertical displacements.

3. Trapdoor faulting at Sierra Negra is likely caused by magma excess pressure in a shallow ($\sim$2 km) sill intrusion whose lateral extent (half-length) has become greater ($\sim$3 km) than its depth. However, other magma chamber shapes than a sill may be possible.

4. The magma density may be higher than in the vesicular caldera floor, causing the floor to move up like a piston with increasing magma pressure. This mechanism may contribute to the trapdoor faulting to some extent.

4.7 Appendix A: Area Covered during 2001 Fieldwork

The fieldwork was carried out in January 2001, some 3 years after the faulting occurred. Fieldwork on Isabela island is logistically difficult for several reasons. Flights from Quito arrive at Baltra airport, near Santa Cruz island in the central Galápagos archipelago. From Santa Cruz island one can either travel by a small plane or a boat to Villamil on southern Isabela island. There are no roads on Isabela, except on the south flank on Sierra Negra, making it the easiest caldera to access. On Sierra Negra one can drive from the town of Villamil to within 2 km of the southeast caldera rim (Figure 4-1). From there one has to either go by foot or rent horses. Large parts of the Isabela island are covered with aa flows that can be immensely difficult to pass through. This applies to much of Sierra Negra caldera floor and the area around the intra-caldera fault system. The caldera rim is much easier with clear trails in many places, although vegetation can be dense on the southeast rim. All water for the fieldwork (approximately 1 gallon per person per day) had to be brought in by foot (or horses) as there is no surface water available. Dehydration is probably the most dangerous threat during fieldwork as the tropical sun can be intense and temperatures high.

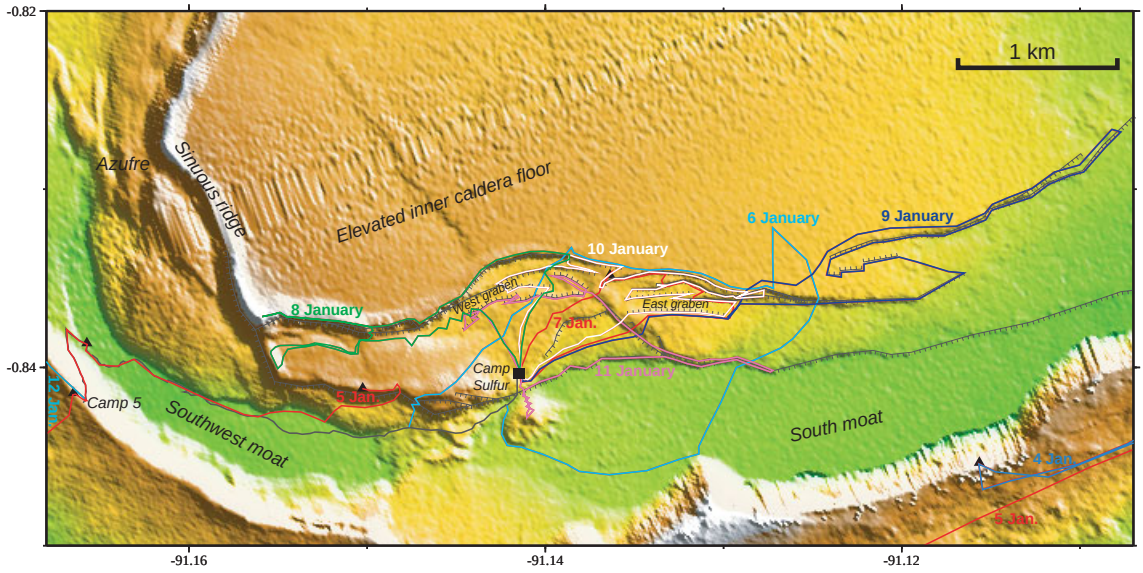

Figure 4-9: A map showing the area investigated during the 2001 fieldwork. Most of the work was conducted from Camp Sulfur. The lines show the approximate route taken during each day of the fieldwork.

Only the southern part of the intra-caldera fault system was investigated during the 2001 fieldwork because the InSAR data did not indicate any faulting along the western part of the fault system. Figure 4-9 shows the area covered during the fieldwork with the approximate route taken each day. The entire southern part of the fault system was investigated, fault by fault, except the easternmost part of the fault furthest to the south.

4.8 Appendix B: Description of Faulting Evidence

This appendix has description of the evidence we found of recent faulting at the southern intra-caldera fault system during fieldwork in January 2001. The evidence was put into three categories depending on how clearly it was exposed at the fault. The different categories are described in Table 4.1. Descriptions of the different locations where fresh faulting was observed are shown in Table 4.2. The first column has numbers that refer to locations shown in Figure 4-4 and waypoint numbers (third column) refer to logged GPS locations along the fault scarps. The GPS locations are available electronically upon request from the author.

Table 4.1: Signs of recent faulting were put into three categories depending on how clear the detected evidence was.

Category	*Description*
1	Clear evidence for faulting. Continuous fresh break-outs in the fault-wall, and/or quantifiable displacement visible.
2	Faulting suggested. Some clear break-outs or fresh fault faces, often continuous or nearly continuous along the fault. Usually not quantifiable.
3	Indirect possible evidence of faulting, fresh break-outs in fault face, or fresh talus. Usually not continuous along the fault. These features can also possibly be due to weathering.

Table 4.2: List and description of the locations where evidence of recent faulting was detected in the field. The numbers refer to locations shown in Figure 4-4 and the evidence category is explained in Table 4.1. Waypoint numbers refer to GPS locations available from the author upon request.

No.	*Cat.*	*Waypoints*	*Description*
1	1	50	The easternmost evidence of faulting found at this location. Three scratched stones found with some 5 cm here.
2	2	52	Some evidence seen in stretched vegetation, circa 5 cm.
3	1	52.8-53	Continuous evidence of faulting for 50 m, estimated magnitude 5-10 cm.
4	3	54-55	Some scattered indirect evidence for faulting, fresh break-outs.
5	2	55	Fresh break in an only 1.5 m high wall, break about 2 m wide.
6	3	55.7-56	Some possible evidence found on a 50 m long stretch.
7	1	56.4-56.6	Clear evidence of faulting on a 50 m long stretch, estimated faulting about 10 cm.
8	3	60	Small fresh breaks, possible indirect evidence of faulting, could be weathering.

continued on next page

continued from previous page

No.	*Cat.*	*Waypoints*	*Description*
9	3	64	Some fresh breaks, not continuous, could simply be weathering.
10	3	62.5	Some fresh breaks, not continuous, could be weathering.
11	3	70-71	A few breakouts here, no clear evidence of faulting.
12	1	99-71	Clear and continuous evidence of faulting.
13	1	71.3	Clear evidence of faulting found here, at least 45 cm.
14	3	15	Large break-out from the main wall of the fault, about 5 m wide from 5-10 m high wall. The largest fresh break seen in the whole fault system on Sierra Negra.
15	1	97-98	More or less continuous evidence of faulting. In one place it looked like 25-50 cm of movement.
16	2	72-79	Some discontinuous evidence of faulting here, probably less than 10 cm.
17	2	80-81	Some minor evidence of faulting.
18	1	81	A fault scratch stone found, with 5 cm displacement.
19	1	27	Two parallel scratch stones found, with 30 cm displacement.
20	1	92.8-93.3	About 100 m stretch of faulting evidence. In the western part it shows up as loose gravel movement, maybe about 15 cm. Further to the east it looks more like 50-100 cm, also in loose gravel. The movement may be less though as some moss found in the stretched part.
21	1	89-90	Discontinuous, but clear evidence of faulting found here, probably less than 10 cm.
22	1	11-18 R011018A	Evidence of faulting found.
23	1	16 R011018A	Very clear fresh break, looks like 1 m of fresh emergence, but it is probably less.
24	2	18-26 R011018A	Continuation of no. 22, but somewhat less clear evidence of faulting.

continued on next page

continued from previous page

No.	*Cat.*	*Waypoints*	*Description*
25	1	20 R011018A	A fresh face indicating some 25-50 cm of faulting.
26	3	73-74	A lot of fresh talus, no direct evidence of faulting, could simply be weathering (or due to shaking), the aa lava is fragile here.
27	3	4-5 R011115A	Some indirect evidence, like discontinuous break-outs from the fault wall.
28	1	1-4 R011115A	A 15 cm break found here, and a scratch stone with some 5-8 cm displacement.
29	3	31.5-32	Some fresh break-outs on these recent faults.
30	3	33	A few fresh break-outs in a 1 m high fault, maybe indicating small displacement.
31	3	11	Many fresh faults at this location. The area is covered with fragile aa lava and could easily have accommodated 1 m of faulting.

Chapter 5

A Shallow-Dipping Dike fed the 1995 Flank Eruption at Fernandina Volcano, Galápagos, Observed by Satellite Radar Interferometry

In the past two chapters we studied the deformation on western Galápagos volcanoes on Isabela and Fernandina islands. In particular, we analyzed InSAR observations from Darwin and Sierra Negra volcanoes. In this chapter we investigate what we can learn from InSAR measurements about the 1995 flank eruption on Fernandina volcano. The deformation observations indicate that a non-vertical dike propagated from the central caldera into the southwest flank to feed this radial fissure eruption. We use the InSAR data to image the dimensions and location of the dike intrusion. The material of this chapter has been published in Geophysical Research Letters [*Jónsson et al.,* 1999].

5.1 Abstract

Satellite radar interferometry data reveal strong localized uplift in a semi-circular pattern on the southwest flank of Fernandina volcano, Galápagos, where an eruption took place in 1995. The observations show a maximum decrease in radar range of 0.75 m, and they are consistent with a model of a shallow-dipping dike intrusion feeding this fissure eruption. We solve for the best-fit single rectangular dislocation dike source using non-linear inversion techniques where simulated annealing searching algorithm is used to avoid local minima. The best-fit dike is 3.8 km long, 2.3 km high, 0.86 m thick and with a 34° dip. The total dike volume (7.5×10^{-3} km^3) is ∼40% of the volume of extrusive materials estimated to have been produced during the eruption. The data do not permit a sub-vertical dike, implying that the least principal stress direction is not horizontal as is usually assumed.

5.2 Introduction

The Galápagos archipelago is located on the Nazca plate about 1000 km west of Ecuador, just south of the east-west trending Galápagos spreading center (Fig. 5-1a). The islands are a cluster of about 20 basaltic volcanoes that typically have large summit calderas. Unlike Hawaiian basaltic volcanoes, they do not have well-developed rift zones, but instead have a pattern of arcuate vents near the caldera rim and radial vents further away on the flanks [*Chadwick and Howard,* 1991].

Fernandina Island is about 30 km in diameter and consists of a single volcano with a maximum elevation of 1470 m with a nearly 1000 m deep central caldera [*Rowland,* 1996] (Fig. 5-1b). Fernandina is among the most active volcanoes in the world; it erupted at least 13 times during 1950-1998 [*Rowland and Munro,* 1992]. The eruption of 1968 was followed by the largest historical caldera collapse on any basaltic volcano, with a maximum subsidence of about 300 m [*Simkin and Howard,* 1970]. The most recent activity at Fernandina includes intracaldera eruptions in 1988 and 1991, and a radial fissure eruption on the SW flank in 1995 [*Chadwick et al.,* 1991; *Rowland and Munro,* 1992; *Global Volcanism Network,* 1995; *Wooster and Rothery,* 1997].

The 1995 eruption began on around January 25 and lasted for about 10 weeks [*Global Volcanism Network,* 1995]. The uppermost vents at elevations of 600-1100 m produced a negligible amount of lava [*Rowland,* 1996]. The main vent was located at 250 m elevation and produced about 0.02 km^3 lava, assuming a 3 m average thickness [*Wooster and Rothery,* 1997]. The lava covered a subaerial area of 8.2 km^2 extending 9 km from the uppermost vent to the ocean [*Rowland,* 1996].

Here we examine the 1995 eruption using Synthetic Aperture Radar (SAR) interferometry satellite data. SAR has proven to be an important tool for investigating crustal deformation and dynamics of active volcanoes, e.g. at Etna volcano in Italy and Krafla volcano, Iceland [*Massonnet et al.,* 1995; *Lanari et al.,* 1998; *Sigmundsson et al.,* 1997].

5.3 Data Analysis and Results

We present data from the European satellites ERS-1 and ERS-2 acquired over Fernandina in 1992 and 1997. Two interferograms were formed, an interferogram spanning the five years (Sept. 12, 1992 - Sept. 30, 1997) and an interferogram that spans only one day (Sept. 29-30, 1997). Both interferograms include phase information about the island's topography

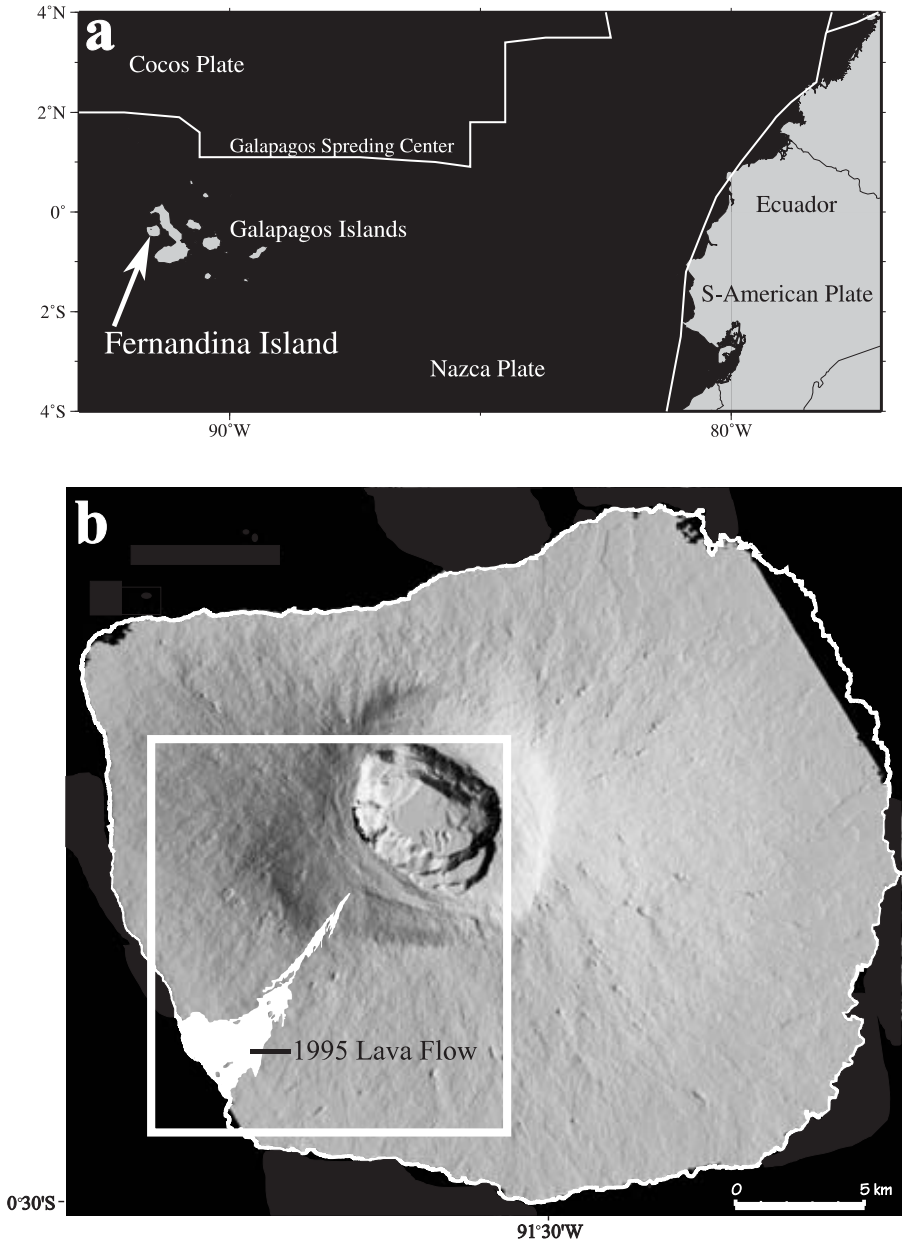

Figure 5-1: a) Galápagos Islands are located about 1000 km west of Ecuador on the Nazca plate, just south of the Galápagos spreading center. Fernandina Island is the westernmost island in the archipelago. White lines mark plate boundaries. b) A shaded relief map of Fernandina Island. The area covered by the 1995 lava flows is shown on the SW flank as mapped from a SPOT image [*Rowland,* 1996]. The box marks the area covered in Fig. 5-2.

but the five-year interferogram additionally has information about the deformation that occurred during this time span [*Zebker et al.,* 1994].

We isolated the deformation signature by two different methods, revealing the same results. First, we removed the topographic effect using the three-pass method [*Zebker et al.,* 1994], using the one-day interferogram as a reference. We also removed the topography using the two-pass approach [*Massonnet et al.,* 1993], producing a simulated interferogram from a pre-existing Digital Elevation Model (DEM) and subtracting it from the five-year interferogram. In the latter, we used a DEM generated during the 1993 airborne Topographic Synthetic Aperture Radar (TOPSAR) mission to the Galápagos islands [*Rowland,* 1996; *Zebker et al.,* 1992b]. This second approach gives a more complete differential interferogram, because in certain areas near the caldera, the topographic information in the one-day interferogram is lost due to decorrelation. We also avoid estimating a second set of baselines and are free of possible atmospheric disturbances that may be included in the one-day interferogram. Both resulting differential interferograms contain phase signatures mainly from deformation that occurred during the five years from 1992 to 1997.

We unwrapped the phase of the two-pass differential interferogram (Fig. 5-2b) using the residue-cut algorithm of *Goldstein et al.* [1988] to obtain absolute values of the range changes for each pixel rather than ambiguous phase values ranging from 0 to 2π. The whole interferogram of the island unwrapped readily, except where surface scattering changed over the five years, e.g. on areas of relatively dense vegetation near the caldera, and on the area covered by the 1995 lava flow [*Zebker et al.,* 1996] (Fig. 5-2a-b and 5-3a).

The five-year differential interferograms reveal a strong semi-circular signal of range decrease on the SW flank of the volcano. The signal of about 27 28-mm-fringes represents 0.75 m of decrease in range, i.e. the ground moving towards the radar (Fig. 5-2b and 5-3a). Since the ERS SARs have an incidence angle of 23° from vertical this is presumably mainly uplift. The deformation pattern is not purely semi-circular in nature. The amplitude of the deformation pattern decreases from its maximum towards the caldera with a minimum at 2 km from the caldera rim, where it increases again (Fig. 5-2b). This increase likely results from a second subsurface feature, but the incomplete nature of the signature due to decorrelation precludes simple analysis, hence an interpretation of the larger deformation pattern only is given below. Another, much smaller, semi-circular pattern is observed on the western side of the 1995 lava flow. This signal has an opposite sign, representing an increase in range of about two fringes, or 56 mm (Fig. 5-2b).

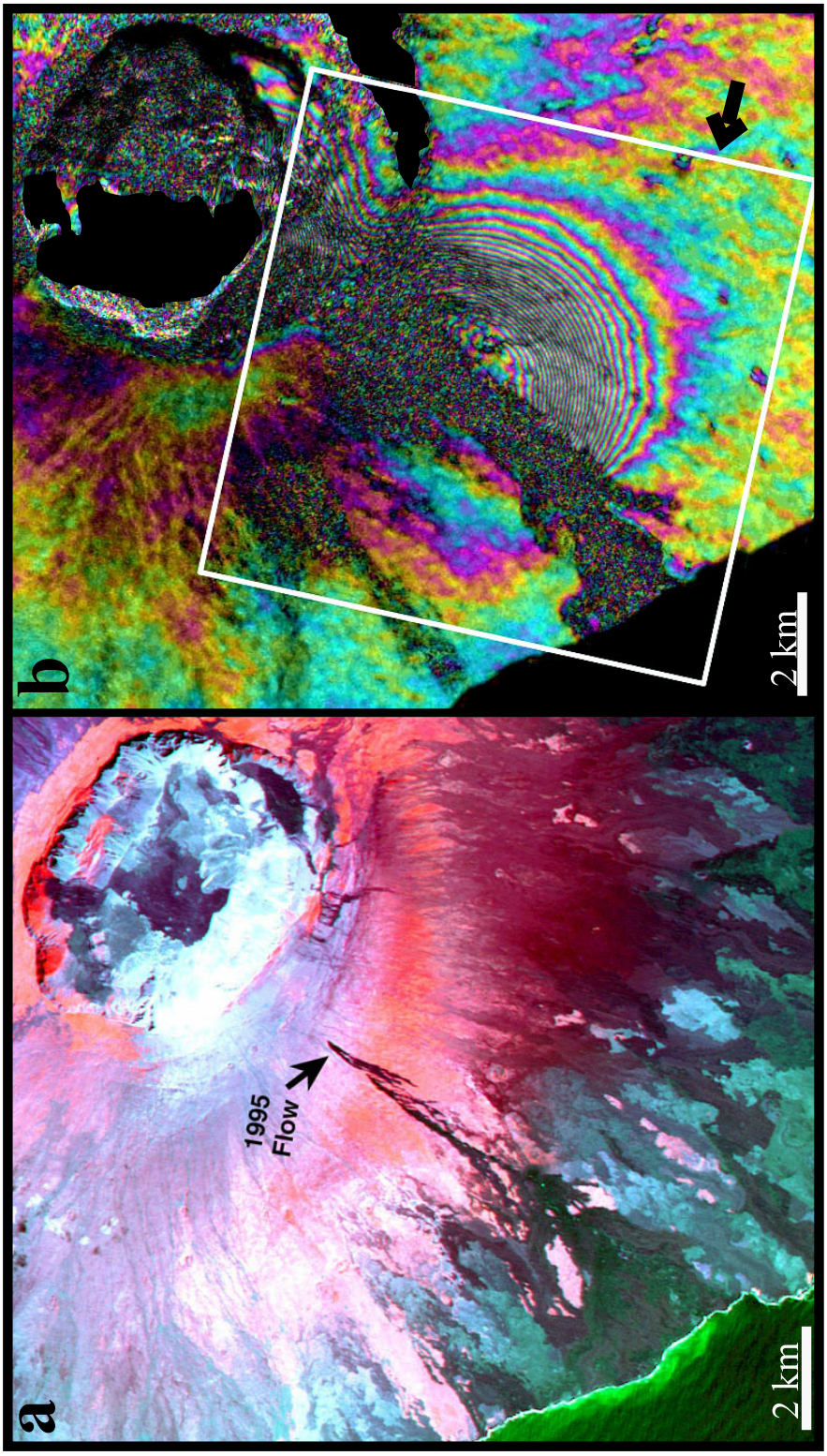

Figure 5-2: a) A SPOT image of the SW flank of Fernandina Volcano from July 6, 1995. Red colors denote vegetated areas. The upper part of the 1995 lava flow can clearly be seen where it covered an area of relatively dense vegetation, but it is less clear near the coast. © SPOT image 1995. b) The 1992-1997 interferogram of the SW flank of Fernandina. The arrow indicates the look direction of the satellite down from the ESE. The strong semi-circular pattern has a maximum decrease in radar range of about 27 fringes, or 0.75 m, representing mostly uplift above the intrusion. The box marks the area covered in Fig. 5-3.

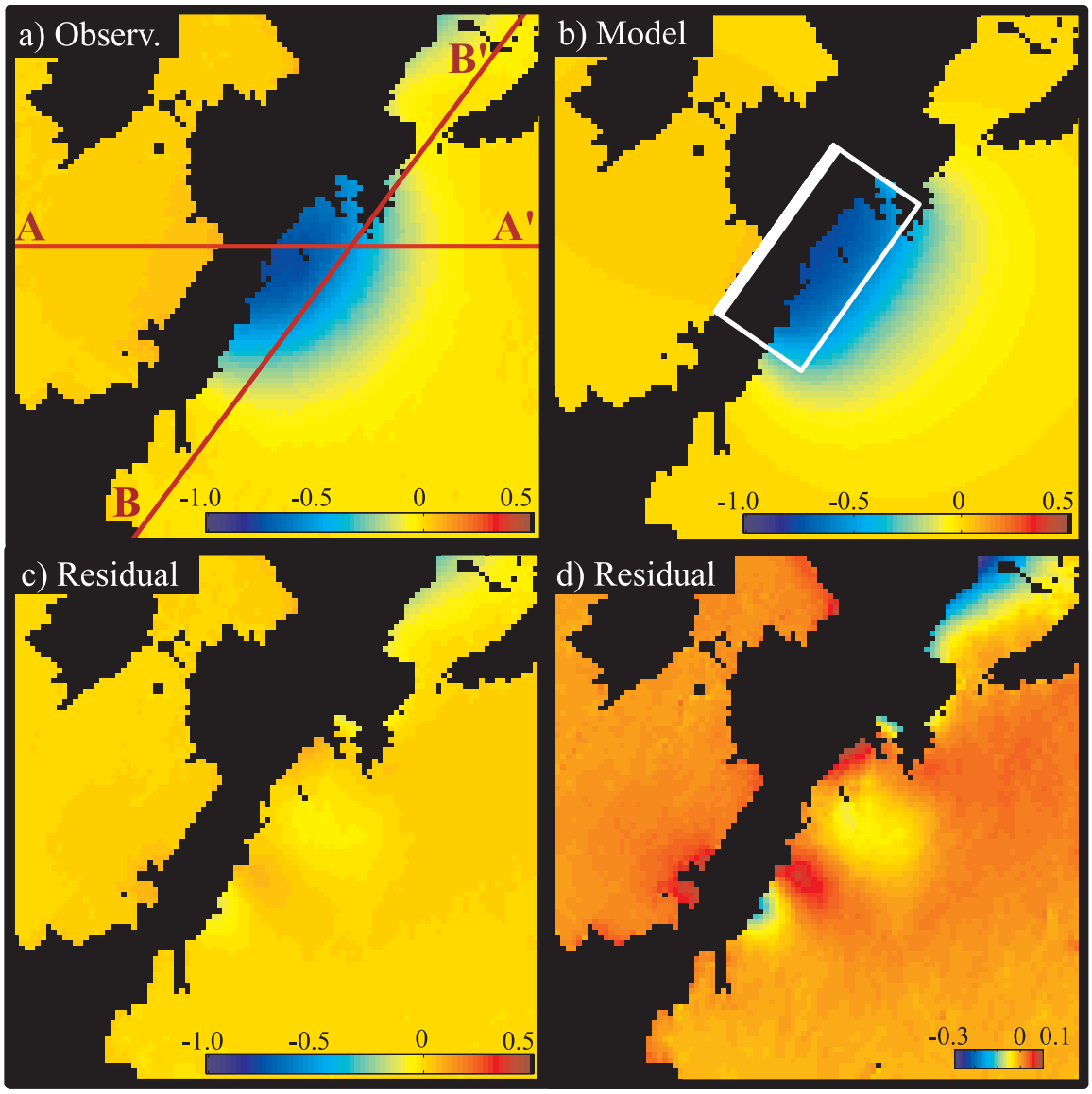

Figure 5-3: a) The unwrapped interferogram gives absolute values of the range change. The scale shows range change in meters. Marked in black is the area that could not be unwrapped because of decorrelation, partly due to the 1995 lava flow. Profiles A-A' and B-B' are shown in Fig. 5-4. b) The best-fit model of a shallow-dipping dike presented in radar coordinates. The white rectangle marks the projection of the best-fit dike onto the surface, and the thick sideline indicates where it hits the surface. c) The residual between the observations (Fig. 5-3a) and the model (Fig. 5-3b). d) Same as Fig. 5-3c, except another color scale.

5.4 Modeling

We use a single rectangular dislocation surface in an elastic half-space [*Okada,* 1985] to simulate ground deformation due to a dike intrusion. Ten parameters define the dislocation: length, height, strike, dip, and location (three parameters) and the three parameters of displacement across the dislocation: dip-slip, strike-slip, and opening. In the inversion we constrain the dip-slip and the strike-slip to be zero because no radial faulting has been observed on Fernandina; other parameters are freely determined. We use a simulated annealing algorithm to avoid local minima in this non-linear problem [*Cervelli et al.,* 2001]. The covariance matrix is assumed to be diagonal, i.e. errors of the range change observations are taken to be independent of one another. Because the correlations vary from one interferogram to another, and because wavelengths and amplitudes of atmospheric disturbances vary from place to place and from one day to another [*Zebker et al.,* 1997], this assumption could slightly distort our estimate of the source geometry.

The resulting best-fit model is a gently dipping dike, about 3.8 km long, 2.3 km high, 0.86 m thick, striking N47° E, and dipping 34° from horizontal to the SE (Table 5.1). The inversion places the upper edge of the dike at the surface, coincident with where the eruption took place. Fig. 5-3b shows the deformation in radar coordinates as predicted by the model; it matches the observations with less than 0.05 m residual over most of the signal (Fig. 5-3c-d). Profiles showing range changes across the observed area are compared to the modeling results in Fig. 5-4. Sensitivity analysis of the inversion procedure using bootstrap techniques [*Efron and Tibshirani,* 1993] shows that the dike length, depth, and opening are relatively well resolved, but the dike dip and the dike height are less well constrained (Table 5.1). The volume of the best-fit dike is found to be 7.5×10^{-3} km^3, or around 40% of the estimated lava volume.

5.5 Discussion and Conclusions

Our estimation of the dike geometry gives new unexpected information about the stress field at Fernandina volcano. Geological investigations show that vents and presumably underlying dikes on the caldera rim have an arcuate, caldera-parallel orientation, but vents further away from the rim have radial orientations [*Chadwick and Howard,* 1991; *Rowland,* 1996]. Because the minimum compressional stress, σ_3, is generally perpendicular to dikes, it has a radial orientation at the caldera-rim, and is circumferential further down the volcano.

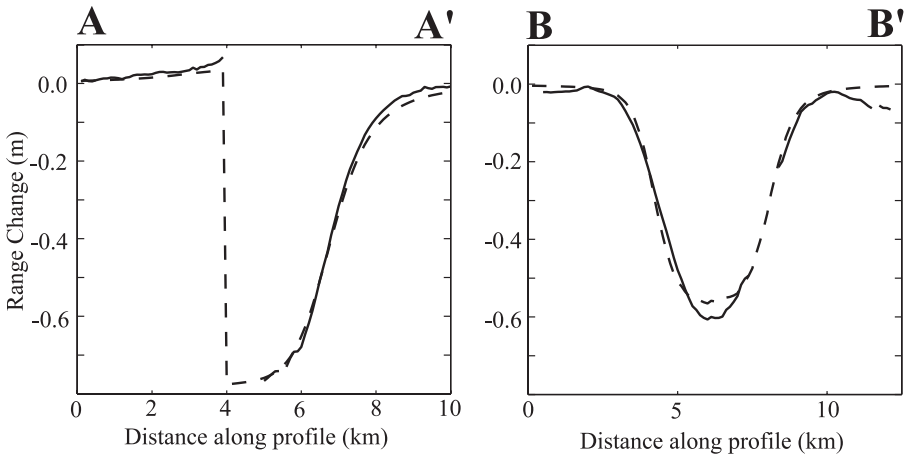

Figure 5-4: Comparison of observed (solid lines) and modeled (ticked lines) range changes along profiles A-A' and B-B' in Fig. 5-3a and 5-3b (profiles only shown in Fig. 5-3a). Note that negative range change represents ground displacement up towards the satellite radar.

Hence, the two categories of vents at Fernandina volcano indicate a change in the stress field from the caldera rim down to the flanks [*Chadwick and Dieterich,* 1995]. A few circumferential dikes on Fernandina are exposed in the caldera wall. There they are observed to be vertical or nearly vertical, and they are about 1 m thick [*Chadwick and Howard,* 1991]. Even though the orientation of the minimum compressional stress axis changes from the near-caldera region out to the flanks, it has been assumed that the axis would still be horizontal [*Chadwick and Dieterich,* 1995]. In other words, the radial dikes have been considered vertical as well. Our best-fit model of the 1995 radial dike intrusion is far from being vertical, it has a tilt of about 34° from horizontal. This indicates not only a rotation of the minimum compressional stress axis in the horizontal plane about the vertical axis, from the caldera-rim down to the flanks, but also a rotation about a horizontal axis, at least at shallow depths.

No conventional geodetic network exists on Fernandina, so if not for SAR observations, we would know little about this event, except that a radial dike intruded and reached the surface. While our spatial coverage of the Fernandina event is very good, consisting of thousands of observations on an area as little as 4×6 km^2, our temporal resolution is quite limited since we could only difference two scenes acquired in 1992 and 1997. However, we have been able to constrain parameters and dimensions of the dike intrusion relatively well.

In summary, ERS radar interferograms of Fernandina volcano permit detailed spatial

Dike parameter	*Value*		*Dike parameter*	*Value*
Length (km)	$3.8^{+0.1}_{-0.1}$		Opening (m)	$0.86^{+0.21}_{-0.01}$
Height (km)	$2.3^{+0.1}_{-0.8}$		Volume (km^3)	$\left[7.5^{+0.4}_{-1.4}\right] \times 10^{-3}$
Depth (km)	$0.0^{+0.0}_{-0.5}$		Latitude (°S)	$0.414^{+0.0km}_{-0.4km}$
Dip (°)	34^{+15}_{-3}		Longitude (°W)	$91.585^{+0.0km}_{-0.5km}$
Strike (N°E)	47^{+8}_{-3}			

Table 5.1: The parameters for the best-fit dike. Uncertainties show 95% confidence. The location shown is the center location of the upper edge of the dike.

observation and analysis of crustal deformation, such as the 1995 dike emplacement. We find that a non-linear inversion of the data, using a single rectangular dislocation source, results in a dike that is 3.8 km long, 2.3 km high, 0.86 m thick, and dipping 34° to the SE. In addition, the dip of the best-fit dike indicates that the orientation of σ_3 may not only rotate about the vertical axis from the caldera-rim out to the flanks, but also about a horizontal axis, at least at shallow depths.

Chapter 6

Fault Slip Distribution of the 1999 M_w7.1 Hector Mine Earthquake, California, estimated from Satellite Radar and GPS Measurements

In past three chapters we analyzed volcanic deformation in the Galápagos, caused by a variety of subsurface processes. Now we turn our attention to seismic deformation observed by InSAR, which is the subject of the remainder of this thesis.

In this chapter we examine the coseismic deformation of the magnitude 7.1 Hector Mine earthquake that occurred in southern California on 16 October 1999. This right-lateral strike-slip earthquake caused up to 5 m of surface displacements and the coseismic deformation was observed by InSAR from both ascending and descending orbits, and by GPS. We use all these deformation measurements and information about the surface rupture to infer about the fault geometry and the slip distribution of this earthquake. The material in this chapter has been published in the Bulletin of the seismological society of America [*Jónsson et al.,* 2002a].

6.1 Abstract

We use a combination of satellite radar and GPS data to estimate the slip distribution of the 1999 M_w7.1 Hector Mine Earthquake, a right-lateral strike-slip earthquake that occurred on a northwest-southeast striking fault in the southern California Mojave Desert. The data include synthetic aperture radar interferograms (InSAR) from both ascending and descending orbits, radar amplitude image offset fields (SARIO) for both ascending and descending azimuth directions, and campaign GPS observations from 55 stations provided

by *Agnew et al.* [2002]. We model the fault with nine segments derived from the field-mapped fault rupture, the SARIO data, and aftershock locations. We first estimate the dip of each fault segment as well as a single constant strike-slip component across each segment, resulting in an average dip of 83° to the northeast and slip of up to 5.6 m. Then, we fix the optimal fault segment dip, discretize the fault segments into 1.5 km × 1.5 km patches, and solve for the variable slip distribution using a nonnegative least-squares method that includes an appropriate degree of smoothing. Our preferred solution has both right-lateral strike-slip and reverse faulting. The estimated geodetic moment is 5.93×10^{19} Nm (M_w7.1), similar to seismological estimates, indicating that there are insignificant interseismic and postseismic deformation signals in the data. We find strike-slip displacements of up to 6.0 m and reverse faulting of up to 1.6 m, with the maximum slip located just northwest of the epicenter. Most of the slip is concentrated northwest and south of the epicenter, while little slip is found on the northeastern branch of the fault. The SARIO data and our modeling indicate that the amount and extent of surface fault rupture were underestimated in the field.

6.2 Introduction

The M_w7.1 Hector Mine earthquake occurred on 16 October 1999 in a remote and sparsely populated area of the Mojave Desert, southern California (Figure 6-1). It was a right-lateral strike-slip event on a northwest-southeast oriented fault, with up to 5 meters of observed surface offset [*Scientists of the USGS et al.,* 2000]. The Hector Mine earthquake involved rupture on the Buillon and Lavic Lake faults (Figure 6-1), two previously mapped faults [*Scientists of the USGS et al.,* 2000]. The Harvard Centroid Moment Tensor (CMT) solution for the earthquake has a moment of 5.98×10^{19} Nm, rake of 174°, and fault dip of 80° to the northeast. A single-fault model derived from teleseismic data indicates that the rupture was bi-lateral with a seismic moment of 6.0×10^{19} Nm [*Ji,* 2000]. Inversion of strong motion data for slip distribution yields a dip of 77°, rake of 180° and a seismic moment of 6.7×10^{19} Nm [*Kaverina et al.,* 2002].

The Hector Mine earthquake occurred 7 years after the 1992 M_w7.3 Landers earthquake, also a right-lateral strike-slip earthquake, on a parallel fault 20 km to the west. The Landers coseismic stress changes did not bring the Hector Mine hypocentral region closer to failure, as the Coulomb stress change was negative [*Scientists of the USGS et al.,* 2000] unless

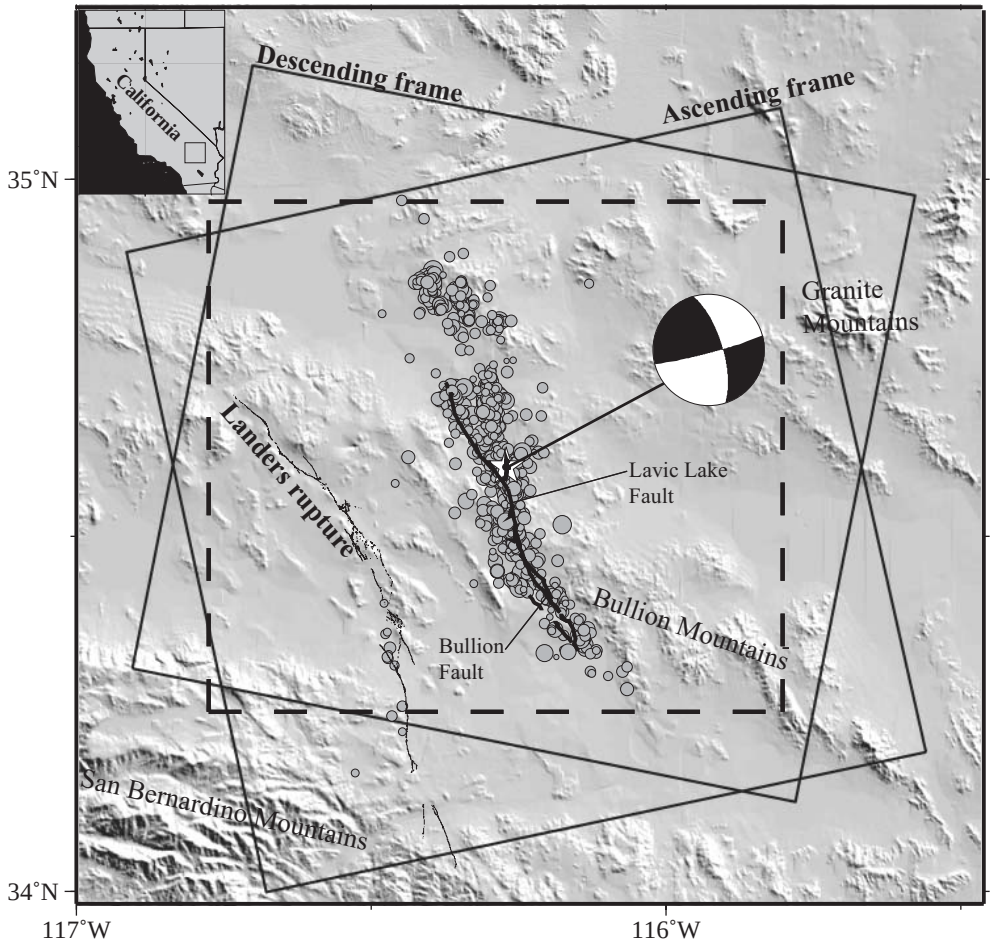

Figure 6-1: Shaded-relief topographic map of the area where the Hector Mine earthquake occurred in Mojave Desert, southern California (inset shows California). Mapped surface fault rupture is shown as thick line [*Scientists of the USGS et al.,* 2000], the epicenter is denoted with a star, and aftershocks during the first month following the earthquake are shown as circles [*Hauksson et al.,* 2002]. The surface rupture of the 1992 Landers earthquake is shown as thin line. Rectangles show the area covered by the descending and ascending radar scenes. Dashed rectangle shows the area covered in Figures 6-2, 6-3, 6-9, and 6-10.

the Hector Mine fault friction was high [*Parsons and Dreger,* 2000]. However, viscoelastic modeling of postseismic ductile flow in the lower crust or upper mantle show gradual Coulomb stress increase during the 7 years between the two earthquakes [*Freed and Lin,* 2001; *Zeng,* 2001]. These results suggest delayed triggering of the Hector Mine earthquake by viscoelastic stress transfer after the Landers event.

The Landers earthquake was the first earthquake that was imaged with Synthetic Aperture Radar Interferometry (InSAR) [*Massonnet et al.,* 1993; *Zebker et al.,* 1994]. These studies demonstrated the usefulness of satellite radar data for observing crustal deformation and were the beginning of a number of spaceborne radar studies of crustal and ice deformation. Radar observations of the Landers area also shed new light on postseismic processes near fault zones, including vertical movements in fault step-overs due to pore-fluid flow [*Peltzer et al.,* 1996, 1998]. Both InSAR and GPS measurements were used to estimate variations in slip along the fault in the Landers event [e.g., *Hernandez et al.,* 1999]. The slip distribution was found to be heterogeneous with right-lateral strike-slip of up to 7 m [*Hernandez et al.,* 1999].

In this study we use satellite InSAR data with multiple acquisition geometries from ascending and descending orbits along with radar image azimuth offset fields and GPS data to estimate spatial slip variations along the Hector Mine rupture. Among the questions we address are: Where was the slip concentrated on the Hector Mine rupture? How well can we resolve fault slip with these data? How was slip partitioned amongst segments of the complex rupture? Was there a significant dip-slip component in the earthquake or was it a pure strike-slip event?

6.3 Data Analysis

6.3.1 Radar Interferograms

We used radar data acquired by the European radar satellites ERS-1 and ERS-2 before and after the earthquake from both ascending and descending orbits (Table 6.1). We formed interferograms by calculating the phase difference between two radar images. The interferometric phase difference contains information about deformation occurring between the two passes as well as about the topography of the imaged area. We remove the topographic signature by forming additional short-term interferograms that contain topographic information only (no deformation) and subtracting this signal component from our original interferograms. The remaining phase difference is a measure of the ground displacement in the line of sight (LOS) to the satellite. The ERS radar incidence angle is approximately 23° from vertical, so the measurements are most sensitive to vertical ground displacements. The measured interferometric phase is measured modulo 2π (wrapped) and needs to be integrated (unwrapped) to determine absolute LOS displacements. The interferograms were

Interferogram	Scene 1	Scene 2	$T_\perp$	$B_\perp$
Deformation (descending pass)	Orbit 23027 15 Sept. 1999	Orbit 23528 20 Oct. 1999	35 days	21 m
Deformation (ascending pass)	Orbit 2937 12 Nov. 1995	Orbit 23979 21 Nov. 1999	4 years	55 m
Topography (descending pass)	Orbit 24664 (E1) 3 Apr. 1996	Orbit 4991 4 Apr. 1996	1 day	114 m
Topography (ascending pass)	Orbit 23111 (E1) 16 Dec. 1995	Orbit 3438 17 Dec. 1995	1 day	310 m

Table 6.1: Interferograms used in this study. All scenes were acquired by the ERS-2 satellite except those marked by (E1) that are from ERS-1. $T_\perp$ is the time separation between the two satellite passes and $B_\perp$ is the perpendicular baseline.

unwrapped using a statistical minimum cost-flow unwrapping algorithm optimized for deformation interferograms [*Chen and Zebker,* 2001]. The coherence of the interferograms is generally high, because of the dry and stable surface condition in Mojave Desert, which results in reliable unwrapping.

Figure 6-2 shows the ascending and descending deformation interferograms. The two interferograms are dissimilar, due to different viewing geometries (arrows in Figure 6-2). The descending interferogram (Fig. 6-2a) shows positive LOS displacement east of the fault, as the east side moved to the south (right-lateral strike-slip), and negative LOS displacement west of the fault. In the ascending interferogram (Figure 6-2b) the radar look direction is perpendicular to the fault strike, and fault parallel ground displacements cause no LOS displacements. In this case the interferogram shows four LOS displacement quadrants. The northwest quadrant exhibits strong positive LOS displacement, as horizontal displacements are towards the radar (away from the fault) and because it is a compressional quadrant (with uplift) of this right-lateral strike-slip fault. The southwest quadrant shows strong negative LOS displacement, as the ground moved away from the radar towards the fault and the area subsided. The LOS displacements of the northeast and southeast quadrants are smaller because of cancelling effects. In the northeast, positive LOS displacement from horizontal displacement towards the fault and negative LOS displacement from ground subsidence tend to cancel each other in this extensional quadrant. Similarly, in the southeast compressional quadrant we have uplift (positive LOS) and eastward horizontal displacement (negative LOS), resulting in almost no LOS displacement.

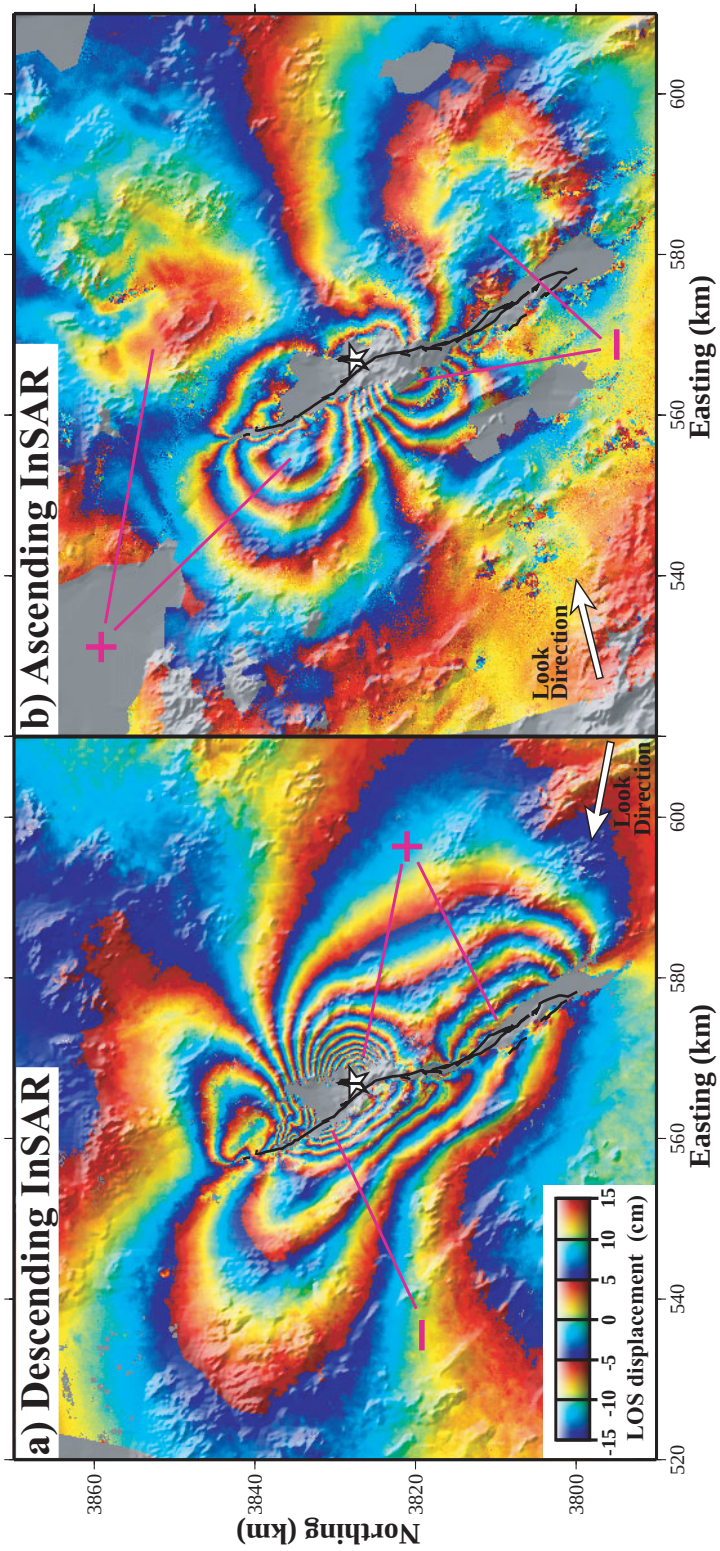

Figure 6-2: (a) Descending and (b) ascending interferograms showing the deformation of the Hector Mine earthquake. Each color cycle represents 10 cm of line-of-sight (LOS) displacement toward (yellow-red-blue) or away from (yellow-blue-red) the satellite. Arrows show the horizontal component of the look direction from the radar satellites. Purple + and − signs point to areas of positive and negative LOS displacement. The mapped fault trace is shown as thick line and the epicenter is denoted with a star. Coordinates are universal transverse Mercator (UTM) coordinates (zone 11S) in kilometers.

6.3.2 Azimuth offsets of radar amplitude images

When an interferogram is formed, the two radar scenes are co-registered to sub-pixel accuracy. Alignment follows from cross-correlation of local regions within the two radar amplitude (backscatter) images. Often it suffices to estimate the average offset between the two images at the top and the bottom of the two scenes and linearly interpolate in between; however, it is possible to estimate the offsets between the two amplitude images for many subimages to form a map of the offsets [*Michel et al.,* 1999a, 1999b]. We estimated the offset field using 32-pixel subimages and estimated the offsets for every 32 pixels in azimuth and 8 pixels in range. The ground-range resolution of radar images is 4 m in the azimuth direction (along track) and 20 m in the range direction (across track). The offsets were estimated to about 1/32 of a pixel or to about 12.5 cm in the azimuth direction. This offset field information can therefore be useful when horizontal displacements are large. We use here the term SARIO (synthetic aperture radar image offsets) data when referring to the azimuth offset fields.

The peak-to-peak amplitude of the SARIO data is $\sim$6 m across the central part of the fault (Figure 6-3), consistent with field estimates [*Scientists of the USGS et al.,* 2000]. The descending SARIO image shows positive offset values on the east side of the fault as the east side moved to the south in the flight direction of the satellite (see arrow in Figure 6-3a). In contrast, the ascending SARIO image exhibits positive offsets on the west side of the fault as the west side moved to the northwest in the ascending azimuth direction (Figure 6-3b). The ascending SARIO data are noisier because the two ascending radar scenes span 4 years while the two descending scenes span only 1 month. Precise cross-correlation of small sub-images becomes increasingly difficult with longer time separation between radar images because erosion changes the ground surface over time.

Although the SARIO measurements are much noisier than the InSAR measurements, the azimuth SARIO data provide information about displacements that are perpendicular to the InSAR line-of-sight displacements (Figure 6-3). The offsets also provide information near the fault trace, where no InSAR data are available due to decorrelation. Hence, the SARIO data can be used to determine the location of the fault trace if it is not previously well known [*Peltzer et al.,* 1999].

We do not use the range offset data because they are much noisier than the azimuth offsets, due to the low range resolution. The magnitude of the range offsets is also smaller than the magnitude of the azimuth offsets, because the surface displacements are mostly

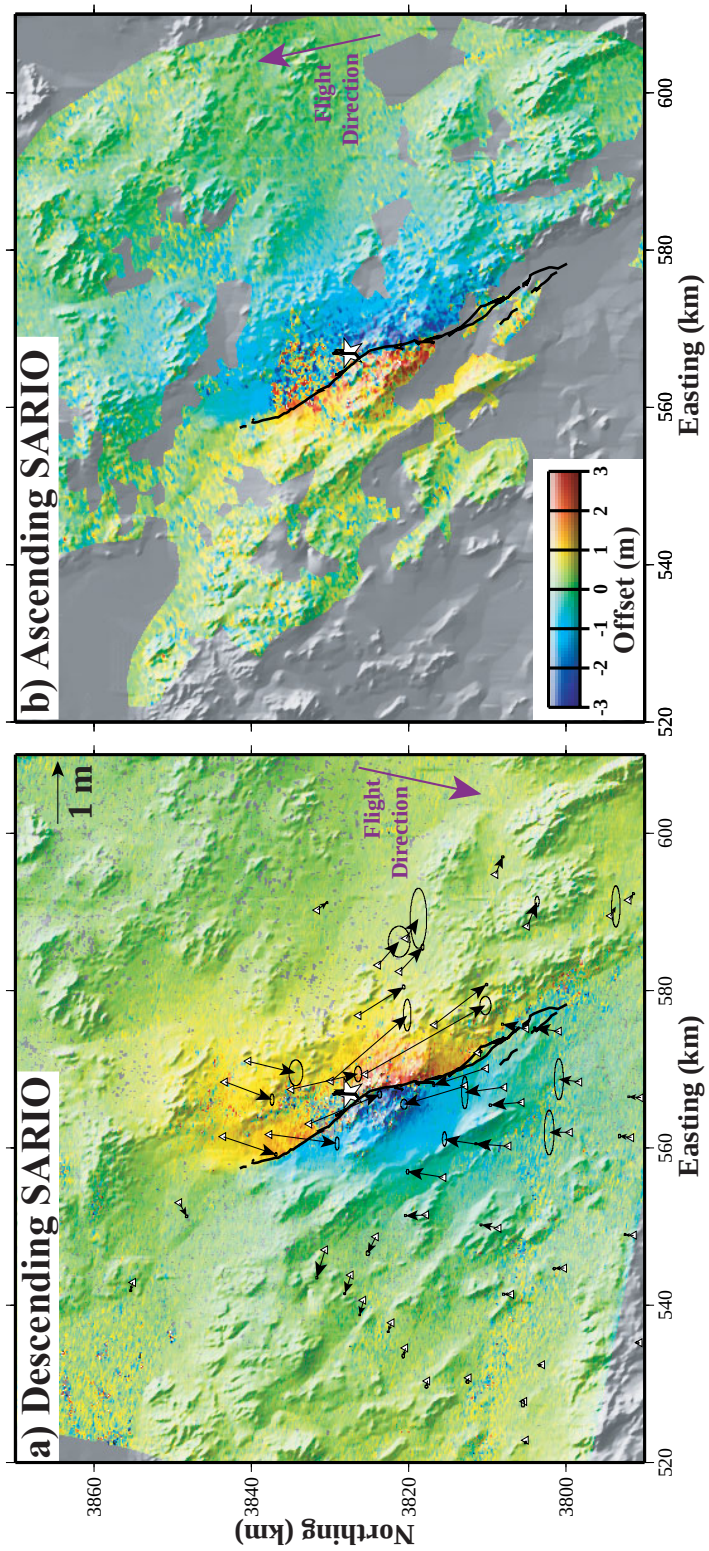

Figure 6-3: The synthetic aperture radar image offsets (SARIO) in the azimuth direction for (a) descending and (b) ascending orbits. Large purple arrows show the satellite flight direction in which the azimuth offsets are measured. The peak-to-peak amplitude of the offsets across the fault is about 6 m. Horizontal GPS campaign displacements [*Agnew et al.*, 2002] are overlaid on the offsets in (a). The mapped fault trace is shown as thick line and the epicenter is denoted with a star.

horizontal and parallel to the fault. Furthermore, the range offsets provide no significant additional information than provided by the InSAR data as both are sensitive to displacements parallel to the radar look direction.

6.3.3 Campaign GPS data

Campaign GPS data were provided by *Agnew et al.* [2002]. Measurements were conducted at 55 stations 7-23 months before the earthquake and again after the earthquake (Figure 6-3a). About half of the stations were observed in the first week following the earthquake, but some stations were observed as late as 6 months after the earthquake. The GPS displacements have been corrected for interseismic deformation but not for postseismic deformation [*Agnew et al.,* 2002]. The estimated displacement uncertainties vary by more than an order of magnitude from one station to another (Table 6.2) but the average uncertainties for the east, north and vertical components are 3.3 cm, 1.5 cm, and 6.1 cm. The stations are nearly evenly distributed across the central and southern part of the fault, but few stations cover the area to the north (Figure 6-3a). The largest observed horizontal displacement is 2.2 m at a station located 3 km east of the central part of the fault, just southeast of the epicenter (Figure 6-3a).

6.3.4 Comparison Between Datasets

The radar interferograms can be compared to the GPS data by projecting the GPS observations into the radar line of sight direction. The LOS unit vectors are given in Table 6.2. The root mean square (rms) differences between the GPS and the descending and ascending interferograms show 5.8 cm and 6.4 cm mismatch, respectively. The large differences may partly be explained by tilts in the images. InSAR data exhibit large-scale tilts due to orbit uncertainties. When we corrected for our lack of precise orbit knowledge by removing the tilts, the rms differences between the GPS and the descending and ascending interferograms were reduced to 4.9 cm and 4.8 cm. The remaining large difference is caused by poor accuracy of the vertical component of the GPS displacements (Table 6.2) as the two sets of differences are found to be highly correlated. The radar LOS is 23° from vertical, so the vertical GPS component contributes 70% to the projected LOS value.

The SARIO data can also be compared to the GPS observations. In this case we project the horizontal GPS observations into the azimuth direction. The rms difference is found to

Data set	Data size	Data size used	σ	Weight	Unit vector
Descending InSAR	1.48×10^6	843	3 cm	49%	[-0.38, 0.07, -0.92]
Ascending InSAR	1.27×10^6	452	3 cm	26%	[0.38, 0.08, -0.92]
Descending SARIO	1.45×10^6	194	15 cm	2%	[-0.19, -0.98 0]
Ascending SARIO	0.66×10^6	164	30 cm	1%	[-0.21, 0.98 0]
GPS, east	55	55	0.6-19.4 cm	8%	[1, 0, 0]
GPS, north	55	55	0.6-7.0 cm	10%	[0, 1, 0]
GPS, vertical	55	55	0.7-30.7 cm	4%	[0, 0, 1]
Total	4.86×10^6	1818	-	100%	-

Table 6.2: Information about the datasets. The size of the radar datasets is shown before and after quadtree partioning. The estimated uncertainty is also shown, along with the weight that each dataset has. The unit vector shows the direction [East,North,Up] in which the datasets have sensitivity. The negative sign of the InSAR z-component is due to the fact that ground uplift is observed as range decreases.

be 15 and 40 cm for the descending and ascending SARIO images, respectively. The high rms value in the ascending case drops to 23 cm if two of the GPS stations are excluded. These two stations are located where the SARIO image is particularly noisy. The rms values above represent well the accuracy of the SARIO data as the GPS horizontal displacements are much more precise than the azimuth offsets and can be treated as true displacements in this comparison.

6.3.5 Data Reduction

The multilooked radar interferograms used in this study are formed by averaging to 80 m× 80 m pixels and consist of about 1.5 million points each. The deformation data are highly correlated spatially and can be reduced without losing significant information. We reduce the interferograms with a two-dimensional quantization algorithm known as quadtree [e.g., *Welstead*, 1999]. In this procedure, the scene is divided into four quadrants and the mean of each quadrant is calculated. If the rms scatter about the mean exceeds a given threshold, the quadrant is divided into four new quadrants, and the mean of each calculated and again compared with the data. The process continues iteratively until convergence. Data reduced in this manner then represent the statistically significant portion of the signal, with far fewer sampling points.

Figure 6-4 shows the quadtree result for the descending interferogram using an rms threshold of 2.83 cm (one-half radar wavelength). Although the rms noise of the interferogram far from the deformation is somewhat lower, we picked a higher threshold value to obtain a more manageable dataset size. The quadtree partitioning puts relatively few large

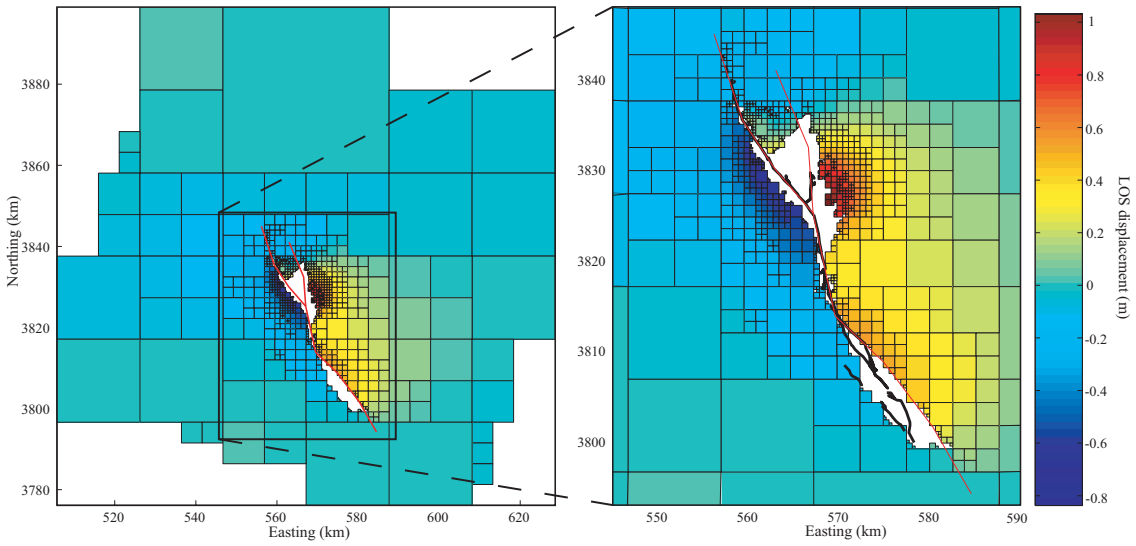

Figure 6-4: Quadtree partitioning of the descending interferogram, both the whole image (left) and a close up of the fault zone (right). This method reduced the number of data points from $\sim$1.5 million to 843. The smallest rectangles are 360 m $\times$ 360 m. Also shown are the mapped fault trace (in heavy black lines) and the fault approximated as 9 segments (in red).

squares away from the fault but many close to the fault where strong LOS gradients occur. The resulting 843 data points, 0.06% of the original $\sim$ 1.5 million in the interferogram, can reconstruct the original interferogram within 2.83 cm uncertainty using bilinear interpolation. We also use this procedure for the ascending interferogram (same threshold) and for the SARIO images. The quadtree threshold is set to 15 and 30 cm for the descending and ascending SARIO data (Table 6.2).

After reduction of the InSAR and SARIO data, a total of 1818 datapoints remain (GPS included) making model computations more feasible. We treat all the observations as independent (diagonal covariance matrix) with estimated uncertainty of 3 cm for the InSAR data, 15 and 30 cm for the descending and ascending SARIO data, and scaled formal errors for the GPS data. From these uncertainties we can calculate the relative weight of the different datasets. The relative weights of the descending and the ascending InSAR datasets are 49% and 26%, 2% and 1% in case of the descending and ascending SARIO datasets, and 22% in case of the GPS data.

6.4 Modeling

We use inverse modeling to estimate spatial slip variations along the faults that ruptured in the Hector Mine earthquake. We use analytical solutions that relate surface displacements to offsets across many small rectangular dislocations in a homogeneous elastic halfspace [*Okada,* 1992] to solve for slip using the geodetic data described above. The mapped surface offset of the Hector Mine rupture shows that the slip at surface varies from 0 to about 5 meters and that the fault is not a straight line (Figure 6-1) [*Scientists of the USGS et al.,* 2000]. Using only one rectangular dislocation with a constant slip is therefore an oversimplification, although it may lead to a reasonable first-order solution [*Hurst et al.,* 2000] (Table 6.3).

6.4.1 Fault Trace

Estimating the location, size, dip, orientation and slip across multiple rectangular dislocations is a numerically challenging task given the number of data points we have and the number of parameters we would need to estimate for these dislocations. We therefore use information from the mapped fault trace to constrain several parameters of the fault. We find that nine fault segments can reasonably represent the surface fault trace. For each of these segments we fix the location, length, and orientation such they agree with the mapped fault trace (Figure 6-4b). At the two locations where the fault zone has major bends the fault appears to fork into two branches. At the southern bend we use the azimuth offset data to constrain the location of our fault segments as the mapped surface trace does not follow a regular pattern and does not extend as far southeast as the offset data indicate (Figure 6-4b). At the northern bend, near the epicenter, we let the fault segments extend north of the mapped surface rupture as implied by aftershock activity [*Hauksson et al.,* 2002]. We also fix the dip-slip displacement to 0 and the vertical extent of each fault segment to 15 km, the maximum depth of seismicity in the area [*Deng et al.,* 1998]. These constraints decrease the number of parameters to be estimated for each of the nine fault segment from nine to two. The remaining parameters are the dip of each segment and the amount of strike-slip offset across the dislocations.

6.4.2 Fault Dip

The observed surface displacements **d** can be described as a function g of the fault model parameters **m**:

$$\mathbf{d} = g(\mathbf{m}) + \boldsymbol{\varepsilon} \tag{6.1}$$

where $\boldsymbol{\varepsilon}$ are observational errors. Function g describes how slip across rectangular dislocation causes displacement at the ground surface [e.g., *Okada,* 1992]. The surface displacements are nonlinear functions of the fault dip but the slip components are linear. We seek the model **m** that minimizes the L2-norm of the misfit function:

$$\Phi = ||\mathbf{W}(\mathbf{d} - g(\mathbf{m}))||_2 \tag{6.2}$$

where **W** is the weight matrix from Cholesky decomposition of the data covariance matrix inverse: $\mathbf{W^T W} = \boldsymbol{\Sigma}^{-1}$. We find the optimal model using a simulated annealing nonlinear searching scheme [*Cervelli et al.,* 2001] followed by a derivative based method. The former method helps us to locate the valley that contains the global misfit minimum, and the second method brings us the bottom of that valley.

We solve for the dip and the strike-slip component of the nine fault segments. The resulting model has right-lateral strike-slip offset of up to 5.6 m and a geodetic moment of 7.08×10^{19} Nm (Table 6.3). The segment dips range from vertical to 72° to the northeast. The dips of the northern and central segments are better constrained than the dips of the southernmost segments. The average dip is 83°. This estimate agrees with a moment tensor solution derived from both broadband and strong motion data which has an 82° dip [*Dreger and Kaverina,* 2000], and it is similar to the result from finite source modeling of strong motion data that yields 77° [*Kaverina et al.,* 2002]. Our estimate is also similar to a single dislocation model solution of 84.2° estimated from GPS measurements [*Hurst et al.,* 2000].

6.4.3 Variable Strike-Slip

To determine finer details of the strike-slip distribution we next discretize the fault segments into 1.5 km × 1.5 km fault patches, extend the depth of each fault segment to 21 km down dip, and fix the dip of every fault segment to 83^o. This restricted problem is linear and we can write equation 6.1 in matrix form as $\mathbf{d} = \mathbf{Gm}$, where **d** is the data vector, **m** is the

vector of model parameters (strike-slip values for every patch), and **G** are the data kernels relating the surface displacements to the model. The data require weighting as before and our weighted system of equation becomes:

$$\mathbf{d}' = \mathbf{G}'\mathbf{m} \tag{6.3}$$

where $\mathbf{d}' = \mathbf{W}\mathbf{d}$ and $\mathbf{G}' = \mathbf{W}\mathbf{G}$.

To avoid oscillations in the fault slip we smooth the solution by additionally minimizing the two-dimensional second derivative (Laplacian) of the fault slip. We include the smoothing by solving for the following system of coupled equations:

$$\begin{bmatrix} \mathbf{d}' \\ \mathbf{0} \end{bmatrix} = \begin{bmatrix} \mathbf{G}' \\ \kappa^2\mathbf{D} \end{bmatrix} \mathbf{m} \tag{6.4}$$

where **D** is a second-order finite-difference operator (see Appendix A) and the Lagrange multiplier κ^2 determines the weight of smoothing. We solve this system of equations using nonnegative least squares [*Lawson and Hanson,* 1974], i.e. only allowing for right-lateral strike-slip.

The smoothing parameter κ^2 depends on data weighting and on the number of data points; e.g., if we estimate two solutions, one by using all the data and one by only using the InSAR data, then two different values of κ^2 are needed to obtain equally smooth solutions. We therefore define a new parameter, solution roughness, which is better suited to compare different solutions. The solution roughness is the average second-order finite-difference sum of each fault patch:

$$\rho = \frac{\Sigma_i |p_i|}{2N} \tag{6.5}$$

where $\mathbf{p} = \mathbf{D}\mathbf{m}$ and N is the number of fault patches. The constant 2 is the result of smoothing the solution both along the fault strike and across strike. The units of ρ are cm/km indicating the average slip gradient.

Figure 6-5 shows examples of strike-slip distribution solutions along the Hector Mine fault for three different smoothing weights. For a low smoothing weight ($\rho = 24$ cm/km) the fault slip is highly oscillatory with maximum slip of almost 12 m, and it is not likely to be plausible (Figure 6-5a), but for a higher value of κ^2 ($\rho = 0.9$ cm/km) the slip distribution is overly smooth (Figure 6-5b). The oscillatory and the overly smooth solutions result in

Model	N_d	n_p	ν	χ^2/ν	Dip	Max. s_1	Max. s_2	M_o (Nm)
Hurst - 1	1	6	1812	240	90^o	3.8 m	0	3.72×10^{19}
Hurst - 2	1	8	1818	296	84.2^o	3.0 m	1.5 m	3.79×10^{19}
Constant slip	9	18	1800	13.5	variable	5.6 m	0	7.08×10^{19}
Strike-slip only	714	714	-	-	83^o	7.2 m	0	5.78×10^{19}
Preferred soln.	714	1428	-	-	83^o	6.0 m	1.6 m	5.93×10^{19}

Table 6.3: Information about different models showing the number of dislocations used N_d, number of parameters estimated n_p, the number of degrees of freedom ν, the normalized χ^2 sum (χ^2/ν), the dip of the fault(s), the maximum estimated strike-slip (max. s_1) and dip-slip (max. s_2) components, and estimated geodetic moment of each model. Parameters of the first two models come from *Hurst et al.* [2000].

moments of 5.54×10^{19} Nm (M_w7.1) and 6.48×10^{19} Nm (M_w7.2), respectively. We choose the amount of smoothing from a trade-off curve with misfit function Φ (Equation 6.2) plotted as a function of solution roughness ρ (Figure 6-6). We pick a roughness of $\rho = 4.0$ cm/km for our final solution, as lower ρ results in significantly worse misfit but higher ρ does not improve the misfit much.

Our final strike-slip solution shows slip concentrated at the northwestern fault branch, with maximum slip of 7.2 m at 7 km depth (Figure 6-5c). The estimated geodetic moment is 5.78×10^{19} Nm corresponding to a M_w7.1 earthquake. The amount of slip sharply decays to zero north of the area of maximum slip, but it decays more slowly towards the south, where the area of high slip becomes shallower. The northeastern branch is found to have slip up to 3 m near the epicenter and 17% of the total moment while the northwestern branch has 50%. Very little slip is found below 15 km depth.

6.4.4 Strike-Slip Distribution Determined from each Dataset Independently

When the five datasets are used independently to determine the strike-slip distribution using the previously obtained solution roughness, similar solutions with strike-slip concentrated on the northwestern branch result (Fig. 6-7). The differences between solutions describe each dataset's contributions to the optimal strike-slip solution. The solution based on the descending interferogram (weight 49%, Fig. 6-7) is very similar to the final strike-slip solution (Fig. 6-5c). The main difference is that the descending InSAR solution shows up to 2 m of slip at the bottom of the southern part of the fault, which is likely to be an

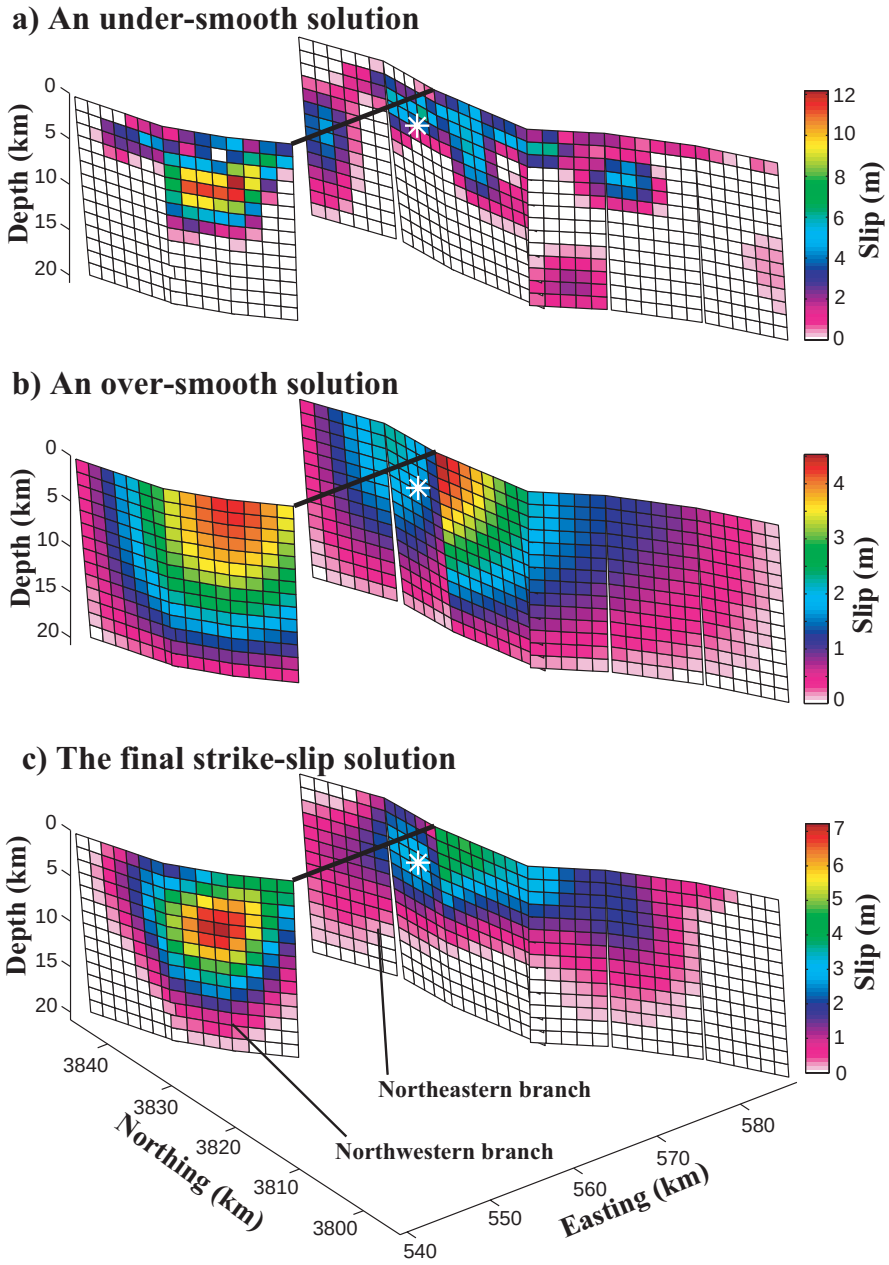

Figure 6-5: Estimated strike-slip distribution for three different smoothing weights. (a) Little weight on the smoothing resulting in an oscillatory solution ($\rho = 24$ cm/km). (b) Smoothing weight is strong resulting in an overly smooth solution ($\rho = 0.9$ cm/km). (c) Final strike-slip solution, which has roughness of $\rho = 4.0$ cm/km. Star is the Hector Mine hypocenter. The northwestern branch is shifted to the left for displaying purposes.

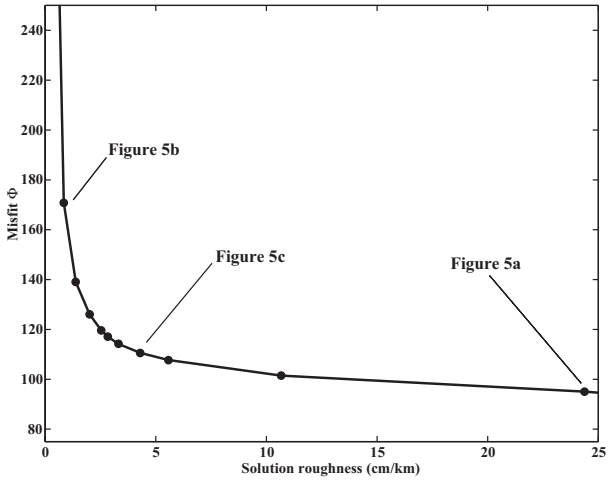

Figure 6-6: Trade-off curve with misfit function Φ plotted as function of average solution roughness ρ (Equations 6.2 and 6.5). The misfit improves with increasing solution roughness. We pick a solution roughness of $\rho = 4.0$ cm/km. Additional slip roughness will not improve the misfit significantly.

artifact. The solution based on the ascending InSAR data (weight 26%, Fig. 6-7b) shows a slip maximum just south of the fault junction that extends into the northeastern branch. These data appear to be the main influence driving slip onto the northeastern branch in the final strike-slip solution near the epicenter (Fig. 6-5c).

The solution based on the descending SARIO data only (Fig. 6-7c) is quite similar to the final strike-slip solution, although these data have only 2% weight in the final solution. The ascending SARIO solution (weight 1%, Fig. 6-7d) has strong slip near the bottom of the fault that is likely to be an artifact. The GPS solution (weight 22%, Fig. 6-7e) appears to be similar to the optimal strike-slip solution (Fig. 6-5c), although it shows stronger slip on the shallow central part of the fault than the other solutions.

These results show that the GPS, descending InSAR, and even the descending SARIO data could have been used alone to derive the fault slip distribution fairly accurately. The fact that the ascending InSAR data result in a different slip distribution may indicate the importance of observing ground motion parallel to the main slip direction. The ascending InSAR radar look direction is perpendicular to the fault strike and not sensitive to fault parallel ground displacements.

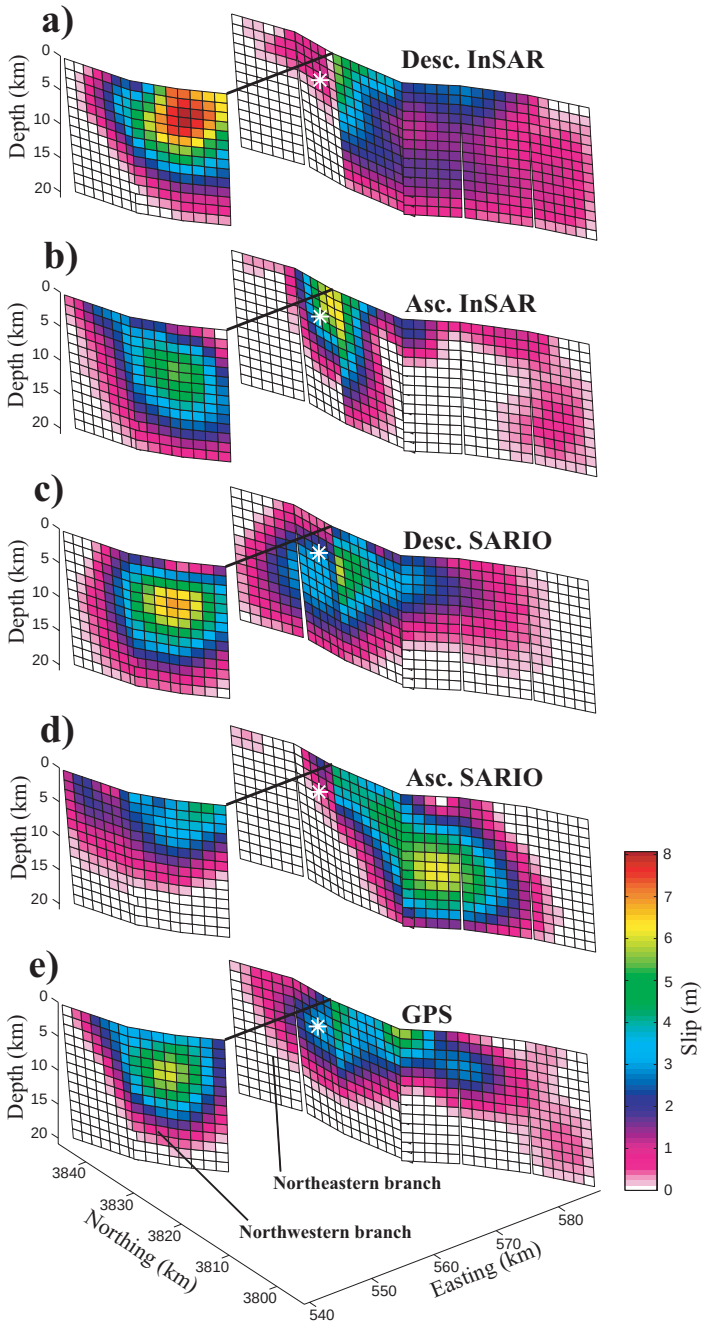

Figure 6-7: Strike-slip models using different datasets independently: (a) descending InSAR, (b) ascending InSAR, (c) descending SARIO, (d) ascending SARIO, (e) GPS. All the solutions show strong right-lateral strike-slip on the northwestern branch.

6.4.5 Importance of Dip-Slip

The Harvard Centroid Moment Tensor (CMT) solution for the Hector Mine earthquake has a rake of 174° and a fault dip of 80° to the northeast. Furthermore, another moment tensor solution from long period seismic data shows a rake of 175° and a fault dip of 70° to the northeast [*Dreger and Kaverina,* 2000]. This may imply that the earthquake had a small amount of dip-slip (reverse faulting) as well as right-lateral strike-slip. However, inversion for slip distribution of strong motion data yields only a "very low" amount of dip-slip [*Kaverina et al.,* 2002].

When we solve for both strike-slip and dip-slip on all the patches, the misfit decreases by 32%, 11%, and 8% in case of the InSAR, SARIO, and GPS data, respectively. The maximum strike-slip is 6.0 m, and the maximum dip-slip is 1.6 m (Figure 6-8). In both cases the maximum slip is found on the northwestern branch although the dip-slip appears to be more localized than the strike-slip. Interestingly, the strike-slip of the northeastern branch decreases when dip-slip is included, and this branch now has only 9% of the total moment, comparing to 17% in the strike-slip-only solution. The seismic moment of the northwestern branch decreases as well from 50% to 44%.

But is the improvement in fit to the data significant? A common method to test a goodness of fit is the χ^2 test, calculating the normalized χ^2/ν sum (where ν is the degree of freedom; i.e., the number of data points minus the number of parameters estimated). Smoothing introduces correlations between the model parameters, so here we have no good way of calculating ν. Therefore, we use cross-validation to find out if the fit improvement is significant. We take out the GPS observations and use all the InSAR and SARIO data to calculate two solutions, one with only strike-slip and another one with both dip-slip and strike-slip. The fit to the GPS data improves by 15% when dip-slip is included. This suggests that the amount dip-slip that occurred is significant and our final preferred solution is the one that includes both strike-slip and dip-slip.

The total geodetic moment of our preferred solution is 5.93×10^{19} Nm (M_w7.1), similar to the strike-slip-only solution (5.79×10^{19} Nm). The strike-slip component accounts for 92% of the moment and the dip-slip component 8%, resulting in an average rake of 175° which agrees with the moment-tensor solutions. The fact we consistently obtain geodetic moments similar to seismologically derived estimates implies we have no significant amount of postseismic or interseismic deformation in our geodetic data.

The InSAR data predictions of the final model resemble the data well (Figures 6-2

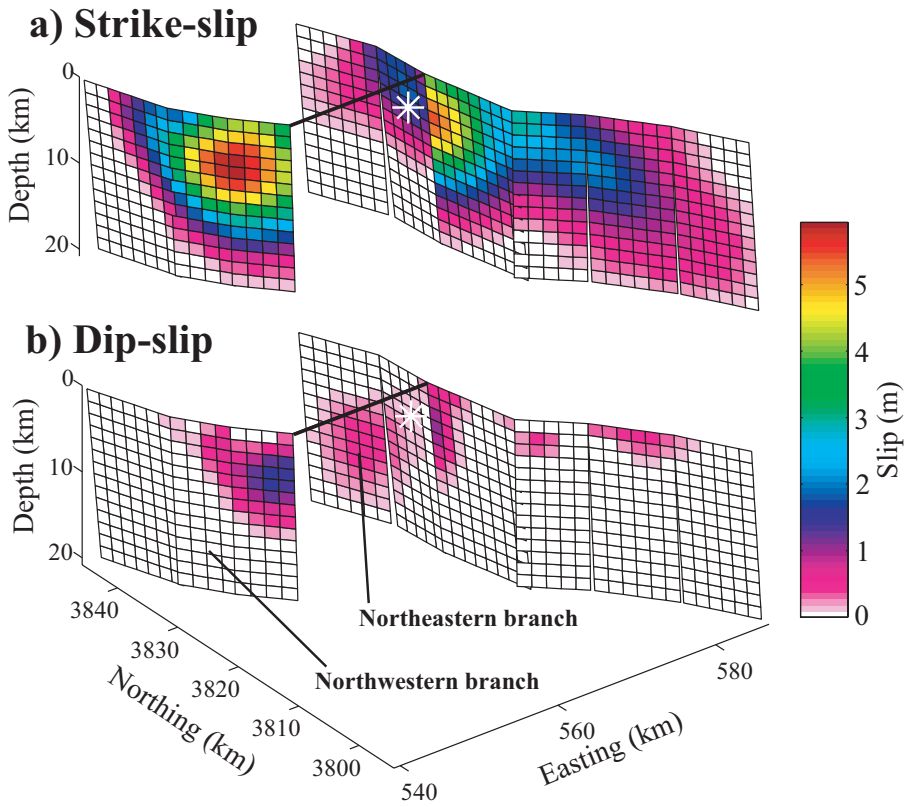

Figure 6-8: (a) Strike-slip and (b) dip-slip distribution of the preferred model. The model has up to 6.0 m of right-lateral strike-slip and up to 1.6 m of reverse faulting.

and 6-9). The residuals are largest close to the fault trace. The SARIO data predictions are qualitatively similar to the SARIO data, but large residuals occur near the fault (Figures 6-3 and 6-10a-d). The GPS data predictions match the observations well, as shown in Figure 6-10e-f.

6.4.6 Comparison with Mapped Fault Offset

We also compare the mapped surface offset along the fault to the fault slip solutions and to the SARIO data. The mapped surface offsets show right-lateral offset, varying from zero about 15 km north of the epicenter to a maximum of 5 m close to the epicenter (Figure 6-11) [*Scientists of the USGS et al.,* 2000]. The mapped surface slip decays to zero about 20 km

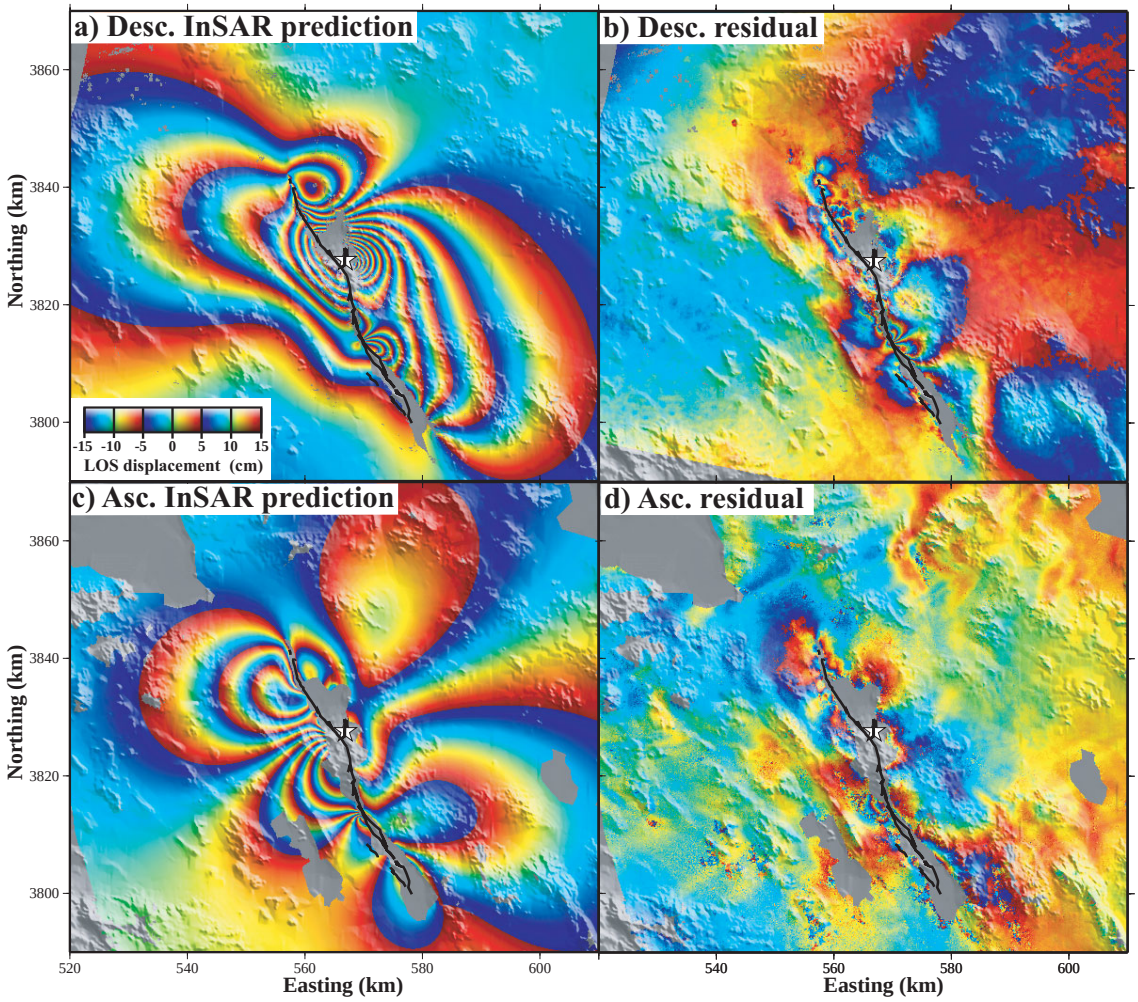

Figure 6-9: The model prediction and residuals for the InSAR observations. (a-b) Descending InSAR model prediction and the residual between the InSAR data (Figure 6-2) and the model prediction. (c-d) Ascending InSAR model prediction and residual.

south of the epicenter (Figure 6-11).

We estimate the surface fault offset from the descending SARIO data (Fig. 6-3a) by comparing median filtered values on both sides of the fault every 0.5 km and projecting them into fault-parallel direction. The SARIO fault offset increases from 0 m in the north to 5 m just south of the epicenter (Fig. 6-11). The measurements show large scatter in the epicentral area, where the fault splits into two branches. The SARIO fault offset decays to zero about 40 km south of the epicenter.

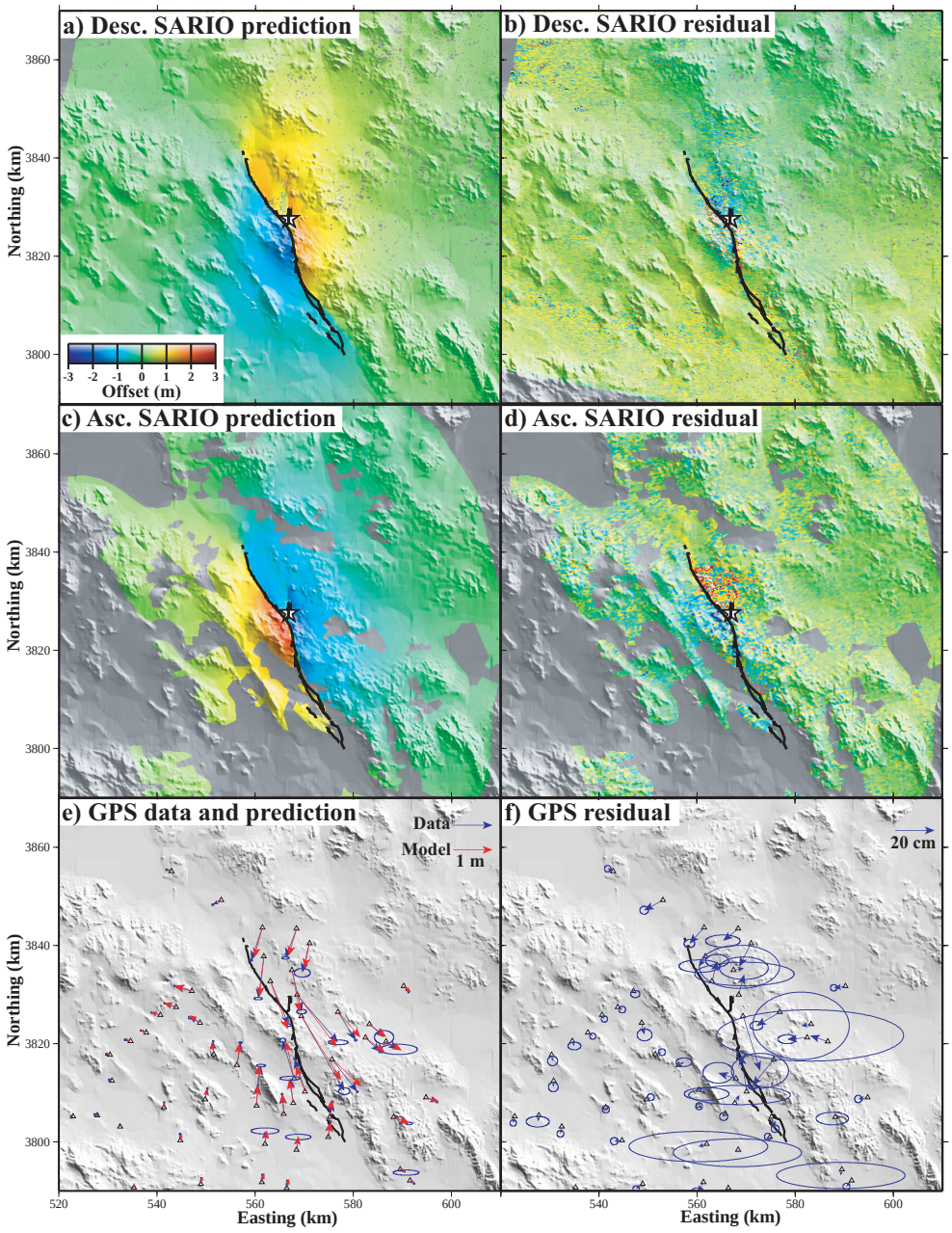

Figure 6-10: Model predictions and residuals for the SARIO and GPS data. (a-b) Descending SARIO model prediction and the residual between the SARIO data (shown in Figure 6-3) and the model prediction. (c-d) Ascending SARIO model prediction and residual. (e) Observed (blue arrows) and predicted (red arrows) horizontal GPS displacements. (f) Residual between the observed and predicted GPS displacements. Note different scales for arrows in (e) and (f).

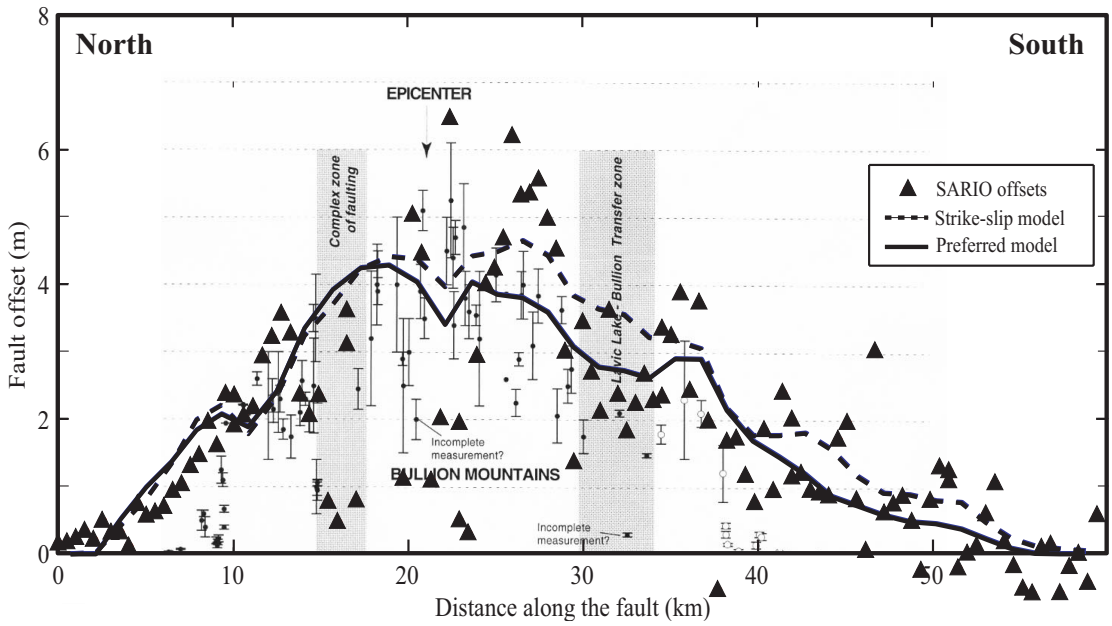

Figure 6-11: Comparison between surface fault offsets measured from the SARIO data (triangles), the surface slip of the final strike-slip model (dashed line), the preferred model (solid line), and the mapped fault offset (open and solid dots with error bars). The mapped fault offset was adopted from *Scientists of the USGS et al.,* [2000], where open dots represent cumulative slip estimates (slip values obtained by adding slip values from multiple parallel fault strands) and solid dots represent direct measurements. The SARIO data and the model results suggest that slip at surface continued 5 km further north and 15 km further south than detected in the field.

The surface slip of the final preferred solution is similar to strike-slip-only solution with maximum slip of $\sim$4.5 m in the epicenter area. Both fault slip solutions are in an agreement with the SARIO fault offset (the descending SARIO data have only 2% weight in the slip solutions). Both slip models and the SARIO data show more surface slip than mapped in the field, except in the epicentral area. In addition, our results indicate that the extent of the field mapped rupture was also underestimated. We find that surface slip extends 5 km further to the north and 15 km further to the south than detected in the field. This implies that field measurements of surface fault offset should be taken as a lower bound of the fault slip near surface.

6.5 Conclusions

We have estimated variations of the fault slip along the Hector Mine fault using a combination of five datasets: descending and ascending interferograms, descending and ascending azimuth offset fields, and GPS observations. We find the surface fault trace to be sufficiently approximated by nine straight fault segments and we estimate that the average dip of these segments is 83° to the northeast. Our final preferred solution includes both right-lateral strike-slip and reverse faulting. The maximum strike-slip and dip-slip are 6.0 m and 1.6 m at a depth of 6 km on the northwestern branch of the Hector Mine rupture, just northwest of the epicenter. The geodetic moment of the northeastern branch is only 9% of the total moment; the northwestern branch has 44%. The total geodetic moment is 5.93×10^{19} Nm (M_w7.1), similar to seismological estimates. This indicates that no significant interseismic or postseismic deformation signal is seen in the geodetic data. The SARIO data and the final model indicate that the amount and extent of the surface fault rupture were underestimated in the field.

6.6 Appendix A: Smoothing Operator D

The slip solutions are smoothed by minimizing a second-order derivative (Laplacian) of the fault slip, in addition to the residual norm. As the slip is determined on discrete patches we write the Laplacian as two-dimensional second-order finite-difference sum:

$$\frac{s_{i-1,j} - 2s_{i,j} + s_{i+1,j}}{(\Delta l_1)^2} + \frac{s_{i,j-1} - 2s_{i,j} + s_{i,j+1}}{(\Delta l_2)^2} \tag{6.6}$$

where $s_{i,j}$ is the amount of slip on the patch in the ith row and jth column of the fault and Δl_1 and Δl_2 are the distances between adjacent patches (Figure 6-12a).

Special care is needed where the fault forks into two branches. The slip of the elements just south of the junction are smoothed to the weighted sum of the slip on elements north of the junction (here we assume $\Delta l_1 = \Delta l_2 = 1$ km, to simplify the equations):

$$s_{i+1,j} + s_{i-1,j} + s_{i,j-1} + c_1 s^1_{i,j+1} + c_2 s^2_{i,j+1} - 4s_{i,j} \tag{6.7}$$

where $s^1_{i,j+1}$ and $s^2_{i,j+1}$ are the slip values of the two branch patches north of the junction (Figure 6-12b). The c_1 and c_2 are weight constants that depend on the orientation of the

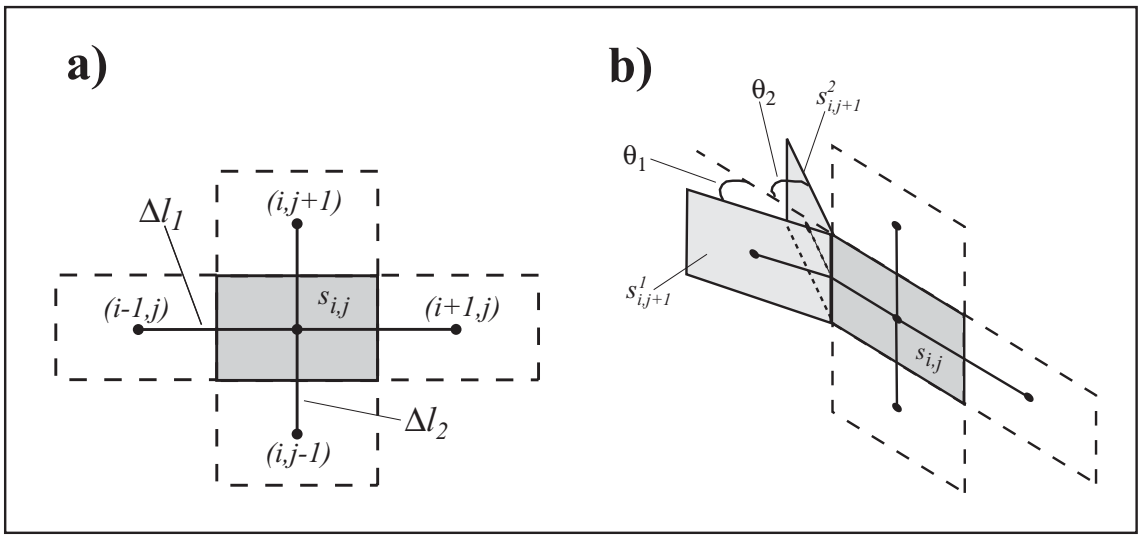

Figure 6-12: Schematic figure of fault patches. (a) A fault patch in the ith row and jth column is smoothed to patches at all sides. (b) The slip on a patch south of the junction is smoothed to a linear combination of the slip on the two branch patches north of the junction.

branches relative to the fault segment south of the junction:

$$c_1 = \frac{\cos\theta_1}{\cos\theta_1 + \cos\theta_2} \qquad c_2 = \frac{\cos\theta_2}{\cos\theta_1 + \cos\theta_2} \tag{6.8}$$

where θ_1 and θ_2 are strike deviations of the two branch segments from the strike of the south segment. Similarly, each of the segments north of the junction is smoothed to the slip south of the junction; e.g., a slip on a patch at the south edge of the northwestern branch would have the following finite difference sum:

$$s^1_{i+1,j+1} + s^1_{i-1,j+1} + s^1_{i,j+2} + (1-c_2)s_{i,j} - 4s^1_{i,j+1} \tag{6.9}$$

Chapter 7

Fault Geometry and Slip Distribution of the June 17 and June 21, 2000 Earthquakes (M_w6.5) in South Iceland

In the previous chapter we studied how we can use multiple geodetic observations of coseismic deformation to solve for the fault geometry and slip distribution in large earthquakes. There we studied the magnitude 7.1 Hector Mine earthquake that occurred in southern California in October 1999. In this chapter we carry out similar analysis for two magnitude 6.5 earthquakes that occurred in south Iceland in June of 2000. We use the observed coseismic deformation to estimate the geometry and the slip distribution of the two faults. We compare our results to various other data such as the aftershock distribution, mapped fault ruptures, and teleseismic observations. The material in this chapter is a contribution to a collaborative study with scientists at the Nordic Volcanological Institute in Iceland that as of this writing is being prepared for a journal submission [*Pedersen et al.,* 2002].

7.1 Abstract

Here we estimate the fault geometry and fault slip distribution of the two June 2000 South Iceland earthquakes using Synthetic Aperture Radar Interferometry (InSAR) and GPS measurements. The InSAR data come from the ERS-2 satellite and consist of two coseismic interferograms and the GPS data are campaign measurements of 37 stations in the area. We estimated the geometry of both faults simultaneously assuming simple planar faults. The optimal fault geometry indicates that the earthquakes occurred on two parallel and near-vertical faults that are separated by 18 km and strike N2-3°E. Both earthquakes were predominantly right-lateral strike-slip events with a small dip-slip component (east side up)

although the dip-slip is not distinguishable from zero at a 95% confidence level. The fault geometry is in a broad agreement with distribution of aftershocks, but mapped surface ruptures indicate more complex fault geometry. When solving for spatial variations in fault slip the June 17 fault is 14 km long with up to 2.5 m of slip. The June 21 fault is longer, or 17 km, with maximum fault slip of 3 m occurring at 4 km depth on the northern part of the fault. The June 21 slip extended deeper on the southern part of the fault than in the north, a result that is supported by the aftershock distribution. Estimated moments are 4.7×10^{18} Nm and 4.9×10^{18} for the June 17 and June 21 earthquakes, both of which correspond to a moment magnitude of 6.4. Our results provide important information for future studies on stress transfer and stress triggering between the two faults and on other faults in the area.

7.2 Introduction

South Iceland Seismic Zone (SISZ) is a left-lateral transform zone connecting two sections of the Mid-Atlantic ridge in Iceland (Figure 7-1). The full spreading rate of the ridge at this latitude is 1.94 cm/year [*DeMets et al.,* 1990] causing left-lateral shear across the SISZ that is accommodated by bookshelf faulting on many parallel North-South striking faults [*Sigmundsson et al.,* 1995; *Jónsson et al.,* 1997]. Historical accounts indicate that sequences of several large (M6.5-7) earthquakes occur in the SISZ every 45-112 years [*Einarsson et al.,* 1981]. For example, such sequences occurred in 1732-4, 1784, and in 1896. The 1896 sequence consisted of five large earthquakes, followed by a single event in 1912. Subsequently, the seismic zone was relatively quiet with the largest event (M_w5.9) occurring in the eastern SISZ in 1987 [*Bjarnason and Einarsson,* 1991].

The two M_w6.5 earthquakes hit on June 17th and June 21st, 2000, rupturing two of the parallel N-S faults [*Pedersen et al.,* 2001; *Árnadóttir et al.,* 2001]. Preliminary aftershock locations delineate the two faults clearly (Figure 7-1) indicating that the June 17 earthquake occurred on a $\sim$12 km long fault extending to 10 km depth while the June 21 aftershocks are consistent with a $\sim$17 km long fault that extends to a depth of 9 km. Mapping of the surface ruptures shows that the overall trend of the June 17 fault is near due North while the rupture pattern of the June 21 earthquake is more complex with a central segment of conjugate E-W left-lateral faulting [*Clifton and Einarsson,* 2000]. The earthquakes caused clear pressure changes in a number of geothermal wells in the area such that pressure

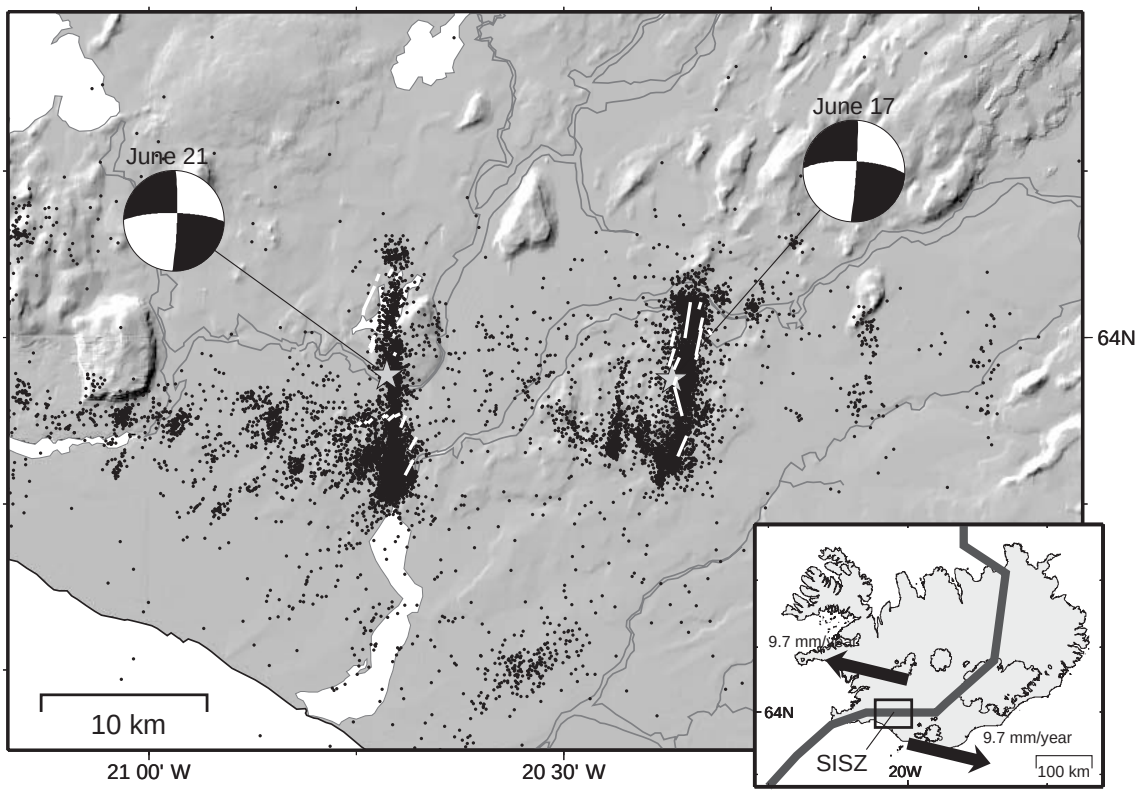

Figure 7-1: Shaded relief map of the South Iceland Seismic Zone (SISZ). The inset shows the Mid-Atlantic Plate boundary in Iceland that has a full spreading rate of 1.94 cm/year [*DeMets et al.,* 1990]. The map shows the focal mecanisms (Harvard CMT) and epicenters (stars) of the two June 2000 mainshocks. Aftershocks are shown as small black dots and mapped surface ruptures as thick white lines [*Clifton and Einarsson,* 2000].

increased in wells located in the compressional quadrants near the faults and decreased in extensional quadrants [*Björnsson et al.,* 2001]. The water level recovered in most wells during the first 1-3 months following the events.

Árnadóttir et al. [2001] used campaign GPS measurements from 1995, 1999, and 2000 to invert for the location and geometry of the two faults. They found the June 17 fault to be 9.5 km long, extending to a depth of 10 km with 2 m of right-lateral slip while the June 21 fault was longer (12.3 km) extending to 8 km depth and with 1.5 m slip using a single rectangular dislocation with uniform slip to represent each fault. Two Synthetic Aperture Radar Interferograms (InSAR) of the coseismic deformation were analyzed by *Pedersen et al.* [2001] to estimate fault parameters for the two quakes. They found these data call for

more complex fault models than used by *Árnadóttir et al.* [2001] and used three uniform dislocations to represent each fault. Their total fault lengths were 16 km and 15 km with strike-slip up to 2.39 m and 2.15 m for the June 17 and June 21 faults, respectively.

This study is an extension of the two former studies by *Pedersen et al.* [2001] and *Árnadóttir et al.* [2001]. Here we take both the InSAR and GPS data and combine these datasets into a joint inversion. We estimate the fault geometry of both faults simultaneously using all the data, and subsequently solve for the slip distribution on both faults. The results tell us about where the faults are located and where slip concentrated on the fault planes. This information is important to estimate how the earthquakes changed the stress-field in the area, that in turn will help to identify potential location of future major earthquakes.

7.3 Observed Coseismic Ground Deformation

In this study we use two coseismic radar interferograms provided by Rikke Pedersen and coseismic GPS displacements provided by Thóra Árnadóttir (both at the Nordic Volcanological Institute in Iceland). The InSAR data and the GPS data are the same as used by *Pedersen et al.* [2001] and by *Árnadóttir et al.* [2001]. Volumetric strain data exist from several stations in the area that show clear signals from the earthquakes [*Kristján Ágústsson, pers. comm.,* 2002]. These data were not available to us at the time this study was written.

7.3.1 InSAR Data

The radar data were processed using the PRISME/DIAPASON radar software package where the topographic signature was removed from the interferograms using a simulated interferogram based on a 90 m×90 m resolution digital elevation model of the SISZ. Several coseismic interferograms were formed, but only two remain usable as most of them were decorrelated in the area of interest [*Rikke Pedersen, pers. comm.,* 2002]. Interferometric decorrelation is of major concern in the South Iceland Seismic Zone. Due to winter snow we can only use scenes acquired during summer months to produce coherent interferograms. In addition, interferograms formed using scenes from two consecutive summers tend to be decorrelated as well due to agricultural activity in the SISZ. Thus, the only option to form coherent interferograms in the area is to combine scenes acquired 1-3 months apart during May to September [*Rikke Pedersen, pers. comm.,* 2002].

The two usable interferograms cover the time period from June 16, 2000 (a day before

the first earthquake) to July 21, 2000, and June 19, 2000 (between the two earthquakes) to July 24. In the following discussion we refer to the June 16 to July 21 interferogram as "T52" and the June 19 to July 24 interferogram as "T95", as corresponding radar scenes were acquired from satellite tracks 52 and 95. Both interferograms were acquired from descending satellite orbits with the radar looking down to the ground from the ESE with an incidence angle of $\sim 23^{\circ}$. InSAR is only sensitive to ground displacements into the line-of-sight (LOS). Thus, the satellite geometry for the South Iceland earthquakes is far from optimal, as coseismic ground displacements were predominantly horizontal parallel to the N-S strike-slip faults.

Interferogram T52 only covers the area east of the June 17 earthquake, but it clearly shows uplift southeast of the fault and subsidence northeast of the fault, as expected from the right-lateral rupture (Figure 7-2a). Interferogram T95 covers the entire area, but in time it only spans the June 21 event. This interferogram shows clearly that the LOS displacements east of the June 21 fault are much larger than west of it (Figure 7-2b). The explanation is that east of the fault the horizontal and vertical ground displacements compliment each other resulting in strong LOS displacements while west of the fault they nearly cancel each other.

The interferograms were unwrapped using the residue-cut unwrapping algorithm to get absolute LOS displacements [*Zebker and Lu,* 1998]. This algorithm only unwraps areas where coherence is high, but leaves out areas of low coherence. We preferred this unwrapping algorithm to avoid the risk of having unwrapping errors near the faults, but in turn we do not have much data coverage near them.

The unwrapped interferograms were quantized to reduce the number of datapoints to ease model calculations. A simple two-dimensional quantization algorithm was used where an unwrapped image is split up into four quadrants, the variance of unwrapped phase values in each quadrant is calculated. When a quadrant variance exceeds a given threshold, the quadrant is split up into four new quadrants, and the algorithm continues until convergence. When a quadrant variance is lower than the threshold, the median value of the quadrant is assigned to the center coordinate of that quadrant as one data point. This algorithm, called quadtree, can reduce the data quantity by a few orders of magnitude without a loss of details of the deformation (Table 7.1). Here we used a quadtree threshold of 1 cm and maximum cell size to be 5×5 km^2. The quantized interferograms show clearly strong positive LOS displacement (uplift towards the radar) southeast of the faults and strong negative LOS

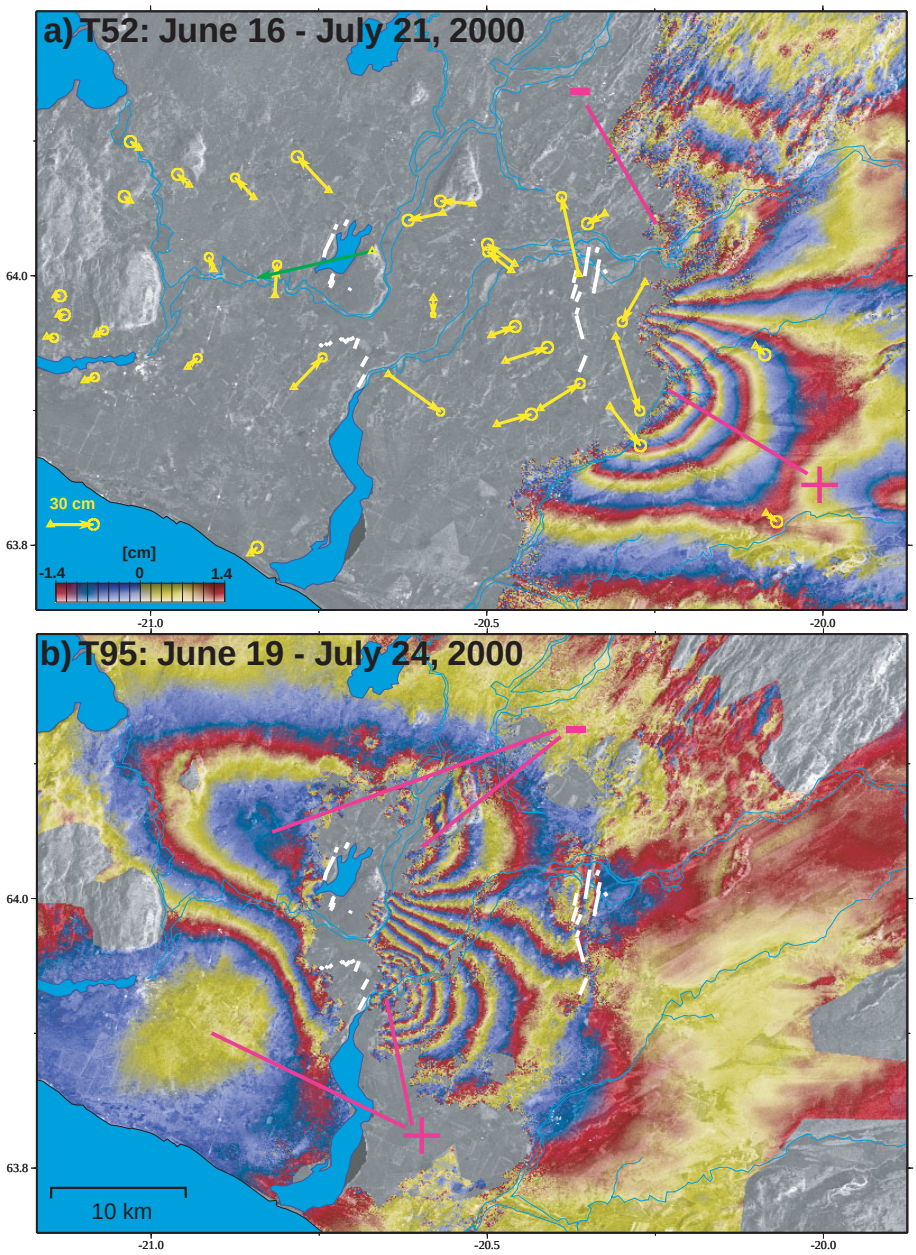

Figure 7-2: Coseismic interferograms and horizontal GPS displacements showing ground deformation due to the June 17 and June 21, 2000, earthquakes. The figures shows the same area as Figure 7-1. The interferograms span the time from (a) June 16 to July 21, and (b) June 19 to July 24, 2000. Purple + and - signs point to areas of positive and negative LOS displacement. One GPS displacement vector (green) was excluded in the modeling. Mapped fault ruptures are shown as white lines.

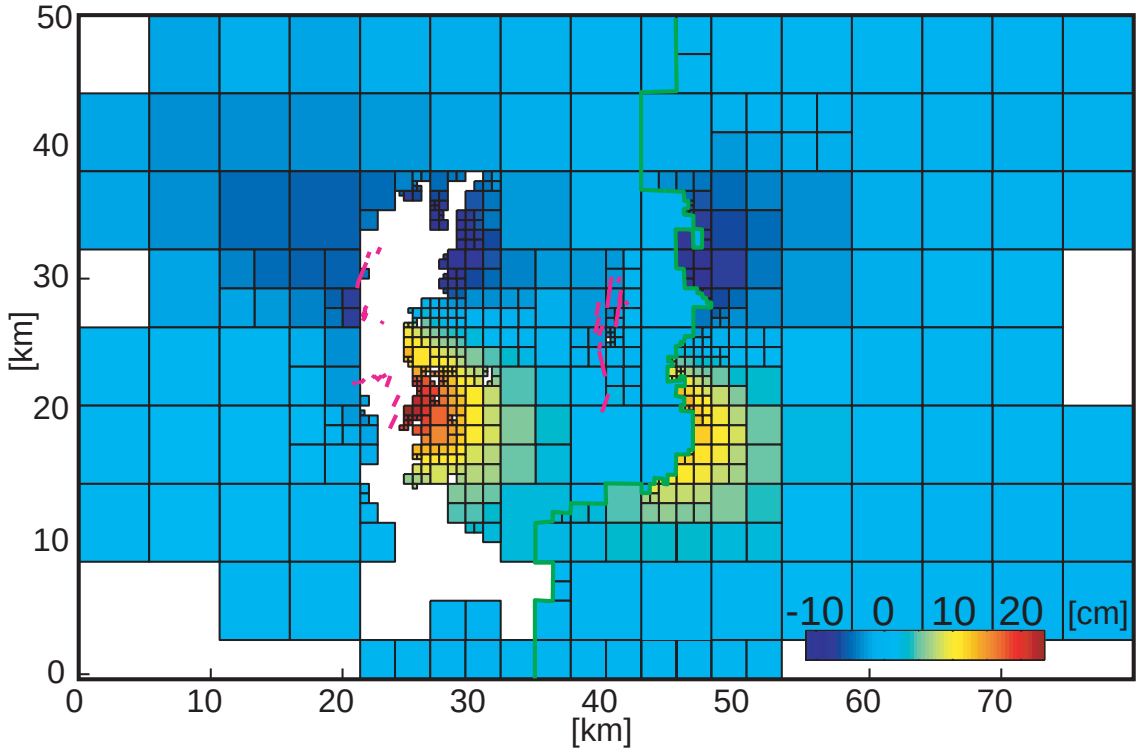

Figure 7-3: Two-dimensional quantization of the unwrapped interferograms showing line-of-sight (LOS) ground displacements. In this figure the interferogram from track 52 (Figure 7-2a) is overlaid on top of the interferogram from track 95 (Figure 7-2b) with a green line marking the boundary. Mapped surface ruptures are shown as purple lines.

displacements northeast of them (Figure 7-3).

7.3.2 Coseismic GPS Displacements

The GPS stations were observed in 1995 and again during the first two weeks after the earthquakes. In addition, a few stations were observed in 1999. The GPS data were analyzed using the Bernese V4.2 software package and the accuracy of the horizontal displacement components is estimated to be 1.1-1.6 cm and 3-4 cm for the vertical component. The measurements have been corrected for 5 years interseismic of motion using the 1995-1999 displacements [*Árnadóttir et al.,* 2001]. The correction is not very accurate as only a part of the network was occupied in 1999 and the interseismic rates on other stations had to be estimated based these results. The uncertainty of this correction is included in the displacement uncertainties.

Data set	*Data size*	*Data size used*	σ	*Weight*	*Unit vector*
InSAR, T52	2.2×10^5	197	1 cm	29.7%	[0.43, -0.12, 0.90]
InSAR, T95	3.2×10^5	403	1 cm	60.9%	[0.38, -0.11, 0.92]
GPS - East	38	37	1.1-1.6 cm	3.9%	[1, 0, 0]
GPS - North	38	37	1.1-1.6 cm	3.9%	[0, 1, 0]
GPS - vertical	38	37	3-4 cm	1.5%	[0, 0, 1]
Total	-	714	-	100%	-

Table 7.1: Information about the datasets. The size of the radar data is shown before and after quantization. The estimated uncertainty is also shown along with the weight of each dataset. The unit vector shows the direction [East,North,Up] in which the datasets are sensitive.

The GPS displacement vectors show clear right-lateral motion across the two faults with a counter-clockwise rotation of the block between the faults (Figure 7-2a). One station near the June 21 rupture shows anomalously large displacement in a direction that is not consistent with simple right-lateral strike slip faulting (green vector in Figure 7-2). This station may be unstable or may have been influenced by local deformation [*Árnadóttir et al.,* 2001]. We excluded this station in our inversion modeling.

7.4 Estimating the Geometry of the Two Faults

To learn more about these earthquakes from the observed ground deformation we seek to find what faults can best explain the observations. The mapped surface ruptures suggest that the fault geometry is quite complex, especially for the second earthquake [*Clifton and Einarsson,* 2000]. However, the depth distribution of aftershocks indicates that both earthquakes occurred on fairly straight, near-vertical, planar faults. Therefore, we begin with a simple model of two rectangular faults with uniform slip across them.

7.4.1 The Fault Geometry Problem

We simplify the earth as a homogeneous elastic halfspace with material properties that are typical for undrained rocks (Poisson's ratio: $\nu_u = 0.31$ [*Wang,* 2001]). Offsets (or slip) across rectangular dislocations in the halfspace cause surface displacements that can be described analytically [*Okada,* 1992]. Using these relations we can write the observed surface displacements $\mathbf{d}$ as a function g of the fault model parameters $\mathbf{m}$:

$$\mathbf{d} = g(\mathbf{m}) + \boldsymbol{\varepsilon} \tag{7.1}$$

where $\boldsymbol{\varepsilon}$ are observational errors. Model vector $\mathbf{m}$ consists of ten fault parameters for each fault, seven for the fault geometry and three for the displacement across the fault. The geometry is described with the fault length and width, fault dip, strike, and depth to the upper fault edge, as well as the East and North location of the center of the upper fault edge. The three displacement parameters are the amount of strike-slip, dip-slip, and opening across the fault.

In this study, we do not allow for any fault opening or fault closure, and we fix the upper fault edge at surface because significant surface faulting occurred in both earthquakes. These constraints reduce the number of parameters to be estimated from 10 to 8 for each fault. In addition to the fault parameters, we estimate two constants (ambiguities), one for each interferogram, to correct for an arbitrary shift in the unwrapped data. The interferograms shown in Figure 7-2 are subsets of full 100×100 km^2 interferograms. Tilts in the large interferograms, due to orbital inaccuracies, were manually removed before the subsets were created. Therefore, we do not include a tilt correction in the inversion.

The surface displacements are a non-linear function of the fault geometry but the slip components are linear. Thus, for one fault we can write Equation 7.1 as:

$$\mathbf{d} = s g^s(\mathbf{m}') + t g^t(\mathbf{m}') + \boldsymbol{\varepsilon} \tag{7.2}$$

where s and t are amounts of strike-slip and dip-slip, respectively. Now the model vector $\mathbf{m}'$ only has 7 parameters that describe the fault geometry. For our problem we can write this system of quasi-linear equations as:

$$\mathbf{d} = \begin{bmatrix} \mathbf{d}^{\mathrm{T52}} \\ \mathbf{d}^{\mathrm{T95}} \\ \mathbf{d}^{\mathrm{gps}} \end{bmatrix} = \begin{bmatrix} g^s(\mathbf{m}^{\mathrm{j17}}) & g^t(\mathbf{m}^{\mathrm{j17}}) & g^s(\mathbf{m}^{\mathrm{j21}}) & g^t(\mathbf{m}^{\mathrm{j21}}) & 1 & 0 \\ 0 & 0 & g^s(\mathbf{m}^{\mathrm{j21}}) & g^t(\mathbf{m}^{\mathrm{j21}}) & 0 & 1 \\ g^s(\mathbf{m}^{\mathrm{j17}}) & g^t(\mathbf{m}^{\mathrm{j17}}) & g^s(\mathbf{m}^{\mathrm{j21}}) & g^t(\mathbf{m}^{\mathrm{j21}}) & 0 & 0 \end{bmatrix} \begin{bmatrix} s^{\mathrm{j17}} \\ t^{\mathrm{j17}} \\ s^{\mathrm{j21}} \\ t^{\mathrm{j21}} \\ a^{\mathrm{T52}} \\ a^{\mathrm{T95}} \end{bmatrix} + \varepsilon \tag{7.3}$$

where $\mathbf{d}^{\mathrm{T52}}$ and $\mathbf{d}^{\mathrm{T95}}$ are the quantized interferograms from tracks 52 and 95, and $\mathbf{d}^{\mathrm{gps}}$ is a vector containing all the GPS displacement values. Vectors $\mathbf{m}^{\mathrm{j17}}$ and $\mathbf{m}^{\mathrm{j21}}$ describe the geometry of the two faults. Strike-slip values (s^{j17} and s^{j21}), and dip-slip values (t^{j17} and t^{j21}) for the two faults as well as ambiguities for the two interferograms (a^{T52} and a^{T95}) are also shown. Note the 'zeros' in the matrix (2nd line, columns 1-2) that are due to the fact interferogram T95 does not span the June 17 earthquake, and therefore, can not influence the June 17 fault parameter estimation.

Our task is find the model vector $\mathbf{m}$ that minimizes the norm of the misfit function

$$\Phi = \|\mathbf{W}[\mathbf{d} - g(\mathbf{m})]\| \tag{7.4}$$

where $\mathbf{W}$ is the weight matrix from Cholesky decomposition of the data covariance matrix inverse: $\mathbf{W^T W} = \Sigma^{-1}$. We do not separate the problem by first solving for the non-linear parameters and then solve the linear part as it has been recommended against for several reasons [*Cervelli et al.,* 2001]. Instead we search for the best set of all model parameters simultaneously using non-linear optimization and evaluate the misfit with the standard L2 measure. We begin by using a simulated annealing searching scheme to identify a good set of model parameters within reasonable bounds [*Cervelli et al.,* 2001]. The algorithm randomly samples the model parameter space in the beginning and then it progressively performs a more thorough search near previously sampled parameters that gave low misfits. This random search implementation allows the algorithm to avoid local minima. Once the algorithm has identified a good set of model parameters, we use it as an input for a derivative based method to find the neighboring minimum. For every case we studied, we ran the optimization several times achieving nearly identical model parameters in each run,

indicating that the true global minimum was found.

7.4.2 The Optimal Fault Geometry

We first estimated all the fault parameters simultaneously (8 for each fault) using all the data. The resulting model parameters are shown in Tables 7.2 and 7.3 (model UFS-1) and in Figure 7-4a. Both faults extend to 8 km depth, are nearly vertical, with a strike slightly east of north, and both are found to be predominantly strike-slip. The June 21 fault is longer (12.0 km) than the June 17 fault (10.3 km). The RMS misfit is 1.34 cm and is dominated by high GPS residuals. The GPS RMS misfit is higher than the a priori GPS measurement uncertainty. This is also true when we only use the GPS measurements in the optimization. This either suggests that more complex fault model is needed to fit the GPS measurements or that the GPS measurement uncertainties are underestimated. The InSAR RMS misfit is 0.72 cm and 0.90 cm for the T52 and T95 interferograms, respectively, or slightly lower than the a priori uncertainties. Many data residuals near the fault are larger indicating that we are not overfitting the data, but maybe overestimating the data uncertainties. However, our interpretation is that this simple model of two straight planar faults is acceptable, and that the data do not require more complex fault geometry.

Most of the optimal fault parameters agree with the aftershock distribution. However, some do not. For example, the dip of the June 17 fault was found to be 86° to the west while the aftershocks indicate a fault dip of 87° to the east. A probable reason for this discrepancy is our inability to constrain the June 17 fault dip because interferogram T52 (Figure 7-2a) has coverage only east of the fault while we have no InSAR data west of the fault, only a few GPS stations. When we fix the June 17 fault dip to 87° east the optimal values of other parameters are almost identical to what we found before (model UFS-2), except the June 17 fault width changes from 8.0 km to only 6.8 km. The aftershocks, however, suggest that the June 17 fault extends to 10 km depth. If we include more information from the aftershock distribution and fix the dip of both faults and the strike of the June 17 fault, the results are similar to what we obtained before (UFS-3, Tables 7.2 and 7.3). Yet, the location of the June 17 fault seems to be offset by 0.5-0.6 km to the east relative to the aftershocks (Figure 7-4b).

What data can we believe? There is no doubt that the mapped surface ruptures are correctly located as they were mapped in the field using differential GPS measurements. However, the surface ruptures are complex, and do not delineate simple straight faults as the

June 17 Earthquake	N_{dis}	n_p	ν	*Length* [km]	*Width* [km]	*Depth* [km]	*Dip* [°E]	*Strike* [N°E]	*Lon.* [°W]	*Lat.* [°N]	*SS* [m]	*DS* [m]	*Rake*	M_o [Nm] $\times 10^{18}$	M_w
UFS - 1	1	8	0.31	10.3	8.0	0*	93	3	20.3261	63.9687	1.84	0.12	176°	4.5	6.4
Estimated 2σ				2.9	2.6	-	11	6	1.2 km	0.9 km	0.43	0.16	-	1.1	-
UFS - 2	1	7	0.31	10.3	6.8	0*	87*	2	20.3333	63.9682	1.80	0.11	177°	3.8	6.4
UFS - 3	1	6	0.31	10.2	6.4	0*	87*	5*	20.3338	63.9689	1.87	0.15	175°	3.7	6.3
InSAR only	1	7	0.31	10.5	7.4	0*	87*	0	20.3421	63.9718	1.72	0	180°	4.1	6.4
GPS only	1	8	0.31	9.4	9.9	0*	91	2	20.3321	63.9671	1.95	0.27	172°	5.5	6.5
DFS	140	140	0.31	∼14	∼9	0	93*	3*	20.3261*	63.9687*	0-2.7	0*	180° *	4.7	6.4
Harvard CMT				-	-	-	87	4	20.470	63.990	-	-	173°	7.1	6.5
NEIC				-	-	-	75	-1	20.487	63.966	-	-	-164°	4.3	6.4
Surface Rupture				11	-	0	-	4	-	-	0.1-1	-	-	-	-
Aftershocks				12	10	-	87	4	20.3446	63.9722	-	-	-	-	-
Árnadóttir et al.	1	8	0.25	9.5	9.8	0.1	90*	3	20.351	63.970	2.0	0.2	174°	5.6	6.5
Pedersen et al.	3	18	0.25	16	10.0*	0*	86*	5*	20.3415	63.9792	0.25-2.39	0.02-0.21	175°	5.44	6.5

Table 7.2: Information about the June 17 fault estimated from various different datasets. The table shows information about the dislocation models: the number of dislocations N_{dis}, number of fault parameters estimated n_p, and Poisson's ratio (ν) used. Also shown are the resulting fault geometry for the two faults, the right-lateral strike-slip (SS) and dip-slip (DS, east side up), as well as the moment (M_o) assuming a shear modulus of $\mu = 30$ GPa. UFS and DFS stand for uniform fault slip and distributed fault slip. Fault dip is measured as a dip to the east, so 95° dip is equal to 85° dip to the west. The fault location is at the center of the fault upper edge. A star "*" indicates that a parameter was held fixed in the inversion. In comparison are fault parameters from various sources.

June 21 Earthquake	N_{dis}	n_p	ν	*Length* [km]	*Width* [km]	*Depth* [km]	*Dip* [°E]	*Strike* [N°E]	*Longitude* [°E]	*Latitude* [°N]	*SS* [m]	*DS* [m]	*Rake*	M_o [Nm] $\times 10^{18}$	M_w
UFS - 1	1	8	0.31	12.0	8.0	0*	86	2	20.7002	63.9864	1.65	0.07	178°	4.8	6.4
Estimated 2σ				1.0	1.0	-	4	3	0.5 km	0.4 km	0.14	0.06	-	0.5	-
UFS - 2	1	8	0.31	12.0	7.9	0*	86	2	20.7006	63.9865	1.67	0.07	178°	4.8	6.4
UFS - 3	1	7	0.31	11.8	8.0	0*	90*	3	20.6970	63.9863	1.77	0.07	178°	5.0	6.4
InSAR only	1	8	0.31	11.8	8.4	0*	86	2	20.7038	63.9857	1.60	0.08	177°	4.8	6.4
GPS only	1	8	0.31	13.1	4.4	0*	72	1	20.7088	63.9901	2.03	-0.02	-179°	3.6	6.3
DFS	140	140	0.31	∼17	∼9	0	86*	2*	20.7002*	63.9864*	0-3.1	0*	180° *	4.9	6.4
Harvard CMT				-	-	-	85	2	20.850	63.980	-	-	173°	5.4	6.5
NEIC				-	-	-	79	-4	20.758	63.980	-	-	-167°	5.2	6.4
Surface Rupture				14	-	0	-	-3	-	-	0.1-1	-	-	-	-
Aftershocks				16	9	-	90	-1	20.6959	63.9749	-	-	-	-	-
Árnadóttir et al.	1	7	0.25	12.3	8.0*	0*	90*	0.5	20.691	63.984	1.5	0	180°	4.5	6.4
Pedersen et al.	3	18	0.25	15.0	9.0*	0*	90*	0*	20.7034	63.9821	0.45-2.15	0	180°	5.06	6.4

Table 7.3: Information about the June 21 fault estimated from various different datasets. The table shows information about the dislocation models: the number of dislocations used N_{dis}, number of fault parameters estimated n_p, and Poisson's ratio (ν) used. Also shown are the resulting fault geometry for the two faults, the right-lateral strike-slip (SS) and dip-slip (DS, east side up), as well as the moment (M_o) assuming a shear modulus of $\mu = 30$ GPa and the moment magnitude using $M_w = \frac{2}{3}\log M_o - 6.03$. UFS and DFS stand for uniform fault slip and distributed fault slip. Fault dip is measured as a dip to the east, so 95° dip is equal to 85° dip to the west. A star "*" indicates that a parameter was held fixed in the inversion.

aftershocks suggest and the deformation data are consistent with. The aftershock locations are preliminary catalog locations from the South Iceland Lowland (SIL) seismic network operated by the Iceland Meteorological Office. The earthquake locations are accurate to $\sim$0.5 km and the depth to $\sim$3 km [*Steinunn Jakobsdóttir, pers. comm.,* 2002]. Systematic offsets in the earthquake locations are not unlikely as a simple 1D velocity model is used to locate events.

When compared, the aftershock locations and the surface rupture data are consistent in some places. At the June 17 fault, the surface ruptures fall into three main segments. The northern half with several parallel strands striking NNE, a south central segment striking NNW, and a southernmost segment, again with a NNE strike. The overall trend of the ruptures is approximately N4°E (Figure 7-4). Most of the June 17 aftershocks occurred at 3-10 km depth on a plane dipping 87° to the east. When this trend is extended to the surface it coincides roughly with, or is slightly east of the mapped ruptures. At the June 21 fault the whole scenario is more complex. Again we can categorize the mapped ruptures into three parts. In the northwest are several parallel strands striking NNE, then there is the E-W left-lateral conjugate faulting, and in the southeast there are a few segments with an overall N-S trend (Figure 7-4). Here the aftershocks delineate a clear vertical N-S fault that roughly coincides the southernmost part of the mapped ruptures. Some off-fault aftershocks are associated with the E-W conjugate faulting, but almost no aftershocks occurred near the ruptures in the northwest part.

Uncertainties of the model parameters estimated from the GPS and InSAR data are not easy to quantify. The bootstrap method, suggested by *Cervelli et al.* [2001], does not work in this case. The modeling results are essentially the same each time the InSAR data are resampled with replacement, due to correlations in the large number of InSAR data, leading to artificially small uncertainty estimates. Another way to find out how well the parameters are estimated is to examine the elements of the Jacobian matrix at the global minimum. For n datapoints and p model parameters the Jacobian is the following $n \times p$ matrix of derivatives:

$$\mathbf{J}(\mathbf{d},\mathbf{m}) = \begin{bmatrix} \frac{\partial d_1}{\partial m_1} & \cdots & \frac{\partial d_1}{\partial m_p} \\ \vdots & \ddots & \vdots \\ \frac{\partial d_n}{\partial m_1} & \cdots & \frac{\partial d_n}{\partial m_p} \end{bmatrix} \tag{7.5}$$

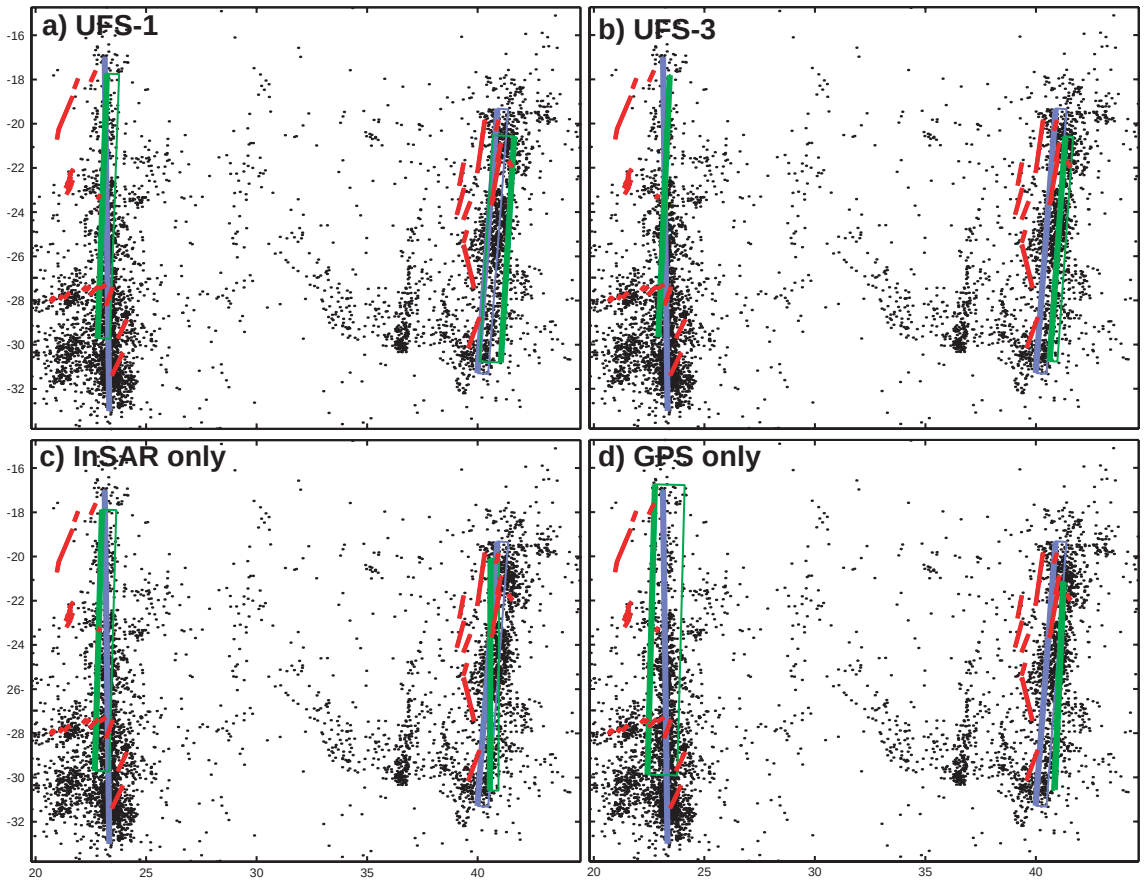

Figure 7-4: Comparison between aftershock locations (dots) and the fault planes they delineate (blue), mapped surface ruptures (red), and the estimated fault geometry (green). Model parameters are shown in Tables 7.2 and 7.3. Thick line marks the upper edge of the fault at surface while thinner lines show the projection of the fault outline onto surface (when the fault is not vertical). Coordinates are in km.

In practice we approximate the Jacobian with finite differences. Elements of $\mathbf{J}$ provide a simple measure of how a small change in model parameter m_j changes predicted data d_i. The matrix derivatives give information on how well the model parameters are constrained relative to one another (in that minimum) but they do not provide absolute uncertainty estimates. Another problem with this approach is that it cannot easily identify correlations between different model parameters and it does not address other candidate models in other (local) minima.

We estimated the relative uncertainties from the weighted mean of the absolute values of the Jacobian matrix columns. The estimated uncertainties are shown in Tables 7.2 and

7.3. The parameters of the June 21 fault are significantly better constrained than those for the June 17 fault. The uncertainties suggest that we cannot distinguish between the two optimal faults and two vertical faults, and that the estimated dip-slip on both faults is not significant at a 95% confidence level. In addition, these uncertainties indicate that the optimal faults are not inconsistent with the aftershock fault planes. The main difference is that the aftershocks suggest longer faults and wider (i.e., extending to a greater depth), than the results of the inversion modeling indicate. However, the modeled optimal faults would be longer and wider if we allow the slip to taper off near the edges.

7.5 Variable Fault Slip

The main problem with the single dislocation model above is that it is not realistic because it does not allow any slip heterogeneties on the fault plane and it has sharp slip discontinuities at the edges causing stress singularities. To create a more realistic model we discretize the faults and solve for variable slip by applying smoothing to the solution. We then perform resolution tests to find out what we can really resolve about the fault slip with our data and what we can not. We only solved for strike-slip and fixed the dip-slip to zero as the previously estimated dip-slip on the faults was not significant.

7.5.1 The Slip Distribution Problem

To determine variations of strike-slip on the faults we discretized the faults into 1.5 km $\times$ 1.5 km fault patches, and extended the fault lengths to 21 km and widths to 15 km. We fixed the strike, dip, and location of both faults to optimal values found in the non-linear inversion (model UFS-1, see Tables 7.2 and 7.3). This restricted problem is linear and we can write equation 7.1 in matrix form as $\mathbf{d} = \mathbf{Gm} + \boldsymbol{\varepsilon}$, where $\mathbf{G}$ are the data kernels relating the surface displacements to the model. The data require weighting as before and our weighted system of equation becomes (now ignoring $\boldsymbol{\varepsilon}$):

$$\mathbf{d}' = \mathbf{G}'\mathbf{m} \tag{7.6}$$

where $\mathbf{d}' = \mathbf{Wd}$ and $\mathbf{G}' = \mathbf{WG}$. To avoid oscillations in the fault slip we smooth the solution by additionally minimizing the two-dimensional second derivative (Laplacian) of the fault slip. We include the smoothing by solving the following system of coupled equations:

$$\begin{bmatrix} \mathbf{d}' \\ \mathbf{0} \end{bmatrix} = \begin{bmatrix} \mathbf{G}' \\ \kappa^2 \mathbf{D} \end{bmatrix} \mathbf{m} \tag{7.7}$$

where $\mathbf{D}$ is a second order finite difference operator and the Lagrange multiplier κ^2 determines the weight of the smoothing. Remember that interferogram T95 (Figure 7-2b) spans only the June 21 earthquake while T52 interferogram and the GPS observations span both earthquakes. Thus, the full expression of Equation 7.7 for this problem becomes:

$$\begin{bmatrix} \mathbf{d}^{\mathrm{T52}} \\ \mathbf{d}^{\mathrm{T95}} \\ \mathbf{d}^{\mathrm{gps}} \\ \mathbf{0} \end{bmatrix} = \begin{bmatrix} d_1^{\mathrm{T52}} \\ \vdots \\ d_n^{\mathrm{T52}} \\ d_1^{\mathrm{T95}} \\ \vdots \\ d_m^{\mathrm{T95}} \\ d_1^{\mathrm{gps}} \\ \vdots \\ d_p^{\mathrm{gps}} \\ 0 \\ \vdots \\ 0 \\ 0 \\ \vdots \\ 0 \end{bmatrix} = \begin{bmatrix} G_{1,1}^{\mathrm{t52}} & \cdots & G_{1,k}^{\mathrm{T52}} & G_{1,k+1}^{\mathrm{T52}} & \cdots & G_{1,k+l}^{\mathrm{T52}} & 1 & 0 \\ \vdots & & \vdots & \vdots & & \vdots & \vdots & \vdots \\ G_{n,1}^{\mathrm{T52}} & \cdots & G_{n,k}^{\mathrm{T52}} & G_{n,k+1}^{\mathrm{T52}} & \cdots & G_{n,k+l}^{\mathrm{T52}} & 1 & 0 \\ 0 & \cdots & 0 & G_{1,k+1}^{\mathrm{T95}} & \cdots & G_{1,k+l}^{\mathrm{T95}} & 0 & 1 \\ \vdots & & \vdots & \vdots & & \vdots & \vdots & \vdots \\ 0 & \cdots & 0 & G_{m,k+1}^{\mathrm{T95}} & \cdots & G_{m,k+l}^{\mathrm{T95}} & 0 & 1 \\ G_{11}^{\mathrm{gps}} & \cdots & G_{1,k}^{\mathrm{gps}} & G_{1,k+1}^{\mathrm{gps}} & \cdots & G_{1,k+l}^{\mathrm{gps}} & 0 & 0 \\ \vdots & & \vdots & \vdots & & \vdots & \vdots & \vdots \\ G_{p,1}^{\mathrm{gps}} & \cdots & G_{p,k}^{\mathrm{gps}} & G_{p,k+1}^{\mathrm{gps}} & \cdots & G_{p,k+l}^{\mathrm{gps}} & 0 & 0 \\ \kappa^2 D_{1,1} & \cdots & \kappa^2 D_{1,k} & 0 & \cdots & 0 & 0 & 0 \\ \vdots & & \vdots & \vdots & & \vdots & \vdots & \vdots \\ \kappa^2 D_{k,1} & \cdots & \kappa^2 D_{k,k} & 0 & \cdots & 0 & 0 & 0 \\ 0 & \cdots & 0 & \kappa^2 D_{1,1} & \cdots & \kappa^2 D_{1,l} & 0 & 0 \\ \vdots & & \vdots & \vdots & & \vdots & \vdots & \vdots \\ 0 & \cdots & 0 & \kappa^2 D_{l,1} & \cdots & \kappa^2 D_{l,l} & 0 & 0 \end{bmatrix} \begin{bmatrix} s_1^{\mathrm{j17}} \\ \vdots \\ s_k^{\mathrm{j17}} \\ s_1^{\mathrm{j21}} \\ \vdots \\ s_l^{\mathrm{j21}} \\ a^{\mathrm{T52}} \\ a^{\mathrm{T95}} \end{bmatrix} \tag{7.8}$$

where $\mathbf{d}^{\mathrm{T52}}$ and $\mathbf{d}^{\mathrm{T95}}$ are the weighted datavectors of the quantized interferograms, and $\mathbf{d}^{\mathrm{gps}}$ the weighted GPS datavector. The model vector $\mathbf{m}^{\mathbf{T}} = [(\mathbf{s}^{\mathrm{j17}})^{\mathbf{T}}, (\mathbf{s}^{\mathrm{j21}})^{\mathbf{T}}, \mathbf{a}^{\mathbf{T}}]$ consists of k slip values $\mathbf{s}^{\mathrm{j17}}$ for the June 17 fault patches, and l slip values $\mathbf{s}^{\mathrm{j21}}$ for the June 21 fault patches, as well as constants (ambiguities) a^{T52} and a^{T95} to shift the interferograms up or down. We solved the above system of equations with non-negative least-squares [*Lawson and Hansson,* 1974], i.e., only allowing for right-lateral strike-slip.

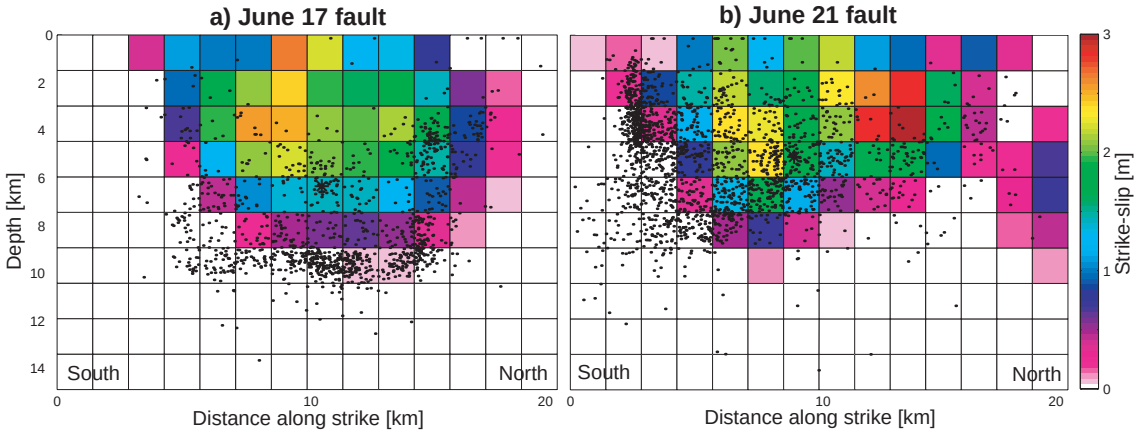

Figure 7-5: Estimated right-lateral strike-slip distribution for the June 17 and June 21 earthquakes. Aftershocks are shown as dots and mainshock hypocenters are shown as stars.

7.5.2 Optimal Strike-slip Distribution

The resulting strike-slip distribution is fairly uniform on both faults (Figure 7-5). The June 17 fault is found to be about $\sim$14 km long with slip extending to $\sim$9 km depth or slightly less than the aftershocks. The depth to which slip ceases is sensitive to the choice of Poisson's ratio. For a smaller Poisson's ratio (e.g. 0.25), the optimal slip extends to a greater depth and the total moment is larger. The reason is that using material with smaller Poisson's ratio requires more slip to produce the same vertical displacements.

The June 21 fault is longer than the June 17 fault, or $\sim$17 km, with slip extending to 9 km depth in the southern part but to a lesser depth in the north (Figure 7-5b). The aftershocks also indicate that the slip extended deeper in the south than in the north. Maximum slip of $\sim$3 m is found at 4 km depth on the northern part of the fault. This maximum is robust and is not sensitive to small changes in the fault geometry. On the other hand, the slip at the northern edge of the fault (at 4-8 km depth) is an artifact that disappears when the fault dip is changed slightly.

7.5.3 Slip Distribution Resolution

To explore how well the slip distribution is resolved we produced simulated data sets for given slip distributions and examined how well the variable slip was reproduced in the estimation. A checker-board slip distribution is commonly used in resolution tests although

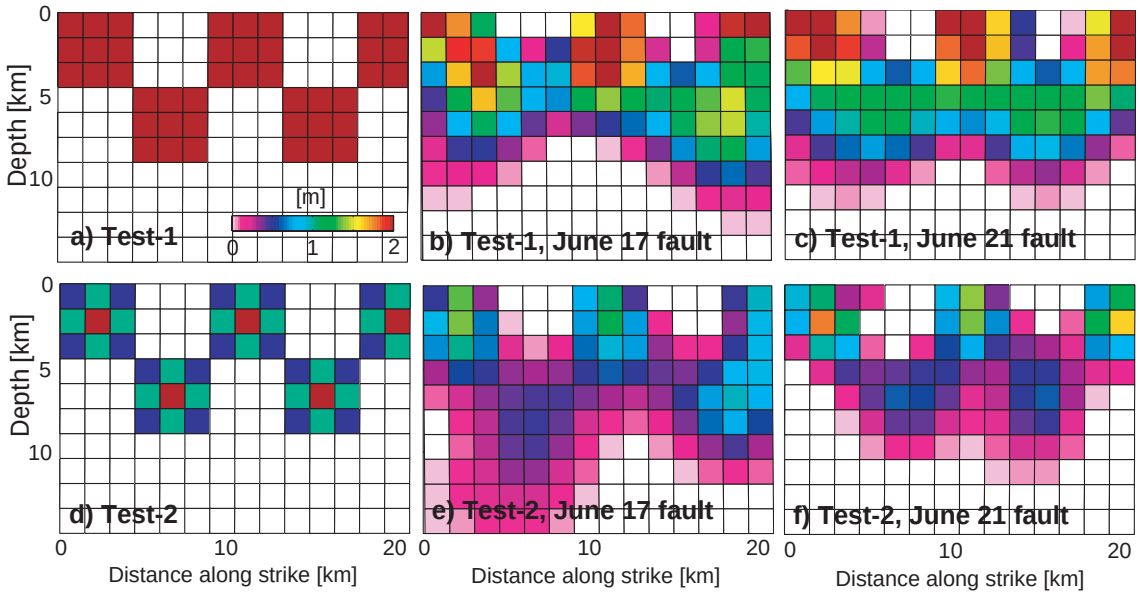

Figure 7-6: Two checkerboard tests to examine how well variable strike-slip can be resolved on the two fault planes. Test-1 has sharp patches with 2 m of right-lateral strike-slip while test-2 has smother patches.

such slip distribution would never occur in nature. It is also impossible to recover exactly through the inversion as we apply smoothing to the slip solution. However, we produced simulated data from a checkerboard slip distribution and added normally distributed random noise to the simulated data with variance equal to the actual data variance. We then inverted the simulated data for slip distribution on both faults and the results are not surprising (Figure 7-6a-c). First, they do not match the checkerboard input well, second, the resolution is better in the upper 5 km than at 5-10 km depth, and third, the resolution on the June 21 fault is better than on the June 17 fault.

We also tested a more reasonable slip distribution, a smoothed checkerboard (Figure 7-6d). The results are better with estimated slip distribution that is more similar to the input than in the previous test. The implications are the same showing that slip is better resolved at 0-5 km depth than below 5 km depth, and that we can resolve slip in more details on the June 21 fault, than on the June 17 fault.

7.5.4 Model Prediction

The variable slip model in Figure 7-5 fits the data with RMS misfit of 0.62 cm and 0.77 cm for the T52 and T95 interferograms and 2.1 cm and 3.3 cm for the horizontal and vertical GPS. The model predictions and residuals are shown in Figures 7-7 and 7-8.

The GPS model prediction shows clearly right-lateral motion across the faults and the counter-clockwise rotation of the block between the faults (Figure 7-7a). The largest difference between the observed and modeled GPS displacements is near the southern part of the June 21 fault that may be related to the complex surface faulting. The model prediction for interferogram T52 matches the observations well with no high frequency residuals near the June 17 fault. However, there is a long period residual seen in the northern and southern part of the residual image (Figure 7-7b). This residuals are of unknown cause, but they could be due to atmospheric heterogeneties. The longer period signals are better predicted for the T95 interferogram but a few high frequency residuals remain near the June 21 fault rupture (Figure 7-8). LOS residual of 3 cm is found near the west end of the June 21 E-W left-lateral conjugate faulting and a larger residual is found north of the June 21 fault. These residuals are likely due to the simple straight fault geometry we used in the modeling. Significant residuals are also found near the June 17 fault rupture showing one month of postseismic deformation. The sense of the postseismic LOS displacements is reversed to the right-lateral coseismic displacements (Figure 7-8b). The postseismic deformation is analyzed and discussed in detail in the next chapter.

7.6 Future Improvements

There are a number of possibilities to extend this study to get a better estimate for the fault geometry and slip distribution of these two earthquakes. The InSAR data could be analyzed again using a higher resolution DEM providing higher resolution interferograms with more complete data coverage near the two faults. It is also possible to use more interferograms. A few of the coseismic interferograms had patchy coherence and were not used in this study. However, it is possible to include these data without unwrapping, e.g., by using phase gradients [*Sandwell and Price,* 1998].

The radar data can be used to measure horizontal ground displacements parallel to the satellite flying direction (azimuth offsets) like *Jónsson et al.* [2002a] did for the Hector Mine earthquake. Although these data are noisy they can provide important information about

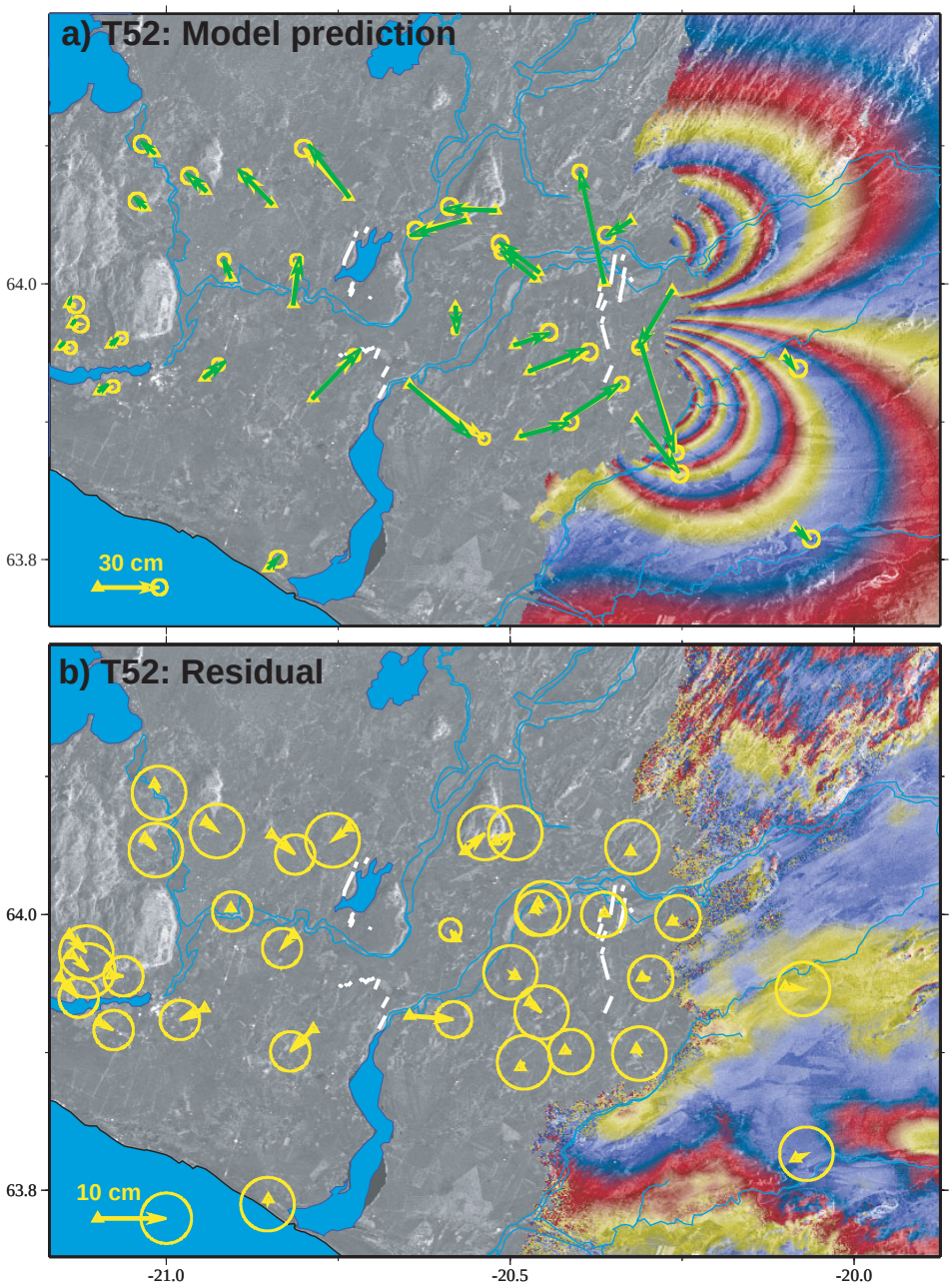

Figure 7-7: Model prediction and residual for the T52 interferogram (Figure 7-2a). Also shown in (a) are the observed (yellow) and predicted (green) GPS displacements and in (b) the residual GPS displacements. Note different scales for GPS displacements in (a) and (b). Error ellipses show 95% confidence level.

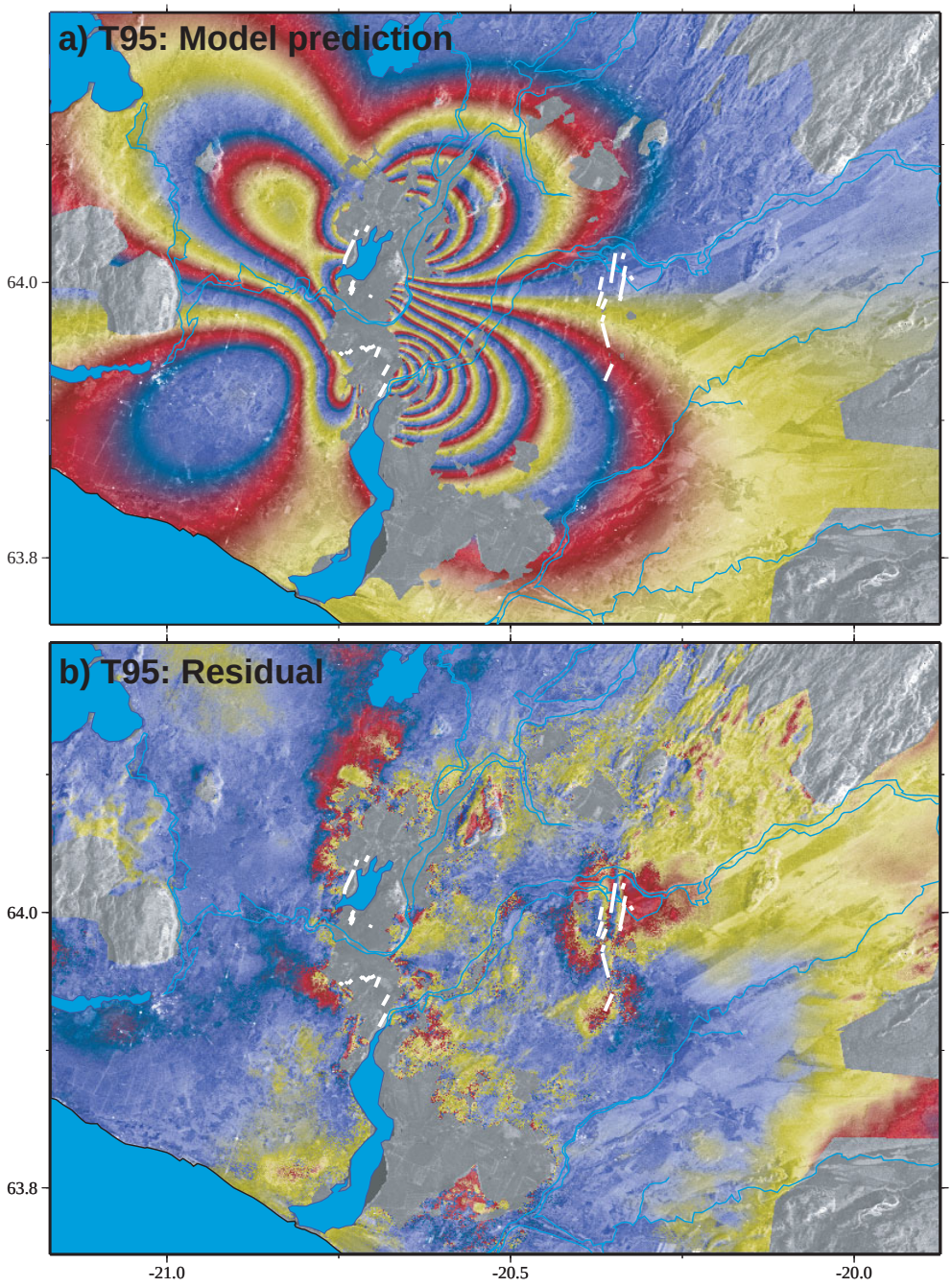

Figure 7-8: Model prediction and residual for the T95 interferogram (Figure 7-2b).

displacements close to the fault ruptures and constrain the fault location at the surface.

Volumetric strain data exist from a few stations in the area. These data could further constrain the fault parameters if included in the inversion. However, they were not available at the time of writing. Relocation of aftershocks will provide tighter bounds on the fault planes that ruptured in the earthquakes and may reveal that the fault geometry is more complex than single straight faults. Finally, combining all available geodetic data and seismic waveform data would not only provide better information about the faults and the fault slip, but can also give information about the rupture history [e.g., *Hernandez et al.,* 1999].

7.7 Conclusions

We have used both InSAR and GPS measurements to estimate the fault location, geometry, and variable slip for the two June 2000, South Iceland earthquakes. The main results of our study are the following:

1. The earthquakes occurred on two parallel and near vertical N-S faults located 18 km apart.

2. Both earthquakes were predominantly right-lateral strike-slip events with small amount of dip-slip (east side up). However, the amount of dip-slip is not significant at a 95% confidence level.

3. The fault ruptured on June 21 was longer ($\sim$17 km) than the June 17 fault ($\sim$14 km).

4. The maximum slip in the June 21 earthquake was $\sim$3 m occurring at 4-5 km depth on the northern part of the fault. Fault slip extended deeper on the southern part of the fault ($\sim$9 km) than on the northern part.

5. The maximum slip on the June 17 fault was probably smaller than on the June 21 fault, or around 2.5 m.

6. The estimated fault slip moments are 4.7×10^{18} Nm and 4.9×10^{18} Nm for the June 17 and June 21 earthquakes, respectively, assuming Poisson's ratio $\nu_u = 0.31$ and shear modulus of $\mu = 30$ GPa. These moments indicate that both earthquakes were of magnitude $M_w = 6.4$.

Our results will provide information for future studies that take on many interesting questions, such as: How did the two earthquakes change the stress field in the SISZ? Did the June 17 earthquake trigger the June 21 earthquake? And if so, why did 3.5 days pass between the two events? Are any other faults in the area where Coulomb stress was significantly increased by these quakes?

Chapter 8

Poro-elastic Rebound after the two June 2000 South Iceland Earthquakes: Implications for Aftershock Decay

In previous two chapters we studied the coseismic deformation due to the 1999 Hector Mine earthquake and due to two south Iceland earthquakes that occurred in June of 2000. We used InSAR and GPS observations of the coseismic deformation to estimate the fault geometries and slip distributions involved in these events. Here we take on the postseismic deformation observed after the two south Iceland earthquakes. The postseismic signal shows a pattern similar to the coseismic deformation, but it is much weaker and opposite in sign. We test several potential mechanisms that could be responsible for the deformation, such as afterslip on the coseismic fault, viscoelastic relaxation of the lower crust, and poro-elastic rebound. We conclude that the deformation is caused by poro-elastic rebound during pore-pressure re-adjustment following the earthquakes. The deformation transient lasts only 1-2 months while aftershocks are projected to last for 3-4 years, which implies that pore-pressures may not control the aftershock activity.

8.1 Abstract

Earthquakes interact elastically with one another, as is amply demonstrated by the occurrence of aftershocks. Despite considerable research, it is still not clear what controls the timing of triggered events. Time dependent postseismic processes can be related to (1) afterslip on the mainshock rupture [*Bechor et al.,* 2001], (2) viscous flow of the lower crust and upper mantle [*Pollitz et al.,* 2001], (3) pore-fluid flow in the upper crust [*Nur and Booker,* 1972], and (4) a delayed response of the triggered fault as predicted by rate and state friction

[*Dieterich,* 1994]. Here we present a case where it is possible to distinguish between these processes that may help answering what controls aftershock decay. We find that observed postseismic deformation after two M_w6.5 South Iceland earthquakes is neither due to afterslip nor visco-elastic relaxation, but is consistent with poro-elastic rebound of the crust near the faults, an interpretation that is further supported by water level measurements in numerous geothermal wells in the area. However, the duration of aftershocks, projected to be 3-4 years, is much longer than the two-month long duration of the poro-elastic deformation. Thus, although poro-elastic effects dominate the observed postseismic deformation, the decay of aftershocks is better explained by rate and state processes on receiver faults, a model that predicts 2.5-10 years aftershock duration for these earthquakes.

8.2 Introduction

South Iceland has suffered from many large earthquakes since settlement began in the 9th century AD. Although historical accounts are not complete, more than 30 earthquakes caused documented damage in the area [*Einarsson and Eiríksson,* 1982]. This earthquake prone region, called the South Iceland Seismic Zone (SISZ), is a left-lateral transform zone connecting two sections of the Mid-Atlantic plate boundary in Iceland (Figure 8-1). The area does not have one major transform fault, like typical Mid-Ocean Ridge transform zones, but instead the East-West left-lateral transform motion is accommodated by many parallel North-South oriented right-lateral faults [*Einarsson,* 1991; *Sigmundsson et al.,* 1995].

The June 2000 earthquakes ruptured two of the parallel N-S faults, separated by 17 km [*Pedersen et al.,* 2001 and 2002; *Árnadóttir et al.,* 2001] (Figure 8-1). The earthquakes hit on June 17th and 21st after a relatively quiet period that followed the last major earthquake in 1912. Although the 1912 earthquake was a single event, several large earthquakes typically cluster in time. For example, five large earthquakes occurred during a period of only two weeks in 1896 [*Einarsson et al.,* 1981]. Historical accounts indicate that the recurrence interval of these sequences of large earthquakes is 45-112 years [*Einarsson et al.,* 1981].

8.3 Observed Postseismic Deformation

Satellite radar interferograms of the SISZ exhibit several centimeters of postseismic ground deformation near the June 2000 fault ruptures (Figure 8-2). An interferogram spanning

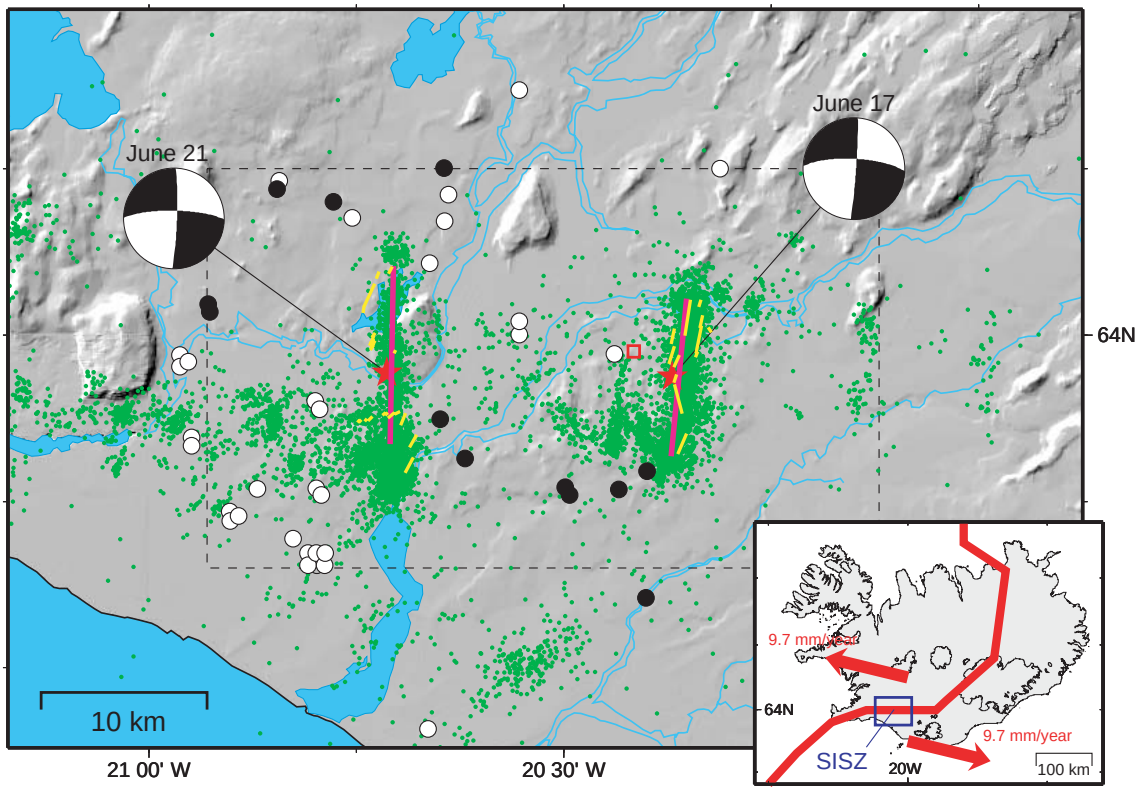

Figure 8-1: Map showing the location of the two June 2000 (M_w6.5) earthquakes in South Iceland. Inset shows the approximate location of Mid-Atlantic plate boundary in Iceland, which has a full spreading rate of 1.94 cm/year [*DeMets et al.,* 1990]. The South Iceland Seismic Zone (SISZ) is an East-West oriented left-lateral transform zone (small box marks area shown in detail). The map shows mainshock epicenters (red stars) and focal mechanisms (Harvard CMT), aftershocks (green dots), mapped surface ruptures [*Clifton and Einarsson,* 2000] (yellow lines), fault upper edges as estimated from coseismic deformation data (purple lines), and strain meter station SAU (red square). Also shown is the June 21 coseismic water-level increase (black dots) and decrease (white dots) in geothermal wells in the area [*Björnsson et al.,* 2001]. Dashed rectangle marks the area shown in Figure 8-2.

the time interval from June 19 (between the two earthquakes) to July 24 shows a localized postseismic deformation pattern near the June 17 rupture after the coseismic deformation of the June 21 earthquake has been removed using modeled displacements [*Pedersen et al.,* 2001; 2002] (Figure 8-2a). The sense of the observed postseismic motion is opposite to the right-lateral coseismic motion. The ground moved up (into line-of-sight (LOS) towards the satellite radar) in quadrants of coseismic extension (NE and SW of the fault) and down in quadrants of coseismic compression (NW and SE of the fault). The maximum LOS displacement (-3.5 cm) is observed NW of the fault while other quadrants exhibit smaller signal, especially the two quadrants to the south.

Two other postseismic interferograms, one spanning 70 days from June 21 (acquired 22 hours after the June 21 earthquake) to August 30 (not shown) and another spanning 35 days from June 24 to July 29 (shown in Figure 8-2b), exhibit similar deformation near the June 17 rupture as the interferogram in Figure 8-2a, except insignificant deformation is observed near the south end of the fault. Additionally, these interferograms provide postseismic data near the June 21 rupture where LOS subsidence and uplift are observed NW and NE of the fault, respectively, but only LOS subsidence near the south end of the fault.

The postseismic deformation near the faults was a transient that only lasted for 7-8 weeks as a fourth interferogram, spanning 35 days from August 12 to September 16 shows little or no significant deformation in the area (Figure 8-2e). LOS displacement profiles across the northern part of the faults show that deformation slowed down with time, consistent with exponential decay time of 16 days.

8.4 Mechanisms for postseismic Deformation

Postseismic deformation is usually associated with one, two, or all three of the following mechanisms: (1) Postseismic creep (or afterslip) on the mainshock source fault or on a downward extension of the fault. An example is the 1999 Chi-Chi earthquake where afterslip models explain the bulk of the postseismic deformation [*Bechor et al.,* 2001]. (2) Postseismic flow in the lower crust and upper mantle driven by stresses induced by the mainshock (visco-elastic relaxation). The deformation observed after the 1999 Hector Mine, Southern California, earthquake is found to be consistent with this mechanism [*Pollitz et al.,* 2001]. (3) Poro-elastic rebound due to pore-fluid flow after pore-pressure changes caused by the mainshock. Observed deformation in fault step-overs after the 1992 Landers, Southern

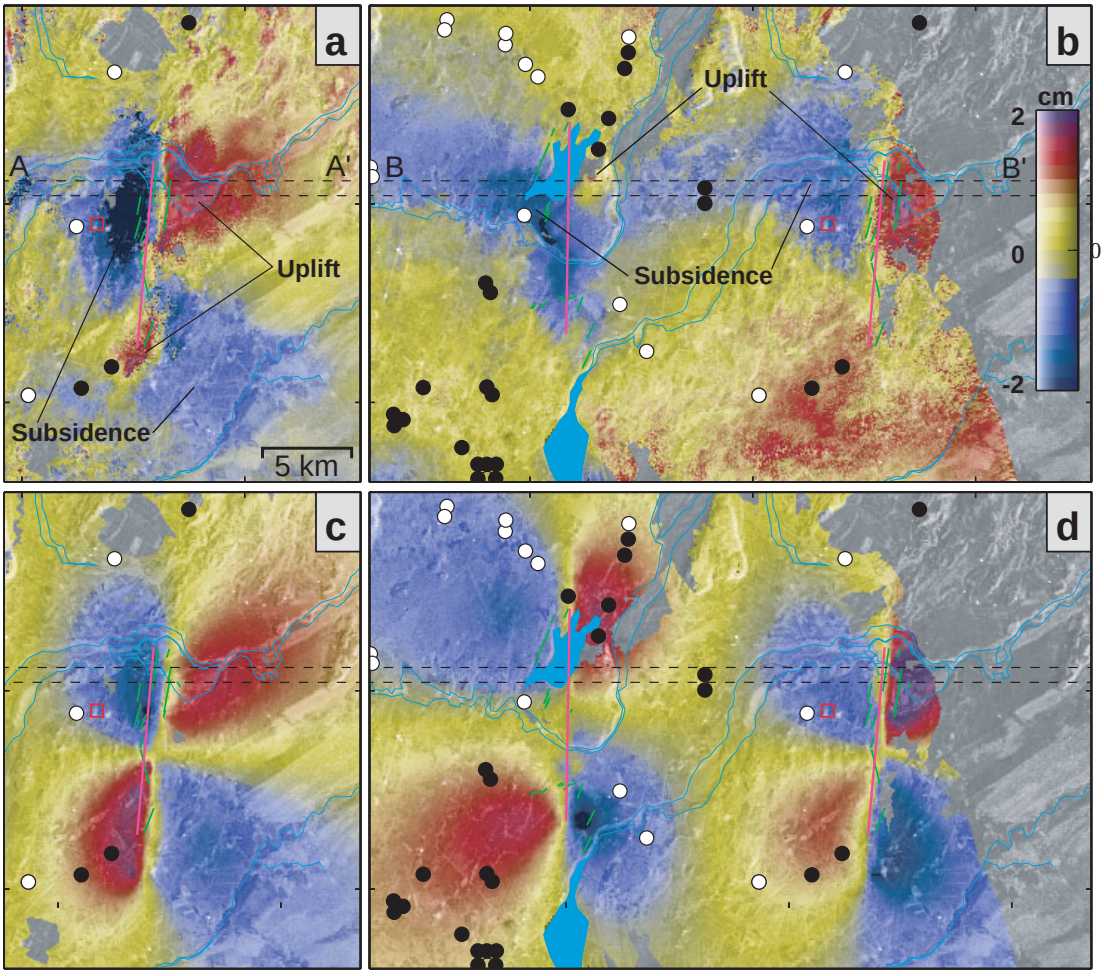

Figure 8-2: Synthetic Aperture Radar Interferograms (InSAR) showing postseismic deformation in South Iceland. The interferograms are unwrapped [Chen and Zebker, 2001] and show ground displacements in the line-of-sight (LOS) towards the European radar satellite ERS-2. The measurement is most sensitive to vertical ground motion as the LOS vectors are roughly [East, North, Up]=[0.35, -0.10, 0.93] for image (a) acquired from a descending orbit and [-0.41, -0.11, 0.90] for image (b) from an ascending orbit. The postseismic interferograms span (a) June 19 to July 24 and (b) June 24 to July 29. Also shown are the mapped fault ruptures (green lines), estimated fault locations (purple lines), strain meter SAU (square), and postseismic water-level increase (black dots) and decrease (white dots) after June 21. (c-d) Simulated interferograms of postseismic deformation predicted by a poro-elastic model using undrained Poisson ratio 0.31 and a drained Poisson ratio of 0.27.

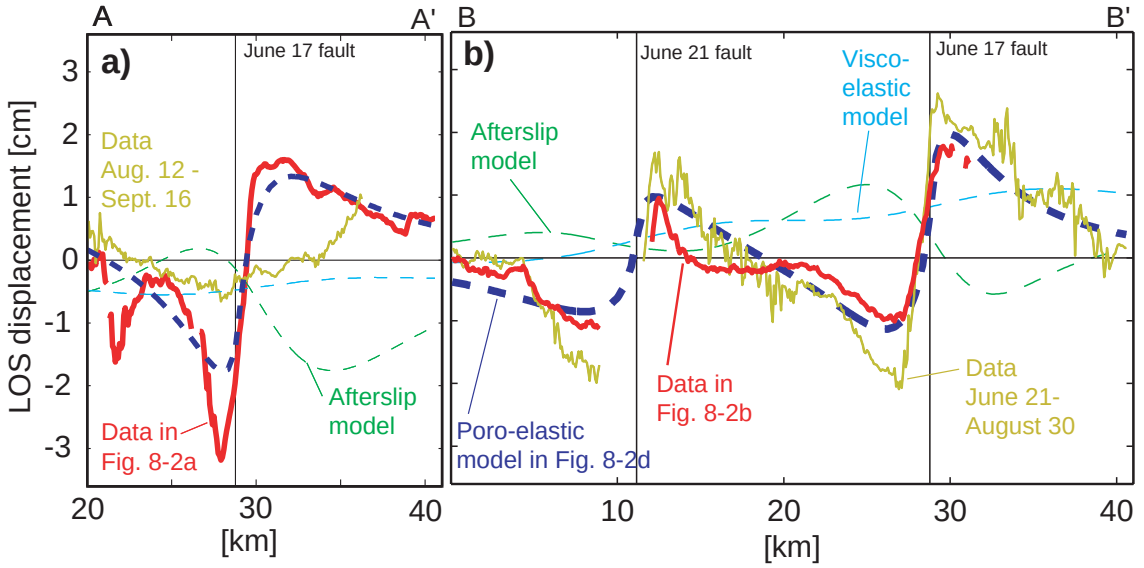

Figure 8-3: LOS displacements along profile A-A' and B-B' in Figure 8-2 as well as LOS profiles from two other interferograms (not shown) spanning the time intervals from June 21 to August 30 and August 12 to September 16. LOS profiles as predicted by the poro-elastic model, an afterslip model, and a visco-elastic model ($\eta = 10^{17}$ Pa·s) are also shown.

California, earthquake was explained by this mechanism [*Peltzer et al.,* 1998]. The South Iceland postseismic deformation is consistent with poro-elastic rebound but inconsistent with both afterslip and visco-elastic relaxation, below we explain why.

The sense of the observed postseismic motion is opposite to the right-lateral coseismic motion; hence, to explain the data with an afterslip model, left-lateral fault slip (backslip) is needed. Although the June 21 earthquake caused stress changes in the area, these changes do not favor backslip on the June 17 fault. In addition, to match the observed deformation data, backslip models require a significant vertical slip component on the near vertical faults, which is neither observed nor likely. Therefore, we rule out afterslip and backslip as possible mechanisms for the observed postseismic deformation in South Iceland.

Viscous flow of the lower crust and upper mantle is also not a plausible explanation for the observed postseismic deformation because of two main reasons. Firstly, the short time duration of the deformation transient requires viscosity of the order of 10^{17} Pa·s (relaxation time of 2-3 weeks), which is much lower than viscosity estimates for the lower crust and upper mantle in Iceland, which range from 1×10^{18} to 5×10^{19} Pa·s [*Sigmundsson,* 1991; *Sigmundsson and Einarsson,* 1992; *Pollitz and Sacks,* 1996; *Hofton and Foulger,* 1996]. The

second argument against this mechanism is the limited spatial extent of the postseismic deformation, all of which is observed within 5-10 km from the faults. Viscous flow under 8-10 km thick brittle crust causes spatially more extensive ground deformation (Figure 8-3).

Large earthquakes cause pore pressure increases in areas of compression and pore pressure decrease where dilation occurs [*Nur and Booker,* 1972; *Björnsson et al.,* 2001; *Chia et al.,* 2001]. Consequently, groundwater flows from areas of increased pore pressure to areas of lower pressure or pore-pressure changes dissipate by vertical flow [*Roeloffs,* 1996]. The ground deforms in response to these postseismic pore-fluid pressure changes. The poro-elastic rebound results in subsidence in coseismic compressional quadrants and uplift in coseismic extensional quadrants. A poro-elastic model for two right-lateral strike slip faults predicts a quadrantal deformation pattern that is similar to the observed postseismic deformation (Figure 8-2). We assume the rocks become fully drained during the time between the earthquake and the observations. In this model we used the fault slip distribution of the two earthquakes (see Figure 7-5) with undrained and drained poisson ratio of $\nu_u = 0.31$ and $\nu = 0.27$, respectively [*Rice and Cleary,* 1976; *Peltzer et al.,* 1998; *Wang,* 2001]. While the modeled displacements do not match the observations perfectly, the main features are similar, with subsidence NW of the faults and uplift NE of them (Figures 8-2 and 8-3). The main difference is near the south end of both faults. Near the southern end of the June 17 fault we observe little deformation indicating weak rebound or rebound so fast that it was not detected. Near the southern end of the June 21 fault we observe only subsidence in an area where the most complex surface faulting occurred (Figure 8-2b). Along with the N-S right-lateral faulting, a conjugate E-W oriented left-lateral faulting took place here [*Clifton and Einarsson,* 2000] while the poro-elastic model is only based on a single vertical N-S fault.

Our poro-elastic interpretation is supported by water level changes observed in numerous geothermal boreholes throughout the region. The sign of the coseismic water level changes exhibits a quadrantal pattern consistent with the predicted undrained response [*Björnsson et al.,* 2001] (Figure 8-4a). While the postseismic behavior varies from well to well, the duration of the water level recovery of many wells is 1-2 months (Figure 8-4), consistent with the duration of the deformation transient. Interestingly, the two wells located just south of the June 17 fault show faster water level recovery due to highly permeable rocks [*Björnsson et al.,* 2001] (see well HR in Figure 8-4). This is consistent with the weak deformation signal observed in this area as most of the rebound probably occurred during

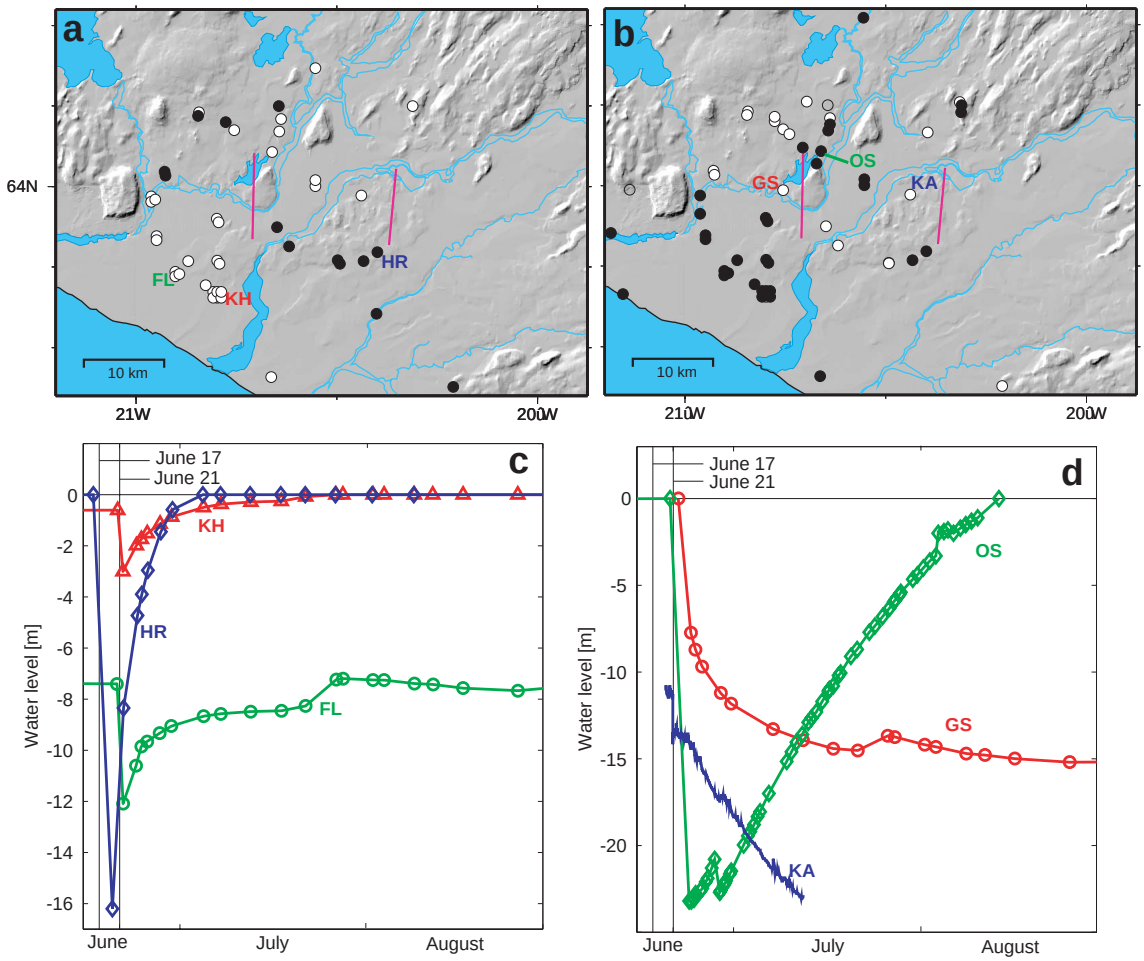

Figure 8-4: Water level changes in geothermal wells in South Iceland. (a) The June 21 coseismic water level increase (black dots) and decrease (white dots), and (b) the postseismic water level changes after June 21. (c-d) Water level change in several wells showing water level recovery of 1-2 months. Wells KA and GS are located in coseismic compressional quadrants and experience postseismic water level decline, while wells KH, FL, OS, and HR are located in coseismic extensional quadrants and exhibit postseismic water-level increase. Note the rapid water level recovery of well HR, located just south of the June 17 fault.

the first few days after the earthquake, and thus were not captured by the interferograms. In addition to the water level data, a volumetric strain meter, located ∼2 km west of the June 17 fault (Figure 8-2a), exhibits a month long extensional transient, which is consistent with our observations and further supports our interpretation [*Kristján Ágústsson, pers. comm.,* 2002].

8.5 Implications for Aftershock Decay

We next test whether the aftershock decay follows the predicted changes in effective stress, induced by poro-elastic effects. Off-fault aftershocks preferentially occur in quadrants that experienced coseismic unclamping on N-S oriented faults and postseismic pore-pressure increase, i.e., NE and SW of the faults (Figure 8-1). However the duration of the aftershock sequence is much longer than the duration of the pore-pressure transients. Extrapolation of the ongoing Omori-like decay predicts an aftershock duration of 3-4 years (Figure 8-5). Therefore, the aftershock decay cannot be controlled by pore-pressure changes near the faults.

Rate of earthquake activity can be modeled as dependent on some stressing history, e.g., a step-like stress change due to a large earthquake. One such model has been implemented using solutions for nucleation of unstable fault slip on faults with rate- and state-dependent fault properties [*Dieterich,* 1994]. This model predicts an aftershock duration t_a that is proportional to average recurrence interval t_r, but also depends on effective normal stress σ and earthquake stress drop $\Delta\tau$:

$$t_a = t_r \frac{A\sigma}{-\Delta\tau} \tag{8.1}$$

where A is an experimentally determined fault constitutive parameter (0.005-0.02 for most rocks) [*Dieterich,* 1994]. For the SISZ, where similar events recur roughly every 100 years, this model predicts an aftershock duration of 2.5-10 years (using typical values for $-\Delta\tau/A\sigma$ of 10-40), which is in good accord with the observed aftershock decay. We thus conclude that although poro-elastic rebound dominates the observed postseismic deformation, the duration of the aftershock sequence is better explained by rate- and state-dependent processes acting at "receiver faults" rather than by poro-elastic changes in effective stress.

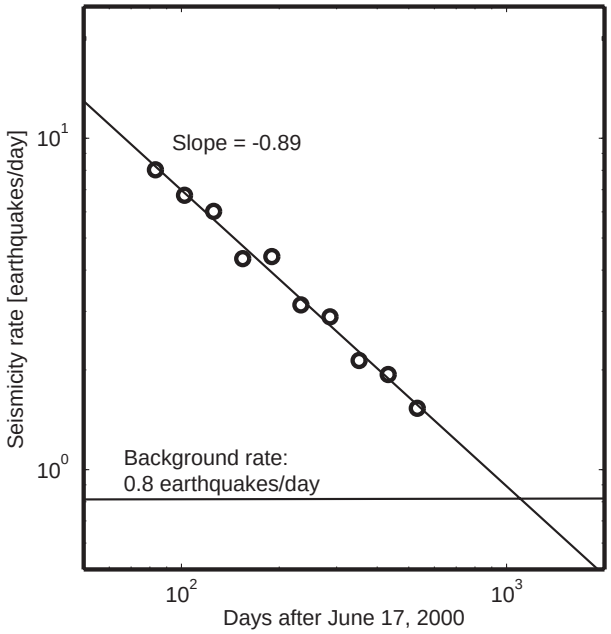

Figure 8-5: Aftershock decay after the south Iceland earthquakes. The decay follows a power-law with a slope of -0.89. Extrapolation of the ongoing aftershock sequence predicts a total duration of 3-4 years.

Chapter 9

Bibliography

Agnew, D. C., S. Owen, Z.-K. Shen, G. Anderson, J. Svarc, H. Johnson, K. E. Austin, and R. Reilinger (2002), Coseismic displacements from the Hector Mine, California, earthquake: results from survey-mode GPS measurements, *Bull. Seismol. Soc. Am.,* **92**, (in press).

Allen, J. F., and T. Simkin (2000), Fernandina Volcano's evolved, well-mixed basalts: Mineralogical and petrological constraints on the nature of the Galápagos plume, *J. Geophys. Res.,* **105**, 6017-6041.

Amelung, F., S. Jónsson, H. Zebker, and P. Segall (2000a), Widespread uplift and trapdoor faulting on Galápagos volcanoes observed with radar interferometry, *Nature*, **407**, 993-996.

Amelung, F., C. Oppenheimer, P. Segall, and H. Zebker (2000b), Ground deformation near Gada 'Ale volcano, Afar, observed by radar interferometry, *Geophys. Res. Lett.,* **27**, 3093-3096.

Árnadóttir, T., P. Segall, and M. Matthews (1992), Resolving the discrepancy between geodetic and seismic fault models for the 1989 Loma Prieta, California, earthquake, *Bull. Seismol. Soc. Am.,* **82**, 2248-2255.

Árnadóttir, T., S. Hreinsdóttir, G. Gudmundsson, P. Einarsson, M. Heinert, and C. Völksen (2001), Crustal deformation measured by GPS in the South Iceland Seismic Zone due to two large earthquakes in June 2000, *Geophys. Res. Lett.,* **28**, 4031-4033.

Avallone, A., A. Zollo, P. Briole, C. Delacourt, and F. Beauducel (1999), Subsidence of Campi Flegrei (Italy) detected by SAR interferometry, *Geophys. Res. Lett.,* **26**, 2303-2306.

Beauducel F., P. Briole, and J.-L. Froger (2000), Volcano wide fringes in ERS SAR interferograms of Etna: Deformation or tropospheric effect? *J. Geophys. Res.,* **105**, 16,391-16,402.

Bechor, N., P. Segall, Y. Hsu, J. McGuire, and S. Yu (2001), Time-depended inversion for post-seismic slip following the 1999 Chi-Chi Taiwan earthquake using GPS observations, *Eos Trans. AGU,* **82(47)**, Fall Meet. Suppl., Abstract G22D-01.

Bjarnason, I. Th., and P. Einarsson (1991), Source mechanism of the 1987 Vatnafjöll earthquake in south Iceland, *J. Geophys. Res.,* **96,** 4313-4324.

Björnsson, G., Ó. G. Flóvenz, K. Saemundsson, and E. H. Einarsson (2001), Pressure changes in Icelandic geothermal reservoirs associated with two large earthquakes in June 2000, *Proc. to 26th workshop on Geothermal Reservoir Engin.*, **SGP-TR-168**.

Bonafede, M., and M. Mazzanti (1998), Modelling gravity variations consistent with ground deformation in the Campi Flegrei caldera (Italy), *J. Volcanol. Geotherm. Res.,* **81**, 137-157.

Bracewell, R. N. (1995), *Two-Dimensional imaging*, Prentice Hall, Englewood Cliffs, New Jersey, 689 pp.

Briole, P., D. Massonnet, and C. Delacourt (1997), Post-eruptive deformation associated with the 1986-87 and 1989 lava flows on Etna detected by radar interferometry, *Geophys. Res. Lett.,* **24**, 37-40.

Bürgmann, R., D. Schmidt, R. M. Nadeau, M. d'Alessio, E. Fielding, D. Manaker, T. V. McEvilly, and M. H. Murray (2000), Earthquake potential along the northern Hayward fault, California, *Science*, **289**, 1178-1182.

Bürgmann R., M. E. Ayhan, E. J. Fielding, T. J. Wright, S. McClusky, B. Aktug, C. Demir, O. Lenk, and A. Türkezer (2002), Deformation during the 12 November 1999 Düzce, Turkey, earthquake from GPS and InSAR data, *Bull. Seismol. Soc. Am.,* **92**, 161-171.

Cervelli, P., M. H. Murray, P. Segall, P., Y. Aoki, and T. Kato (2001), Estimating source parameters from deformation data, with an application to the March 1997 earthquake swarm off the Izu Peninsula, Japan, *J. Geophys. Res.,* **106**, 11,217-11,238.

Chadwick Jr, W. W., and K. A. Howard (1991), The pattern of circumferential and radial eruptive fissures on the volcanoes of Fernandina and Isabela islands, Galapagos, *Bull. Volcanol.,* **53**, 259-275.

Chadwick Jr, W. W., T. De Roy, and A. Carrasco (1991), The September 1988 intracaldera avalanche and eruption at Fernandina volcano, Galapagos Islands, *Bull. Volcanol.,* **53**, 276-286.

Chadwick Jr, W. W., and J. H. Dieterich (1995), Mechanical modeling of circumferential and radial dike intrusion on Galapagos volcanoes, *J. Volcanol. Geotherm. Res.,* **66**, 37-52.

Chen, C. W., and H. A. Zebker (2001), Two-dimensional phase unwrapping with use of statistical models for cost functions in nonlinear optimization, *J. Opt. Soc. Am.*, **18**, 338-351.

Chia, Y., Y.-S. Wang, J. J. Chiu, and C.-W. Liu (2001), Changes of groundwater level due to the 1999 Chi-Chi earthquake in the Choshui river alluvial fan in Taiwan, *Bull. Seismol. Soc. Am.,* **91**, 1062-1068.

Clifton, A., and P. Einarsson (2000), Styles of surface rupture accompanying the June 17 and 21, 2000 earthquakes in the South Iceland Seismic Zone (abstract), Geosci. Soc. of Iceland Autumn meeting, 1.

Delacourt, C., P. Briole, and J. Achache (1998), Troposhheric corrections of SAR interferograms with strong topography: Application to Etna, *Geophys. Res. Lett.,* **25,** 2849-2852.

DeMets, C., R. G. Gordon, D. F. Argus, and S. Stein (1990), Current plate motions, *Geophys. J. Int.,* **101**, 425-478.

Deng, J., M. Gurnis, H. Kanamori, and E. Hauksson (1998), Viscoelastic flow in the lower crust after the 1992 Landers, California, earthquake, *Science*, **282**, 1689-1692.

Dieterich, J. (1994), A constitutive law for rate of earthquake production and its application to earthquake clustering. *J. Geophys. Res.,* **99**, 2601-2618.

Dreger, D., and A. Kaverina (2000), Seismic remote sensing for the earthquake source process and near-source strong shaking: a case study of the October 16, 1999 Hector Mine earthquake, *Geophys. Res. Lett.,* **27** 1941-1944.

Dvorak, J. J., and D. Dzurisin (1997), Volcano geodesy: the search for magma reservoirs and the formation of eruptive vents. *Rev. Geophys.,* **35**, 343-384.

Efron, B., and R. J. Tibshirani (1993), *An introduction to the bootstrap*, Monogr. on Stat. and Appl. Probab. **57**, Chapman & Hill, New York, 436 pp.

Einarsson, P., S. Björnsson, F. Foulger, R. Stefánsson, and Th. Skaftadóttir (1981), Seismicity pattern in the south Iceland seismic zone. In: *Earthquake prediction - an international review*, D. W. Simpson and P. G. Richards (editors), American Geophysical Union, **4**, 141-151.

Einarsson, P., and F. Eiríksson (1982), Earthquake fractures in the districts Land and Rangárvellir in the South Iceland Seismic Zone, *Jökull,* **32**, 113-119.

Einarsson, P. (1991), Earthquakes and present-day tectonism in Iceland, *Tectonophysics,* **189**, 261-279.

Feigl, K., A. Sergent, and D. Jacq (1995), Estimation of an earthquake focal mechanism from a satellite radar interferogram: Application to the December 4, 1992 Landers aftershock, *Geophys. Res. Lett.,* **22**, 1037-1040.

Feigl, K., J. Gasperi, F. Sigmundsson, and A. Rigo (2000), Crustal deformation near Hengill volcano, Iceland 1993-1998: Coupling between magmatic activity and faulting inferred from elastic modelling of satellite radar interferograms, *J. Geophys. Res.,* **105**, 25,655-25,670.

Feigl, K. L., F. Sarti, H. Vadon, S. McClusky, S. Ergintav, P. Durand, R. Bürgmann, A. Rigo, D. Massonnet, and R. Reilinger (2002), Estimating slip distribution for the Izmit mainshock from coseismic GPS, RADARSAT, ERS-1, and SPOT measurements, *Bull. Seismol. Soc. Am.,* **92**, 138-160.

Fialko, Y. (2001), On origin of near-axis volcanism and faulting at fast spreading mid-ocean ridges, *Earth Planet. Sci. Lett.,* **190**, 31-39.

Fialko, Y., and M. Simons (2001), Evidence for on-going inflation of the Socorro magma body, New Mexico, from interferometric synthetic aperture radar imaging, *Geophys. Res. Lett.,* **28,** 3549-3552.

Fialko, Y., M. Simons, and D. Agnew (2001), The complete (3-D) surface displacement field in the epicentral area of the 1999 M_w7.1 Hector Mine earthquake, California, from space geodetic observations, *Geophys. Res. Lett.,* **28**, 3063-3066.

Freed, A. M., and J. Lin (2001), Delayed triggering of the 1999 Hector Mine earthquake by viscoelastic stress transfer, *Nature*, **411**, 180-183.

Fruneau, B., E. Pathier, D. Raymond, B. Deffontaines, C. T. Lee, H. T. Wang, J. Angelier, J. P. Rudant, and C. P. Chang (2001), Uplift of Tainan tableland (SW Taiwan) revealed by SAR interferometry, *Geophys. Res. Lett.,* **28**, 3071-3074.

Fujiwara, S., H. Yarai, S. Ozawa, M. Tobita, M. Murakami, H. Nakagawa, K. Nitta, P. A. Rosen, C. L. Werner (1998), Surface displacement of the March 26, 1997, Kagoshima-ken-hokuseibu earthquake in Japan from synthetic aperture radar interferometry, *Geophys. Res. Lett.,* **25**, 4541-4544.

Geist D., K. A. Howard, A. M. Jellinek, and S. Rayder (1994), The volcanic history of Volcán Alcedo, Galápagos archipelago: A case study of rhyolitic oceanic volcanism, *Bull. Volcanol.,* **56**, 243-260.

Geist, D., T. Naumann, P. Larson (1998), Evolution of Galápagos magmas: Mantle and crustal level fractionation without assimilation, *J. Petrol.*, **39**, 953-971.

Global Volcanism Network (1995), Smithsonian Inst. Bull., **20(1-3, 5, 8)**.

Goldstein R. M., H. A. Zebker, and C. Werner (1988), Satellite radar interferometry: Two-dimensional phase unwrapping, *Radio Sci.,* **23**, 713-720.

Goldstein, R. (1995), Atmospheric limitations to repeat-track radar interferometry, *Geophys. Res. Lett.,* **22**, 2517-2520.

Gudmundsson M. T. H. Björnsson, and F. Pálsson (1995), Changes in jökulhlaup sizes in Grímsvötn, Vatnajökull, Iceland, 1934-91, deduced from in-situ measurements of subglacial lake volume, *J. Glaciol.,* **41**, 263-272.

Gudmundsson M. T. F. Sigmundsson, and H. Björnsson (1997), Ice-volcano interaction of the 1995 Gjálp subglacial eruption, Vatnajökull, Iceland, *Nature,* **389**, 954-957.

Hanssen, R. F., T. M. Weckwerth, H. A. Zebker, and R. Klees (1999), High-resolution water vapor mapping from interferometric radar measurements, *Science*, **283**, 1297-1299.

Hanssen, R. (2001), *Radar interferometry - data interpretation and error analysis*, Kluwer Academic Press, Dordrecht, The Netherlands, 308 pp.

Hauksson, E., L. M. Jones, and K. Hutton (2002), The 1999 Mw7.1 Hector Mine earthquake sequence: complex conjugate strike-slip faulting, *Bull. Seismol. Soc. Am.,* **92**, (in press).

Henriot, O., T. Villemin, and F. Jouanne (2001), Long period interferogram reveal 1992-1998 steady rate of deformation at Krafla volcano (North Iceland), *Geophys. Res. Lett.,* **28**, 1067-1070.

Hernandez, B., F. Cotton, and M. Campillo (1999), Contribution of radar interferometry to a two-step inversion of the kinematic process of the 1992 Landers earthquake, *J. Geophys. Res.,* **104**, 13,083-13,099.

Hofton M., and G. R. Foulger (1996), Postrifting anelastic deformation around the spreading plate boundary, north Iceland: 1. Modeling of the 1987-1992 deformation field using a visco-elastic earth structure, *J. Geophys. Res.,* **101**, 25,403-25,421.

Hurst, K. J., D. Argus, A. Donnellan, M. Heflin, D. Jefferson, G. Lyzenga, J. Parker, M. Smith, F. Webb, and J. Zumberge (2000), The coseismic geodetic signature of the 1999 Hector Mine earthquake, *Geophys. Res. Lett.,* **27**, 2733-2736.

Ji, C. (2000), Slip history of 1999 Hector Mine, California earthquake (abstract), *Seismol. Res. Lett.,* **71**, 224.

Jónsson, S., P. Einarsson, and F. Sigmundsson (1997), Extension across a divergent plate

boundary, the Eastern Volcanic Rift Zone, south Iceland, 1967-1994, observed with GPS and electronic distance measurements, *J. Geophys. Res.,* **102**, 11913-11929.

Jónsson, S., N. Adam, and H. Björnsson (1998), Effects of subglacial geothermal activity observed by satellite radar interferometry, *Geophys. Res. Lett.,* **25**, 1059-1062.

Jónsson, S., H. Zebker, P. Cervelli, P. Segall, H. Garbeil, P. Mouginis-Mark, and S. Rowland (1999), A shallow-dipping dike fed the 1995 flank eruption at Fernandina volcano, Galapagos, observed with satellite radar interferometry, *Geophys. Res. Lett.,* **26**, 1077-1080.

Jónsson, S., H. Zebker, P. Segall, and F. Amelung (2002a), Fault slip distribution of the 1999 Mw7.1 Hector Mine earthquake, California, estimated from satellite radar and GPS measurements, *Bull. Seismol. Soc. Am.,* **92**, (in press).

Jónsson, S., R. Pedersen, and P. Segall (2002b), What controls aftershock decay? (in preparation).

Kanamori, H., and D. L. Anderson (1975), Theoretical basis of some empirical relations in seismology, *Bull. Seismol. Soc. Am.,* **65**, 1073-1095.

Kaverina, A., D. Dreger, and E. Price (2002), The combined inversion of seismic and geodetic data from the source process of the 16 October 1999 Mw7.1 Hector Mine, California, earthquake, *Bull. Seismol. Soc. Am.,* **92**, (in press).

Lanari, R., P. Lundgren, and E. Sansosti (1998), Dynamic deformation of Etna volcano observed by satellite radar interferometry, *Geophys. Res. Lett.,* **25**, 1541-1544.

Lawson, C. L., and R. J. Hanson (1974), *Solving Least Squares Problems*, Prentice-Hall, Englewood Cliffs, New Jersey, 340 pp.

Lipman, P. W., J. G. Moore, and D. A. Swanson (1981), Bulging of the north flank before the May 18 eruption - geodetic data. In: The 1980 eruptions of Mount St. Helens, Washington, *U.S. Geol. Surv. Prof. Pap.,* **1250**, 143-155.

Lu, Z., R. Fatland, M. Wyss, S. Li, J. Eichelberger, K. Dean, and J. Freymueller (1997), Deformation of New Trident volcano measured by ERS-1 interferometry, Katmai National Park, Alaska, *Geophys. Res. Lett.,* **24,** 695-698.

Lu, Z., and J. Freymueller (1998), Synthetic aperture radar interferometry coherence analysis over Katmai volcano group, Alaska, *J. Geophys. Res.,* **103,** 29,887-29,894.

Lu, Z., D. Mann, and J. Freymueller (1998), Satellite radar interferometry measures deformation at Okmok volcano, *Eos, Transactions,* **79**, 467-468.

Lu, Z., C. Wicks, D. Dzurisin, W. Thatcher, J. Freymueller, S. McNutt, and D. Mann (2000a), Aseismic inflation of Westdahl volcano, Alaska, revealed by satellite radar interferometry, *Geophys. Res. Lett.,* **27,** 1567-1570.

Lu, Z., C. Wicks, J. A. Power, and D. Dzurisin (2000b), Ground deformation associated with the March 1996 earthquake swarm at Akutan volcano, Alaska, revealed by satellite radar interferometry, *J. Geophys. Res.,* **105**, 21,483-21,496.

Lu, Z., D. Mann, J. Freymueller, and D. Meyer (2000c), Synthetic aperture radar interferometry of Okmok volcano, Alaska: Radar observations. *J. Geophys. Res.,* **105,** 10791-10806.

Mann, D., J. Freymueller, and Z. Lu (2002), Deformation associated with the 1997 eruption of Okmok volcano, Alaska, *J. Geophys. Res.,* (in press).

Massonnet, D., M. Rossi, C. Carmona, F. Adragna, G. Peltzer, K. Feigl, and T. Rabaute (1993), The displacement field of the Landers earthquake mapped by radar interferometry, *Nature*, **364**, 138-142.

Massonnet, D., K. Feigl, M. Rossi, and F. Adragna (1994), Radar interferometric mapping of deformation in the year after the Landers earthquake, *Nature*, **369**, 227-230.

Massonnet, D., and K. L. Feigl (1995), Satellite radar interferometric map of the coseismic deformation field of the M=6.1 Eureka Valley, California earthquake of May 17, 1993, *Geophys. Res. Lett.,* **22**, 1541-1544.

Massonnet, D., P. Briole, and A. Arnaud (1995), Deflation of Mount Etna monitored by spaceborne radar interferometry, *Nature*, **375**, 567-570.

Massonnet, D., W. Thatcher, and H. Vadon (1996), Detection of postseismic fault-zone collapse following the Landers earthquake, *Nature*, **382**, 612-616.

Massonnet, D., and K. Feigl (1998), Radar interferometry and its application to changes in the Earth's surface, *Rev. Geophys.,* **35(4)**, 441-500.

Massonnet, D., and F. Sigmundsson (2000), Remote sensing of volcano deformation by radar interferometry from various volcanoes. In: *Remote Sensing of Active Volcanism,* Geophysical Monograph Vol. **116**, 207-221, American Geophysical Union.

Meyer, B., R. Armijo, D. Massonnet, J. B. de Chabalier, C. Delacourt, J. C. Ruegg, J. Achache, P. Briole, and D. Papanastassiou (1996), The 1995 Grevena (northern Greece) earthquake: Fault model constrained with tectonic observations and SAR interferometry, *Geophys. Res. Lett.,* **23,** 2677-2680.

Michel, R., J.-P. Avouac, J. Taboury (1999a), Measuring ground displacements from SAR amplitude images: Application to the Landers earthquake, *Geophys. Res. Lett.,* **26**, 875-878.

Michel, R., J.-P. Avouac, and J. Taboury (1999b), Measuring near field coseismic displacements from SAR images: Application to the Landers earthquake, *Geophys. Res. Lett.,* **26**, 3017-3020.

Mogi, K. (1958), Relations between the eruptions of various volcanoes and the deformation of the ground surface around them. *Bull. Earth. Res. Inst. Univ. Tokyo,* **36**, 99-134.

Mouginis-Mark, P. J., S. K. Rowland, and H. Garbeil (1996), Slopes of western Galapagos volcanoes from airborne interferometric radar. *Geophys. Res. Lett.,* **23**, 3767-3770.

Mouginis-Mark, P. J., H. Snell, and R. Ellisor (2000), GOES satellite observations of the 1998 eruption of Volcan Cerro Azul, Galapagos Islands. *Bull. Volcanol.,* **62**, 188-198.

Munro, D. C., and S. K. Rowland (1996), Caldera morphology in the western Galápagos and implications for volcano eruptive behavior and mechanisms of caldera formation. *J. Volcanol. Geotherm. Res.,* **72**, 85-100.

Murakami, M., M. Tobita, S. Fujiwara, T. Saito, and H. Masaharu (1996), Coseismic crustal deformations of the 1994 Northridge, California, earthquake detected by interferometric JERS 1 synthetic aperture radar, *J. Geophys. Res.,* **101**, 8605-8614.

Murray, J. B. (1988), The influence of loading by lavas on the siting of volcanic eruption vents on Mt Etna. *J. Volcanol. Geotherm. Res.,* **35**, 121-139.

Naumann, T., and D. Geist (2000), Physical volcanology and structural development of Cerro Azul volcano, Isabela island, Galápagos: Implication for the development of Galápagos-type shield volcanoes, *Bull. Volcanol.,* **61**, 497-514.

Newhall, C. G., and D. Dzurisin (1998), Historical unrest at large calderas of the world, *U.S. Geol. Surv. Bull.,* **1855(1)**, 509-520.

Nishimura, T., S. Fujiwara, M. Murakami, M. Tobita, H. Nakagawa, T. Sagiya, and T. Tada (2001), The M6.1 Earthquake triggered by volcanic inflation of Iwate volcano, northern Japan, observed by satellite radar interferometry, *Geophys. Res. Lett.,* **28**, 635-638.

Nur, A., and J. R. Booker (1972), Aftershocks caused by pore fluid flow? *Science,* **175**, 885-887.

Okada, Y. (1985), Surface deformation due to shear and tensile faults in a half-space, *Bull. Seismol. Soc. Am.,* **75**, 1135-1154.

Okada, Y. (1992), Internal deformation due to shear and tensile faults in a half-space, *Bull. Seismol. Soc. Am.,* **82**, 1018-1040.

Ozawa, S., M. Murakami, S. Fujiwara, and M. Tobita, Synthetic aperture radar interferogram of the 1995 Kobe earthquake and its geodetic inversion, *Geophys. Res. Lett.,* **24**, 2327-2330.

Parsons, T., and D. S. Dreger (2000), Static-stress impact of the 1992 Landers earthquake sequence on nucleation and slip at the site of the 1999 M=7.1 Hector Mine earthquake, southern California, *Geophys. Res. Lett.,* **27**, 1949-1952.

Pedersen, R., F. Sigmundsson, K. L. Feigl, and T. Árnadóttir (2001), Coseismic interferograms of two $M_S = 6.6$ earthquakes in the South Iceland Seismic Zone, June 2000. *Geophys. Res. Lett.,* **28**, 3341-3344.

Pedersen, R., S. Jónsson, F. Sigmundsson, and T. Árnadóttir (2002), Fault geometry and fault slip distribution of the two June 2000 $M_S = 6.6$, south Iceland earthquakes, estimated from InSAR and GPS measurements. *J. Geophys. Res.,* (in preparation).

Peltzer, G., and P. Rosen (1995), Surface displacement of the 17 May 1993 Eureka Valley, California, earthquake observed by SAR interferometry, *Science*, **268**, 1333-1336.

Peltzer, G., P. Rosen, F. Rogez, and K. Hudnut (1996), Postseismic rebound in fault stepovers caused by pore fluid flow, *Science*, **273**, 1202-1204.

Peltzer, G., P. Rosen, F. Rogez, and K. Hudnut (1998), Poroelastic rebound along the Landers 1992 earthquake surface rupture, *J. Geophys. Res.,* **103**, 30,131-30,145.

Peltzer, G., F. Crampé, and G. King (1999), Evidence of nonlinear elasticity of the crust from the Mw7.6 Manyi (Tibet) earthquake, *Science*, **286**, 272-276.

Pollitz, F. F., and I. S. Sacks (1996), Viscosity structure beneath northeast Iceland, *J. Geophys. Res.,* **101**, 17771-17793.

Pollitz, F. F., C. Wicks, and W. Thatcher (2001), Mantle flow beneath a continental strike-slip fault: Post-seismic deformation after the 1999 Hector Mine earthquake, *Science,* **293**, 1814-1818.

Reynolds, R. W., and D. J. Geist (1995), Petrology of lavas from Sierra Negra volcano, Isabela island, Galápagos archipelago, *J. Geophys. Res.,* **100**, 24,537-24,553.

Reynolds, R. W., D. Geist, and M. D. Kurz (1995), Physical volcanology and structural development of Sierra Negra volcano, Isabela island, Galápagos archipelago, *GSA Bull.*, **107**, 1398-1410.

Rice, J. R., and M. P. Cleary (1976), Some basic stress diffusion solutions for fluid-saturated elastic porous media with compressible constituents, *Rev. Geophys. Space Sci.,* **14**, 227-241.

Roeloffs, E. A. (1996), Poroelastic techniques in the study of earthquake-related hydrologic phenomena. In R. Dmowska editor: *Advances in Geophysics,* vol. **37**, 133-195, Academic Press, San Diego.

Rosen, P., C. Werner, E. Fielding, S. Hensley, S. Buckley, and P. Vincent (1998), Aseismic creep along the San Andreas fault northwest of Parkfield, California measured by radar interferometry, *Geophys. Res. Lett.,* **25**, 825-828.

Rowland, S. K., and D. C. Munro (1992), The caldera of volcan Fernandina: A remote sensing study of its structure and recent activity, *Bull. Volcanol.,* **55**, 97-109.

Rowland, S., D. C. Munro, and V. Perez-Oviedo (1994), Volcán Ecuador, Galápagos islands: Erosion as a possible mechanism for the generation of steep-sided basaltic volcanoes, *Bull. Volcanol.,* **56**, 271-283.

Rowland, S. K. (1996), Slopes, lava flow volumes, and vent distributions on volcán Fernandina, Galápagos islands, *J. Geophys. Res.,* **101**, 27,657-27,672.

Sandwell, D. T., and E. J. Price (1998), Phase gradient approach to stacking interferograms, *J. Geophys. Res.,* **103**, 30,183-30,204.

Scientists of the U.S. Geological Survey, Southern California Earthquake Center, and California Division of Mines and Geology (2000), Preliminary report on the 10/16/1999 M7.1 Hector Mine, California earthquake, *Seismol. Res. Lett.,* **71**, 11-23.

Sigmundsson, F. (1991), Post-glacial rebound and asthenosphere viscosity in Iceland, *Geophys. Res. Lett.,* **18**, 1131-1134.

Sigmundsson, F., and P. Einarsson (1992), Glacio-isostatic crustal movements caused by historical volume change of the Vatnajokull ice cap, Iceland, *Geophys. Res. Lett.,* **19**, 2123-2126.

Sigmundsson, F., P. Einarsson, R. Bilham, and E. Sturkell (1995), Rift-transform kinematics in south Iceland: Deformation from global positioning system measurements, 1986-1992, *J. Geophys. Res.,* **100**, 6235-6248.

Sigmundsson, F., H. Vadon, and D. Massonnet (1997), Readjustment of the Krafla spreading segment to crustal rifting measured by satellite radar interferometry, *Geophys. Res. Lett.,* **24**, 1843-1846.

Sigmundsson, F., P. Durand, and D. Massonnet (1999), Opening of an eruptive fissure and seaward displacement at Piton de la Fournaise volcano measured by RADARSAT satellite radar interferometry, *Geophys. Res. Lett.,* **26**, 533-536.

Simkin, T., and K. A. Howard (1970), Caldera collapse in the Galápagos islands, 1968, *Science*, **169**, 429-437.

Simkin, T., and L. Siebert (1994), *Volcanoes of the World*, 2nd ed., Geoscience Press, Tucson, Arizona, 349 pp.

Stein, A., F. Van Der Meer, and B. Gorte editors (1999), *Spatial statistics for remote sensing*, Kluwer Academic Press, Dordrecht, The Netherlands, 284 pp.

Stevens, N. F., G. Wadge, C. A. Williams, J. G. Morley, J.-P. Muller, J. B. Murray, and M. Upton (2001) Surface movements of emplaced lava flows measured by SAR interferometry, *J. Geophys. Res.,* **106**, 11293-11315.

Tatarski, V. L. (1961), *Wave propagation in a turbulent medium*, McGraw-Hill, New York, 285 pp.

Thatcher, W., and D. Massonnet (1997), Crustal deformation at Long Valley Caldera, eastern California, 1992-1996 inferred from satellite radar interferometry, *Geophys. Res. Lett.,* **24**, 2519-2522.

Tobita, M., S. Fujiwara, S. Ozawa, R. A. Rosen, E. J. Fielding, C. L. Werner, M. Murakami, H. Nakagawa, K. Nitta, M. Murakami (1998), Deformation of the 1995 north Sakhalin earthquake detected by JERS-1/SAR interferometry, *Earth Planets Space,* **50**, 313-325.

Treuhaft, R. N., and G. E. Lanyi (1987), The effect of the dynamic wet troposphere on radio interferometric measurements, *Radio Sci.,* **22**, 251-265.

Vadon, H., and F. Sigmundsson (1997), Crustal deformation from 1992 to 1995 at the Mid-Atlantic ridge, southwest Iceland, mapped by satellite radar interferometry, *Science*, **275**, 193-197.

Wang, H. F. (2001), *Theory of linear poro-elasticity with applications to geomechanics and hydrogeology,* Princeton Univ. Press, Princeton, New Jersey, 287 pp.

Welstead, S. T. (1999), *Fractal and wavelet image compression techniques*, SPIE Optical Engineering Press, Bellingham, Washington, 232 pp.

Wicks Jr., C., W. Thatcher, and D. Dzurisin (1998), Migration of fluids beneath Yellowstone caldera inferred from satellite radar interferometry, *Science*, **282**, 458-462.

Williams, S., Y. Bock, and P. Fang (1998), Integrated satellite interferometry: Tropospheric noise, GPS estimates and implication for interferometric synthetic aperture radar products, *J. Geophys. Res.,* **103**, 27,051-27,067.

Wooster, M. J., and D. A. Rothery (1997), Time-series analysis of effusive volcanic activity using the ERS along track scanning radiometer: The 1995 eruption of Fernandina volcano, Galápagos islands, *Remote Sens. Environ.*, **62**, 109-117.

Wright, T. J., B. E. Parsons, J. A. Jackson, M. Haynes, E. J. Fielding, P. C. England, P. J. Clarke (1999), Source parameters of the 1 October 1995 Dinar (Turkey) earthquake from SAR interferometry and seismic bodywave modelling, *Earth Planet. Sci. Lett.,* **172**, 23-37.

Wright, T., B. Parsons, and E. Fielding (2001a), Measurement of interseismic strain accumulation across the North Anatolian fault by satellite radar interferometry, *Geophys. Res. Lett.,* **28**, 2117-2120.

Wright, T., E. Fielding, and B. Parsons (2001b), Triggered slip: Observations of the 17 August 1999 Izmit (Turkey) earthquake using radar interferometry, *Geophys. Res. Lett.,* **28**, 1079-1082.

Zebker, H. A., and J. Villasenor (1992a), Decorrelation in interferometric radar echoes, *IEEE Trans. Geosci. Remote Sensing,* **30**, 950-959.

Zebker, H. A., S. N. Madsen, J. Martin, K. B. Wheeler, T. Miller, Y. Lou, G. Alberti, S. Vetrella, and A. Cucci (1992), The TOPSAR interferometric radar topographic mapping instrument, *IEEE Trans. Geosci. Remote Sensing,* **30**, 933-940.

Zebker, H. A., P. A. Rosen, R. M. Goldstein, A. Gabriel, and C. L. Werner (1994), On the derivation of coseismic displacement fields using differential radar interferometry: The Landers earthquake, *J. Geophys. Res.,* **99**, 19,617-19,634.

Zebker, H. A., P. Rosen, S. Hensley, P. Mouginis-Mark (1996), Analysis of active lava flows on Kilauea volcano, Hawaii, using SIR-C radar correlation measurements, *Geology*, **24**, 495-498.

Zebker, H. A., P. A. Rosen, and S. Hensley (1997), Atmospheric effects in interferometric synthetic aperture radar surface deformation and topographic maps, *J. Geophys. Res.,* **102**, 7547-7563.

Zebker, H., and Y. Lu (1998), Phase unwrapping algorithms for radar interferometry: residue-cut, least-squares, and synthesis algorithms, *J. Opt. Soc. Am.*, **16**, 586-598.

Zebker, H. A., F. Amelung, and S. Jónsson (2000), Remote sensing of volcano surface and internal processes using radar interferometry. In: *Remote Sensing of Active Volcanism,* Geophysical Monograph Vol. **116**, 179-205, American Geophysical Union.

Zeng, Y. (2001), Viscoelastic stress-triggering of the 1999 Hector Mine earthquake by the 1992 Landers earthquake, *Geophys. Res. Lett.,* **28**, 3007-3010.